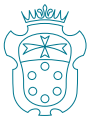

Scuola Normale Superiore

Classe di Scienze

PhD Thesis

Assessment of models and methodologies for the study of the effects of nuclear motions in molecular spectroscopies

A thesis submitted in fulfillment of the requirements
for the degree of Doctor of Philosophy
in
Methods and models for molecular sciences

Candidate:
Lorenzo Paoloni

Supervisor:
Prof. Vincenzo Barone

Co-Supervisor:
Prof. Sergio Abbate

Academic year 2019/2020

Contents

*The results and the text of this section can be found (with slight modifications) in *J. Chem. Theory Comput.*, **2019**, 15, 7, 4280-4294.

*The results provided in this subsection (together with more details concerning experimental and computational methods) can be found in *J. Phys. Chem. A*, **2020**, 124, 5, 1011-1024.

†Part of the results provided in this section (together with more details about experimental and computational methods) can be found in *Phys. Chem. Chem. Phys.*, **2019**, 21, 9419-9432.

‡The results provided in this section were published in *J. Chem. Theory Comput.*, **2020**, 16, 8, 5218-5226.

Introduction

Nowadays, the importance of spectroscopy in the field of physical chemistry is well known. During the XX century, the enormous advancements in the field of experimental spectroscopy have provided a pletora of powerful techniques to investigate features, properties and dynamics of molecular systems. Molecular systems are inherently complex, and the study of their interaction with electromagnetic radiation (which is the object of molecular spectroscopy) is a stimulating and very active field of research.

A classification of the experimental spectroscopies currently at disposal of the scientific community is not trivial: a useful classification criterium to identify a spectroscopic technique is the energy of the radiation employed. Another classification criterium is based on the experimental observables monitored during the measurement: the measurement of the absorbed radiation provides data which are different from the data obtained with the measurement of emitted radiation; distinct spectroscopies arise if the differential absorption, instead of the absorption of electromagnetic radiation, is measured. A distinction can be done between spectroscopic techniques that deal with non linear optical effects and spectroscopic techniques employed for the measurement of linear optical effects.

Many (if not all) of these techniques are sensitive to the nuclear configuration and motions of the molecular systems under investigation, although this sensitivity depends on the spectroscopic technique employed and on the molecular system studied. Besides the classification criteria employed, the main object of this work is the role played by nuclear configuration and motions in the context of molecular spectroscopy.

In this work the pivotal role of numerical calculations must be recognized and deserves further comments.

First of all, when an analytical solution of a theoretical formulation given to a scientific problem is not known, the access to a numerical solution allows the comparison (otherwise impossible) with the experimental data. In other words, numerical calculations enable to test a theoretical formulation with real-world results: this fact is one of the causes of the paramount role of computational science in fundamental research.

The need of numerical solutions for problems of chemical interest has given rise to the field of computational chemistry , recognizing a central role

to the development of computational models and their implementation. Effectiveness and robustness of such computational models must be tested and evaluated: in other words, a computational model must be validated.

The usefulness of the original results presented and discussed in this thesis is related also (but not exclusively) to their use for the validation of computational models. More generally, the results provided in this work (together with the review of pertinent and interesting results already available in literature) show the potential benefit of a synergic approach combining computational and experimental spectroscopy for the physico-chemical characterization of increasingly complex molecular systems.

The Born-Oppenheimer approximation

In molecular spectroscopy, the experimental measurements (due to absorption, emission or scattering of electromagnetic radiation) are rationalized in terms of transitions between molecular states. Therefore, the determination of these molecular states and their relation with nuclear configuration and nuclear motions must be preliminarily introduced. The starting point is the formulation (in atomic units) of the molecular hamiltonian in the non relativistic limit:[a]

$$\begin{aligned}\hat{H} = &-\frac{1}{2}\sum_{a=1}^{N}\frac{1}{m_a}\frac{\partial^2}{\partial \mathbf{r}_a^2} - \frac{1}{2}\sum_{i=1}^{N_{el}}\frac{\partial^2}{\partial \boldsymbol{\xi}_i^2} + \sum_{i=1}^{N_{el}}\sum_{j>i}^{N_{el}}\frac{1}{|\boldsymbol{\xi}_i - \boldsymbol{\xi}_j|} + \\ &+ \sum_{a}^{N}\sum_{b>a}^{N}\frac{Z_a Z_b}{|\mathbf{r}_a - \mathbf{r}_b|} - \sum_{a=1}^{N}\sum_{i=1}^{N_{el}}\frac{Z_a}{|\mathbf{r}_a - \boldsymbol{\xi}_i|} = \\ &= \hat{T}_n(\mathbf{r}) + \hat{T}_{el}(\boldsymbol{\xi}) + \hat{V}_{ee}(\boldsymbol{\xi}) + \hat{V}_{NN}(\mathbf{r}) + \hat{V}_{Ne}(\boldsymbol{\xi}, \mathbf{r}),\end{aligned} \tag{1}$$

where N is the number of nuclei and N_{el} the number of electrons in the molecular system under investigation, m_a the mass and $\mathbf{r}_a$ the position of the nucleus a, $\boldsymbol{\xi}_i$ the position of the i-th electron and Z_a is the (positive) charge of the nucleus a (equal to the atomic number of the corresponding atom).

The time evolution of the molecular system is described by the Time-Dependent Schrödinger equation (TDSE), which reads as follows (in atomic units):[b]

$$i\frac{\partial \Psi(\boldsymbol{\xi}, \mathbf{r}, t)}{\partial t} = \hat{H}\Psi(\boldsymbol{\xi}, \mathbf{r}, t), \tag{3}$$

[a] See, for example, eq. 2.2 in ref. 1. In atomic units, $\hbar$ (Planck's constant divided by 2π), m_e (the mass of the electron) and $-e$ (the charge of the electron) are set equal to one and can be omitted in the expression of the molecular hamiltonian (eq. 1).

[b] For a clear and general introduction to the employment of the TDSE, see ref. 2. As already mentioned above, in atomic units $\hbar = 1$. If other units are employed, $\hbar$ must be

where $\Psi(\boldsymbol{\xi}, \mathbf{r}, t)$ is the time-dependent molecular wave function. In the standard interpretation of quantum mechanics, assuming that $\Psi(\boldsymbol{\xi}, \mathbf{r}, t)$ is normalized, i.e.:

$$\int_{-\infty}^{+\infty} |\Psi(\boldsymbol{\xi}, \mathbf{r}, t)|^2 d\mathbf{r} d\boldsymbol{\xi} = 1, \tag{4}$$

$|\Psi(\boldsymbol{\xi}, \mathbf{r}, t)|^2$ is the probability density associated to the molecular system (with nuclear and electron positions specified, respectively, by $\mathbf{r}$ and $\boldsymbol{\xi}$) at time t. If $\Psi(\boldsymbol{\xi}, \mathbf{r}, 0)$ (the time-dependent molecular wave function at $t = 0$) is given, a complete solution of eq. 3 is the time-dependent wave function $\Psi(\boldsymbol{\xi}, \mathbf{r}, t)$ at all nuclear and electron positions ($\mathbf{r}$ and $\boldsymbol{\xi}$) and all times.

The molecular hamiltonian provided in eq. 1 is not time-dependent, because any external stimulus was neglected in eq. 1. Although the absence of external stimuli is an idealization,[a] it allows the formulation of a time-independent version of eq. 3 which can be solved in terms of stationary wave functions. With a time-independent hamiltonian, a general solution of eq. 3 can be written as follows:[b]

$$\Psi(\boldsymbol{\xi}, \mathbf{r}, t) = \Psi(\boldsymbol{\xi}, \mathbf{r}) \cdot e^{-iEt}. \tag{5}$$

Eq. 5 provides a solution of eq. 3 if E and $\Psi(\boldsymbol{\xi}, \mathbf{r})$ (the stationary molecular wave function) are solutions of the following eigenvalue problem (the time-independent Schrödinger equation, TISE):

$$\hat{H}\Psi(\boldsymbol{\xi}, \mathbf{r}) = E\Psi(\boldsymbol{\xi}, \mathbf{r}). \tag{6}$$

In Eq. 1, the contemporary dependence of $\hat{V}_{Ne}$ from the positions of nuclei and electrons does not allow a separation in an electronic term ($\hat{H}_{el}$) and a nuclear term ($\hat{H}_n$). This means that the solution of the corresponding eigenvalue problem leads to a set of eigenvectors $\Psi_n(\boldsymbol{\xi}, \mathbf{r})$ (the molecular wave functions) which cannot be partitioned in an electronic and a nuclear contribution. The use of the so-called Born-Oppenheimer (BO) approximation allows the partition of the time independent Schrödinger equation in the following manner:[c]

---

included in the TDSE and eq. 3 is rewritten as follows:

$$i\hbar \frac{\partial \Psi(\boldsymbol{\xi}, \mathbf{r}, t)}{\partial t} = \hat{H}\Psi(\boldsymbol{\xi}, \mathbf{r}, t). \tag{2}$$

[a] In the real world, a molecular system cannot be *perfectly* isolated: the effects due to the surrounding environment can be minimized, but they are *never* absent. However, in some cases these effects can be safely neglected.

[b] Eq. 5 is written in atomic units. In the general case (i.e. when $\hbar \neq 1$) the exponential factor on the right hand side (RHS) is $e^{-\frac{iEt}{\hbar}}$.

[c] An introduction to the separation of electronic and nuclear motions can be found in section 3.2 of ref. 3 (more specifically, the BO approximation is introduced in section

$$\begin{aligned}&\hat{H}_{el}\phi_m(\boldsymbol{\xi};\mathbf{r}) = \\ &[\hat{T}_{el}(\boldsymbol{\xi}) + \hat{V}_{ee}(\boldsymbol{\xi}) + \hat{V}_{NN}(\mathbf{r}) + \hat{V}_{Ne}(\boldsymbol{\xi},\mathbf{r})]\phi_m(\boldsymbol{\xi};\mathbf{r}) = E_m(\mathbf{r})\phi_m(\boldsymbol{\xi};\mathbf{r}),\end{aligned} \tag{7}$$

$$\hat{H}_n\chi_{mk}(\mathbf{r}) = [\hat{T}_n(\mathbf{r}) + E_m(\mathbf{r})]\chi_{mk}(\mathbf{r}) = E_m^k\chi_{mk}(\mathbf{r}), \tag{8}$$

Where the molecular wavefunction is factorized as follows:

$$\Psi_{mk}(\boldsymbol{\xi},\mathbf{r}) = \phi_m(\boldsymbol{\xi};\mathbf{r})\chi_{mk}(\mathbf{r}). \tag{9}$$

The dependence of $\hat{H}_{el}$ from $\mathbf{r}$ is only parametric, due to the absence of a differential operator involving nuclear coordinates in eq. 7. Therefore the electronic problem (eq. 7) can be solved fixing the positions $\mathbf{r}$ of the nuclei and the eigenvalues $E_m(\mathbf{r})$ are obtained solving out eq. 7 (also known as time independent electronic Schrödinger equation) and used for the solution of eq. 8 (known as time independent nuclear Schrödinger equation, TINSE).

The original work presented and discussed in this thesis is mainly related to the solution of the TINSE (eq. 8).[a] The assumption of the Born-Oppenheimer approximation allows the definition of a Potential Energy Surface (PES) for each electronic state m, namely the eigenvalues $E_m(\mathbf{r})$ of the electronic Schrödinger equation determines the potential energy which governs the motion of the nuclei in the electronic state m.

Structure of this thesis

This thesis is organized in three chapters:

- In Chapter 1 a series of methodologies suitable for the optimization of molecular geometries and for the construction of PESs are presented and discussed: in other words, changes of the values of the potential term $E_m(\mathbf{r})$ at varying of $\mathbf{r}$ are considered; original applications concerning the study of cyclic molecular systems through curvilinear Cremer-Pople coordinates are illustrated and discussed (these results were published in *J. Chem. Theory Comput.*, **2019**, 15, 7, 4280-4294);

3.2.3 of ref. 3). It should be noticed that the theoretical assumptions commonly employed to perform the separation of electronic and nuclear motions leads to subtle conceptual problems concerning the structure of molecules.[4] A detailed discussion of these aspects is beyond the scope of this thesis: however, attempts to extract (at least) elements of molecular structure from all-particle (nuclei and electrons) wave functions were carried out and are available in literature.[5,6]

[a] Exceptions are section 3.1 (which is devoted to the introduction of the electron propagator theory for the solution of the electronic problem) and sections B.3 and B.4 of appendix B (in which a formalism suitable for the calculation of VCD intensities is introduced).

- In Chapter 2, after a brief discussion of the nuclear kinetic energy term $\hat{T}_n(\mathbf{r})$ the solution of the nuclear Schrödinger equation for ground electronic states is discussed, particularly for what concerns local modes approximation (LMA) and Vibrational second-order level of perturbation theory (VPT2); Calculations of properties associated to transitions between two vibrational states pertaining to the same electronic states are discussed; original applications to organic and organometallic systems (published in *J. Phys. Chem. A*, **2020**, 124, 5, 1011-1024 and *Phys. Chem. Chem. Phys.*, **2019**, 21, 9419-9432) are illustrated and a systematic comparison between calculated and experimental spectra is presented;

- In Chapter 3, transitions between two different electronic states are considered; the time independent approach to the calculation of the vibrational structure associated to a transition between two different electronic states is presented and discussed; original applications to a number of rigid organic molecules (published in *J. Chem. Theory Comput.*, **2020**, 16, 8, 5218-5226) are presented, providing additional evidences about the importance of a suitable modelization of the vibrational fine structure in order to accurately reproduce experimental Ultraviolet Photoelectron Spectra (UPS).

Chapter 1

The exploration of the conformational space of a molecular system

Assuming the validity of the Born-Oppenheimer approximation, the ground-state conformational space of a single molecular system can be represented with a global PES, an hypersurface which contains a set of points providing the energy of the single molecular system as a function of $3N-6$ non-redundant internal coordinates (N is the total number of atoms of the system; the number of internal coordinates is reduced to $3N-5$ if the object of the study is a simple biatomic molecule). Several approaches have been proposed for the construction of global PESs (see, for example, ref. 7), with the aim of a good compromise between the computational cost and the accuracy of the result of a series of calculations. The choice of the most suitable approach depends on the specific molecular system under consideration and on the observables of interest. In this chapter various approaches for the construction of global PESs (and of n-dimensional cuts of global PESs) are considered and discussed, together with the description of a number of applications.

The most obvious approach to the problem addressed here is a grid approach with a discretization along each internal coordinate q_i (where $i = 1, 2, ..., 3N-6$). If a fixed number of single points k for each coordinate is used the number of points needed to map out the global PES is equal to:

$$k^{3N-6} = e^{(3N-6)\cdot \ln k} \tag{1.1}$$

The number of single points needed to construct the global PES has an exponential increase with the number of internal coordinates, making this approach currently unfeasible for more than 6 internal coordinates (i.e. for the study of molecules with more than 4 atoms). However, the possibility of exploit a grid approach for a molecular system with more than 4 atoms is still

feasible if a reduced dimensionality approach is adopted (see section 1.2). In some cases, a good reproduction of the experimental observables could be obtained with a reconstruction of the potential energy surface around the energy minimum/a at harmonic or beyond the harmonic (see section 1.1) level.

1.1 Approximation of PESs through the knowledge of their minima

When the approach chosen is the expansion of the PES around an energy minimum, the first task to be performed is an unconstrained optimization of the molecular structure (see subsection 1.1.1) aiming at obtaining the molecular structure associated with a minimum of the PES (i.e. an energy minimum). This essential task can be carried out using a variety of softwares for quantum chemical calculations. The localization of more than one minimum on the same PES is often required for a complete description of the molecular system under investigation. When all the relevant minima of the PES have been located, an approximated expansion around each energy minimum can be performed (see subsection 1.1.2).

1.1.1 Optimization of molecular structures

For what concerns the optimization of molecular structures several computational strategies have been devised (see, for example, ref. 8) and are implemented in many of the available suites of programs for quantum chemical calculations.

A review of the algorithms available to efficiently optimize molecular structures is beyond the scope of this thesis, but a general discussion of the factors affecting the efficiency of an optimization task and a brief presentation of the algorithm employed to perform the calculations reported and discussed in this thesis must be provided.

With the exception of direct search methods (i.e. energy-only algorithms which employ only the energy value, obtained as a scalar function of $3N-6$ internal coordinates if the validity of the Born-Oppenheimer approximation is assumed)[9–11], the geometry optimization methods employed in quantum chemistry calculations require the calculation of the derivatives of the energy with respect to the nuclear displacements (derivative-based geometry optimization methods).

The knowledge of $\mathbf{g}$ and $\mathbf{H}$ allows the construction of a local quadratic approximation of the PES:

$$E(\mathbf{x}) = E(\mathbf{x}_0) + \mathbf{g}_0^T \Delta\mathbf{x} + \frac{1}{2}\Delta\mathbf{x}^T \mathbf{H}_0 \Delta\mathbf{x} \tag{1.2}$$

where $\mathbf{g}_0$ (with elements $\frac{\partial E}{\partial x_i}$)and $\mathbf{H}_0$ (with elements $\frac{\partial^2 E}{\partial x_i \partial x_j}$)are, respectively, the gradient and the hessian (expressed in cartesian coordinates) at $\mathbf{x}_0$ and $\Delta\mathbf{x} = \mathbf{x} - \mathbf{x}_0$. Looking at eq. 1.2 it is clear that $\mathbf{g}$ and $\mathbf{H}$ can be used to characterize the point of the PES labeled with the subscript 0. More specifically, a molecular structure with coordinates $\mathbf{x}_0$ is characterized as a minimum if all the components of the gradient vector $\mathbf{g}_0$ are 0 (i.e. $\frac{\partial E}{\partial x_i} = 0$ for $i = 1, ..., 3N$)[a] and the $3N - 6$ eigenvalues that differ from zero[b] of the $\mathbf{H}_0$ square matrix are positive.

The local quadratic approximation of the PES is the basis for most non-linear optimization algorithm. If eq. 1.2 is differentiated with respect to the coordinates the following approximation of the gradient is obtained:

$$\mathbf{g} = \mathbf{g}_0 + \mathbf{H}_0 \Delta\mathbf{x} \tag{1.3}$$

with $\mathbf{g} = \mathbf{g}(\mathbf{x})$ and $\mathbf{g}_0 = \mathbf{g}(\mathbf{x}_0)$. At a stationary point $\mathbf{g} = 0$ and eq. 1.3 become:

$$\Delta\mathbf{x} = -\mathbf{H}_0^{-1}\mathbf{g}_0 \tag{1.4}$$

In eq. 1.4, $\Delta\mathbf{x}$ is the displacement to the minimum known as the Newton step. The assumption of a quadratic nature for the PES is an approximation: real PES are rarely quadratic and various Newton steps are required to reach a stationary point.

Eq. 1.4 is the central equation of two classes of geometry optimization algorithms: Newton and quasi-Newton methods[8]. The difference between the two approaches concerns the hessian calculation: $\mathbf{H}_0$ in eq. 1.4 is calculated each time at the current point when a Newton method is employed, while in the case of quasi-Newton methods an approximated $\mathbf{H}_0$ is used in eq. 1.4 and this approximated $\mathbf{H}_0$ is updated at each step (almost always exploiting the gradient vector). It should be underlined that the step will be towards a minimum if and only if the hessian $\mathbf{H}_0$ is positive defined (i.e. all its eigenvalues are positive)[c]. This means that the method can converge also to a saddle point or to a maximum of the PES: therefore, the optimization step can be also directed towards a first order saddle point (i.e. a transition

[a] for a numerical implementation, this condition means that each of the $3N$ components of the $\mathbf{g}$ vector must be smaller than a certain small value: when all the components of $\mathbf{g}$ are smaller than this value, the gradient is considered to be numerically equal to 0

[b] the 6 values equal to 0 are related to the 3 rotations and the 3 translations of the molecular system

[c] this drawback is not a general feature of derivative-based optimization methods: for example, the simplest derivative-based optimization method (called steepest descent) follows the direction of $-\mathbf{g}_0$ and, therefore, must converge to a minimum. The drawback of the steepest descent method is that, near the minimum, the convergence to the desired solution is extremely slow. Therefore, the efficiency of steepest descent method frequently turns out to be lower than that of Newton and quasi-Newton methods.

state), but if and only if the hessian has one and only one negative eigenvalue (and the corresponding eigenvector is roughly parallel to the reaction path).

In what follows a concise exposition of the default algorithm implemented in the GAUSSIAN16 suite of programs[12] (for quantum chemical methods for which analytical gradients are available) is provided. Technical details (formulae for the determination of the approximated hessian for quasi-Newton methods, step-size control exc.) and a description of the others existing derivative-based optimization algorithms can be found elsewhere (see, for example, ref. 8 and references therein).

The attempt of exploiting the advantages (in terms of computational cost and accuracy) and minimizizing the drawbacks of a series of optimization methodologies led to a strategy based on the employment of an hybrid geometry optimization scheme[13]: the choice of one of the three algorithms here described is done on the basis of suitable switching criteria optimized from tests on the set of molecules reported in ref. 14.

At the beginning of the geometry optimization the Rational Function Optimization (RFO) method is used[a]. In the RFO method the quadratic approximation of eq. 1.2 is replaced by a rational function of the following form[b]:

$$E(\mathbf{x}) - E(\mathbf{x}_0) = \frac{\mathbf{g}_0^T \Delta\mathbf{x} + \frac{1}{2}\Delta\mathbf{x}^T \mathbf{H}_0 \Delta\mathbf{x}}{1 + \Delta\mathbf{x}^T \mathbf{S} \Delta\mathbf{x}} \tag{1.5}$$

It can be easily shown (with $\Delta E = E(\mathbf{x}) - E(\mathbf{x}_0)$) that $\frac{\partial \Delta E}{\partial x_i} = g_i$ and $\frac{\partial^2 \Delta E}{\partial x_i \partial x_j} = H_{ij}$ at $\mathbf{x}_0$. The same results hold for eq. 1.2. Alternatively, a matrix formulation of eq. 1.5 can be given:

$$\Delta E = \frac{1}{2} \frac{\begin{bmatrix} \Delta\mathbf{x} & 1 \end{bmatrix} \begin{bmatrix} \mathbf{H} & \mathbf{g} \\ \mathbf{g}^T & 0 \end{bmatrix} \begin{bmatrix} \Delta\mathbf{x} \\ 1 \end{bmatrix}}{\begin{bmatrix} \Delta\mathbf{x} & 1 \end{bmatrix} \begin{bmatrix} \mathbf{S} & 0 \\ 0 & 1 \end{bmatrix} \begin{bmatrix} \Delta\mathbf{x} \\ 1 \end{bmatrix}} \tag{1.6}$$

The matrix formulation of the fundamental equation for the RFO method can be easily obtained minimizing eq. 1.5 with respect to $\Delta\mathbf{x}$ (i.e. $\frac{d\Delta E}{d\Delta\mathbf{x}} = 0$ is required):

$$\begin{bmatrix} \mathbf{H} & \mathbf{g} \\ \mathbf{g}^T & 0 \end{bmatrix} \begin{bmatrix} \Delta\mathbf{x} \\ 1 \end{bmatrix} = \xi \begin{bmatrix} \mathbf{S} & 0 \\ 0 & 1 \end{bmatrix} \begin{bmatrix} \Delta\mathbf{x} \\ 1 \end{bmatrix} \tag{1.7}$$

eq. 1.7 is an eigenvalue equation, with $\mathbf{S}$ tipically chosen as a diagonal matrix[16] and $\xi = 2\Delta E$. If $\mathbf{S}$ is chosen as a constant times the identity matrix

[a] An early version of this method was first proposed, discussed and clearly illustrated in ref. 15; to the best of the author's knowledge, the name Rational Function Optimization to denote the method was introduced in ref. 16.

[b] From the mathematical point of view, the idea is to replace a Taylor expansion (eq. 1.2) with a Padé approximant of order [2/2] (eq. 1.5) of the energy.

the top row of eq. 1.7 can be written in the following form:

$$\Delta\mathbf{x} = (\xi\mathbf{I} - \mathbf{H}_0)^{-1}\mathbf{g}_0 \tag{1.8}$$

the eigenvalue ξ of the eq. 1.7 is equal to twice the change of energy associated to the RFO step $\Delta\mathbf{x}$ (which is determined from the eigenvector of eq. 1.7 associated to the eigenvalue). The choice of the eigenvalue and the eigenvector to be used during the optimization depends on the nature of the stationary point searched: if the target is a minimum point, the lowest eigenvalue ξ and the associated eigenvector are used for each step; if the optimization of a first-order saddle point is attempted (i.e. a transition state search)[a], the second lowest eigenvalue ξ and its associated eigenvector are used[16]. It is worth to mention two important feature of the RFO method: an algorithm based on this method can be shown to converge quadratically[16] and can be used to reach and optimize the desired stationary point even if at the starting point the hessian has not the right number of positive eigenvalue. For example, if the hessian has one negative eigenvalue the iterative use of the Newton step can converge only to a transition state, while the RFO step (with the choice of the lowest eigenvalue and its associated eigenvector as solutions of the eigenvalue eq. 1.7) can be iteratively employed to reach a minimum.

The optimization algorithm implemented in the GAUSSIAN16 suite of programs exploits the RFO method for the first and the subsequent steps of an optimization until the root-mean-square (RMS) force experimented by the molecular structure under investigation at a given step is calculated to be less than $10^{-2}au$: when the RMS force decreases below this value, the optimization algorithm switch to the use of the Geometry Optimization Using Energy-Represented Direct Inversion in the Iterative Subspace (GEDIIS) method[13].

The family of Direct Inversion in the Iterative Subspace (DIIS) methods has been introduced in the community of computational chemistry by Pulay[b]. The idea is to construct an improved solution to the optimization problem at hand as a suitable linear combination of the results from prior iterations. When a DIIS method is employed, the nuclear positions at the next optimization step can be expressed in the following manner:

[a] In order to increase the stability of the RFO method when the search and the optimization of a saddle point is attempted a partitioned RFO method has been proposed[8,16,17]; using this partitioned RFO method the possibility of follow other modes (different from the lowest hessian mode) during the search of a first-order saddle point arise: with this aim, another approach based on the original RFO method with a specific scaling of the coordinate along the hessian mode of interest has been proposed[18].

[b] An early version suitable for the solution of the Self-Consistent Field (SCF) problem in the context of electronic structure theory can be found in ref. 19. An improvement of the first version (still devoted to the solution of the SCF problem) is reported in ref. 20. To the best of the author's knowledge the first application of a DIIS method to the geometry optimization problem is presented and briefly discussed in ref. 21.

$$\mathbf{x}_{n+1} = \sum_{i=1}^{n} c_i(\mathbf{x}_i + \mathbf{e}_i) = \overbrace{\sum_{i=1}^{n} c_i \mathbf{x}_i}^{\mathbf{x}^*} + \overbrace{\sum_{i=1}^{n} c_i \mathbf{e}_i}^{\Delta\mathbf{x}} \qquad \text{with} \qquad \sum_{i=1}^{n} c_i = 1 \tag{1.9}$$

The coefficients c_i are obtained through a constrained minimization of a suitable working function: the specific DIIS method applied to the geometry optimization is determined by the working function used. The GEDIIS method[a] employs an energy function as working function and enforces the coefficients c_i to be positive definite[b]. To derive an expression for the working function, a first-order expansion at $\mathbf{x}_i$ of the energy of the structure at the next point of the optimization is reported in eq. 1.10.

$$E(\mathbf{x}^*) = E(\mathbf{x}_i) + (\mathbf{x}^* - \mathbf{x}_i)\mathbf{g}_i \tag{1.10}$$

$E(\mathbf{x}_i)$ and $\mathbf{g}_i$ denote, respectively, the energy and the gradient (with respect to the nuclear displacements) of the structure $\mathbf{x}_i$. If both sides of eq. 1.10 are multiplied by c_i and a summation over n points (the n geometries of the previous optimization steps) is taken, the result is (using $\mathbf{x}^* = \sum_1^n c_i \mathbf{x}_i$, see eq. 1.9):

$$E(\mathbf{x}^*) = \sum_{i=1}^{n} c_i \left[E(\mathbf{x}_i) + \Big(\sum_{j=1}^{n} c_j \mathbf{x}_j\Big)\mathbf{g}_i - \mathbf{x}_i \mathbf{g}_i \right] \tag{1.11}$$

After further manipulations the GEDIIS working function is obtained:

$$\begin{aligned}
E(\mathbf{x}^*) &= \sum_{i=1}^{n} c_i E(\mathbf{x}_i) + \sum_{i,j=1}^{n} c_i c_j \mathbf{x}_j \mathbf{g}_i - \sum_{i=1}^{n} c_i \mathbf{x}_i \mathbf{g}_i \\
&= \sum_{i=1}^{n} c_i E(\mathbf{x}_i) + \frac{1}{2}\sum_{i,j=1}^{n} c_i c_j \mathbf{x}_j \mathbf{g}_i + \frac{1}{2}\sum_{i,j=1}^{n} c_j c_i \mathbf{x}_i \mathbf{g}_j - \sum_{i,j=1}^{n} c_i c_j \mathbf{x}_i \mathbf{g}_i \\
&= \sum_{i=1}^{n} c_i E(\mathbf{x}_i) + \frac{1}{2}\sum_{i,j=1}^{n} c_i c_j \mathbf{x}_j \mathbf{g}_i + \frac{1}{2}\sum_{i,j=1}^{n} c_j c_i \mathbf{x}_i \mathbf{g}_j \\
&\qquad - \frac{1}{2}\sum_{i,j=1}^{n} c_i c_j \mathbf{x}_i \mathbf{g}_i - \frac{1}{2}\sum_{i,j=1}^{n} c_i c_j \mathbf{x}_j \mathbf{g}_j \\
&= \sum_{i=1}^{n} c_i E(\mathbf{x}_i) - \frac{1}{2}\sum_{i,j=1}^{n} c_i c_j (\mathbf{x}_i - \mathbf{x}_j)(\mathbf{g}_i - \mathbf{g}_j)
\end{aligned} \tag{1.12}$$

[a] The application of the algorithm presented and discussed in ref. 13 follows the application of the same idea to the electronic problem (SCF-EDIIS for SCF convergence)[22].

[b] In this manner the optimization step can be viewed as an interpolation. If no constraint are imposed on the sign of c_i the optimization step is an extrapolation: when the geometry is far from convergence an extrapolation can led to an erroneus step away from the optmized geometry.

The last term of eq. 1.12 can be easily written in matrix form:

$$E(\mathbf{x}^*) = \mathbf{c}^T\mathbf{E} - \frac{1}{2}\mathbf{c}^T\mathbf{A}\mathbf{c} \tag{1.13}$$

In eq. 1.13, $\mathbf{A}$ is a square matrix of dimensions $n \times n$ with elements $A_{ij} = (\mathbf{x}_i - \mathbf{x}_j)(\mathbf{g}_i - \mathbf{g}_j)$ and $\mathbf{E}$ is a vector with dimension equal to n. Therefore the following optimization problem must be solved:

$$\inf\left\{\mathbf{c}^T\mathbf{E} - \frac{1}{2}\mathbf{c}^T\mathbf{A}\mathbf{c}, c_i \geqslant 0, \sum_{i=1}^{n} c_i = 1\right\} \tag{1.14}$$

The problem can be easily solved employing the method of Lagrange multipliers. The coefficients c_i are obtained solving out the following matrix problem:

$$\begin{bmatrix} \mathbf{A} & \mathbf{1} \\ \mathbf{1}^T & 0 \end{bmatrix} \begin{bmatrix} \mathbf{c} \\ \lambda \end{bmatrix} = \begin{bmatrix} \mathbf{E} \\ 1 \end{bmatrix} \tag{1.15}$$

where $\mathbf{1}$ is a vector of dimension n whose elements are equal to 1 and the dimensions of the first matrix on the left hand side of eq. 1.15 are $(n+1) \times (n+1)$. The geometry $\mathbf{x}^*$ is associated with the optimal energy only to a first-order approximation: the second order correction is estimated through an RFO step[a]

$$\mathbf{x}_{n+1} = \mathbf{x}^* + \Delta\mathbf{x} = \sum_{i=1}^{n} c_i\mathbf{x}_i - \sum_{i=1}^{n} c_i \frac{\mathbf{g}_i}{\mathbf{H} - \xi} \tag{1.16}$$

if the RMS value of the RFO step $\Delta\mathbf{x}$ (see eq. 1.8 and eq. 1.16) is below the threshold of $2.5 \cdot 10^{-3} a.u.$ for the latest point, the optimization algorithm switch to the use of a modified version of the Geometry Optimization using Direct Inversion on the Iterative Subspace (GDIIS)[23] method until convergence.

The idea behing the GDIIS method is to minimize the square of the residuum vector $\Delta\mathbf{x}$ (see eq. 1.9). The square of the residuum vector can be written as follows:

$$|\Delta\mathbf{x}|^2 = \Big(\sum_{i=1}^{n} c_i\mathbf{e}_i\Big)\Big(\sum_{i=1}^{n} c_j\mathbf{e}_j\Big) = \sum_{i,j=1}^{n} c_i c_j A_{ij} \tag{1.17}$$

where $A_{ij} = \mathbf{e}_i^T\mathbf{e}_j$ are elements of the square matrix $\mathbf{A}$ of dimensions $n \times n$. The solution of the following optimization problem:

[a] Note that the RFO step estimates the distance between $\mathbf{x}^*$ and the minimum structure; in GAUSSIAN16, the hessian in eq. 1.16 is calculated with the updating method described in ref. 13 by default.

$$\inf\left\{\mathbf{c}^T\mathbf{A}\mathbf{c}, \sum_{i=1}^{n} c_i = 1\right\} \tag{1.18}$$

can be obtained with the method of Lagrange multipliers. The coefficients c_i are the solutions of the matrix problem given in eq. 1.19.

$$\begin{bmatrix} \mathbf{A} & \mathbf{1} \\ \mathbf{1}^T & 0 \end{bmatrix} \begin{bmatrix} \mathbf{c} \\ \lambda \end{bmatrix} = \begin{bmatrix} \mathbf{0} \\ 1 \end{bmatrix} \tag{1.19}$$

where $\mathbf{0}$ is a vector of dimension n whose elements are equal to 0. In the original version of the GDIIS method[21] $\mathbf{e}_i$ is defined to be equal to the newton step at the point i ($\mathbf{e}_i = -\mathbf{H}_i^{-1}\mathbf{g}_i$), while in the modified version implemented in GAUSSIAN16 the RFO step is employed ($\mathbf{e}_i = (\xi\mathbf{I} - \mathbf{H}_i)^{-1}\mathbf{g}_i$)[23]. A detailed discussion of the acceptance criteria and of the method chosen for the hessian updating[23] is beyond the scope of this thesis.

The efficiency of a geometry optimization is relevantly affected by the system of coordinates employed[8]. An inspection of the hessian matrix can be used to evaluate if a certain coordinate system is suitable for an efficient geometry optimization. A relevant decrease of the efficiency can be due to a strong coupling between coordinates (in this case, the hessian exhibits off-diagonal elements of magnitude similar to that of diagonal elements), to a strong anharmonicity (relevant changes of the hessian from one point to the next one during the optimization) or to a combination of stiff and flexible coordinates (the eigenvalues of the hessian are a combination of very small and very large numbers).

A detailed discussion of this topic is beyond the scope of this thesis, but for the sake of completeness the coordinate systems employed for the optimization of almost all the geometries of the chemical systems considered in this thesis have to be specified. By default, optimizations carried out with GAUSSIAN16 are performed in a system of redundant internal coordinates (a detailed description is given in ref. 24)[a]. A different coordinate system to carry out the geometry optimization can be easily specified in the input file.

The conversion from redundant internal ($\mathbf{s}$) to cartesian coordinates ($\mathbf{r}$) cannot be trivially accomplished due to the nonlinear relationship between redundant (and curvilinear) internal and cartesian coordinates (see Eq. A.1). When an optimization is carried out in redundant internal coordinates, a reliable protocol to provide the nuclear positions in cartesian coordinates is needed. This task can be performed iteratively, with a scheme[27] based on the following expression:

[a] Although the usefulness of redundant internal coordinates for geometry optimizations has been recognized by Schlegel in ref. 25, the possibility of carrying out optimizations *directly* in redundant internal coordinates has been opened by the article of Pulay and Fogarasi[26].

$$\mathbf{r}_{k+1} = \mathbf{r}_k + (\mathbf{B}^T)^{-1}{}_k(\mathbf{s} - \mathbf{s}_k). \tag{1.20}$$

Where $\mathbf{s}$ is the new geometry in internal coordinates and the expression is employed iteratively: the first step ($k = 1$) is carried out with the old cartesian coordinates ($\mathbf{r}_{k=1}$), the old $\mathbf{B}$ matrix ($(\mathbf{B}^T)^{-1}{}_{k=1}$) and the old internal coordinates ($\mathbf{s}_{k=1}$); the iteration is stopped when the difference $\mathbf{s} - \mathbf{s}_k$ (where $\mathbf{s}_k$ is generated from $\mathbf{r}_k$ at each k-th iteration) is below a given threshold value. This iterative protocol requires the construction and the inversion (through eq. A.8) of the $\mathbf{B}$ matrix at each step[a].

The computational cost associated to an optimization calculation depends also on the availability of the analytic gradients for the chosen calculation method[b]. However, even if the analytical gradients are not available for the chosen calculation method, the use of a gradient-based optimization method (with a numerical evaluation of the gradient vector) can be computationally cheaper than a direct search method (whose efficiency decreases as the number of degree of freedom increases)[32].

Another important aspect is the starting point (i.e. the initial molecular structure) of a geometry optimization. The choice of the initial geometry affects the result of the optimization (i.e. the specific minimum of the global PES reached: this is true if and only if the PES of the molecular system studied has more than one minimum) and the number of steps needed to reach a minimum. This means that to locate all the relevant minima of the PES of a system (i.e. all the minima with comparable energies separated by low energy barriers) without resorting to a grid approach, a clever selection of the starting points of a series of optimizations is needed. General reviews on this important topic can be found elsewhere (for an introduction, see ref. 33) .

1.1.2 PESs approximation around their minima

After the first step discussed in the previous section, various methods can be employed to approximate the structure of the PES of the molecular system

[a] when the geometry optimization is carried out in the context of a quantum chemical calculation the computational bottleneck is not related to this specific point; otherwise, with the adoption of eq. 1.20 the transformation from internal to cartesian coordinates can be rather expensive from the computational point of view due to the repeated calculation of the inverse of $\mathbf{B}$ at each iteration; two possible solutions to this problem are: (i) the retaining of the original inverse throughout all the iterations (already suggested in ref. 27) with the consequence of an higher number of iterations needed to reach the convergence [28]; (ii) the exploitation of a subset of intermediate primitive internal coordinates adopted only for the transformation from internal to cartesian coordinates, avoiding the expensive inversion of a $\mathbf{B}$ matrix (proposed and discussed in ref. 28)

[b] The importance of this problem was recognized very early by Bratoz ; the first formulations of analytical gradients of the energy with respect to nuclear displacement for the Hartree-Fock method are given in ref. 29 and ref. 30; for DFT methods see ref. 31 and references therein.

of interest in the neighborhood of an energy minimum: a concise review of the most popular ones is provided in this section.

A useful method is based on the employment of the energy derivatives with respect to nuclear coordinates in order to construct an approximation of the PES through a finite number of elements of a Taylor series expansion of the potential energy. In this framework, the potential energy term can be written in the following way:

$$\begin{aligned}\hat{V}(\mathbf{Q}) =& \frac{1}{2!}\sum_{k=1}^{3N-6}\left(\frac{\partial^2\hat{V}}{\partial {Q_k}^2}\right)_{\mathbf{0}} {Q_k}^2 + \\ & \frac{1}{3!}\sum_{k=1}^{3N-6}\sum_{j=1}^{3N-6}\sum_{i=1}^{3N-6}\left(\frac{\partial^3\hat{V}}{\partial Q_k \partial Q_j \partial Q_i}\right)_{\mathbf{0}} Q_k Q_j Q_i + \\ & \frac{1}{4!}\sum_{k=1}^{3N-6}\sum_{j=1}^{3N-6}\sum_{i=1}^{3N-6}\sum_{l=1}^{3N-6}\left(\frac{\partial^4\hat{V}}{\partial Q_k \partial Q_j \partial Q_i \partial Q_l}\right)_{\mathbf{0}} Q_k Q_j Q_i Q_l.\end{aligned} \tag{1.21}$$

In Eq. 1.21, the Taylor series has been truncated at the fourth order and the potential energy is expressed as a function of normal coordinates[a]. If the harmonic approximation is employed, the expression given in Eq. 1.21 is further truncated and only the second order term is retained. Second order derivatives of the energy with respect to nuclear coordinates can be routinely obtained employing several commercial softwares. Depending on the level of theory employed to explore the PES of the molecular system of interest, analytic second order derivatives of the energy with respect to the nuclear coordinates can be available or not[b]: in the case of the Gaussian[12] suite of programs, analytic second order derivatives are available for all the commonly used Density Functional Theory (DFT) methods. Despite some efforts in this direction[c], suitable analytic expression for third and fourth order derivatives of the energy with respect to the nuclear coordinates are

[a] A system of normal coordinates is a system of rectilinear internal coordinates defined as $\mathbf{Q} = \mathbf{L}(\mathbf{r} - \mathbf{r}^{eq})$ (see also section A.1 of appendix A). This coordinate system is carefully introduced and discussed in ref. 34. However, the convention adopted in ref. 34 to label the physical quantities of interest is different: in particular, $\mathbf{L}$ is employed for the transformation from normal to internal coordinates (see eq. 2 of appendix VIII in ref. 34), while $\mathbf{l}$ is employed for the transformations between normal coordinates and mass weighted cartesian coordinates. In this thesis, the dependence from the nuclear masses is left implicit (see appendix A).

[b] In some cases the analytic expression of second order derivatives are unknown, or an expression of the analytic second order derivatives for a given quantum chemical calculation method can be known and available in literature but not yet implemented in a certain commercial software.

[c] the theoretical formulation and the implementation of third and fourth order derivatives have been proposed for the Restricted Hartree-Fock method[35–37] and for DFT methods[38].

currently not available on commercial softwares, and therefore their calculation is performed numerically: this means that additional single-point calculations are needed in the neighborhood of the minimum[a].

The expansion of the potential energy term given in Eq. 1.21 suggests a computationally feasible protocol (at least for molecular systems up to medium size) to obtain an anharmonic approximation of the PES[39], but has two relevant drawbacks: first, the expression given in Eq. 1.21 has not the correct asymptotic behaviour (it diverges while the real potential reach a constant limiting value); second, when a strongly anharmonic region of a PES is considered, the higher order terms neglected in Eq. 1.21 are not negligible if an accurate approximation of the PES in these regions is needed.

To overcome the problems just mentioned, a more flexible expansion of the potential energy term can be employed:[b]

$$\begin{aligned} V(Q_1,...,Q_{3N-6}) =& V_0 + \sum_{i=1}^{3N-6} V_i(Q_i) + \sum_{j=1}^{3N-6}\sum_{i<j} V_{ij}(Q_i,Q_j) + \\ &+ \sum_{k=1}^{3N-6}\sum_{j<k}\sum_{i<j<k} V_{ijk}(Q_i,Q_j,Q_k) + ... \end{aligned} \tag{1.22}$$

Where the following relations holds:

$$V_i(Q_i) \equiv V(Q_i, Q_m = 0) \quad \text{with} \quad m \neq i. \tag{1.23}$$

$$V_{ij}(Q_i,Q_j) \equiv V(Q_i,Q_j,Q_m=0) - V_i - V_j \quad \text{with} \quad m \neq i,j. \tag{1.24}$$

$$\begin{aligned} V_{ijk}(Q_i,Q_j,Q_k) \equiv& V(Q_i,Q_j,Q_k,Q_m=0) - V_{ij} - V_{jk} - \\ & V_{ik} - V_i - V_j - V_k \quad \text{with} \quad m \neq i,j,k. \end{aligned} \tag{1.25}$$

The expression given in Eq. 1.22 is more flexible than a truncated Taylor series, but suggests a time-consuming, computationally expensive route. An example of a currently available implementation of a PES approximation

[a] More specifically, the protocol implemented in Gaussian is based on the calculation of second order derivatives of the energy with respect to the nuclear coordinates (i.e. harmonic frequency calculations) for $2(3N-6)+1$ points: the first calculation is carried out at the optimized geometry of the molecular system; the others are performed for geometries corresponding to a small displacement along each normal coordinate in both the directions (i.e. $-\delta Q_i$ and $+\delta Q_i$); it is clear that this approach is computationally feasible only if an analytic expression for the calculation of second order derivatives is implemented (as it is in the case of the Gaussian suite of programs for DFT-based methods).

[b] See, for example, eqs. 2-3 of ref. 40.

based on Eq. 1.22 can be found in ref. 41[a]. The relevant computational cost of a strategy based on Eq. 1.22 has limited its usefulness to applications for which the availability of an extremely accurate PES representation is needed (such as the solution of the nuclear schröedinger equation by variational methods).[41,42]

1.2 Construction of n-dimensional cuts of PESs through a grid approach

Although an accurate, local approximation of a PES in the neighborhoods of the most relevant energy minima is useful and allow (as part of the nuclear hamiltonian of the molecular system of interest) the calculation of reliable values of some important experimental observables, a suitable methodology to take into account the shape and the values of the global PES also in regions that are far from the minima (often between two of them) is often needed to reproduce experimental observables in the context of high-resolution molecular spectroscopy (even in the case of stationary, not time-resolved techniques).

Although the sampling of the entire global PES of a molecular system with more than 4 atoms is computationally challenging[b], the sampling of one (1D-PES) or two (2D-PES) dimensional cuts of a PES is feasible and useful for the study of larger molecular systems. In this case, the PES is sampled at fixed values of one (in the case of 1D-PES) or two (in the case of 2D-PES) internal variables, chosen to give a suitable description of a physicochemical phenomenon under investigation; all the other variables describing the nuclear configuration of the molecular system of interest are optimized: therefore, a constrained optimization with respect to the energy of the investigated molecular system is performed for each of the chosen sampling points. An estimation of n-dimensional cuts of a PES at a given level of theory can be obtained with a fit of the energy values calculated at each sampling points as a function of the fixed internal variables. Despite its apparent simplicity, there are some pivotal choices behind this approach which determine the usefulness and the meaningfulness of the results. More specifically:

- **Choice of the internal coordinates employed for the sampling of the n-dimensional cut of the PES:** this choice depends on the phenomenon and the molecular system under investigation, and its

[a] the implementation described in ref. 41 is based on a polynomial fit for each of the V_i, V_{ij}, V_{ijk} and V_{ijkl} terms; despite the efforts devoted to optimize the entire procedure, the computational cost limits the usefulness of this approach to small molecular systems (at least for a full-dimensional calculation).

[b] The redundancies of the configuration space can be exploited in order to obtain global PESs of molecular systems with more than 4 atoms which contains identical atoms.[43]

importance for the meaningfulness of the computational analysis here considered cannot be overestimated. These coordinates are often chosen in order to give a suitable description of a low energy path (and of its neighborhoods) of particular significance for the phenomenon under investigation. One or two suitable primitive internal coordinates are often a good choice (for example, the careful choice of a dihedral angle is often a good choice for the description of a internal rotation such that of a methyl group), but sometimes the employment of more complex coordinate systems is needed: this is the case of the ring puckering motion of 5-term ring systems presented and discussed in the next section.

- **Choice of the sampling method:** besides the obvious choice of a uniform, regular sampling there are many other possible choices for the sampling of the n-dimensional cut of the PES. The aim is to identify and to sample the nuclear configurations allowing the construction of an accurate portion of the PES with a number of points as small as possible. For example, if a greater accuracy in the reproduction of a low energy region is required, a protocol which increases the number of sampling points in a low energy region at expense of the number of sampling points employed for an high energy region would be desirable.

- **Choice of the analytical representation of the n-dimensional cut of the PES:** generally speaking, the idea is to adopt an analytical representation with a small, physically meaningful number of parameters. Various solutions have been proposed[44–46], depending on the size and the features of the molecular system of interest and the investigated phenomena.

The next Section (1.3) of this chapter is devoted to a series of applications and evidences the usefulness of the calculation (in conjunction with a careful analysis) of 2D-PES for the study of ring-puckering motion in 5-term flexible ring systems.

1.2.1 Constrained optimization of molecular structures

The need of specific methods to deal with constrained optimizations depends on the kind of constraints[a] introduced and the coordinate system chosen for the description of the molecular system. In the simplest case of a non-redundant internal coordinate system with a simple constraint (for example, a non-redundant choice of $3N-6$ primitive internal coordinates of whom two are kept constant at their original values) the problem can be easily solved with the exclusion of the internal coordinate to be kept fixed from the

[a] In this chapter, only equality constraints are considered

optimization protocol employed (see subsection 1.1.1), but this straightforward solution is often not feasible (e.g. when a cartesian coordinate system is employed and a constraint on a primitive internal coordinate must be enforced[47,48]); therefore, for the construction of n-dimensional cuts of PESs the availability of efficient and reliable methods for the constrained optimization of molecular structures is a relevant technical issue. Although a detailed presentation of this technical issue and its possible and most widely employed solutions are beyond the scope of this thesis, a brief illustration of the issue devoted to highlight its essential features is important.

Three approaches to this technical problem have been proposed and discussed in literature[8,47]: the employment of penalty functions, the use of Lagrange multipliers and the application of projection operators. These approaches are needed when complex equality constraints are applied to the system under investigation and/or redundant coordinate systems are employed.

The approach based on penalty functions[a] has been adopted in the past, but nowadays is considered inefficient with respect to the other two approaches[8,47].

The solution most commonly employed is based on Lagrange multipliers: Baker (*et al.*) has proposed and discussed[47,48] the implementation of a constrained optimization algorithm for a molecular structure given in cartesian coordinates; another contribution of the same author[53] has been devoted to the presentation of a constrained optimization algorithm for a molecular structure given in delocalized internal coordinates[b].

An attractive feature of the two approaches just mentioned is the possibility of enforce the desired constraints in the final, optimized structure of the molecular system studied also when the desired constraints are not fulfilled in the starting structure. This possibility is absent when a constraint is enforced through an elimination of the coordinate subject to the constraint from the space of the variables to be optimized.

The third solution is based on the application of suitable projection operator with the aim to make orthogonal each optimization step to the directions which violate the constraints to be enforced during the optimization. An example of a protocol employing this solution for the optimization of a molecular structure is given in ref. 55. This kind of solution can be employed also carrying out constrained optimizations with the Gaussian[12] suite of programs (see ref. 24).

[a] to the best of the author's knowledge, the employment of this approach has been proposed for the first time in a chemical context (more specifically in the context of molecular mechanics calculations) in ref. 49 and ref. 50; see also ref. 51 and a subsequent contribution by two of the same authors[52] in which the advantages of an approach based on Lagrange multipliers are recognized and the approach employed in their computer program replaced accordingly.

[b] this coordinate system is presented in ref. 54

1.3 The use of Cremer-Pople coordinates for the computational investigation of ring puckering motions in 5-term flexible ring systems *

In this section, the results obtained in the investigation of ring-puckering motions in twelve flexible 5-term ring molecules (see Figure 1.1) are reported and discussed. More specifically: in Section 1.3.1, the Cremer-Pople formalism is briefly summarized and the possibility of exploiting symmetry considerations to speed up the construction of the 2D-PES is discussed; in Section 1.3.2, the employed computational methodology is outlined; in Section 1.3.3, the computed 2D-PES for the twelve considered molecules is discussed and results are compared with available experimental and computational data; in Section 1.3.4, the fitting of the computed 2D-PESs through suitable functional forms using a limited number of parameters is addressed.

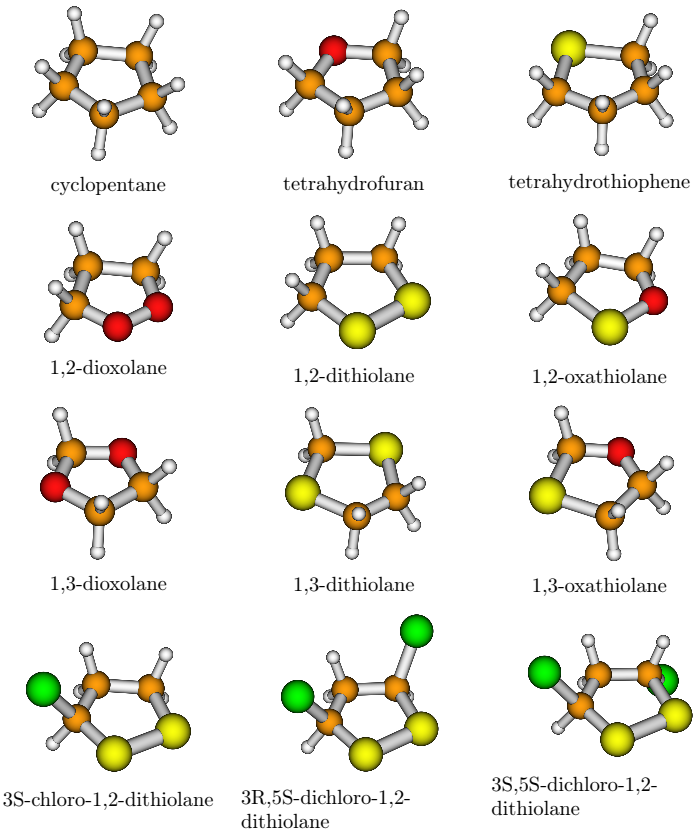

Figure 1.1: Structures of the 5-term saturated ring systems studied in this work.

*The results and the text of this section can be found (with slight modifications) in *J. Chem. Theory Comput.*, **2019**, 15, 7, 4280-4294.

1.3.1 Theoretical background: Cremer-Pople coordinates and symmetry considerations

Cremer-Pople coordinates for the study of ring-puckering motions in flexible cyclic molecules have been described in detail in Refs. 56,57. In order to provide the reader with useful information for a clearer reading of the forthcoming sections and graphical representations of the 2D-PESs, we briefly review here the formalism and add some considerations on symmetry.

Cremer-Pople coordinates for N-term rings

In what follows, mathematical and physical formulations are referred only to the atoms that are part of the ring structure, and not to all the atoms of the molecule (e.g. in a cyclopentane molecule, only to carbon atoms). The aim is to give a formulation of Cremer-Pople coordinates in terms of the cartesian coordinates of the atoms directly involved in the ring structure.

Let us denote the positions of the atoms directly involved in the ring structure through a series of position vectors $\mathbf{r}_j (j = 1, ..., N)$. Given the structure of the entire molecule in cartesian coordinates, the reference frame of the cartesian framework must be changed according to the following prescriptions: the origin of the cartesian framework must coincide with the geometrical center of the atoms involved in the ring structure (Eq. 1.26):

$$\sum_{j=1}^{N} \mathbf{r}_j = 0 \,, \tag{1.26}$$

and the z axis (Eq. 1.29) must be perpendicular to a mean-plane chosen to pass through the origin on which the vectors $\mathbf{r}'$ and $\mathbf{r}''$ (defined, respectively, in Eq. 1.27 and Eq. 1.28) lie:

$$\mathbf{r}' = \sum_{j=1}^{N} \mathbf{r}_j \sin\Big(\frac{2\pi(j-1)}{N}\Big) \tag{1.27}$$

$$\mathbf{r}'' = \sum_{j=1}^{N} \mathbf{r}_j \cos\Big(\frac{2\pi(j-1)}{N}\Big) \tag{1.28}$$

$$\hat{\mathbf{z}} = \frac{\mathbf{r}' \times \mathbf{r}''}{|\mathbf{r}' \times \mathbf{r}''|} \,. \tag{1.29}$$

Using Eq. 1.26 and Eq. 1.29, the z_j coordinate of each atom involved in the ring structure can be obtained through the following equation:

$$z_j = \mathbf{r}_j \cdot \hat{\mathbf{z}} \,. \tag{1.30}$$

Within the Cremer-Pople formalism, for the description of ring-puckering motions in an N-term ring only $N - 3$ coordinates are necessary (e.g., for

a 5-term ring only 2 coordinates). Following the original article,[56] if N is odd and $N > 3$ Cremer-Pople coordinates q_m and θ_m are defined using the following equations:

$$q_m \cos\theta_m = \left(\frac{2}{N}\right)^{\frac{1}{2}} \sum_{j=1}^{N} z_j \cos\left[\frac{2\pi m(j-1)}{N}\right] \tag{1.31}$$

$$q_m \sin\theta_m = -\left(\frac{2}{N}\right)^{\frac{1}{2}} \sum_{j=1}^{N} z_j \sin\left[\frac{2\pi m(j-1)}{N}\right] . \tag{1.32}$$

Eqs. 1.31 and 1.32 apply for $m = 2, ..., (N-1)/2$. Amplitudes q_m must be positive and phase angles θ_m must assume a value in the interval between 0 and 2π. If N is even, Eqs. 1.31 and 1.32 apply for $m = 2, ..., (N-2)/2$ and another puckering coordinate (Eq. 1.33) is needed in order to describe the puckering amplitude of the crown form

$$q_{N/2} = \left(\frac{1}{N}\right)^{\frac{1}{2}} \sum_{j=1}^{N} z_j \cos[(j-1)\pi] . \tag{1.33}$$

In Eq. 1.33, $q_{N/2}$ can have both positive and negative value.

More explicitly, q_m and θ_m can be separated by combining Eqs. 1.31 and 1.32, using pythagorean trigonometric identity (Eq. 1.34) and the inverse tangent function (Eq. 1.35):

$$(q_m^2 \cos^2\theta_m + q_m^2 \sin^2\theta_m)^{\frac{1}{2}} = [q_m^2(\cos^2\theta_m + \sin^2\theta_m)]^{\frac{1}{2}} = q_m \tag{1.34}$$

$$\begin{aligned} \arctan\left(\frac{q_m \sin\theta_m}{q_m \cos\theta_m}\right) &= \arctan\left(\frac{\sin\theta_m}{\cos\theta_m}\right) = \\ = \arctan(\tan\theta_m) &= \begin{cases} \theta_m & \text{if } \cos\theta_m > 0 \\ \pi + \theta_m & \text{if } \cos\theta_m < 0 \end{cases} . \end{aligned} \tag{1.35}$$

With Eqs. 1.34 and 1.35, q_m and θ_m can be written as functions of z_j:

$$\begin{aligned} q_m = \left(\frac{2}{N}\right)^{\frac{1}{2}} \Bigg\{ &\left[\sum_{j=1}^{N} z_j \cos\left(\frac{2\pi m(j-1)}{N}\right)\right]^2 + \\ &+ \left[\sum_{j=1}^{N} z_j \sin\left(\frac{2\pi m(j-1)}{N}\right)\right]^2 \Bigg\}^{\frac{1}{2}} \end{aligned} \tag{1.36}$$

$$\theta_m = \begin{cases} \arctan\left[-\dfrac{\sum_{j=1}^{N} z_j \sin\left(\frac{2\pi m(j-1)}{N}\right)}{\sum_{j=1}^{N} z_j \cos\left(\frac{2\pi m(j-1)}{N}\right)}\right] & \text{if } \cos\theta_m > 0 \\ \arctan\left[-\dfrac{\sum_{j=1}^{N} z_j \sin\left(\frac{2\pi m(j-1)}{N}\right)}{\sum_{j=1}^{N} z_j \cos\left(\frac{2\pi m(j-1)}{N}\right)}\right] + \pi & \text{if } \cos\theta_m < 0 \end{cases} . \tag{1.37}$$

Other two useful equations giving the displacements z_j as functions of q_m, θ_m and, eventually, $q_{N/2}$ can be easily worked out. Eqs. 1.38 and 1.39 are sufficient to uniquely fix the mean plane whose orientation is determined by its normal vector $\hat{\mathbf{z}}$ and can be viewed, together with Eqs. 1.26, 1.31, 1.32 and 1.33, as a set of N linear equations for the N displacements z_j:

$$\sum_{j=1}^{N} z_j \sin\Big(\frac{2\pi(j-1)}{N}\Big) = 0; \tag{1.38}$$

$$\sum_{j=1}^{N} z_j \cos\Big(\frac{2\pi(j-1)}{N}\Big) = 0\,. \tag{1.39}$$

The solution can be exploited to obtain the displacements z_j in terms of the Cremer-Pople coordinates explicitly defined in Eqs. 1.33, 1.36 and 1.37. If N is odd, the displacements z_j are given by:

$$z_j = \Big(\frac{2}{N}\Big)^{\frac{1}{2}} \left\{ \sum_{m=2}^{(N-1)/2} q_m \cos\Big[\theta_m + \frac{2\pi m(j-1)}{N}\Big] \right\}\,; \tag{1.40}$$

otherwise, if N is even, they are given by:

$$\begin{aligned} z_j = {} & \Big(\frac{1}{N}\Big)^{\frac{1}{2}} q_{N/2}(-1)^{j-1} + \\ & + \Big(\frac{2}{N}\Big)^{\frac{1}{2}} \left\{ \sum_{m=2}^{(N-2)/2} q_m \cos\Big[\theta_m + \frac{2\pi m(j-1)}{N}\Big] \right\}\,. \end{aligned} \tag{1.41}$$

The case of 5-term rings and symmetry considerations

In the case of 5-term rings, the use of Cremer-Pople coordinates allows for the complete description of ring-puckering motions using only 2 coordinates: one puckering amplitude q, and one pseudorotation angle θ. Therefore, this kind of system can be described using a 2D-PES and plotting the energy as a function of the two polar coordinates q and θ (with $q > 0$ and $0 < \theta < 2\pi$) minimized with respect to all remaining coordinates, i.e. performing a so-called 'relaxed scan' in q and θ.

Clearly, in this kind of plots each couple (q, θ) is associated with a specific conformation. The value of the amplitude q can be thought of as a measure of the distances (along the direction of $\hat{\mathbf{z}}$) of the 5 vertices of the ring from the mean plane defined by Eqs. 1.38 and 1.39. Thus, for example, if $q = 0$ then the 5 vertices lie on the mean plane, and the conformation of the 5-term ring is planar. As to the pseudorotation angle θ, the connection between its value and the conformation of a 5-term ring cannot be described in a simple

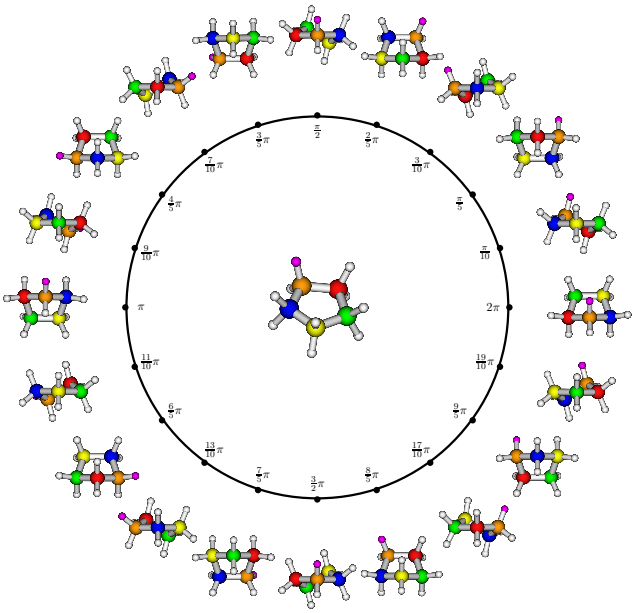

Figure 1.2: Graphical representation of 20 conformations of a 5-term saturated ring system with the corresponding value of pseudorotation angle θ specified in radiants. For each displayed ring, the puckering amplitude is fixed at $q = 0.55$. At the center of the circle, the planar conformation ($q = 0$) is also shown.

way. Figure 1.2 gives a graphical representation (firstly proposed by Altona and Sundaralingam[58] and used by other authors[59–61] since) that clarifies the physical meaning of the pseudorotation angle through a representation of each conformation associated to a particular value of θ: 20 different values of θ are considered and accordingly 20 different conformations are depicted, each one corresponding to a particular value of the pseudorotation angle.

In many cases, the use of symmetry can lead to significant savings of computational resources as only the calculation of portions of the 2D-PES may be required. For the case of 5-term rings, a summary of the simplifications brought by symmetry is given in Table 1.1. To give an example, say the K points are necessary to perform a relaxed scan of the 2D-PES in the intervals $0 < q < 1$ and $0 < \theta < 2\pi$. In the case of 3S-chloro-1,2-dithiolane, in the absence of symmetry all K calculations are required. Turning to cyclopentane, on the other hand, symmetry can be exploited to limit the calculations to the range $[0, \frac{\pi}{10}]$: each point of the relaxed scan calculation performed in such range can be extended to other points of the 2D-PES in the range $[\frac{\pi}{10}, 2\pi]$ using the relations $E(q, \theta) = E(q, \theta + \frac{\pi}{5})$ and $E(q, \theta) = E(q, -\theta)$. Therefore, the sampling of 2D-PES in the intervals $0 < q < 1$ and $0 < \theta < 2\pi$ on all K

points can be performed with a relaxed-scan calculation of only $K/20$ points. Similarly, in the case of tetrahydrofuran the relaxed-scan calculations shall be limited to values of the pseudorotation angle in the range $[0, \frac{\pi}{2}]$, because the relations $E(q,\theta) = E(q,\theta+\pi)$ and $E(q,\theta) = E(q,-\theta)$ allow for the construction of the 2D-PES in the range $[\frac{\pi}{2}, 2\pi]$ without the need to performing the related calculations. Thus, the 2D-PES can be sampled on K points in the range $[0,1]$ for q and $[0,2\pi]$ for θ with a relaxed-scan calculations of only $K/4$ points. In Table 1.1 the reader can find the indication of when and how symmetry can be used (as has been done in this work) for the construction of the 2D-PESs.

1.3.2 Methodology

All calculations were performed using the Gaussian 16[12] suite of programs. Each electronic-structure calculation was carried out with Density Functional Theory (DFT) by employing B2PLYP as exchange-correlation functional[62] (the reliability of the results obtained employing this functional has been already verified in a number of works[63–65] for what concerns organic molecules) combined with Grimme's D3BJ dispersion[66,67] and maug-cc-pVTZ basis set introduced by Truhlar and coworkers[68,69] (proposed after the augmented correlation consistent family of basis sets introduced by Dunning and coworkers[70–73]). Each point of the twelve relaxed scans was calculated independently through a constrained optimization. Each input was constructed using both cartesian and internal coordinates in the same z-matrix. Cartesian coordinates in the reference frame defined by Eqs. 1.26, 1.30 of Section 1.3.1 have been used in order to specify the positions of the five atoms involved in the ring structure, while internal coordinates have been used to specify the position of all the other atoms (e.g. in the cyclopentane molecule, all the hydrogen atoms). During the constraint optimization, the z_j (Eq. 1.30) cartesian coordinates of the atoms involved in the ring structure are kept fixed: in this manner the puckering amplitude q (Eq. 1.36) and the pseudorotation angle θ (Eq. 1.37) are fixed during the optimization.[a] Input files (each one corresponding to a specific couple (q, θ)) have been written automatically with an home-made python script.

The saturated 5-term rings taken into account in this study do not exhibit a minimum in correspondence of the planar conformation ($q = 0$). Therefore, the use of a uniformly spaced polar grid directly employing Cremer-Pople coordinates q and θ for the sampling of the 2D-PES would be ineffective, because the density of the sampling would reach a maximum correspondingly to the origin of the polar grid and would constantly decrease with incresing puckering amplitude q. Instead, a uniformly-spaced rectangular grid (i.e.

[a] θ is a dimensionless quantity, but q has the dimension of a length: therefore, a measurement unit for the values of q provided in this section must be specified. All the values of q are specified in Angström.

D_{5h}	C_{2v}	C_s		C_2	C_1
		mirror plane parallel to ring plane	mirror plane perpendicular to ring plane		
$E(q,\theta) = E(q,\theta+\frac{\pi}{5})$ $E(q,\theta) = E(q,-\theta)$	$E(q,\theta) = E(q,\theta+\pi)$ $E(q,\theta) = E(q,-\theta)$	$E(q,\theta) = E(q,\theta+\pi)$	$E(q,\theta) = E(q,-\theta)$	$E(q,\theta) = E(q,\pi-\theta)$	-
cyclopentane	tetrahydrofuran tetrahydrothiophene 1,2-dioxalane 1,3-dioxolane 1,2-dithiolane 1,3-dithiolane	1,3-oxathiolane 1,2-oxathiolane	3R,5S-dichloro-1,2-dithiolane	3S,5S-dichloro-1,2-dithiolane	3S-chloro-1,2-dithiolane

Table 1.1: The 5-term rings of Fig. 1.1 are ordered with respect to the symmetry point group (column header) of the planar form (in the case of C_s symmetry point group, the orientation of the mirror plane with respect to the plane on which the planar ring lies is also specified). A reduction of the computational cost required for the construction of 2D-PESs can be achieved using the expressions for $E(q,\theta)$ reported for each symmetry point group.

molecule	q interval	θ interval	number of calculated points	spacing
cyclopentane	$0 \leq q \leq 0.65$	$0 \leq \theta \leq \frac{\pi}{10}$	500	0.01181818
tetrahydrofuran	$0 \leq q \leq 0.6$	$0 \leq \theta \leq \frac{\pi}{2}$	1295	0.015
tetrahydrothiophene	$0 \leq q \leq 0.75$	$0 \leq \theta \leq \frac{\pi}{2}$	1297	0.01875
1,2-dioxolane	$0 \leq q \leq 0.75$	$0 \leq \theta \leq \frac{\pi}{2}$	1297	0.01875
1,3-dioxolane	$0 \leq q \leq 0.75$	$0 \leq \theta \leq \frac{\pi}{2}$	2012	0.015
1,2-dithiolane	$0 \leq q \leq 0.75$	$0 \leq \theta \leq \frac{\pi}{2}$	1297	0.01875
1,3-dithiolane	$0 \leq q \leq 0.75$	$0 \leq \theta \leq \frac{\pi}{2}$	1297	0.01875
1,2-oxathiolane	$0 \leq q \leq 0.75$	$0 \leq \theta \leq \pi$	1344	$3/116$ ($\simeq 0.026$)
1,3-oxathiolane	$0 \leq q \leq 0.75$	$0 \leq \theta \leq \pi$	1255	$3/112$ ($\simeq 0.027$)
3R,5S-dichloro-1,2-dithiolane	$0 \leq q \leq 0.75$	$0 \leq \theta \leq \pi$	649	0.0375
3S,5S-dichloro-1,2-dithiolane	$0 \leq q \leq 0.75$	$-\frac{\pi}{2} \leq \theta \leq \frac{\pi}{2}$	649	0.0375
3S-chloro-1,2-dithiolane	$0 \leq q \leq 0.8$	$0 \leq \theta < 2\pi$	1257	0.04

Table 1.2: Details of the 2D-PES samplings for the twelve considered molecules (see text for discussion).

employing $q\cos\theta$ and $q\sin\theta$ instead of q and θ) has been adopted in this work.

For each of the systems investigated in this study, a maximum value (depending on the specific system) of the puckering amplitude q has been chosen for the sampling of the related 2D-PES. In Table 1.2 the various intervals employed to sample 2D-PESs of the molecules studied in this work are reported (the interval of puckering amplitudes and the interval of pseudorotation angles are reported, respectively, in the second and in the third columns). For what concerns pseudorotation angles, in Section 1.3.3 computational results are shown and discussed in the interval $0 < \theta \leq 2\pi$ for each molecule: as already mentioned, the extension of the intervals reported in Table 1.2 to the complete range of values $0 < \theta \leq 2\pi$ can be straightforwardly carried out exploiting the expressions given in Table 1.1 with a significant reduction of computational cost. The number of points used (e.g. the number of constrained optimizations carried out) to sample 2D-PESs is reported in the fourth column of Table 1.2 for each molecule, while in the fifth column the spacing adopted between two adjacent points of the uniformly-spaced rectangular grid employed for the sampling of each 2D-PES is reported. The origin of the rectangular grid used to perform the sampling is, in all cases considered in this work, the value $q = 0$ (which corresponds to a planar conformation of the ring and is explicitly sampled for all the molecules treated in this work).

The 2D-PESs displayed in Section 1.3.3 were extrapolated through cubic spline interpolations, except for 1,2-oxathiolane and 1,3-oxathiolane molecules for which linear interpolations were used. Data given in this Section should allow for a complete reproduction of the results reported and discussed in Section 1.3.3.

1.3.3 Computational results: 2D-PES calculations

In this Section, the computed 2D-PESs are reported in the form of contour-map plots and briefly discussed.

For each of the considered twelve 5-term rings, experimental and computational data already available in the literature are briefly reviewed and compared with the results of this work. The results are summarized in table 1.3 and in each of the following subsections a discussion devoted to each of the molecule considered in this study is provided. The reader not interested in a detailed discussion concerning each of the 5 term rings investigated in this work can skip to the next section without losing the more relevant computational and theoretical insights of this work. Further information on the minima of the computed 2D-PES is available in the SI of the original article.

Cyclopentane

Cyclopentane has been extensively studied by many authors.[59,74–78] The early description of the pseudorotational motion of cyclopentane proposed by Kilpatrick et al.[110] in terms of a ring puckering amplitude and a phase angle has been recognized[56] as a particular case of Eq. 1.40 when $N = 5$. Nowadays, the description of this molecule as a puckered ring which exhibits a nearly free pseudorotational motion along the phase angle θ is confirmed[59,74,76,77] by various experiments and computations and, therefore, is widely accepted.

The computed 2D-PES for cyclopentane is shown in Fig. 1.3.

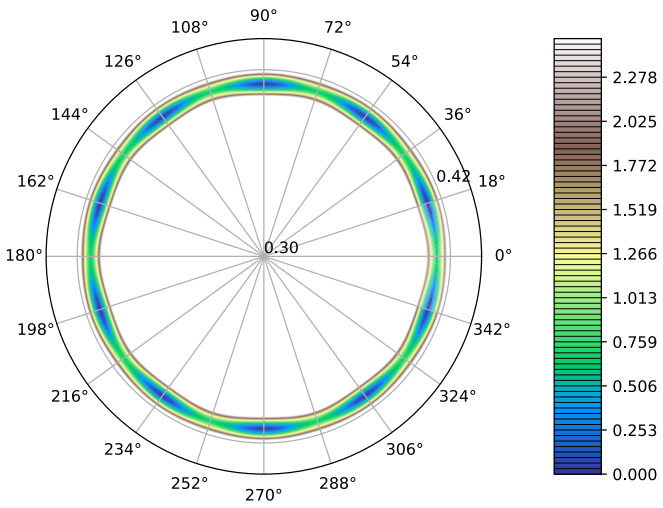

Figure 1.3: 2D-PES of cyclopentane; energy values (given on the right of the colorbar) are in cm^{-1}.

molecule	symmetry	minima		transition states		second-order saddle points		references	
		(q,θ)	ΔE	(q,θ)	ΔE	(q,θ)	ΔE	exp. data	comp. data
cyclopentane	D_{5h}	$(0.411, \frac{\pi}{10})$ $(0.411, \frac{3\pi}{10})$ $(0.411, \frac{\pi}{2})$ $(0.411, \frac{7\pi}{10})$ $(0.411, \frac{9\pi}{10})$ $(0.411, \frac{11\pi}{10})$ $(0.411, \frac{13\pi}{10})$ $(0.411, \frac{3\pi}{2})$ $(0.411, \frac{17\pi}{10})$ $(0.411, \frac{19\pi}{10})$	0 0 0 0 0 0 0 0 0 0	$(0.411, \frac{\pi}{5})$ $(0.411, \frac{2\pi}{5})$ $(0.411, \frac{3\pi}{5})$ $(0.411, \frac{4\pi}{5})$ $(0.411, \pi)$ $(0.411, \frac{6\pi}{5})$ $(0.411, \frac{7\pi}{5})$ $(0.411, \frac{8\pi}{5})$ $(0.411, \frac{9\pi}{5})$ $(0.411, 2\pi)$	< 1 < 1 < 1 < 1 < 1 < 1 < 1 < 1 < 1 < 1	$(0, nr)$	1768	74–78	59, 75–77
tetrahydrofuran	C_{2v}	$(0.378, \frac{\pi}{2})$ $(0.378, \frac{3\pi}{2})$ $(0.376, \pi)$ $(0.376, 2\pi)$	0 0 10 10	$(0.374, 0.794)$ $(0.374, \pi - 0.794)$ $(0.374, \pi + 0.794)$ $(0.374, 2\pi - 0.794)$	38 38 38 38	$(0, nr)$	1219	79–86	85–91
tetrahydrothiophene	C_{2v}	$(0.44, \frac{\pi}{2})$ $(0.44, \frac{3\pi}{2})$	0 0	$(0.51, \pi)$ $(0.51, 2\pi)$	799 799	$(0, nr)$	2341	92–96	96
1,2-dioxolane	C_{2v}	$(0.45, \frac{\pi}{2})$ $(0.45, \frac{3\pi}{2})$	0 0	$(0.0.395, \pi)$ $(0.395, 2\pi)$	721 721	$(0, nr)$	2380	97, 98	61
1,3-dioxolane	C_{2v}	$(0.357, 0.694)$ $(0.357, \pi - 0.694)$ $(0.357, \pi + 0.694)$ $(0.357, 2\pi - 0.694)$	0 0 0 0	$(0.345, \pi)$ $(0.345, 2\pi)$ $(0.355, \frac{\pi}{2})$ $(0.355, \frac{3\pi}{2})$	29 29 63 63	$(0, nr)$	1050	99–104	61, 105
1,2-diothiolane	C_{2v}	$(0.66, \frac{\pi}{2})$ $(0.66, \frac{3\pi}{2})$	0 0	$(0.47, \pi)$ $(0.47, 2\pi)$	313 313	$(0, nr)$	3242	-	-
1,3-dithiolane	C_{2v}	$(0.519, 1.108)$ $(0.519, \pi - 1.108)$ $(0.519, \pi + 1.108)$ $(0.519, 2\pi - 1.108)$	0 0 0 0	$(0.49, \frac{\pi}{2})$ $(0.49, \frac{3\pi}{2})$ $(0.53, \pi)$ $(0.53, 2\pi)$	21 21 839 839	$(0, nr)$	2281	106, 107	-
1,2-oxathiolane	C_s	$(0.442, 2.325)$ $(0.442, 2.325 + \pi)$	0 0	$(0.443, 0.527)$ $(0.443, 0.527 + \pi)$	620 620	$(0, nr)$	2303	108	-
1,3-oxathiolane	C_s	$(0.423, 2.176)$ $(0.423, 2.176 + \pi)$	0 0	$(0.467, 0.315)$ $(0.467, 0.315 + \pi)$	659 659	$(0, nr)$	2032	109	-
3R,5S-dichloro-1,2-dithiolane	C_s	$(0.645, -1.997)$ $(0.645, 1.997)$ $(0.529, -0.929)$ $(0.529, 0.929)$	0 0 238 238	$(0.625, -1.386)$ $(0.625, 1.386)$ $(0.4, 2\pi)$ $(0.49, \pi)$	395 395 503 1038	$(0.037, \pi)$	3527	-	-
3S,5S-dichloro-1,2-dithiolane	C_2	$(0.544, 0.948)$ $(0.544, \pi - 0.948)$	0 0	$(0.6, \frac{\pi}{2})$ $(0.71, \frac{3\pi}{2})$	200 588	$(0.075, \frac{3\pi}{2})$	3596	-	-
3S-chloro-1,2-dithiolane	C_1	$(0.465, 0.184)$ $(0.611, 2.027)$ $(0.668, 4.467)$	0 178 448	$(0.616, 1.432)$ $(0.665, 4.879)$ $(0.479, 3.284)$	363 530 973	$(0.039, -2.122)$	3618	-	-

Table 1.3: Positions and relative energies of the stationary points located on each of the 2D-PESs studied and shown in this work; ΔE are the energy values with respect to the global minimum and are given in cm^{-1}; under the label symmetry is specified the symmetry point group of the planar conformation of the molecule; 'nr' stands for 'not relevant': only one geometry (corresponding to the planar conformation of the ring) corresponds to $q = 0$.

In order to evidence the nearly free pseudorotational path suggested by the computational results obtained in this work, the 2D-PES is depicted only in the range $0.37 < q < 0.44$.

Along the pseudorotational path, ten minima with exactly the same energy (associated to a twisted structure) are separated by ten barriers. The top of each barrier corresponds to a first-order saddle point (associated with a bent structure) and the difference between the energy of a transition state and the energy of a minimum is less than 1 cm^{-1} (Due to the need of taking into account extremely small energy differences the importance of a careful choice of the integration grid used for the numerical integration in the DFT calculations must be pointed out: a discussion of this technical problem is provided in the SI of the original article).

Although other computational surveys already available in the literature suggest the existence of a nearly free pseudorotational path, a general agreement on the geometry associated to minima and transition states has not been reached[76,77] (even for what concerns the number of minima and transition states[76]). The extremely small energy difference between minima and first-order saddle points located along the pseudorotational path have not allowed (at least till now) for an unambiguous experimental determination of the nature of (and the geometry associated to) each of these stationary points: indeed, an energy of the vibrational ground state higher than the extremely small barrier to the pseudorotation can be easily guessed.[77] In this case, the molecule can be considered (with good approximation) a free-pseudorotor. It must be underlined that the use of DFT methods to characterize the pseudorotational pathway of the cyclopentane molecule can be questioned: this molecule is, indeed, small enough to allow the use of coupled cluster methods,[76,77] at least for the characterization of minima and first-order saddle points. The situation is different for what concerns the barrier to planarity (the second-order saddle point of the global PES corresponding to the planar conformation of the cyclopentane molecule), which is estimated to be equal to 1808 cm^{-1} on the basis of experimental data,[75] in good agreement with the value of 1768 cm^{-1} calculated in this work.

Tetrahydrofuran

In the case of tetrahydrofuran (THF), as can be expected, both computational[85–91] and experimental[79–86] results are available in literature. Significant evidences on the existence of a slightly hindered pseudorotational motion are reported in the literature. Various experimental studies support the existence of a pseudorotational motion with four minima separated by four barriers[81–84]; earlier experimental studies suggest a nearly free pseudorotational motion without definite conclusions about the energetic profile along the pseudorotational path[79,80].

For what concerns ab-initio computational studies, different and sometimes conflicting results have been obtained: some authors have calculated four minima (two minima with C_2 symmetry and enantiomeric structures, two minima with C_s symmetry and the same structure)[85,86,90,91], but the small energy difference between bent and twisted conformations have prevented an unambiguous determination of the global minimum. In addition, there are evidences of a strong dependence of the calculated pseudorotational path from the basis-set employed in the calculation[86,90]. Results obtained by Wu and Cremer[89] (two minima with the enantiomeric structures and C_2 symmetry, two transition states with the same structure and C_s symmetry) are in agreement with other earlier calculations[87,88] while in sharp contrast, even qualitatively, with more recent computational results[85,86,90,91] and with the energetic profile of the pseudorotational motion inferred from experiments of rotational spectroscopy[81–84]. On the basis of experimental and computational data the existence of a second-order saddle point corresponding to the planar conformation ($q = 0$) can be inferred.

The 2D-PES computed in this work is shown in Fig. 1.4. With the aim of highlighting the main features of the pseudorotational path, computational results are displayed only in the interval $0.25 < q < 0.5$. The results obtained in this work confirm some earlier findings: two twisted minima with equal energies and enantiomeric structures belonging to C_2 symmetry point group (with puckering amplitude of 0.378 and pseudorotational angles equal to $\frac{\pi}{2}$ and $\frac{3\pi}{2}$), two bent minima with the same energy and a structure pertaining to C_s symmetry point group (with $q = 0.376$ and pseudorotational angles of π and 2π) and, finally, four transition states with equal energies and asymmetric structures (two transition states correspond to a structure with $q = 0.374$ and θ equal to 0.794 and $\pi - 0.794$ and the other two to the enantiomeric form of the same structures, with the same puckering amplitude and pseudorotational angles equal to $\pi + 0.794$ and $2\pi - 0.794$). Furthermore, the results displayed in Fig. 1.4 support the existence of a pseudorotational path and a planar form corresponding to a second-order saddle point of the 2D-PES. A quantitative measurement of the height of each potential energy barrier can be easily obtained through the computation of energetic differences (results are reported in table 1.3).

For this molecule, an extrapolation to the complete basis set (CBS) limit employing a composite scheme based on coupled-cluster single-point calculations (CCSD(T) on top of MP2/aug-cc-pVTZ geometry optimizations)[90] of the energies associated with the two non equivalent energy minima of the 2D-PES has been published. In the present work, the global minimum is associated with a twisted (C_2) structure, while Ref. 90 has predicted a relative minimum associated with the twisted structure and the global minimum in correspondence with a bent (C_s) structure (note that, however, the energy differences between the two molecular structures are very small in both cases).

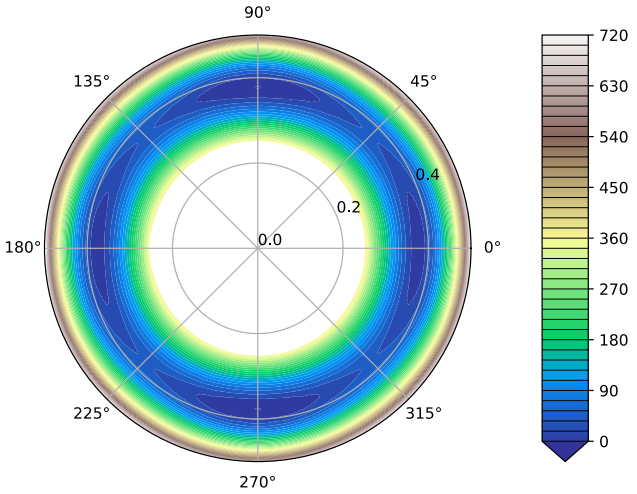

Figure 1.4: 2D-PES of tetrahydrofuran; energy values (given on the right of the colorbar) are in cm^{-1}.

Tetrahydrothiophene

The pseudorotation of tetrahydrothiophene (THT) has been studied by several authors[92–96]. Experimental results obtained with electron diffraction[92], far-infrared[93,94] and rotational[95,96] spectroscopy can be found in the literature.

The 2D-PES computed in this work is displayed in Fig. 1.5. On the basis of experimental evidences and previous calculations, the existence of a pseudorotational circuit with two potential energy minima corresponding to the twisted forms of tetrahydrothiophene (with enantiomeric structures belonging to the C_2 symmetry point group) and two transition states corresponding to the bent one (belonging to the C_s symmetry point group) has been inferred[92–96]. These conclusions are in agreement with the results displayed in Fig. 1.5 and reported in table 1.3.

The height of the barrier to the pseudorotation has been obtained both through extrapolation from experimental results (with values between 770 and 780 cm^{-1}) and from previous calculations. The best agreement between experimental and calculated values available in literature has been obtained with calculations carried out at MP2/6-311+G** level of theory, with a calculated value of 928 cm^{-1} [96]. In this work the calculated barrier height is 799 cm^{-1}, significantly better than the already cited best agreement. The difference between the energy calculated for the planar structure and the energy associated to the two potential-energy minima of the PES is 2341 cm^{-1}, a value that is significantly higher that estimated from experimental results by Wertz et al.[93] (nearly equal to the transition state energy and not coherent with the pseudorotational motion proposed in the same article and in this work) and lower than the one reported by Smithson et al.[94] (4252 cm^{-1}).

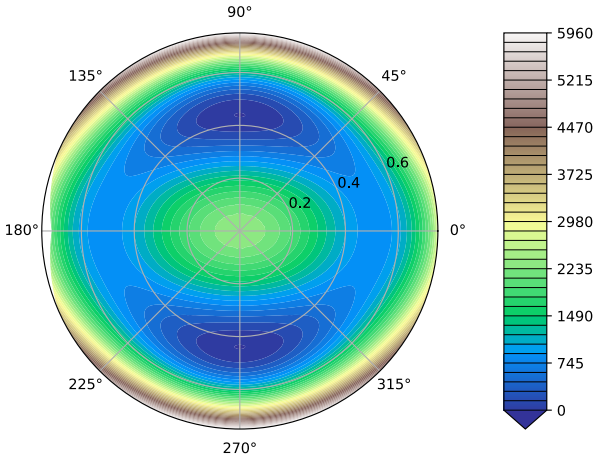

Figure 1.5: 2D-PES of tetrahydrothiophene; energy values (given on the right of the colorbar) are in cm^{-1}.

1,2-dioxolane

To the best of our knowledge, only few authors have devoted their attention to the study of 1,2-dioxolane. Results deduced from microwave[98] and photoelectron[97] spectra of 1,2-dioxolane have been published, while a computation of the 2D-PES has been carried out by Cremer[61] at HF/6-31G* level of theory.

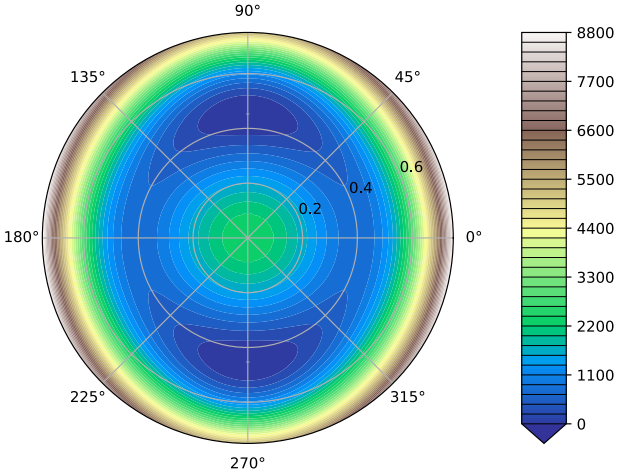

Figure 1.6: 2D-PES of 1,2-dioxolane; energy values (given on the right of the colorbar) are in cm^{-1}.

From previous calculations[61] and experimental data[98], minima of the PES corresponding to two enantiomeric, twisted structures (belonging to the C_2 symmetry point group) of 1,2-dioxolane molecule have been inferred. Furthermore, two transition states corresponding to a bent structure (belonging to the C_s symmetry point group) and a second-order saddle point corresponding to the planar structure have been computationally predicted[61]. The results illustrated in Fig. 1.6 and reported in table 1.3 confirm these earlier findings.

The barrier to the pseudorotation has been calculated as difference between the energy of the transition state (first-order saddle point of the PES) and the energy of the minimum. The value obtained in this work is equal to 721 cm^{-1}, not far from the previously reported calculated value of 781 cm^{-1} [61]. The puckering amplitude q corresponding to minima of the PES (see Fig. 1.6) is equal to 0.45 (in agreement with values already available in literature[61,98]). The energy difference between the second-order saddle point of the PES (corresponding to the planar conformation) and minima of the PES has been calculated: the value is equal to 2380 cm^{-1} in this work, higher than the value of 1988 cm^{-1} previously obtained by Cremer[61]. An experimental study explicitly devoted to the study of the pseudorotational

motion computationally predicted would be desirable.

1,3-dioxolane

The pseudorotation of 1,3-dioxolane has been already studied by some authors. For what concerns experimental studies, results obtained from an electron diffraction investigation[99] and from microwave[100–102] and far-infrared[103,104] spectra are available in the literature. The calculation of the 2D-PES has been performed and published by Cremer et al.[61,105].

In Fig. 1.7, the computed 2D-PES is shown only in the interval $0.2 < q < 0.45$ in order to account for the slightly hindered pseudorotational motion of 1,3-dioxolane molecule. Concerning the results inferred from experimental data, the disagreement between conclusions attained, on one hand, through rotational spectroscopy[100,102] and, on the other hand, with electron diffraction[99], must be pointed out. In the case of the electron diffraction study, a description of pseudorotational motion of 1,3-dioxolane molecule qualitatively similar to that given for 1,2-dioxolane has been proposed: two minima corresponding to two enantiomeric structures (pertaining to C_2 symmetry point group) separated by two barriers (with transition states pertaining to C_s symmetry point group)[99]. This description is in agreement with previously reported computations performed at HF/6-31G* level of theory[61]. Instead, results obtained with rotational spectroscopy suggest four minima with equal energies corresponding to asymmetric conformations of the 1,3-dioxolane molecule and four transition states, two with a structure belonging to C_2 symmetry point group with energies slightly higher than the other two with a structure belonging to C_s symmetry point group[100,102].

Figure 1.7 supports the results suggested by rotational spectroscopy (see also table 1.3): four minima with equal energies and asymmetric conformations, more specifically two minima (with pseudorotation angles θ equal to 0.694 and $\pi - 0.694$) with the same asymmetric structure that is the non-superimposable mirror image of a structure corresponding to the other two minima (with pseudorotation angles equal to $\pi + 0.694$ and $2\pi - 0.694$); four transition states, two corresponding to two enantiomeric structures belonging to C_2 symmetry point group on the top of a potential energy barrier with a height of 63 cm^{-1} (value inferred from experimental data: 73.8 cm^{-1})[102] and two corresponding to a structure belonging to C_s symmetry point group corresponding to a barrier of height of 29 cm^{-1} (value inferred from experimental data: 41.6 cm^{-1})[102].

1,2-dithiolane

Although 1,2-dithiolane is known[111], we are not aware of published studies concerning conformations or pseudorotation of 1,2-dithiolane ring.

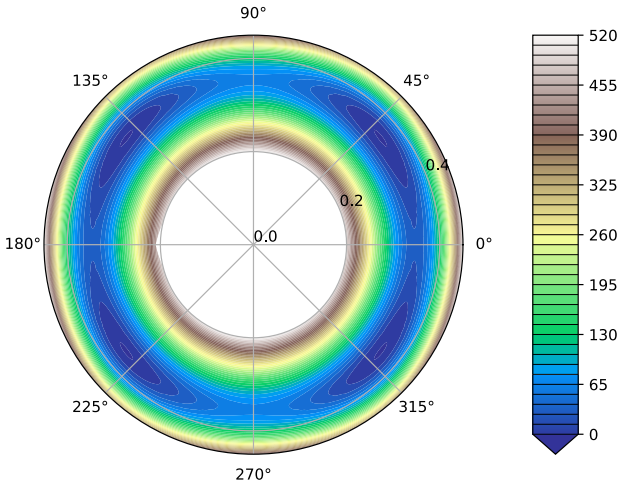

Figure 1.7: 2D-PES of 1,3-dioxolane; energy values (given on the right of the colorbar) are in cm^{-1}.

Positions and relative energies of each of the stationary points are reported in table 1.3. The 2D-PES calculated in this work (see Fig. 1.8) is

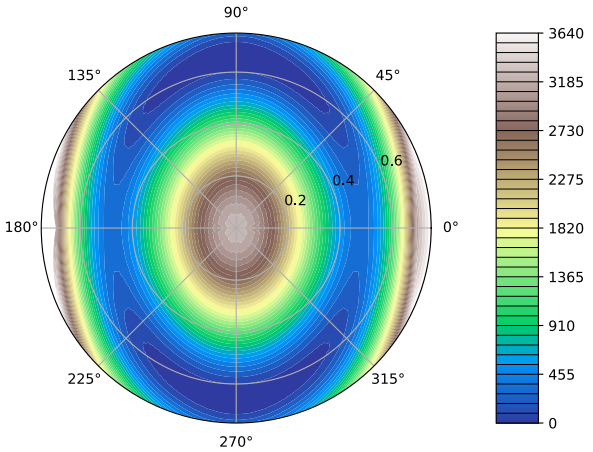

Figure 1.8: 2D-PES of 1,2-dithiolane; energy values (given on the right of the colorbar) are in cm^{-1}.

qualitatively similar to the ones calculated for 1,2-dioxolane and tetrahydrothiophene (see Fig. 1.6 and 1.5),with two equivalent minima (belonging to C_2 symmetry point group) and two transition states with the same structure (pertaining to C_s symmetry point group). An experimental study concerning the physico-chemical characterization of 1,2-dithiolane molecule, particularly the pseudorotational motion envisaged in this work, would be

desirable.

1,3-dithiolane

The only conformational data available for 1,3-dithiolane are based on measurements carried out with vibrational[106] and NMR[107] spectroscopy. The authors are not aware of any previous study concerning the pseudorotation of the 1,3-dithiolane ring.

The computed 2D-PES for this system is shown in Fig. 1.9 (see table 1.3 for positions and relative energies of the stationary points). Computational results are displayed in the interval $0.4 < q < 0.6$ to the purpose of highlighting the change of energy values along the pseudorotational circuit. Experimental data[106,107] suggest a puckered equilibrium structure with a twisted conformation (with a C_2 symmetry) favored on a bent conformation (with C_s symmetry). However, these suggestions must be taken with caution: experimental results available in literature could be relevantly affected by the environment and are not suitable for the study of the pseudorotational motion suggested in Fig. 1.9 of this work. Along the pseudorotational path, there are four minima with the same energy, two with the same asymmetric structure (with pseudorotational angles equal to 1.108 and $\pi - 1.108$) that are separated by a transition state with a twisted structure (with C_2 symmetry and $\theta = \frac{\pi}{2}$) and two which are mirror images of the asymmetric structure already mentioned (with pseudorotational angles equal to $\pi + 1.108$ and $2\pi - 1.108$) that are separated by a transition state with a structure that is the mirror image of the already cited twisted structure (belonging to C_2 symmetry point group, $\theta = \frac{3\pi}{2}$) and are separated from their mirror images by two transition states with the same bent structure (with C_s symmetry, pseudorotational angles of π and 2π).

The need of novel experimental data to properly characterize the pseudorotational motion computationally predicted in this work must be pointed out.

1,2-oxathiolane

The 1,2-oxathiolane compound is known[111], but to the best of our knowledge the attention devoted to its physico-chemical characterization has been scarce. The experimental photoelectron spectrum of 1,2-oxathiolane can be found in the literature[108]. In the same article the authors cautiously suggest a planar conformation of 1,2-oxathiolane ring on the basis of preliminary calculations.

The computed 2D-PES for this system is shown in Fig. 1.10 and the results are reported in table 1.3. The disagreement between these results and the already cited hypothesis available in the literature about the minimum-energy structure of the 1,2-oxathiolane molecule is evident. More specifically,

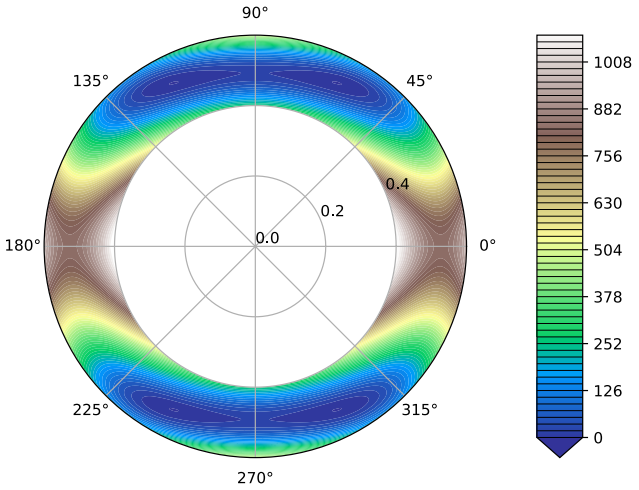

Figure 1.9: 2D-PES of 1,3-dithiolane; energy values (given on the right of the colorbar) are in cm^{-1}.

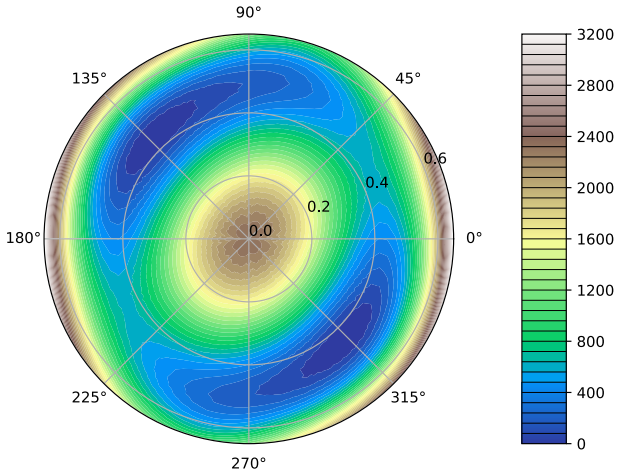

Figure 1.10: 2D-PES of 1,2-oxathiolane; energy values (given on the right of the colorbar) are in cm^{-1}.

the computational results shown in Fig. 1.10 suggest the existence of a pseudorotational motion involving two asymmetric minima which correspond to enantiomeric structures and two asymmetric transition states.

Furthermore, it would be interesting a comparison with an experimental study (currently not available in the literature) explicitly devoted to the characterization of the pseudorotational motion computationally predicted in this work.

1,3-oxathiolane

The pseudorotation of the 1,3-oxathiolane ring has been studied with far-infrared spectroscopy[109].

The computed 2D-PES for this system is shown in Fig. 1.11. The existence of a pseudorotational motion with two minima of equal energy (and two enantiomeric twisted structures of C_2 symmetry point group) corresponding to pseudorotational angles of $\frac{\pi}{2}$ and $\frac{3\pi}{2}$ and two transition states of equal energy (and the same bent structure pertaining to C_s symmetry point group) corresponding to pseudorotational angles of π and 2π has been inferred from experimental data[109]. Results displayed in Fig. 1.11 suggest the existence of a pseudorotational motion with two minima of equal energy and two transition states of equal energy, in agreement with previously reported experimental results[109]. However, an evident discrepancy between the results shown in Fig. 1.11 and what has been inferred from experimental data must be pointed out: the minima of Fig. 1.11 correspond to two different asymmetric structures which are enantiomeric forms , in sharp contrast with the already cited conclusions[109]; the same holds for transition states (although with different values of puckering amplitude and pseudorotational angles, see table 1.3).

The barrier to the pseudorotational motion has been calculated carrying out the difference between energies of, respectively, one of the two first-order saddle points (transition states) and the global minimum of 2D-PES: the result is equal to 659 cm^{-1}, slightly higher than the experimental one of 541 cm^{-1} (which is affected by an error of ± 20 cm^{-1})[109]. The barrier to planarity (a second-order saddle points of the glodal PES and a maximum of the 2D-PES shown in Fig. 1.11) has been computed to be equal to 2032 cm^{-1}, to be compared with a value of 2720 cm^{-1} extrapolated from experimental values (and considered an overestimation by the authors of the experimental study)[109].

3S-chloro-1,2-dithiolane

The author is not aware of any previous study devoted to computational or experimental characterization of 3S-chloro-1,2-dithiolane molecule.

The computed 2D-PES for this system is displayed in Fig. 1.12. Positions and relative energies of each stationary point are listed in table 1.3. Computational results obtained in this work suggest the existence of a pseudorotational path, with three different minima (each one corresponding to a different asymmetric molecular structure and with different energy, see the SI of the original article) and three different transition states (which are three first-order saddle points of the global PES, each one corresponding to a different asymmetric structure). The existence of a second-order saddle point of the global PES is also predicted, but not in correspondence of the

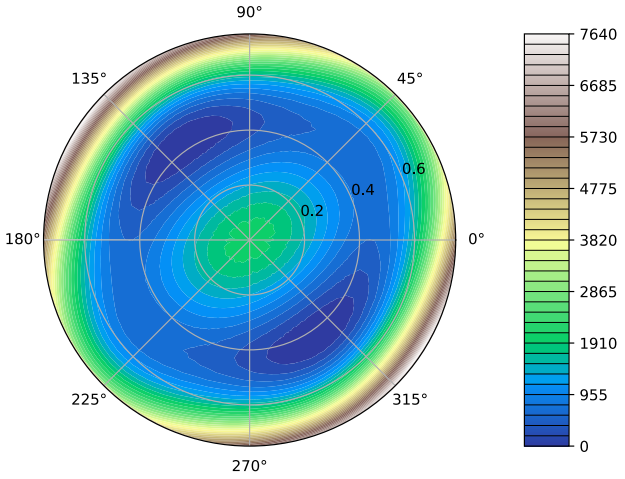

Figure 1.11: 2D-PES of 1,3-oxathiolane; energy values (given on the right of the colorbar) are in cm^{-1}.

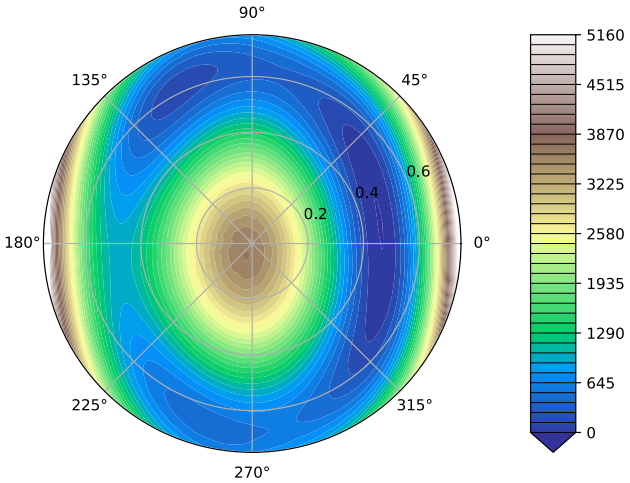

Figure 1.12: 2D-PES of 3S-chloro-1,2-dithiolane; energy values (given on the right of the colorbar) are in cm^{-1}.

planar form ($q = 0$) of the ring, in contrast with the results in Figs. 1.3 to 1.11 but in line with the results in Figs. 1.13 and 1.14.

An experimental physico-chemical characterization of this system in order to confirm (or to question) the results described in this section and illustrated in Fig. 1.12 would be desirable.

3R,5S-dichloro-1,2-dithiolane

To the best of my knowledge, no work has been published on the computational or experimental characterization of the 3R,5S-dichloro-1,2-dithiolane molecule.

In Fig. 1.13, the computed 2D-PES for this system is shown. Positions and relative energies of each stationary point can be found in table 1.3. On the basis of our results, the existence of a pseudorotational path is envisaged. More specifically, along the pseudorotational path four minima and four transition states are predicted: two of the four minima (with puckering amplitude of 0.645 and pseudorotational angles equal to 1.997 and -1.997) have exactly the same energy and correspond to enantiomeric forms, and also the other two correspond to asymmetric and enantiomeric structures with exactly the same energy ($q = 0.529$ and pseudorotational angles equal to 0.929 and -0.929, the energy difference with respect to the energy of the other two minima, which are global minima of 2D-PES, is equal to 238 cm^{-1}).

For what concerns first-order saddle points, two out of four have exactly the same energy and correspond to enantiomeric structures (θ equal to 1.386 and -1.386) while the other two corresponds to bent structures, one with $\theta = 2\pi$ and the other with $\theta = \pi$. The computational prediction of a second-order saddle point of the PES near (but not in correspondence with) the planar form of the ring is clearly illustrated by Fig. 1.13.

In order to evaluate the reliability of computational results reported in this section, a comparison with future data obtained from a physico-chemical experimental characterization of 3R,5S-dichloro-1,2-dithiolane molecule is in order.

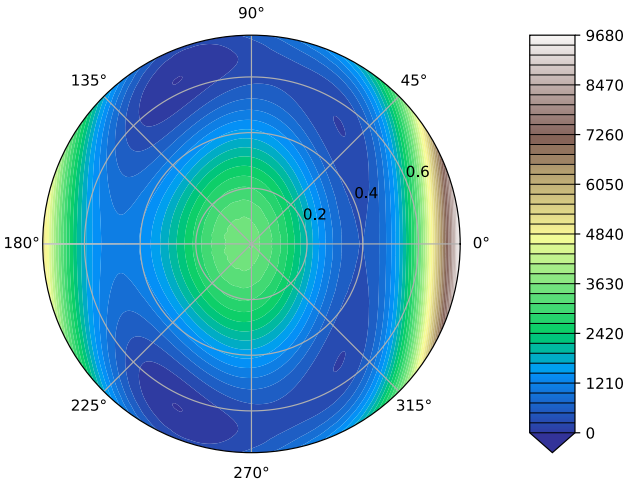

Figure 1.13: 2D-PES of 3R,5S-dichloro-1,2-dithiolane; energy values (given on the right of the colorbar) are in cm^{-1}.

3S,5S-dichloro-1,2-dithiolane

The authors are not aware of any previous results (neither computational nor experimental) currently available in the literature for what concerns the 3S,5S-dichloro-1,2-dithiolane molecule.

The computed 2D-PES for this system is shown in Fig. 1.14. Compu-

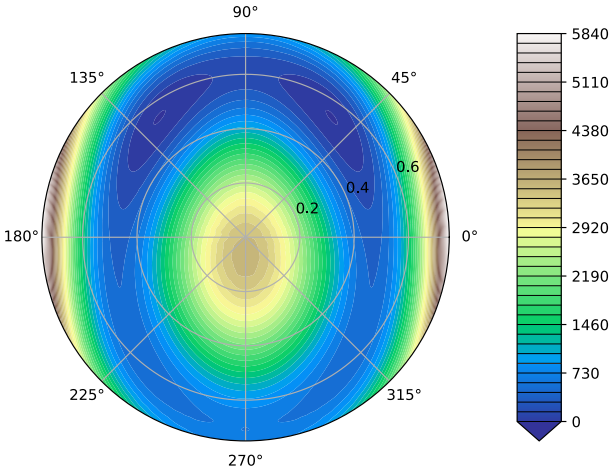

Figure 1.14: 2D-PES of 3S,5S-dichloro-1,2-dithiolane; energy values (given on the right of the colorbar) are in cm^{-1}.

tational results suggest the existence of a pseudorotational path with two minima of equal energy and structure and two transition states, one with $\theta = \frac{\pi}{2}$ and the other with $\theta = \frac{3\pi}{2}$ (puckering amplitudes, pseudorotational angles and relative energies are reported in table 1.3).

The existence of a second-order saddle point of the global PES is predicted near, but not in correspondence with, the planar ring conformation. Also in this last case, a comparison with future experimental data to check the reliability of these computational results is desirable.

1.3.4 Computational results: 2D-PES fitting

A visual inspection of the 2D-PESs reported in the previous Section suggests the possibility of expressing each 2D-PES through an analytical function of the variables q and θ. In the case of free pseudorotation the value of potential energy is independent from θ; the existence of a maximum of the 2D-PES (a second-order saddle point of the global PES) for the value $q = 0$ suggests the functional form of Eq. 1.42 (with k_1 and k_2 assuming, respectively, a negative and a positive value) to take into account the dependence of potential energy on q:

$$V(q) = k_1 q^2 + k_2 q^4 \tag{1.42}$$

In the most general case, the angular dependence of the potential energy can be described by a Fourier series:

$$V(\theta) = \sum_{n=0}^{\infty} \left[w_n^c \cos(n\theta) + w_n^s \sin(n\theta) \right] \tag{1.43}$$

Eq. 1.43 can be greatly simplified if the conformational space of the molecular system exhibits one or more symmetry elements.

A two-dimensional functional form to formulate the dependence on q and θ of a 2D-PES can be easily obtained (and has been proposed by Cremer and Pople[105]) combining eqs. 1.42 and 1.43:

$$V(q, \theta) = a + (k_1 q^2 + k_2 q^4) \sum_{n=0}^{\infty} \left[w_n^c \cos(n\theta) + w_n^s \sin(n\theta) \right] \tag{1.44}$$

In this section, Eq. 1.44 is employed to give an analytical expression of the 2D-PES of each of the systems discussed in Section 1.3.3.

It must be pointed out that, whether some results and discussions of the application of Eq. 1.44 to 5-term rings whose planar form exhibits a D_{5h}[59] or a C_{2v}[105] symmetry are available in literature, the fitting of the 2D-PES is here extended for the first time to systems having further symmetries.

The functional form chosen to fit the sampled points of the 2D-PES of each molecule is reported in Table 1.4 with the numerical value of the coefficient of determination (R^2): the coefficients b_{i-n}^x of Table 1.4 are given by Eq. 1.45 (where k_i and w_n^x are the coefficients of Eqs. 1.42, 1.43 and 1.44). Values of the coefficients are given in the SI of the original article, where a concise discussion of some technical details can be found.

$$b_{i-n}^x = k_i w_n^x \tag{1.45}$$

Some of the coefficients b_{i-n}^x of the Fourier series are equal to zero if the specific 2D-PES considered exhibits specific symmetry elements (see Table 1.1). More specifically:

molecule	functional form	R^2
cyclopentane	$V(q,\theta) = a + b^c_{1-0}q^2 + b^c_{2-0}q^4 + b^c_{1-10}q^2\cos(10\theta) + b^c_{2-10}q^4\cos(10\theta)$	0.9994
1,2-dioxolane	$V(q,\theta) = a + b^c_{1-0}q^2 + b^c_{2-0}q^4 + b^c_{1-2}q^2\cos(2\theta) + b^c_{2-2}q^4\cos(2\theta)$	0.994
tetrahydrofuran	$V(q,\theta) = a + \sum_{l=0}^{2}[b^c_{1-2l}q^2\cos(2l\theta) + b^c_{2-2l}q^4\cos(2l\theta)]$	0.997
tetrahydrothiophene		0.994
1,3-dioxolane		0.999
1,2-dithiolane		0.994
1,3-dithiolane		0.998
1,2-oxathiolane	$V(q,\theta) = a + \sum_{l=0}^{2}\{[b^c_{1-2l}\cos(2l\theta) + b^s_{1-2l}\sin(2l\theta)]q^2 + [b^c_{2-2l}\cos(2l\theta) + b^s_{2-2l}\sin(2l\theta)]q^4\}$	0.995
1,3-oxathiolane		0.997
3R,5S-dichloro-1,2-dithiolane	$V(q,\theta) = a + \sum_{l=0}^{4}[b^c_{1-l}q^2\cos(l\theta) + b^c_{2-l}q^4\cos(l\theta)]$	0.981
3S,5S-dichloro-1,2-dithiolane	$V(q,\theta) = a + \sum_{l=0}^{2}[b^c_{1-2l}q^2\cos(2l\theta) + b^c_{2-2l}q^4\cos(2l\theta)] + \sum_{l=0}^{1}\{b^s_{1-2l+1}q^2\sin[(2l+1)\theta] + b^s_{2-2l+1}q^4\sin[(2l+1)\theta]\}$	0.984
3S-chloro-1,2-dithiolane	$V(q,\theta) = a + \sum_{l=0}^{5}[b^c_{1-l}q^2\cos(l\theta) + b^c_{2-l}q^4\cos(l\theta)] + b^s_{1-1}q^2\sin(\theta) + b^s_{2-1}q^4\sin(\theta)$	0.982

Table 1.4: Functional forms and R^2 of the fitting of the 2D-PESs for the twelve considered systems.

- in the case of cyclopentane (D_{5h} symmetry)[59] only the cosine terms of the Fourier series with order 0 or an order multiple of 10 differ from 0 (i.e. in Eq. 1.44 only values of n equal to 0, 10, 20, 30 ...);

- for what concerns systems in the second column of Table 1.1 (C_{2v} symmetry)[105] only the zero and the pair (i.e. with a pair value of n in Eq. 1.44) cosine terms of the Fourier series are not 0;

- in the case of 1,2-oxathiolane and 1,3-oxathiolane molecules (third column of Table 1.1, C_s symmetry and mirror plane parallel to ring plane) only the sine and the cosine terms of zero and pair order of the Fourier series differ from 0;

- for what concerns 3R,5S-dichloro-1,2-dithiolane molecule (fourth column of Table 1.1, C_s symmetry and mirror plane perpendicular to ring plane) only the cosine terms of the Fourier series differ from 0;

- in the case of 3S,5S-dichloro-1,2-dithiolane molecule (fifth column of Table 1.1, C_2 symmetry) the sine terms of pair order and the cosine terms of odd order of the Fourier series are 0 by symmetry;

- the 3S-chloro-1,2-dithiolane molecule has no symmetry element with the exception of the identity (sixth column of Table 1.1, C_1 symmetry) and all the terms of a Fourier series could differ from 0.

The coefficients of Eq. 1.44 are obtained through a linear fit with the exception of the known argument a which has a transparent physical meaning: it is the height of the barrier to planarity, which has been obtained through the computations already discussed in the former section and, therefore, inserted before the fit and kept fixed.

The truncation of the Fourier series after a certain order has been decided on the basis of the following criteria:

- the qualitative reproduction of the main features of the 2D-PES, with respect to topology and relative energies: this aspect can be assessed by visual inspection (trough comparison with the contour plots displayed in Section 1.3.3);

- the variation of R^2 when the next relevant term of the Fourier series is added: if the entity of the variation is small enough (i.e. has no effect on the first three relevant figures) the expansion is truncated to the former term;

- the value of R^2: if $R^2 > 0.99$ and the first criterion is satisfied no other terms are added in the expansion.

It must be pointed out that the assumption of the location of the second-order saddle point of the global PES in correspondence of the planar conformation of the ring, which is one of the assumptions behind Eq. 1.44, is not always satisfied, as discussed in Section 1.3.3. More specifically, in the case of 3S-chloro-1,2-dithiolane, 3R,5S-dichloro-1,2-dithiolane and 3S,5S-dichloro-1,2-dithiolane the coordinates of the second-order saddle point of the global PES are close to but no exactly $q = 0$. This means that for these three molecules the radial part of Eq. 1.44 is a less accurate approximation (this is clearly reflected in the values of R^2 reported in Table 1.4, which are lower for these molecules), whose adequacy is, in the authors' opinion, as better as smaller is the value of the puckering amplitude of the geometry associated to the second-order saddle point of the global PES.

It is worth noting here that, while for all molecules the fitting was performed using the whole (rather large) set of computed energies, one can expect that the functional forms reported in Table 1.4 should be effective also using a much smaller set of energies. Indeed, considering for instance tetrahydrothiophene, a R^2 of 0.994 is obtained if the whole set of 5052 energies is used (corresponding to a sampling interval of 0.01875, see Table 1.2) while the same accuracy ($R^2 = 0.995$) is obtained if a reduced set of only 101 energies (corresponding to a larger sampling interval of 0.13125) is used. In other words, a rather modest number of electronic-structure calculations is required to obtain an accuarate analytical formulation of the 2D-PES using the functional forms of Table 1.4. Further details on the stability of R^2 with respect to decreasing number of fitted energies are given in the SI of the original article.

Chapter 2

Calculation of energies and properties: dealing with a single electronic state

In the previous chapter different strategies for the construction of PESs have been presented and discussed. However, to provide a satisfying solution of the nuclear problem for a specific electronic state the knowledge of the PES is not enough: a suitable approximation of the entire hamiltonian is needed, and therefore an approximation of the kinetic energy operator is mandatory (see section 2.1). Approximate rewriting of the nuclear hamiltonian and affordable methods to solve the TINSE are discussed in section 2.2 with particular emphasis on VPT2 methods and local mode approximations, while the computation of properties (IR and VCD intensities) is considered and discussed in section 2.3. At the end of the chapter (section 2.4) a series of applications will be considered: reliability and limits of methodologies based on VPT2 and local mode approximations are discussed through a comparison of calculated IR and VCD spectra with their experimental counterparts.[a]

2.1 The kinetic energy operator

Switching from classical kinetic energy to quantum kinetic energy operator (KEO) is not straightforward: the KEO is a differential operator[b] and its analytical formulation depends on the particular coordinate system chosen. More specifically, the simplifications brought about by the employment of a

[a] An account of the history of Vibrational Optical Activity (VOA) can be found in ref. 112. The first measurements of VCD spectra are reported and described in refs. 113–116.

[b] In the position basis, the quantum condition imply: $p \longmapsto -i\hbar\nabla$; this means that the presence of momenta in the classical kinetic energy term imply a differential operator in its quantum analogue.

suitable curvilinear coordinate system for the expression of the potential energy are accompanied by major complications in the expression of the KEO. Moreover, the problems which arise when the separation between rotations and vibrations is taken into account should be mentioned.

2.1.1 Classical kinetic energy

In the case of classical kinetic energy (for a system of N points or nuclei in three spatial dimensions), the expression of the kinetic energy in cartesian coordinates is the following:

$$T(\dot{\mathbf{r}}) = \frac{1}{2}\sum_{i}^{N}\sum_{\alpha}^{3} m_i \dot{r}_{i\alpha}^2 \tag{2.1}$$

where $\dot{r}_{i\alpha}$ is the α-th cartesian component of the velocity of the i-th atom of the molecular system and m_i is the mass of the corresponding nucleus (the position of each nucleus is specified with 3 cartesian components). The features of the simple expression of eq. 2.1 are not necessarily retained if the kinetic energy is formulated in terms of generalized internal coordinates. In presence of constraints, the cartesian coordinates can be replaced with a suitable system of $3N - R$ generalized internal coordinates q_k (where R is the number of constraints to which the system is subject). In the most general case:

$$\mathbf{r} = \mathbf{r}(\mathbf{q}(t), t) \tag{2.2}$$

Assuming the absence of the explicit time dependence of eq. 2.2 (i.e. if the constraints does not depend on time explicitly), the following simplified transformation holds:

$$\mathbf{r} = \mathbf{r}(\mathbf{q}(t)) \tag{2.3}$$

On the basis of eq. 2.3, the total time derivatives of the cartesian coordinates can be written as[a]:

$$\dot{r}_{i\alpha}(\mathbf{q}, \dot{\mathbf{q}}) = \sum_{k=1}^{3N-R} \frac{\partial r_{i\alpha}}{\partial q_k}\dot{q}_k \tag{2.4}$$

Therefore, employing eqs. 2.1 and 2.4 the kinetic energy term can be formulated as follows:

[a] Note that $\frac{\partial x_i}{\partial t} = 0$ only if eq. 2.3 holds; for the most general case, eq. 2.2 holds and $\frac{\partial x_i}{\partial t} \neq 0$: this means that in the most general case the term $\frac{\partial x_i}{\partial t}$ must be included in eq. 2.4.

$$T(\mathbf{q},\dot{\mathbf{q}}) = \frac{1}{2}\sum_{j,k}^{3N-R}\sum_{i=1}^{N}\sum_{\alpha}^{3} m_i \frac{\partial r_{i\alpha}}{\partial q_k}\frac{\partial r_{i\alpha}}{\partial q_j}\dot{q}_k\dot{q}_j = \frac{1}{2}\sum_{j,k}^{3N-R} g_{jk}(q_k,q_j)\dot{q}_k\dot{q}_j. \quad (2.5)$$

Where $g_{jk}(q_k,q_j)$ is an element of the square and symmetric matrix $\mathbf{g}(\mathbf{q})$. The expression of eq. 2.5 gives the generalized classical kinetic energy term for a scleronomous system. Besides the appearance of the number of constraints R and the different coordinate system, the expressions of the kinetic energy given in eqs. 2.1 and 2.5 show other two relevant differences: (i) T depends only by velocities (components of $\dot{\mathbf{r}}$) in eq. 2.1, while in eq. 2.5 T exhibits a dependence from both coordinates (components of $\mathbf{q}$) and velocities (components of $\dot{\mathbf{q}}$); (ii) In eq. 2.1 mixed terms are absent (i.e. terms of the type $\dot{r}_{i\alpha}\dot{r}_{j\beta}$ with $i \neq j$ and/or $\alpha \neq \beta$ are all equal to 0), while they are present in eq. 2.5.

The eq. 2.5 provides the expression of $T(\mathbf{q},\dot{\mathbf{q}})$ in lagrangian form, and can be rearranged in matrix notation:

$$T(\mathbf{q},\dot{\mathbf{q}}) = \frac{1}{2}\dot{\mathbf{q}}^{\mathbf{T}}\cdot\mathbf{g}(\mathbf{q})\cdot\dot{\mathbf{q}}. \quad (2.6)$$

Employing Hamilton's equations, it is possible to write eq. 2.6 in hamiltonian form[a] :

$$T(\mathbf{q},\mathbf{p}) = \frac{1}{2}\mathbf{p}^{T}\cdot\mathbf{G}(\mathbf{q})\cdot\mathbf{p}. \quad (2.7)$$

$\mathbf{G}(\mathbf{q})$ is a square and symmetric matrix (best known as the Wilson's **G** matrix) whose elements are given by the following equation:

$$G^{jk} \equiv G(q_j,q_k) = \sum_{i}^{N}\sum_{\alpha}^{3}\frac{1}{m_i}\frac{\partial q_j}{\partial r_{i\alpha}}\frac{\partial q_k}{\partial r_{i\alpha}}. \quad (2.8)$$

In this chapter the attention will be focused exclusively on the vibrational degrees of freedom. A rigorous treatment shows that the customary separation between vibrations and rotations is an approximation if the nuclei of the molecular system are not rigidly fixed at their equilibrium positions[b], although a reasonable one in many cases.

A diagonal form of the kinetic energy term can be given employing normal coordinates:

[a] the full derivation can be found in chapter 6 of ref. 3.

[b] A rigorous discussion of this point, together with a complete and clear mathematical derivation, can be found in chapter 11 of ref. 34 (see also chapter 2 of ref. 117); in the same references it is shown that a rigorous separation of the three translations (usually referred to the center of mass) can be achieved for the field-free case.

$$T = \frac{1}{2}\sum_{k=1}^{3N}\dot{Q}_k^2 = \frac{1}{2}\sum_{k=1}^{3N}P_k^2. \tag{2.9}$$

Q_k is related to the set of $3N$ mass-weighted cartesian coordinates by a linear transformation[34]. Assuming approximate separation between rotations and vibrations[a], the kinetic energy of vibrations in normal coordinates is given by:

$$T = \frac{1}{2}\sum_{k=1}^{3N-6}\dot{Q}_k^2. \tag{2.10}$$

2.1.2 The quantum operator

The construction of the quantum KEO corresponding to the harmonic approximation for the kinetic energy of vibrations in normal coordinates is straightforward. From eqs. 2.9 and 2.10, transforming the momenta P_k in the corresponding differential operators:

$$\hat{T} = \frac{1}{2}\sum_{k=1}^{3N-6}\hat{P}_k^2 = -\frac{\hbar^2}{2}\sum_{k=1}^{3N-6}\frac{\partial^2}{\partial Q_k^2}. \tag{2.11}$$

Going beyond the harmonic approximation, the separation between rotations and vibrations cannot be achieved exactly.[b] The general expression of the vibration-rotation KEO in normal coordinates for polyatomic molecules is the following[c]:

$$\hat{T} = \frac{1}{2}\sum_{\alpha}^{3}\sum_{\beta}^{3}\mu_{\alpha\beta}(\hat{J}_\alpha - \hat{\pi}_\alpha)(\hat{J}_\beta - \hat{\pi}_\beta) - \frac{\hbar^2}{8}\sum_{\alpha}^{3}\mu_{\alpha\alpha} + \frac{1}{2}\sum_{k=1}^{3N-6}\hat{P}_k^2. \tag{2.12}$$

[a] If the quadratic approximation of the potential energy surface held, the approximation would be exact and six normal modes associated to zero frequencies (and therefore completely free and barrierless) would be obtained, within the Wigner-Eckart-Sayvetz conditions.[34]

[b] An introduction to the construction of vibro-rotational hamiltonian suitable to describe flexible molecules can be found in chapter 9 of ref. 117. In principle, the coupling between rotations and vibrations must be taken into account and therefore a simple formulation dealing only with vibrations cannot be retained. In practice, the coupling between rotations and vibrations can be often minimized: in this way, the coupling between rotations and vibrations can be *approximately* (not *exactly*) decoupled. However, it should be mentioned that particularly challenging cases exist, in which low-energy vibrational and rotational motions cannot be separated even in zeroth-order.[118]

[c] This kind of approach was proposed by Wilson and Howard[119], but their hamiltonian operator was not hermitian; with the modifications proposed by Darling and Dennison[120] an hamiltonian operator which is hermitian and similar to the one obtained by Wilson and Howard can be constructed (the derivation is given in chapter 11 of ref. 34); however, the formulation of the hamiltonian provided in this thesis (which is due to Watson[121]) is a rigorous simplification of the original one.

In eq. 2.12, $\mu_{\alpha\beta}$ is the inertia tensor, $\hat{J}_\alpha$ the total angular momentum operator, $\hat{\pi}_\alpha$ the vibrational angular momentum operator and $\hat{P}_k$ the momentum operator (already seen in eq. 2.11); the indices α and β are referred to the rotational axis, while k is the index for the normal vibrational modes. In this thesis only the vibrational problem is discussed, therefore eq. 2.12 can be further simplified by omitting the total angular momentum operator:

$$\hat{T} = \frac{1}{2}\sum_{\alpha}^{3}\sum_{\beta}^{3}\mu_{\alpha\beta}\hat{\pi}_\alpha\hat{\pi}_\beta - \frac{\hbar^2}{8}\sum_{\alpha}^{3}\mu_{\alpha\alpha} + \frac{1}{2}\sum_{k=1}^{3N-6}\hat{P}_k^2. \tag{2.13}$$

Eq. 2.13 is the starting point (together with eq. 1.21) for the construction of the nuclear hamiltonian presented in eq. 2.18 (see the next section).

Additional complications arise when the construction of a KEO in curvilinear coordinates is considered. Two main approaches have been proposed and employed for the construction of analytical KEOs in curvilinear coordinates[122]. In the first one the classical kinetic energy in the hamiltonian form (eq. 2.7) is derived: the quantization of the classical term is then achieved employing the formalism proposed by Podolsky.[123] The other possibility is to adopt the KEO written in cartesian coordinates[a] as a starting point (this approach is detailed in section 3 of ref. 124): in this case the KEO in curvilinear coordinates is achieved with two applications of the chain rule.

Regardless of the specific approach adopted for the derivation, the general form of the KEO in curvilinear coordinates for rotations and vibrations is the following[b]:

$$\hat{T}^{(c)} = -\frac{\hbar^2}{2}\left(\sum_{i=1}^{3N-3}\sum_{j=1}^{3N-3} f_2^{ij}\frac{\partial^2}{\partial q_i \partial q_j} + \sum_{i=1}^{3N-3} f_1^i \frac{\partial}{\partial q_i}\right). \tag{2.14}$$

Where f_1^i and f_2^{ij} can be identified as follows (see, for example, eqs. 6 and 7 of ref. 125):

$$f_1^i = \sum_{j=1}^{3N-3}\left[\left(G^{ij}\cdot\frac{1}{2}\frac{\partial \ln g}{\partial q_j}\right) + \frac{\partial G^{ij}}{\partial q_j}\right]; \tag{2.15}$$

$$f_2^{ij} = G^{ij}. \tag{2.16}$$

Where G^{ij} is defined in eq. 2.8 (essentially, G^{ij} is an element of the Wilson's $\mathbf{G}$ matrix) and g is the determinant of the matrix $\mathbf{g}(\mathbf{q})$ (eqs. 2.5 and 2.6). Many equivalent formulations of the KEO in curvilinear coordinates can be found in literature: a brief discussion of this aspect (mainly

[a] Starting from the classical term of eq. 2.1, the KEO in cartesian coordinates can be easily obtained: $\hat{T} = -\frac{\hbar^2}{2}\sum_i^N\sum_\alpha^3 \frac{1}{m_i}\frac{\partial^2}{\partial r_{i\alpha}^2}$.

[b] the superscript $^{(c)}$ employed to label the KEO in eq. 2.14 is used to specify the normalization convention adopted for the wavefunction; see appendix B for more details.

devoted to a recognition of the available literature[3,126] on this topic) is provided in appendix B for completeness.

The complexity of a complete analytical expression of the KEO in curvilinear coordinates is a relevant obstacle to the use of curvilinear coordinates for the solution of the nuclear Schrödinger equation (i.e. to set up an entire hamiltonian in curvilinear coordinates, and not only the potential energy term which is simplified by the employment of suitable curvilinear coordinates). In order to bypass the employment of awkward analytical expressions f_1^i and f_2^{ij} can be computed numerically[125]. What is needed to set up an analytical expression of the KEO in curvilinear coordinates is an analytical expression for the elements of the $\mathbf{G}$ matrix, for the determinant g and for their derivatives for each relevant conformations (and in their neighborhoods) of the molecular system of interest: in other words, the knowledge of the explicit relation between $\mathbf{q}$ and $\mathbf{r}$ is needed. The derivation of these quantities is often laborious and leads to complicated expressions[a]: for this reason the efforts were initially focused to small systems (i.e. three or four atoms)[124]. The employment of the symbolic calculus is particularly useful in this field[130], and at least one code specifically devoted to the construction of analytical expressions of the KEO for general polyatomic systems has been proposed.[b]

2.2 Affordable computational methods for the solution of the time independent nuclear Schrödinger equation

Various methods have been proposed to achieve an approximate solution of the TINSE. The need to compromise between computational cost and accuracy must be taken into account.

If the expression of the potential energy given in eq. 1.21 is truncated at second order and combined with the expression of the kinetic energy given in eq. 2.11, a simple approximation of the nuclear hamiltonian for the vibrational problem is obtained and the TINSE of eq. 8 can be written as follows:

[a] See, for example, the following articles devoted to the derivation of an analytic form of the vibrational ($J = 0$) KEO of various systems: ref. 127 (about the vibrational KEO for sequentially bonded molecules in internal coordinates), ref. 128 (in which the derivation of the vibrational KEO in primitive internal coordinates for an hexatomic molecule with A,B—C—D—E,F connectivity is addressed) and ref. 129 (in which a general formulation of the vibrational KEO in terms of primitive internal coordinates is given).

[b] See refs. 131 and 132; in these works, the KEOs are provided in terms of polyspherical coordinates.

$$\hat{H}_n\chi(\mathbf{Q}) = \Big(-\frac{\hbar^2}{2}\sum_{k=1}^{3N-6}\frac{\partial^2}{\partial Q_k^2} + \frac{1}{2}\sum_{i=1}^{3N-6}\lambda_k Q_k^2\Big)\chi(\mathbf{Q}) = W_V\chi(\mathbf{Q}) \qquad (2.17)$$

Where λ_k is the force constant of the k-th oscillator, $\chi(\mathbf{Q})$ is the vibrational wavefunction[a] and W_V is the total vibrational energy[b]. In eq. 2.17, the vibrational problem of a general polyatomic molecule with N atoms is reduced to a set of $3N-6$ uncoupled harmonic oscillators. The analytical solutions of the 1D quantum harmonic oscillator problem are known[c] functions of the quadratic force constant; therefore, to solve out the problem for a general polyatomic molecule the $3N-6$ force constants of the uncoupled harmonic oscillators and the $3N-6$ vibrational normal coordinates must be determined: suitable algorithms to deal with this problem are provided by almost all the commercially available quantum chemical softwares[d].

Although the anharmonic corrections are completely neglected, this kind of approach is not time consuming and in some cases lead to results which are (at least qualitatively) in good agreement with the experimental observables. For more challenging cases (for which the harmonic approximation can lead to incorrect results even from a qualitative point of view) and for quantitative comparisons the inclusion of anharmonic effects is important. Various strategies have been devised; however, many of these strategies retain the solution of the nuclear problem at harmonic level as starting point.

The employment of a zero-order vibrational hamiltonian based on the harmonic approximation means that the coupling among the various internal coordinates (internuclear distances, valence and dihedral bond angles) is already retained in the zero-order model, while cubic and higher order terms

[a] Due to the separability of the nuclear hamiltonian of eq. 2.17, $\chi(\mathbf{Q})$ is the product of $3N-6$ wavefunctions, each one associated with one of the $3N-6$ uncoupled harmonic oscillators

[b] Which is the sum of the energies associated with each one of the $3N-6$ uncoupled oscillators: $W_V = W_1 + W_2 + ... + W_{3N-6}$.

[c] These solutions are provided in several textbooks; see, for example, section 3-2 of ref. 34 for the eigenvalues (energies) and section 3-3 and appendix III of ref. 34 for the eigenvectors (wavefunctions).

[d] The essential steps to solve out the TINSE at the harmonic level are: (i) the calculation of the force constants (i.e. the second derivatives of the energy of the molecular system with respect to the nuclear displacements $\frac{\partial E}{\partial r_{i\alpha}\partial r_{j\beta}}$), needed to build the Hessian matrix $\mathbf{H}$: the availability of the analytical calculation of these constants depends on the level of theory employed and on the quantum chemical software used (in this thesis, the calculation of the force constants at harmonic level is always performed analytically); (ii) the diagonalization of the matrix $\tilde{\mathbf{H}}$ which is equal to $\mathbf{H}$ if mass-weighted cartesian coordinates are employed, while its elements are $\frac{\left(\frac{\partial E}{\partial r_{i\alpha}\partial r_{j\beta}}\right)}{\sqrt{m_i}\sqrt{m_j}}$ if cartesian coordinates are not mass-weighted: the resulting eigenvectors are the normal coordinates (given as linear combinations of the cartesian coordinates) and the eigenvalues are the force constants of the uncoupled oscillators (each one associated with a specific normal coordinate).

of the potential energy expansion are neglected and included as perturbations at higher order[39]. In the case of a variational anharmonic treatment which employ the potential expansion given in eq. 1.22 the solution of the harmonic problem is needed to determine the normal mode coordinates along which the n-mode expansion of eq. 1.22 is performed[a].

Other models which are suitable for the inclusion of anharmonic effects but do not retain the harmonic approximation in the zero-order vibrational hamiltonian have been devised: the local mode approximation[134,135] is an example[b]. In the case of a treatment based on local mode vibrations, the zero-order vibrational hamiltonian includes a relevant part of the diagonal anharmonic correction, while the coupling among the various internal coordinates is taken into account at a higher order, often in a perturbative fashion.

In this thesis the anharmonic effects have been included through computational protocols based on VPT2 and local mode approximations. The choice between the VPT2 and the local mode pictures must be made at the very beginning, and the nature of the molecular vibrations under investigation can suggest the most effective option: for example, the inclusion of the harmonic coupling among the various internal coordinates at the zero-order level neglecting diagonal anharmonic effects is advantageous for the computational reproduction of the fundamental transitions in the mid IR region (900-1600 cm^{-1}) where vibrations are strongly delocalized. The same is no longer true if the vibration under investigation is a high overtone of X—H stretching, whose anharmonicity is not a small perturbation and the corresponding fundamental frequency is quite different from those of other modes. Therefore, the inclusion of anharmonic effects at the zero-order level is highly desirable and the coupling of the other internal coordinates to the internuclear X—H distances is less important.

2.2.1 VPT2: calculation of energies

The hamiltonian in the framework of the VPT2 theory can be easily constructed (see appendix B for the derivation) combining eqs. 1.21 and 2.13, and is given in the following expression (where normal modes coordinates

[a] In this case, second derivatives of the energy with respect to the nuclear displacements has to be obtained only at the beginning of the procedure, and therefore is not the bottleneck of the computational procedure; further, the second derivatives are not employed for the numerical calculation of third and fourth derivatives, which are needed when an anharmonic expansion based on the taylor expansion (eq. 1.21) is adopted, and therefore their accuracy is less relevant than in an ordinary perturbative treatment: this considerations imply that the implementation of the analytical calculation of the second derivatives of the energy is less important in a code which employ this kind of variational anharmonic treatment (for example, the quantum chemical software MOLPRO[133] solve out the harmonic problem with numerical differentiation of the first derivatives of the energy with respect to the nuclear displacement even when DFT methods are employed).

[b] Other examples can be cited: an early one is the flexible model proposed by meyer[136].

and associated momenta are dimensionless as defined in the section B.2 of appendix B):

$$\begin{aligned}\hat{H} =& hc\Bigg\{\frac{1}{2}\sum_{i=1}^{3N-6}\omega_k(p_i^2+q_i^2)+\frac{1}{3!}\sum_{ijr}^{3N-6}\phi_{ijr}q_iq_jq_r+\\ &+\frac{1}{4!}\sum_{ijrs}^{3N-6}\phi_{ijrs}q_iq_jq_rq_s+\frac{1}{2}\sum_{\alpha\beta}^{3}\mu_{\alpha\beta}\hat{\pi}_\alpha\hat{\pi}_\beta\Bigg\}.\end{aligned} \tag{2.18}$$

The vibrational energy (relative to the zero-point energy, ZPE, and for an asymmetric top molecule) of the state $|k\rangle$ is given by equation 2.19:

$$\epsilon_k = hc\Bigg\{\sum_{i=1}^{3N-6}n_i^k\omega_i+\sum_{i}^{3N-6}\sum_{j=i}^{3N-6}\chi_{ij}\Big[n_i^kn_j^k+\frac{1}{2}(n_i^k+n_j^k)\Big]\Bigg\}. \tag{2.19}$$

In Eq. 2.19, N is the number of nuclei of the molecular system considered, ω_i is the harmonic wavenumber associated to the i-th normal mode with n_i^k quanta in state $|k\rangle$ and χ_{ij} is an element of the $\boldsymbol{\chi}$ matrix collecting the anharmonic coefficients. The wavenumbers (in cm^{-1}) associated to fundamental transitions, first overtones ($\Delta n_i = n_i^k - n_i^{k'} = 2$) and combinations ($\Delta n_i = 1$, $\Delta n_j = 1$) are given, respectively, in equations 2.20, 2.21 and 2.22:

$$\nu_i = \omega_i + 2\chi_{ii} + \sum_{r\neq i=1}^{3N-6}\frac{\chi_{ir}}{2} \tag{2.20}$$

$$[2\nu_i] = 2\omega_i + 6\chi_{ii} + \sum_{r\neq i=1}^{3N-6}\chi_{ir} \tag{2.21}$$

$$[\nu_i\nu_j] = \omega_i+\omega_j+2\chi_{ii}+2\chi_{jj}+2\chi_{ij}+\frac{1}{2}\sum_{r\neq\{i,j\}=1}^{3N-6}\big(\chi_{ir}+\chi_{jr}\big) \tag{2.22}$$

Diagonal and off-diagonal elements of the $\boldsymbol{\chi}$ are reported in Equations 2.23 and 2.24:

$$16\chi_{ii} = \phi_{iiii} - \frac{5\phi_{iii}^2}{3\omega_i} - \sum_{j\neq i=1}^{3N-6}\frac{(8\omega_i^2-3\omega_j^2)\phi_{iij}^2}{\omega_j(4\omega_i^2-\omega_j^2)} \tag{2.23}$$

$$\begin{aligned}4\chi_{ij} =& \phi_{iijj} - \frac{2\omega_i\phi_{iij}^2}{(4\omega_i^2-\omega_j^2)} - \frac{2\omega_j\phi_{ijj}^2}{(4\omega_j^2-\omega_i^2)} - \frac{\phi_{iii}\phi_{ijj}}{\omega_i} - \frac{\phi_{jjj}\phi_{iij}}{\omega_j}\\ &+\sum_{r\neq\{i,j\}=1}^{3N-6}\Big[\frac{2\omega_r(\omega_i^2+\omega_j^2-\omega_r^2)\phi_{ijr}^2}{\Delta_{ijr}} - \frac{\phi_{iir}\phi_{jjr}}{\omega_r}\Big] + \frac{4(\omega_i^2+\omega_j^2)}{\omega_i\omega_j}\sum_{\alpha=a,b,c}B_\alpha^{eq}\{\zeta_{ij}^\alpha\}^2\end{aligned} \tag{2.24}$$

ζ_{ij}^{α} and B_{α}^{eq} are, respectively, the Coriolis constant (coupling normal modes i and j) and the rotational constant associated to the principal rotation axis α; ϕ_{ijr} and ϕ_{ijrs} are respectively the cubic and quartic force constants (referred to a potential expanded with non-restrictive summations) and Δ_{ijr} is given in equation 2.25:

$$\Delta_{ijr} = \omega_i^4 + \omega_j^4 + \omega_r^4 - 2(\omega_i^2\omega_j^2 + \omega_i^2\omega_r^2 + \omega_j^2\omega_r^2). \tag{2.25}$$

In ref. 137 complete and detailed derivation (starting with the hamiltonian provided in eq. 2.18) of eqs. 2.19-2.25 can be found. The derivation of ref. 137 is based on Van Vleck perturbation theory.

When eqs. 2.19-2.25 are employed, a special care must be devoted to the following points:

- Resonances must be properly treated in order to provide reliable results. The potential impact of Fermi resonances (FRs)[138] on final results can be easily recognized in the expressions of diagonal and off-diagonal elements of the $\boldsymbol{\chi}$ matrix[a]. These resonances are related to the first-order term of the perturbative expansion of the hamiltonian (see eq. B.13) and therefore often referred to as first-order resonances or 1-2 resonances. A rigorous derivation of these terms is given in subsection 4.2.2 of ref. 137. The effects of Darling-Dennison resonances (DDRs) should be taken into account as well: originally, this name was given to the resonant interaction between two overtone states with similar energies, the fundamental states of which have different simmetries[120] (which is related to the second order of the perturbative expansion of the hamiltonian), but today is used for other types of second-order resonances (more specifically, 2-2 resonances between two different combinations of two modes, 1-3 and 1-1 resonances). These resonances do not affect the elements of the $\boldsymbol{\chi}$ matrix:[b] nevertheless, their effects on the final results can be relevant. Suitable computational protocols to deal with FRs are briefly summarized and discussed in section B.6 of appendix B.

[a] More specifically, the last term on the right hand side of eq. 2.23 can be decomposed as follows: $\frac{(8\omega_i^2-3\omega_j^2)\phi_{iij}^2}{\omega_j(4\omega_i^2-\omega_j^2)} = \frac{\phi_{iij}^2}{2}\left(\frac{1}{2\omega_i+\omega_j} + \frac{4}{\omega_j} - \frac{1}{2\omega_i-\omega_j}\right)$; if $2\omega_i \approx \omega_j$ (FR of type 1) the last term of the previous equation diverge; for what concerns the right hand side of eq. 2.24, the following equivalence holds:$-\frac{2\omega_r(\omega_i^2+\omega_j^2-\omega_r^2)\phi_{ijr}^2}{\Delta_{ijr}} = \frac{\phi_{ijr}^2}{4}\left(\frac{1}{\omega_i+\omega_j+\omega_r} + \frac{1}{-\omega_i+\omega_j+\omega_r} + \frac{1}{\omega_i-\omega_j+\omega_r} - \frac{1}{\omega_i+\omega_j-\omega_r}\right)$; if $\omega_i+\omega_j \approx \omega_r$ (FR of type 2) the right hand side of the previous equation contains a near-singular term; see eqs A8 and A9 of appendix A in ref. 139.

[b] A complete derivation of these terms can be found in subsection 4.2.3 of ref. 137, in which results previously summarized with some typographical errors in ref. 140 are corrected.

- Large Amplitude Motions (LAMs) are not properly treated with VPT2 methods. These motions are not only poorly described by VPT2: they may also contaminate its results, thus leading to large errors on those vibrations (even at high frequency) which are coupled to LAMs. Therefore, a reliable computational protocol should include their identification and exclusion (together with their contribution to the anharmonic force field) from the VPT2 treatment. LAMs are usually connected to internal rotations and inversion motions.

The computational protocol adopted in this thesis for anharmonic calculations based on the VPT2 formulation is known as Generalized VPT2 (GVPT2). Other computational protocols have been devised in the framework of the VPT2 formulation (the main difference among the various protocols is the procedure chosen to deal with resonances). These pivotal aspects are introduced and commented in section B.6 of appendix B.

2.2.2 Local mode approximation: calculation of energies

In the framework of the local mode approximation, the nuclear hamiltonian is set up as follows:

$$\hat{H} = \hat{H}^0_{HCAO} + \sum_{i}^{n-1}\sum_{j>i}^{n}\hat{H}_{ij} = \sum_{i}\left(-\frac{\hbar^2}{2\mu_i}\frac{\partial^2}{\partial x_i^2} + V_i^{morse}\right) + \sum_{i}^{n-1}\sum_{j>i}^{n}\hat{H}_{ij} \quad (2.26)$$

In eq. 2.26, x_i and μ_i, respectively, designate the coordinate and the reduced mass associated to the i-th bond stretching, while V_i^{morse} is defined in the following manner:

$$V_i^{morse} = D_e[1 - e^{-a(x_i - x_i^e)}]^2 \quad (2.27)$$

In eq. 2.27, D_e is the dissociation energy associated to the bond stretching coordinate (referred to the equilibrium distance x_i^e, namely $D_e = E_{x_i \mapsto \infty} - E_{x_i^e}$) and a is a molecular parameter[a] (a and D_e determine the shape of the Morse potential function defined in eq. 2.27).

Eq. 2.26 has been employed prevalently for the calculation of solutions of the vibrational problem associated to the stretching modes[b]. The complete form given in eq. 2.26 has been used for the study of the stretching modes of small molecules of the types XH_2, XH_3 and XH_4 with X labeling an heavy

[a] Determining how fast the Morse curve reaches the asymptote for $x_i \mapsto \infty$.

[b] The decoupling of the bending and the stretching degrees of freedom is a serious limitation of the model presented in this subsection. Strategies to overcome this limitation have been proposed (see section III of ref. 141).

atom[a]: in these simple cases, μ_i is the reduced mass of the X—H fragment, given by:

$$\mu_i = \frac{m_H m_X}{m_H + m_X} \tag{2.28}$$

with m_H and m_X masses of, respectively, H and X nuclei; the interaction between the two bond stretches is modeled through the following term:

$$\hat{H}_{ij} = C_{ij} x_i x_j + G^{ij} \Big(-i\hbar \frac{\partial}{\partial x_i} \Big) \Big(-i\hbar \frac{\partial}{\partial x_j} \Big) \tag{2.29}$$

The first term on the right hand side of eq. 2.29 is related to the potential energy interaction between the two bond stretches labeled with i and j[b], while the second term accounts for the most relevant kinetic interaction (G^{ij} is an element of the Wilson's **G** matrix).

For the investigation of more complex molecular systems, the interaction term $\sum_i^{n-1} \sum_{j>i}^{n} \hat{H}_{ij}$ of the local mode hamiltonian (eq. 2.26) can be partially simplified[c] or totally neglected[d]. Another approximation can be adopted for the evaluation of the matrix elements of the interaction terms of the local mode hamiltonian presented in eq. 2.26. Known as Harmonically Coupled Anharmonic Oscillators (HCAO) model, this approximation is useful for didactic purposes (details can be found in section 2.2 of ref. 134), although its reliability to achieve accurate numerical results has been questioned[134].

In this thesis, the interaction term is totally neglected and therefore the following expression for the vibrational energy of the state $|l\rangle$ associated to the bond stretches (investigated with the local mode approximation) holds:

$$\epsilon_l = \sum_i \Big\{ hc[n_i^l \omega_i + \chi_{ii} n_i^l (n_i^l + 1)] \Big\} \tag{2.30}$$

[a] Three typical examples are H_2O for the XH_2 type, NH_3 for the XH_3 and CH_4 for the XH_4 type.

[b] Sometimes the first term on RHS of eq. 2.29 is given as function of two Morse variables y_i and y_j (where $y_i = 1 - e^{-a(x_i - x_i^e)}$), see for example eq. 44 of ref. 134; the formulation given in eq. 2.29 can be easily obtained retaining the first term of the Taylor expansions of the two Morse variables y_i and y_j (as explained in section II A of ref. 141, pages 46 and 47).

[c] For example, this is the solution adopted in ref. 142 where the stretching modes associated to the vibrational motions of the six C—H bonds in benzene are investigated by means of a local mode hamiltonian constructed as follows: the Morse potential is adopted for the description of each C—H bond, while the C—C bond stretches are treated as harmonic oscillators and the coupling between the C—C stretches is neglected; the kinetic interaction between two bonds is taken into account only if these bonds have a C atom in common.

[d] i.e. the second term on the RHS of eq. 2.26 is completely neglected, $\sum_i^{n-1} \sum_{j>i}^{n} \hat{H}_{ij} = 0$; this approximation has been adopted by Abbate and coworkers[143–145].

Eq. 2.30 is similar to eq. 2.19; the main formal differences are: (i) the absence (in eq. 2.30) of the off-diagonal elements of the anharmonic matrix $\boldsymbol{\chi}$, which appear in eq. 2.19; (ii) the energies are referred to different basis: local modes for what concerns eq. 2.30, normal modes in the case of eq. 2.19 (although a normal mode associated to a high frequency bond stretching can be highly localized and therefore does not involve significant contribution by other internal degrees of freedom in the case of asymmetric top molecules); (iii) the energy given in eq. 2.19 takes into account all the $(3N-6)$ vibrational degrees of freedom (in the framework of the VPT2 approximation), while the energy of eq. 2.30 is associated only with the bond stretchings investigated with the local mode approximation (usually only a selection of the X—H bond stretchings of the molecular system under study).

Surveys focused on the establishment of a connection between local and normal mode basis for the formulation of the vibrational hamiltonian of X—H stretching vibrations can be found in literature[146,147]. With this respect, two results should be pointed out:

- When the Morse potential is expanded (about the equilibrium bond length) as a Taylor series and truncated at the fourth order, the second-order perturbation theory can be easily applied to calculate the vibrational levels (starting from a harmonic vibrational hamiltonian and employing the perturbation theory to introduce cubic and quartic terms): it turns out that the energies associated to the bond stretch under investigation are exactly correct; in other words, the two errors (one due to the truncation of the Taylor expansion and the other own to the employment of second-order perturbation theory) cancel out exactly (see section 2 of ref. 147 for the derivation; this result is mentioned also in section 2 of ref. 124).

- Bearing in mind the previous statement, the following relations hold: if an hamiltonian including a morse potential function for each bond stretch and the quadratic terms of potential and kinetic couplings between each pair of bond oscillators is set up for small molecules of the type XH_n (with $n = 2, 3, 4$), the results obtained adopting local mode basis are identical to the results observed if the normal mode basis is employed[147]; moreover, when the vibrational excitation is low the pattern exhibited by the energy levels is closer to the one predicted by the normal mode approximation, while the pattern exhibited by the energy levels associated to overtone signals is closed to the pattern predicted in the pure local mode limit[147].

To avoid confusion, a small ambiguity in the terminology employed until this point must be explicitly pointed out. Besides its employment in the context of anharmonic calculations, the local mode concept can be a useful tool

to investigate (in the molecular systems of interest) localized structural features of chemical relevance. These features are often hidden (by the coupling among the various internal coordinates) when vibrational normal modes are directly employed for the analysis of calculation results. Therefore, some authors have devoted their efforts to the employment of the local mode concept as a useful analysis tool of results originally given in the normal mode basis (see, for example, ref. 148). Further discussions of this point are beyond the scope of this thesis.

2.3 Simulation of IR and VCD intensities

The methods introduced in the previous section are employed for the calculation of transition frequencies. For a direct comparison with the experimental observables a reliable protocol for the calculation of the intensity associated to each transition frequency is needed.

The physical quantities directly obtained from the experimental measurements are the molar extintion coefficient ε (in the case of IR absorption spectroscopy) and the differential molar extintion coefficient $\Delta\varepsilon$ (in the case of VCD spectroscopy). These quantities are functions of the energy of the incident radiation (in the IR region of the electromagnetic spectrum usually given in wavenumbers) and can be obtained by means of quantum chemical calculations through the following formulas[149]:

$$\varepsilon(\overline{\nu}) = \frac{8\pi^3 \mathcal{N}_A \overline{\nu}}{3000hc \cdot 4\pi\varepsilon_0 \cdot \ln 10} \sum_g \rho_g \sum_e D_{ge}\delta(\epsilon_e - \epsilon_g - \overline{\nu}), \tag{2.31}$$

$$\Delta\varepsilon(\overline{\nu}) = \frac{32\pi^3 \mathcal{N}_A \overline{\nu}}{3000hc^2 \cdot 4\pi\varepsilon_0 \cdot \ln 10} \sum_g \rho_g \sum_e R_{ge}\delta(\epsilon_e - \epsilon_g - \overline{\nu}), \tag{2.32}$$

where $\mathcal{N}_A$ is the Avogadro constant, the subscripts g and e label initial (with wavenumber ϵ_g) and final (with wavenumber ϵ_e) states, δ is the Dirac function, ρ_g is the Boltzmann population of the initial state g and $\overline{\nu}$ labels the wavenumber of the incident radiation[a]. The dipole strength D_{ge} and the rotational strength R_{ge} are defined as follows:

$$D_{ge} = |\langle \boldsymbol{\mu} \rangle_{g,e}|^2, \tag{2.33}$$

$$R_{ge} = \mathrm{Im}[\langle \boldsymbol{\mu} \rangle_{g,e} \cdot \langle \boldsymbol{m} \rangle_{e,g}]. \tag{2.34}$$

[a] Actually, eqs. 2.31 and 2.32 do not take into account the extension of the experimental signals over a range of frequencies (i.e. the broadening of the spectral lines); for this reason, computational results are often displayed employing a suitable bandwidth value and applying it to each spectral line.

In the case of IR and VCD the intensities are related to the transition integrals of the electric dipole ($\langle \boldsymbol{\mu} \rangle_{g,e}$) and the magnetic dipole ($\langle \boldsymbol{m} \rangle_{g,e}$) moments. Therefore, $\langle \boldsymbol{\mu} \rangle_{g,e}$ and $\langle \boldsymbol{m} \rangle_{g,e}$ need to be calculated in order to simulate IR and VCD spectra.

The transition integral $\langle \boldsymbol{P} \rangle_{g,e}$ of a property $\boldsymbol{P}$ is[149]:

$$\langle \boldsymbol{P} \rangle_{g,e} = \frac{\left\langle \psi_{Gg} \middle| \hat{\boldsymbol{\mathcal{P}}} \middle| \psi_{Ge} \right\rangle}{\sqrt{\langle \psi_{Gg} \,|\, \psi_{Gg} \rangle \langle \psi_{Ge} \,|\, \psi_{Ge} \rangle}} \tag{2.35}$$

Eq. 2.35 can be simplified if the wavefunction ψ is partitioned between the electronic (ϕ) and the nuclear (χ) wavefunctions (this is always possible in the framework of the Born-Oppenheimer approximation); moreover, the separation of the vibrational part of the nuclear wavefunction from the translational and (employing the Eckart conditions) the rotational contributions can be accomplished; therefore, only the vibrational part of the nuclear wavefunction is retained:

$$\langle \boldsymbol{P} \rangle_{g,e} = \frac{\left\langle \chi_{Gg} \middle| \hat{\boldsymbol{P}} \middle| \chi_{Ge} \right\rangle}{\sqrt{\langle \chi_{Gg} \,|\, \chi_{Gg} \rangle \langle \chi_{Ge} \,|\, \chi_{Ge} \rangle}}. \tag{2.36}$$

$\hat{\boldsymbol{P}}$ is defined as follows:

$$\hat{\boldsymbol{P}} = \left\langle \phi_G \middle| \hat{\boldsymbol{\mathcal{P}}} \middle| \phi_G \right\rangle = \left\langle \phi_G \middle| (\hat{\boldsymbol{\mathcal{P}}}^{el} + \hat{\boldsymbol{\mathcal{P}}}^{n}) \middle| \phi_G \right\rangle; \tag{2.37}$$

where $\hat{\boldsymbol{\mathcal{P}}}$ is partitioned in two parts: the electric ($\hat{\boldsymbol{\mathcal{P}}}^{el}$) and the nuclear ($\hat{\boldsymbol{\mathcal{P}}}^{n}$) contributions.

For what concerns the calculation of IR and VCD intensities, eq. 2.37 unveils the pivotal importance of the four integrals which follow:

$$\langle \phi_G \,|\, \hat{\boldsymbol{\mu}}^{n} \,|\, \phi_G \rangle; \tag{2.38}$$

$$\langle \phi_G \,|\, \hat{\boldsymbol{\mu}}^{el} \,|\, \phi_G \rangle; \tag{2.39}$$

$$\langle \phi_G \,|\, \hat{\boldsymbol{m}}^{n} \,|\, \phi_G \rangle; \tag{2.40}$$

$$\langle \phi_G \,|\, \hat{\boldsymbol{m}}^{el} \,|\, \phi_G \rangle. \tag{2.41}$$

While the calculation of the integrals provided in eqs. 2.38-2.40 can be performed in the customary framework of the Born-Oppenheimer approximation, to calculate the integral given in eq. 2.41 a more articulate approach must be employed (see, for example, chapters 2 and 4 of ref. 150).

To carry out the calculation of the electronic contribution to the magnetic transition dipole moment, some contribution to the nuclear kinetic energy

(which are omitted when the Born-Oppenheimer approximation is assumed) are taken into account trough first order perturbation theory. In this manner a suitable wavefunction (which is still separable in two components, the nuclear and the electronic ones) can be constructed (more details are given in section B.3 of appendix B) and the calculation of $\langle \phi_G \chi_{Gg} \,|\, \hat{\boldsymbol{m}}^{el} \,|\, \phi_G \chi_{Ge} \rangle$ can be performed going beyond the Born-Oppenheimer approximation with a first-order perturbative correction (see section B.4 of appendix B).

In the next subsections, solutions of eq. 2.36 based on VPT2 and local mode approximation methods are provided and briefly discussed.

2.3.1 VPT2: calculation of properties

The VPT2 method allowed an extension of the number of molecular systems for which the calculation of anharmonic transition frequencies is possible (i.e. accessible at reasonable computational cost). This is due to the good compromise achieved between computational cost and accuracy. For this reason, many efforts have been devoted to derive a formulation of IR and VCD intensities based on VPT2 method and to its implementation. The aim was the simulation of IR and VCD spectra at anharmonic level avoiding a considerable increase of the computational costs sustained for the calculation of anharmonic transition frequencies.

A number of derivations and implementations for the calculation of IR[a] and VCD[b] anharmonic intensities through VPT2 method have been proposed in literature; among these, the formulation provided in ref. 149 has a number of advantages[c] and therefore is briefly presented in this subsection.

Focusing on a single component α of the property $\boldsymbol{P}$, the explicit formulation of the transition integral for a fundamental band $\langle P^\alpha \rangle_{0,1_i}$ is given in eq. 2.42,[149] while the formulation for first overtones ($\langle P^\alpha \rangle_{0,2_i}$) and combination bands ($\langle P^\alpha \rangle_{0,1_i 1_j}$) is provided in eq. 2.43.[d] The physical quantities which correspond to P_i^α, P_{ji}^α, P_{jki}^α and the values of S, s_0, s_1 and s_2 are

[a] For what concerns the employment of contact transformation theory for the calculation of IR anharmonic intensities trough VPT2 method, the first contribution which provided a complete account (and a numerical implementation) of the electric dipole matrix elements needed for the anharmonic correction of the intensities associated to fundamental IR transitions is due to Handy and coworkers[151]; however, some earlier attempts[152–154] can be found in literature. Later contributions employing a formulation based on Rayleigh-Schrödinger perturbation theory are in refs. 155 and 156.

[b] The first formulation (based on contact transformation theory and limited to the anharmonic correction of VCD intensities of fundamental transitions) can be found in ref. 157; a formulation suitable for two quanta transitions (both combinations and overtones) is given in ref. 149.

[c] The formulation given in ref. 149 can be exploited for the calculation of both magnetic and electric vibrational transition dipole moments and is implemented in the Gaussian suite of programs[12].

[d] There is an error in the original formulation given in ref. 149; the correct formulation (reported in this thesis) is provided in eq. 23 of ref. 158.

functions of the specific property of interest (see table 2.1).

$$
\begin{aligned}
&\langle P^\alpha\rangle_{0,1_i} = \\
&s_0\cdot S\cdot P_i^\alpha + \frac{s_2}{2}\sum_j [P_{jij}^\alpha + P_{ijj}^\alpha + SP_{jji}^\alpha] - \frac{s_0}{8}\sum_{jk}\left\{\phi_{ijkk}P_j^\alpha\left[\frac{1}{\omega_i+\omega_j} - \frac{S(1-\delta_{ij})}{\omega_i-\omega_j}\right]\right\} \\
&- \frac{s_1}{8}\sum_{jk}\left\{\phi_{ijk}(P_{jk}^\alpha + P_{kj}^\alpha)\Big(\frac{1}{\omega_i+\omega_j+\omega_k} - \frac{S}{\omega_i-\omega_j-\omega_k}\Big) + \frac{\phi_{jkk}}{\omega_j}[2SP_{ji}^\alpha + (1+S)P_{ij}^\alpha]\right\} \\
&+ \frac{s_0}{2}\sum_{jk}\Big(\sum_\tau B_e^\tau \zeta_{ik}^\tau \zeta_{jk}^\tau\Big)P_j^\alpha\left\{\frac{\sqrt{\omega_i\omega_j}}{\omega_k}\Big(\frac{1}{\omega_i+\omega_j} + \frac{S(1-\delta_{ij})}{\omega_i-\omega_j}\Big) - \frac{\omega_k}{\sqrt{\omega_i\omega_j}}\Big(\frac{1}{\omega_i+\omega_j} - \frac{S(1-\delta_{ij})}{\omega_i-\omega_j}\Big)\right\} \\
&+ \frac{s_0}{16}\sum_{jkl}\phi_{ikl}\phi_{jkl}P_j^\alpha\left\{(1-\delta_{ij})(1-\delta_{ik})(1-\delta_{il})\left[\frac{1}{(\omega_i+\omega_j)(\omega_j+\omega_k+\omega_l)} - \frac{S}{(\omega_i-\omega_j)(\omega_j+\omega_k+\omega_l)}\right.\right. \\
&+ \frac{S}{(\omega_i+\omega_k+\omega_l)(\omega_j+\omega_k+\omega_l)} - \frac{1}{(\omega_i-\omega_k-\omega_l)(\omega_j+\omega_k+\omega_l)} + \frac{S}{(\omega_i-\omega_j)(\omega_i-\omega_k-\omega_l)} \\
&\left.+ \frac{1}{(\omega_i+\omega_j)(\omega_i+\omega_k+\omega_l)}\right] \\
&+ \delta_{ij}(1+\delta_{ik})(1-\delta_{il})\left[\frac{1}{2\omega_i(\omega_i+\omega_k+\omega_l)} - \frac{1}{2\omega_i(\omega_i-\omega_k-\omega_l)} + \frac{S}{2(\omega_i+\omega_k+\omega_l)^2} - \frac{S}{2(\omega_i-\omega_k-\omega_l)^2}\right] \\
&+ (1-\delta_{ij})(1-\delta_{ik})\delta_{il}\left[\frac{1}{\omega_k(\omega_i+\omega_j)} + \frac{2}{(2\omega_i+\omega_k)(\omega_i+\omega_j)} + \frac{3}{(\omega_i+\omega_j)(\omega_i+\omega_j+\omega_k)}\right. \\
&+ \frac{S}{(\omega_i-\omega_j)(\omega_i-\omega_j-\omega_k)} - \frac{2S}{(\omega_i-\omega_j)(\omega_i+\omega_j+\omega_k)} - \frac{3S}{\omega_k(\omega_i-\omega_j)} \\
&\left.\left.- \frac{S}{\omega_k(\omega_i-\omega_j-\omega_k)} + \frac{2S}{(2\omega_i+\omega_k)(\omega_i+\omega_j+\omega_k)} + \frac{3}{\omega_k(\omega_i+\omega_j+\omega_k)}\right]\right\} \\
&+ \phi_{ijk}\phi_{llk}P_j^\alpha\left\{\frac{\delta_{ij}}{\omega_i\omega_k}\Big(1 + \frac{\delta_{ik}\delta_{il}(6-4S)}{9}\Big)\right. \\
&+ (1-\delta_{ij})(1-\delta_{ik})(1-\delta_{il})\left[\frac{1}{(\omega_i+\omega_j)(\omega_i+\omega_j+\omega_k)} + \frac{1}{\omega_k(\omega_i+\omega_j)} - \frac{S}{\omega_k(\omega_i-\omega_j)}\right. \\
&\left.+ \frac{S}{(\omega_i-\omega_j)(\omega_i-\omega_j-\omega_k)} + \frac{1}{\omega_k(\omega_i+\omega_j+\omega_k)} - \frac{S}{\omega_k(\omega_i-\omega_j-\omega_k)}\right] \\
&+ \delta_{ik}(1-\delta_{ij})\left[(1+\delta_{il})\Big(\frac{1}{(2\omega_i+\omega_j)(\omega_i+\omega_j)} - \frac{S}{\omega_i(\omega_i-\omega_j)} + \frac{1}{\omega_i(2\omega_i+\omega_j)}\Big)\right. \\
&+ \delta_{il}\Big(\frac{1}{3\omega_i(\omega_i+\omega_j)} + \frac{S}{3\omega_i(2\omega_i+\omega_j)} - \frac{S}{(\omega_i-\omega_j)(2\omega_i+\omega_j)}\Big) \\
&\left.\left.+ \frac{1}{\omega_i(\omega_i+\omega_j)} - \frac{S}{\omega_j(\omega_i-\omega_j)} + \frac{S}{\omega_i\omega_j}\right]\right\}.
\end{aligned}
\tag{2.42}
$$

The symbols $\boldsymbol{\Pi}$ and $\boldsymbol{\mathcal{A}}$ (employed in table 2.1) labels the Atomic Polar Tensor (APT)[a] and the Atomic Axial Tensor (AAT)[b], respectively.

$$\langle P^{\alpha}\rangle_{0,(1+\delta_{ij})_i(1-\delta_{ij})_j} = [\sqrt{2}+(1-\sqrt{2})\delta_{ij}]\cdot\left\{\frac{s_1\cdot S}{2}(P^{\alpha}_{ij}+P^{\alpha}_{ji}) + \frac{s_0}{4}\sum_k\left[\phi_{ijk}P^{\alpha}_k\left(\frac{S}{\omega_i+\omega_j-\omega_k}-\frac{1}{\omega_i+\omega_j+\omega_k}\right)\right]\right\}. \tag{2.43}$$

$\boldsymbol{P}$	$\boldsymbol{P}_i$	$\boldsymbol{P}_{ji}$	$\boldsymbol{P}_{jki}$	s_0	s_1	s_2	S
$\boldsymbol{\mu}$	$\frac{\partial\boldsymbol{\mu}}{\partial r_i}\equiv\boldsymbol{\Pi}_i$	$\frac{\partial^2\boldsymbol{\mu}}{\partial r_i\partial r_j}\equiv\frac{\partial\boldsymbol{\Pi}_i}{\partial r_j}$	$\frac{\partial^3\boldsymbol{\mu}}{\partial r_i\partial r_j\partial r_k}\equiv\frac{\partial^2\boldsymbol{\Pi}_i}{\partial r_j\partial r_k}$	$\frac{1}{\sqrt{2}}$	$\frac{1}{2\sqrt{2}}$	$\frac{1}{6\sqrt{2}}$	$+1$
$\boldsymbol{m}$	$\boldsymbol{\mathcal{A}}_i$	$\frac{\partial\boldsymbol{\mathcal{A}}_i}{\partial r_j}$	$\frac{\partial^2\boldsymbol{\mathcal{A}}_i}{\partial r_j\partial r_k}$	$\frac{i\hbar}{\sqrt{2}}$	$\frac{i\hbar}{\sqrt{2}}$	$\frac{i\hbar}{2\sqrt{2}}$	-1

Table 2.1

Eqs. 2.42 and 2.43 are explicit solutions of eq. 2.36 obtained through VPT2 method. If $\boldsymbol{P}=\boldsymbol{\mu}$, other equations are not needed; on the other hand, if $\boldsymbol{P}=\boldsymbol{m}$ eq. 2.36 must be rewritten as follows in order to perform the calculation of $\langle\boldsymbol{m}\rangle_{g,e}$:[c,d]

$$\langle\boldsymbol{m}\rangle_{g,e} = \frac{\langle\chi_e\,|\,\hat{\boldsymbol{m}}\,|\,\chi_g\rangle}{\sqrt{\langle\chi_g\,|\,\chi_g\rangle\,\langle\chi_e\,|\,\chi_e\rangle}} - \frac{\langle\chi_g\,|\,\hat{\boldsymbol{m}}\,|\,\chi_e\rangle}{\sqrt{\langle\chi_g\,|\,\chi_g\rangle\,\langle\chi_e\,|\,\chi_e\rangle}}. \tag{2.44}$$

The need of a VPT2 formulation of $\langle P^{\alpha}\rangle_{1_i,0}$, $\langle P^{\alpha}\rangle_{2_i,0}$ and $\langle P^{\alpha}\rangle_{1_i1_j,0}$ (provided in eqs. 2.45 and 2.46) for the calculation of the rotational strength

[a] Polar tensors were proposed in ref. 159, but the popularity of these physical quantities is due to the full recognition of their usefulness which took place later. [160]

[b] The customary definition of the AAT (adopted in this thesis) was proposed by Stephens;[161] an alternative convention for the definition of the AAT has been proposed by Nafie (the simple relationship between the two conventions is explicitly given in eqs. 4.76 and 4.77 of ref. 150).

[c] For what concerns the electronic component of the magnetic vibrational transition dipole moment a treatment beyond the BO approximation is needed: the derivation is provided in section B.4 of appendix B (see in particular eq. B.46); the nuclear component is calculated in the framework of the BO approximation (see section II D of ref. 157), but can be rewritten in order to obtain a formulation similar to the one given for the electronic component (see eq. 29 of ref. 157).

[d] The formulation of $\langle\boldsymbol{m}\rangle_{g,e}$ given in eq. 2.44 is analogous to the formulation provided in ref. 157 and differs from the expression provided in eq. 23 of ref. 149; the difference between the two formulations is related to the convention adopted for magnetic and electric transition dipoles (if the RHS of eq. 23 of ref. 149 is multiplied for -1 the expression provided in ref. 157 and in this thesis is obtained), and the results obtained are exactly the same if the same convention is adopted for both (the essential point is the convention adopted for the positive direction of an electric dipole moment).

is evident from the expression of R_{ge} already provided (see eq. 2.34) and from the formulation of $\langle \boldsymbol{m} \rangle_{g,e}$ given in eq. 2.44.[a]

$$\langle P^{\alpha} \rangle_{1_i,0} = S \cdot \langle P^{\alpha} \rangle_{0,1_i} + \frac{s_2}{2}(1-S)\sum_j (P^{\alpha}_{ijj} + P^{\alpha}_{jij}), \tag{2.45}$$

$$\langle P^{\alpha} \rangle_{(1+\delta_{ij})_i(1-\delta_{ij})_j,0} = S \cdot \langle P^{\alpha} \rangle_{0,(1+\delta_{ij})_i(1-\delta_{ij})_j}. \tag{2.46}$$

An extension of the formulations provided in this subsection to the intensities of three quanta transitions (namely, to transitions of the type $0 \rightarrow 3_i$, $0 \rightarrow 2_i 1_j$ and $0 \rightarrow 1_i 1_j 1_k$) has been published.[158,b]

For the identification of FRs and DDRs which affect the calculated IR and VCD intensities[c] the two step procedure introduced in section B.6 of appendix B has a limited reliability. Another computational protocol (specifically devised to improve the simulation of IR and VCD intensities at anharmonic level) was proposed in ref. 162.

2.3.2 Local mode approximation: calculation of properties

In the framework of local mode approximation, various attempts to calculate the physical quantities needed for the computation of IR and VCD spectra have been reported in literature.

The approach proposed in this thesis is based on the formulation provided in ref. 145, which can be employed for the calculation of IR and VCD intensities associated to fundamental and first overtone transitions of certain X—H stretchings. The starting point is the expansion of $\hat{\boldsymbol{\mu}}$ and $\hat{\boldsymbol{m}}$ around the equilibrium nuclear positions:[d,e]

$$\hat{\mu}^x(\boldsymbol{r}) = \mu_0^x + \sum_{i\alpha}\left[\left(\frac{\partial \hat{\mu}^x}{\partial r_{i\alpha}}\right)_0 r_{i\alpha}\right] + \frac{1}{2}\sum_{i\alpha,j\beta}\left[\left(\frac{\partial^2 \hat{\mu}^x}{\partial r_{i\alpha}\partial r_{j\beta}}\right)_0 r_{i\alpha} r_{j\beta}\right] + \\ + \frac{1}{6}\sum_{i\alpha,j\beta,k\gamma}\left[\left(\frac{\partial^3 \hat{\mu}^x}{\partial r_{i\alpha}\partial r_{j\beta}\partial r_{k\gamma}}\right)_0 r_{i\alpha} r_{j\beta} r_{k\gamma}\right] + \ldots \tag{2.47}$$

[a] For the calculation of R_{ge} the calculation of $\langle \boldsymbol{m} \rangle_{e,g}$ (not $\langle \boldsymbol{m} \rangle_{g,e}$) is needed.

[b] Further extension (for example to four quanta transitions) would require a higher level of perturbation theory (VPT4) or a variational approach.[158]

[c] For what concerns $\langle P^{\alpha} \rangle_{0,1_i}$, the potential impact of FRs and 1-1 DDRs ($\omega_i \approx \omega_j$) can be easily guessed from the denominators of some of the term on the RHS of eq. 2.42.

[d] $\hat{\mu}^x$ and $\hat{m}^x$ are the x-th cartesian components of $\hat{\boldsymbol{\mu}}$ and $\hat{\boldsymbol{m}}$, respectively.

[e] Eq. 2.48 of this thesis is equivalent to eq. 11 of ref. 145, except for an error which is corrected (the expression given in ref. 145 must be multiplied for the imaginary unit i).

$$\hat{m}^x(\boldsymbol{r}) = \sum_{i\alpha}\left[\frac{\hbar^2}{m_i}\mathcal{A}^0_{i\alpha x}\frac{\partial}{\partial r_{i\alpha}}\right] + \sum_{i\alpha,j\beta}\left[\frac{\hbar^2}{m_i}\left(\frac{\partial \mathcal{A}_{i\alpha x}}{\partial r_{j\beta}}\right)_0 r_{j\beta}\frac{\partial}{\partial r_{i\alpha}}\right] + \\ + \sum_{i\alpha,j\beta,k\gamma}\left[\frac{\hbar^2}{m_i}\left(\frac{\partial^2 \mathcal{A}_{i\alpha x}}{\partial r_{j\beta}\partial r_{k\gamma}}\right)_0 r_{j\beta}r_{k\gamma}\frac{\partial}{\partial r_{i\alpha}}\right] + \ldots \tag{2.48}$$

With the expansions given in eqs. 2.47 and 2.48, the first two terms of the transition integrals of $\langle\boldsymbol{\mu}\rangle_{g,e}$ and $\langle\boldsymbol{m}\rangle_{e,g}$ can be written as follows:[a]

$$\langle\mu^x\rangle_{g,e} = \sum_{i\alpha}\left[\Pi^0_{i\alpha x}\langle\chi_{Gg}\,|\,r_{i\alpha}\,|\,\chi_{Ge}\rangle\right] + \frac{1}{2}\sum_{i\alpha,j\beta}\left[\left(\frac{\partial\Pi_{i\alpha x}}{\partial r_{j\beta}}\right)_0\langle\chi_{Gg}\,|\,r_{i\alpha}r_{j\beta}\,|\,\chi_{Ge}\rangle\right]; \tag{2.49}$$

$$\langle m^x\rangle_{e,g} = \sum_{i\alpha}\left[\frac{i\hbar}{m_i}\mathcal{A}^0_{i\alpha x}\left(\left\langle\chi_{Gg}\left|\frac{\hbar}{i}\frac{\partial}{\partial r_{i\alpha}}\right|\chi_{Ge}\right\rangle - \left\langle\chi_{Ge}\left|\frac{\hbar}{i}\frac{\partial}{\partial r_{i\alpha}}\right|\chi_{Gg}\right\rangle\right)\right] + \\ \sum_{i\alpha,j\beta}\left[\frac{i\hbar}{m_i}\left(\frac{\partial\mathcal{A}_{i\alpha x}}{\partial r_{j\beta}}\right)_0\left(\left\langle\chi_{Gg}\left|r_{j\beta}\frac{\hbar}{i}\frac{\partial}{\partial r_{i\alpha}}\right|\chi_{Ge}\right\rangle - \left\langle\chi_{Ge}\left|r_{j\beta}\frac{\hbar}{i}\frac{\partial}{\partial r_{i\alpha}}\right|\chi_{Gg}\right\rangle\right)\right] = \\ -2i\hbar\sum_{i\alpha}\left[\frac{\mathcal{A}^0_{i\alpha x}}{m_i}\left\langle\chi_{Ge}\left|\frac{\hbar}{i}\frac{\partial}{\partial r_{i\alpha}}\right|\chi_{Gg}\right\rangle\right] \\ -2i\hbar\sum_{i\alpha,j\beta}\left[\frac{1}{m_i}\left(\frac{\partial\mathcal{A}_{i\alpha x}}{\partial r_{j\beta}}\right)_0\left\langle\chi_{Ge}\left|r_{j\beta}\frac{\hbar}{i}\frac{\partial}{\partial r_{i\alpha}}\right|\chi_{Gg}\right\rangle\right]. \tag{2.50}$$

Nuclear positions are provided in terms of cartesian coordinates in eqs. 2.47-2.50. To obtain equations suitable for the local mode approximation, all the components of $\boldsymbol{\Pi}$ and $\boldsymbol{\mathcal{A}}$ which are not referred to the atoms X and H of the X—H stretching (the bond stretch treated as a local mode) are assumed to be zero; this approximation reduces the number of terms included in the summations of eqs. 2.49 and 2.50. To further simplify eqs. 2.49 and 2.50, the z axis of the cartesian coordinate system can be oriented along the same direction of the X—H bond.

If z_{eq} is the equilibrium length of the X—H bond and z the bond length, the displacements of X and H atoms from their equilibrium positions (z_X and z_H, respectively) satisfy the following relationship:

[a] The absence of the term $\boldsymbol{\mu}_0$ in eq. 2.49 is due to the ortogonality of the wavefunctions; for what concerns the calculation of $\langle\boldsymbol{m}\rangle_{e,g}$, the relationship provided in eq. 2.44 is employed.

$$z - z_{eq} = z_H - z_X \tag{2.51}$$

z_H and z_X are defined as follows:

$$z_H = \frac{m_X}{m_H + m_X} z = t_H(z - z_{eq}); \qquad z_X = -\frac{m_H}{m_H + m_X} z = t_X(z - z_{eq}). \tag{2.52}$$

With the relationships provided in eqs. 2.51 and 2.52, eqs. 2.49 and 2.50 can be rewritten as follows:[a,b]

$$\begin{aligned} \langle \mu^x \rangle_{g,e} = & \sum_{i=X,H} \left[\Pi^0_{i3x} t_i \langle \chi_{Gg} \,|\, (z - z_{eq}) \,|\, \chi_{Ge} \rangle \right] \\ & + \frac{1}{2} \sum_{i=X,H} \left[\left(\frac{\partial \Pi_{i3x}}{\partial z} \right)_0 t_i \langle \chi_{Gg} \,|\, (z - z_{eq})^2 \,|\, \chi_{Ge} \rangle \right]; \end{aligned} \tag{2.53}$$

$$\begin{aligned} \langle m^x \rangle_{e,g} = & -2i\hbar \sum_{i=X,H} \left[\mathcal{A}^0_{i3x} t_i \frac{1}{\mu_{XH}} \left\langle \chi_{Ge} \left| \frac{\hbar}{i} \frac{\partial}{\partial z} \right| \chi_{Gg} \right\rangle \right] \\ & - 2i\hbar \sum_{i=X,H} \left[\left(\frac{\partial \mathcal{A}_{i3x}}{\partial z} \right)_0 t_i \frac{1}{\mu_{XH}} \left\langle \chi_{Ge} \left| z \frac{\hbar}{i} \frac{\partial}{\partial z} \right| \chi_{Gg} \right\rangle \right]. \end{aligned} \tag{2.54}$$

μ_{XH} labels the reduced mass associated to the X—H bond:

$$\mu_{XH} = \frac{m_X m_H}{m_X + m_H}. \tag{2.55}$$

The transition integrals involved in eqs. 2.53 and 2.54 are provided in tables 2.2 and 2.3; the other quantities[c] needed for the calculation of $\langle \mu^x \rangle_{g,e}$ and $\langle m^x \rangle_{e,g}$ in the framework of the local mode approximation (harmonic wavenumber ω_l and diagonal anharmonic constant χ_{ll}, see tables 2.2 and 2.3; $\mathbf{\Pi}$, $\boldsymbol{\mathcal{A}}$ and their derivatives) can be obtained easily from the output of a series of harmonic calculations[d] (the protocol employed to obtain the results discussed in this thesis is provided in section B.5 of appendix B). In order

[a] A complete derivation of the connection between eq. 2.49 and eq. 2.53 and between eq. 2.50 and eq. 2.54 of this thesis can be found in ref. 145 (eqs. 12-28).

[b] The z cartesian component can be labeled with the number 3.

[c] It should be underlined that the adoption of an alternative convention for the AAT allows a more compact formulation of eq. 2.54, because $\boldsymbol{\mathcal{A}}^{naf} = -2i\hbar \boldsymbol{\mathcal{A}}^{steph}$ (see eqs. 4.76 and 4.77 of ref. 150).

[d] Which can be performed with a quantum chemical software such as the Gaussian [12] suite of programs (employed for the applications presented in the next section).

to give a more compact formulation of the transition integrals provided in tables 2.2 and 2.3, the quantity d (with the dimension of a distance) is defined as follows:

$$d^2 = \frac{h}{2c\mu_{XH}} \frac{1}{\omega_l}, \tag{2.56}$$

and the momentum conjugated to z is written as $p = \frac{\hbar}{i}\frac{\partial}{\partial z}$. The solutions provided in tables 2.2 and 2.3 for the harmonic case are well known and can be easily found in many textbooks.[a] In the anharmonic case, they were produced in a format useful for the calculation of VCD and IR/NIR intensities.

quantity	harmonic case	anharmonic case
$\langle 0 \mid z \mid 1 \rangle$	$\frac{d}{2\pi}$	$\frac{d}{2\pi}(1 - \frac{1}{2}\frac{\chi_{ll}}{\omega_l})$
$\langle 0 \mid z^2 \mid 1 \rangle$	0	$\frac{5d^2}{4\pi^2}(\frac{\lvert\chi_{ll}\rvert}{\omega_l})^{\frac{1}{2}}(1 - \frac{52}{30}\frac{\chi_{ll}}{\omega_l})$
$\langle 0 \mid p \mid 1 \rangle$	$-i\hbar\frac{\pi}{d}$	$-i\hbar\frac{\pi}{d}(1 + \frac{3}{2}\frac{\chi_{ll}}{\omega_l})$
$\langle 0 \mid zp \mid 1 \rangle$	0	$-\frac{5i}{4}\hbar(\frac{\lvert\chi_{ll}\rvert}{\omega_l})^{\frac{1}{2}}(1 + \frac{4}{15}\frac{\chi_{ll}}{\omega_l})$

Table 2.2: Transition Integrals for Fundamental Local Mode Transition

quantity	harmonic case	anharmonic case
$\langle 0 \mid z \mid 2 \rangle$	0	$-\frac{d}{2\pi\sqrt{2}}(\frac{\lvert\chi_{ll}\rvert}{\omega_l})^{\frac{1}{2}}[1 - \frac{3}{2}(\frac{\chi_{ll}}{\omega_l})]$
$\langle 0 \mid z^2 \mid 2 \rangle$	$\frac{d^2}{2\pi^2\sqrt{2}}$	$\frac{d^2}{2\pi^2\sqrt{2}}(1 + 2\frac{\chi_{ll}}{\omega_l})$
$\langle 0 \mid p \mid 2 \rangle$	0	$i\hbar\frac{\sqrt{2}\pi}{d}(\frac{\lvert\chi_{ll}\rvert}{\omega_l})^{\frac{1}{2}}[1 + \frac{3}{2}(\frac{\chi_{ll}}{\omega_l})]$
$\langle 0 \mid zp \mid 2 \rangle$	$-i\hbar\frac{\sqrt{2}}{2}$	$-i\hbar\frac{\sqrt{2}}{2}[1 + 5(\frac{\chi_{ll}}{\omega_l})]$

Table 2.3: Transition Integrals for First Overtone Local Mode Transition

2.4 Applications

In this section, some original applications of the computational methods presented in this chapter are briefly discussed. For each molecular system considered, experimental IR and VCD spectra have been measured (in collaboration with the group of professor Sergio Abbate, university of Brescia). The comparison between experimental and calculated IR and VCD spectra can be extremely useful in two different ways: (i) relating statistical

[a] For example, the harmonic solutions to the 8 transition integrals reported in tables 2.2 and 2.3 can be found in appendix III of ref. 34; the solutions given in this thesis are formulated in terms of wavenumbers and the position coordinates are not mass weighted, while in appendix III of ref. 34 the frequencies are given in hertz and the coordinates are mass-weighted.

and quantum mechanical computed data on one side and experimental data on the other side allows one to discriminate whether the empirical correlations between the experimental spectra can be explained in terms of similar physical-chemical properties and (ii) the comparison between experimental and computational spectra is essential to evaluate the reliability of a computational approach.

2.4.1 IR and VCD spectra of organic compounds: the cases of 2,3-Butanediol and *trans*-1,2-Cyclohexanediol *

In what follows, a comparison between experimental and calculated IR, VCD, NIR and NIR-VCD spectra of the two enantiomeric forms of 2,3-Butanediol[a] and *trans*-1,2-Cyclohexanediol is presented.

The two enantiomeric forms of 2,3-butanediol were characterized by means of several experimental techniques[163–170]: IR (in solution[164,165,168] and in the gas phase[166]), VCD[164,165], photoelectron circular dichroism (PECD)[169] and microwave[167] spectra have been published. Conformer stabilities and harmonic spectra in the region of fundamental transitions were already available in literature when the study presented in this thesis was undertaken.[165,167,170]

Trans-1,2-cyclohexanediol was previously studied experimentally[164,171,172] and computationally:[171,172] IR[164,172] and VCD[164] spectra in the OH stretching region, nuclear magnetic resonance (NMR) data[164], an experimental determination of the crystal structure[173,174] and an experimental evaluation of the gas-phase acidities[171] have also been reported. For what concerns computational characterization, data on the equilibrium structures calculated with DFT methods[171,172] and a two dimensional cut of the global potential energy surface (2D-PES) describing the energetic landscape associated with the rotation of two dihedral angles which determine the orientation of the two OH groups[172] were published.

Experimental and computational methods All the experimental measurements were performed in the laboratory of prof. Abbate. For the measurements of IR and VCD spectra in the regions of mid-IR, fundamental CH- and OH-stretching a commercially available apparatus (FVS-6000 JASCO FTIR) was employed, while the measurements of NIR and NIR-VCD spectra in the first overtone OH-stretching region were carried out with an home-built dispersive apparatus (described in ref. 175). More details about instrumentation, together with details about samples, experimental conditions and protocols can be found in the original article.

*The results provided in this subsection (together with more details concerning experimental and computational methods) can be found in *J. Phys. Chem. A*, **2020**, 124, 5, 1011-1024.

[a]2,3-Butanediol has two enantiomeric forms, (2R,3R) and (2S,3S), and one meso (2R,3S) form.

For what concerns the computational methods, all the calculations were carried out with a development version of the Gaussian suite of programs. Geometry optimizations (performed with the following convergence criteria: $1{\cdot}10^{-5}$ hartree/bohr and $4{\cdot}10^{-5}$ bohr on, respectively, root mean square force and displacements, with maximum values being 1.5 times larger) were carried out with the algorithm proposed in ref. 13 (and presented in section 1.1.1). Minima and transition states were confirmed by hessian evaluations.

For the computation of harmonic force fields analytic derivatives of energy[a] were employed, while for higher order derivatives (cubic and semi-diagonal quartic terms are needed for anharmonic calculations based on VPT2 approximation) a numerical differentiation scheme was exploited (a step of $0.01\text{Å}{\cdot}amu^{1/2}$ was adopted). For the calculation of transition moments an analogous procedure was employed (with the derivatives of electric ad magnetic dipoles instead of the derivatives of energy). Solvent effects were included with the Polarizable Continuum Model (PCM).

All the calculations were performed with DFT methods. More specifically:

- the preliminary analysis of low-lying conformers and LAMs was performed employing B3LYP[176–178] as exchange-correlation functional in conjunction with jul-cc-pVDZ[70,179,180] basis set, including empirical dispersion (D3BJ); for the computational characterization of LAMs, solvent effects were not taken into account, while for the preliminary analysis of low-lying conformers solvent effects were taken into account (with PCM) with a single-point calculation performed on the geometry of the isolated molecule (optimized in vacuum, *without* the inclusion of solvation effects);

- a composite scheme was employed to perform VPT2 calculations: harmonic frequencies, energies and gradients were calculated employing B2PLYP[62,181] functional with empirical dispersion (D3BJ) combined with jun-cc-pVTZ basis set and taking into account solvent effects with the PCM; B3LYP functional with empirical dispersion (D3BJ) and the jul-cc-pVDZ basis set were employed for the evaluation of the cubic and quartic terms (needed to set up the anharmonic force field); moreover, PCM contributions to XH stretchings are not included in the finite differences leading to cubic and quartic force constants because motions related to XH stretchings are too fast to allow solvent equilibration;[182,183]

- anharmonic calculations based on the local mode approach were performed with Gaussian16[12] employing B3LYP functional with TZVP[184,185] basis set.

[a] With respect to the nuclear displacements

For what concerns the calculation of transition dipole moments, the same protocol mentioned above for the calculation of the anharmonic force field at VPT2 level was employed for the calculation of electric dipole transition moments for the simulation of IR spectra. In the case of VCD spectroscopy, B2PLYP functional cannot be employed for the calculation of magnetic dipole transition moment; moreover, the results obtained for the IR spectra suggest a negligible differences between electric dipole transition moments computed at B2PLYP and at B3LYP level: therefore, for the simulation of VCD spectra the transition dipole moments computed at B3LYP level are employed.

LAMs were identified through a preliminary analysis and excluded from the VPT2 treatment. The effects of resonances were taken into account for both energy and property calculations: the two-step procedure implemented in Gaussian were employed for the identification of FRs and DDRs affecting transition frequencies, with default Gaussian thresholds;[a] the identification of FRs affecting intensities was performed with the two-step procedure proposed in ref. 162. Anharmonic spectra were computed with the GVPT2 approach for both compounds in all the spectral regions, with the exception of the CH stretching region in *trans*-1,2-cyclohexanediol.[b]

The computational protocol employed in this work to perform local mode calculations was presented elsewhere and briefly recalled in sections 2.2.2, 2.3.2 and in section B.5 of appendix B. The stretching of each of the two OH bonds for each conformer of the two molecules under investigation were evaluated with a rigid scan in 50 step, with a step size of 0.017 Å, from −0.33 to +0.454 Å with respect to the equilibrium OH bond length. The resulting functions (of the energy given as a function of the length of the OH bond) were interpolated with 8th-degree polynomials and the first three terms ϕ_{ll}, ϕ_{lll} and ϕ_{llll} were employed for the calculations of ω_l and χ_{ll}.

Preliminary analysis of low-lying conformers and computational characterization of LAMs For the calculation of IR and VCD spectra, the identification of low-lying conformers (and of their interconnections[c]) is of pivotal importance.

The low-lying conformers identified for the 1*R*,2*R*-cyclohexanediol molecule are listed in table 2.4.

The label assigned to each conformer is related to its structure. More specifically: the central six-term ring (of six carbon atoms) can assume two

[a] with the exception of the identification of 1-1 DDRs: in this case, states with an energy difference below 50cm^{-1} and an interaction term larger than 5 cm^{-1} are considered as resonant.

[b] In this case, the deperturbed VPT2 (DVPT2) approach was employed because the overestimation of the coupling among those modes in a cartesian-based description can significantly affect the calculations.

[c] In order to exclude LAMs from the VPT2 treatment.

structure	symm	ΔE	$\Delta(E+ZPE)$	ΔG	
		vacuum	vacuum	vacuum	PCM
eq-$C_{H,H}C_{H,OH}$ (**Cd-I**)	C_1	0	0	0	0
eq-$C_{H,H}$H (**Cd-II**)	C_1	26	60	86	39
eq-$C_{H,H}C_{H,H}$	C_2	402	331	197	124
ax-$C_{H,OH}$H	C_1	1262	1225	1208	1154
ax-$C_{H,H}C_{H,OH}$	C_1	1075	1049	1038	1044
ax-$C_{H,OH}C_{H,OH}$	C_2	1032	1004	986	1037
ax-HH	C_2	1540	1477	1445	1255
ax-$C_{H,H}$H	C_1	1212	1185	1170	1128
ax-$C_{H,H}C_{H,H}$	C_2	1144	1115	1109	1062

Table 2.4: Relative energies associated to each conformer of cyclohexane-1*R*,2*R*-diol; level of theory: B3LYP/jul-cc-pVDZ with Grimme's empirical dispersions (with Becke-Johnson damping); the energy differences are given in cm^{-1}; the implicit solvation was taken into account with Polarizable Continuum Model (PCM) with a single-point calculation performed on the geometry of the isolated molecule (optimized in vacuum, *without* the inclusion of solvation effects).

different chair conformations, one with both the hydroxyl groups in equatorial positions (labeled with 'eq-') and another with both the hydroxyl groups in axial positions (labeled with 'ax-'). In addition, the orientation of each hydroxyl group can be specified through a Newman projection oriented along the C—O bond: the substituent bounded to the C atom of the bond considered in the Newman projection which is in *anti* with respect to the hydrogen bounded to the O atom is employed to specify the orientation of the hydroxyl group. For example, if the *anti* substituent is an hydrogen atom the label H is introduced in the label of the conformer; on the other hand, if the *anti* substituent is a carbon atom which is bounded to two hydrogen atoms the label $C_{H,H}$ is adopted.[a] The chair conformation with the hydroxyl groups in equatorial positions (which can be involved in an intramolecular hydrogen bond only in this conformation of the six-term ring) is more stable (see table 2.4) and only the two most populated conformers are employed in this work for the computational simulation of IR and VCD spectra. If the geometry optimizations are carried out including implicit solvation through PCM additional minima can be found: more in detail, one additional minima (a TS in vacuum) with a conformation labeled with eq-HH (belonging to the C_2 symmetry point group) and an energy higher than 800 cm^{-1} has been

[a]The order employed to list the substituents which specify the orientations of the two hydroxyl groups is not relevant. For example, labels 'eq-$C_{H,H}$H' and 'eq-H$C_{H,H}$' specify the same structure (see the molecular structures reported in fig. 2.1).

located.

For what concerns 2*R*,3*R*-butanediol, low-lying conformers identified in this study are listed in table 2.5.

structure	symm	ΔE	$\Delta(E+ZPE)$	ΔG	
		vacuum	vacuum	vacuum	PCM
$G_gC_{H,OH}C_{CH_3}$ (**Bd-I**)	C_1	0	0	0	0
$G_gHC_{CH_3}$ (**Bd-II**)	C_1	16	45	67	44
$G_aHC_{H,OH}$ (**Bd-III**)	C_1	298	254	235	291
$G_aHC_{CH_3}$ (**Bd-IV**)	C_1	396	362	345	342
G_aHH	C_2	549	455	309	326
$G_aC_{CH_3}C_{CH_3}$	C_2	1188	1008	813	729
AHC_{CH_3}	C_1	1003	943	901	823
$AC_{H,OH}C_{CH_3}$	C_1	915	863	834	799
$AC_{CH_3}C_{CH_3}$	C_2	951	905	896	823
AHH	C_2	1218	1140	1077	943
$AHC_{H,OH}$	C_1	1044	961	894	834
$AC_{H,OH}C_{H,OH}$	C_2	891	822	762	771
$G_gC_{H,OH}C_{H,OH}$	C_2	1538	1415	1332	1086
$G_gHC_{H,OH}$	C_1	1598	1445	1304	1035
$G_gC_{CH_3}C_{CH_3}$	C_2	374	307	136	135

Table 2.5: Relative energies associated to each conformer of 2*R*,3*R*-butanediol; level of theory: B3LYP/jul-cc-pVDZ with Grimme's empirical dispersions (with Becke-Johnson damping); the energy differences are given in cm^{-1}; the implicit solvation was taken into account with Polarizable Continuum Model (PCM) with a single-point calculation performed on the geometry of the isolated molecule (optimized in vacuum, *without* the inclusion of solvation effects).

In the case of 2*R*,3*R*-butanediol, the same conventions already presented for the case of 1*R*,2*R*-cyclohexanediol have been employed to specify the orientation of the two hydroxyl groups. For what concerns the dihedral angle O—C(2)—C(3)—O, the same method have been employed: a Newman projection viewed in the direction of the C(2)—C(3) bond gives the relative positions of the two hydroxyl groups. When the two hydroxyl substituents are *anti* with respect to each other, the prefix 'A' is employed in the label of the corresponding conformer, otherwise the label 'G' (standing for *gauche*) is employed. The subscript of 'G' depends on the relative orientation, in the same Newman projection, of the two methyl groups: if the two methyl moieties are *anti* with respect to each other, the subscript 'a' is employed (and the prefix 'G_a' is therefore adopted), otherwise the subscript 'g' is used (and the prefix 'G_g' is adopted).

1*R*,2*R*-cyclohexanediol is a cyclic molecule with a six-membered central

ring of carbon atoms and two adjacent hydroxyl groups in trans relative positions. The ring-puckering of the central ring can be described with three coordinates,[56] and the rotation of the two hydroxyl groups can be described with the two associated dihedral angles. This intuitive description of the conformational flexibility of 1*R*,2*R*-cyclohexanediol in terms of 5 degrees of freedom can be further simplified: an explicit treatment of puckering motion is not necessary because of the same ring conformation (chair conformation with both hydroxyl groups in equatorial position) shared by all the lowest energy structures. Although a series of relative energy minima encompassing chair conformations with both hydroxyl groups in axial positions can be obtained (their relative energies are reported in table 2.4), they are significantly less stable than the previous ones because of the absence of any hydrogen bond between the two hydroxyl groups. In what concerns the two OH-dihedral angles, the 2D-PES reported in Figure 1 of ref. 172 is of particular interest: this figure suggests that the two dihedral rotations are involved in a single LAM described by a combination of the two dihedral rotations. In other words, the conformational flexibility of 1R,2R-cyclohexanediol can be described in terms of 1 (instead of 5) degree of freedom governing the concerted rotation of the two dihedral angle associated with the two hydroxyl groups.

To refine the qualitative description of the LAM given above, we have optimized its minima and transition states: energies and corresponding structures of the relevant stationary points are reported in figure 2.1. One may see that, roughly speaking, the minima are connected by simple, independent HOCC rotations about the CO bonds, with little coupling to other low-frequency modes.

2*R*,3*R*-butanediol is a highly flexible molecule. The conformational flexibility associated with the two hydroxyl groups can be described with two dihedral rotations. Furthermore, this molecule is characterized by two LAMs associated with the internal rotations of the two methyl groups and with another internal rotation involving the O—C—C—O dihedral angle. Therefore, a complete description of the conformational flexibility of this system can be achieved with 5 degrees of freedom. In what follows, the assumption is made that the internal rotation of the two methyl groups can be treated independently from the other 3 degrees of freedom: this assumption appears reasonable because a change in the orientations of the two hydroxyl groups or a rotation of the O—C—C—O dihedral angle does not affect significantly (at least to a first approximation) the barriers to the internal rotation of the two methyl groups. A proper description of the concerted rotation of the two hydroxyl groups needs to take into account its coupling with the rotation of the O—C—C—O dihedral angle. A simplified description of the LAMs in terms of the two HOCC LAMs is sketched in figures 2.3 and 2.4. The LAMs reported in figs. 2.3 and 2.4 can be described as concerted rotations of the HOCC torsions associated with the two hydroxyl groups (qualitatively, it

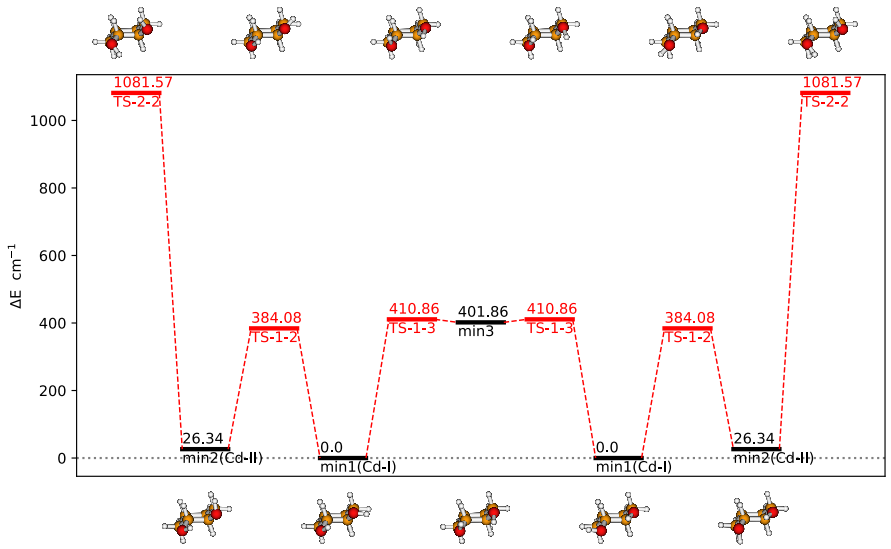

Figure 2.1: Structures and relative energies (in cm^{-1}) for low-energy conformers (in black) of 1*R*,2*R*-cyclohexanediol and for transition states (in red) governing their interconversion. The broken lines connecting stationary points do not have any quantitative meaning and are drawn only for a better visualization. Geometry optimizations were carried out at B3LYP/jul-cc-pVDZ level of theory, *without* the inclusion of solvent effects.

is the same kind of motion suggested for the two enantiomers of trans-1,2-cyclohexanediol, see fig. 2.1); values of the O—C—C—O dihedral angle are almost constant for all the molecular structures showed in the same figure: in other words, all the molecular structures showed in fig. 2.3 correspond to the Newman projection I (see fig. 2.2a) and all the ones showed in fig. 2.4 correspond to the Newman projection II (see fig. 2.2b).

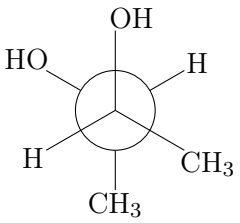

(a) Newman projection I

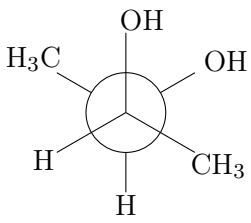

(b) Newman projection II

Figure 2.2: The two most relevant Newman projection of 2*R*,3*R*-butanediol

There is a third Newman projection of 2*R*,3*R*-butanediol, not reported in fig. 2.2, where the two hydroxyl groups are not adjacent. Despite the existence (already pointed out by other authors) of relative energy minima with a structure that can be represented with this third Newman projection

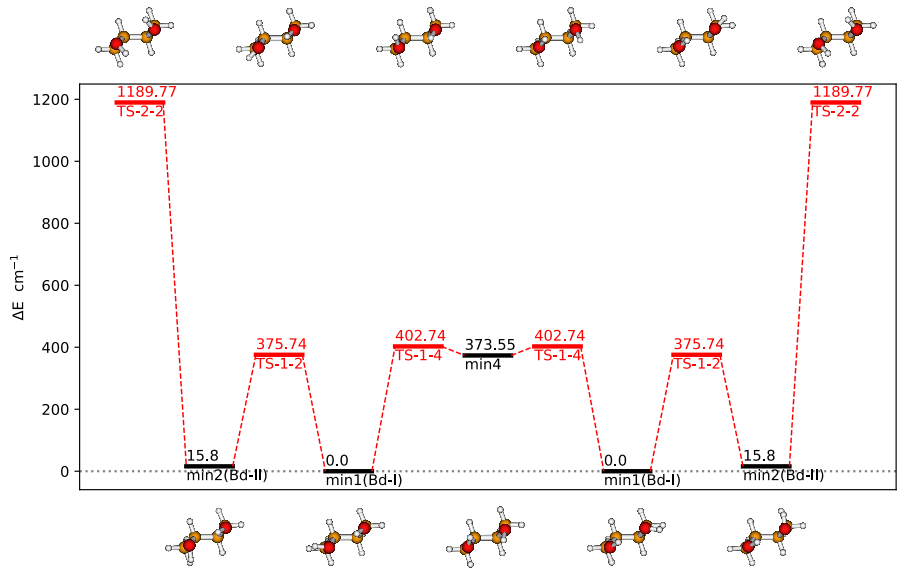

Figure 2.3: Structures and relative energies (in cm^{-1}) for low-energy conformers (in black) of 2*R*,3*R*-butanediol and for transition states (in red) governing their interconversion. The computational protocol is provided in the caption of fig. 2.1. All the structures shown in this figure correspond to the Newman projection I (see fig. 2.2a).

(with an O—C—C—O dihedral angle of about 180°), the structures associated with this projection are not taken into account in the following because the absence of the intramolecular hydrogen bond between the two hydroxyl groups leads to quite higher energies (see table 2.5) and, therefore, a negligible contribution to IR and VCD spectra. Two interconnections between the LAMs shown in figs. 2.3 and 2.4 (i.e. corresponding to the interconversion between the Newman projections I and II shown in fig. 2.2) were identified.[a]

Only the most stable conformers of *trans*-1*R*,2*R*-cyclohexanediol and 2*R*,3*R*-butanediol were taken into account for the calculation of IR and VCD spectra: more specifically, the two most stable conformers of *trans*-1*R*,2*R*-cyclohexanediol (see table 2.4 and figure 2.5) and the four most stable conformers[b] of 2*R*,3*R*-butanediol (see table 2.5 and fig. 2.5) were considered.

[a]The barrier to the interconversion is between 1500 and 1600 cm^{-1} in both cases. For the interested reader, more details are provided in the original article. For a complete characterization of the PES of 2*R*,3*R*-butanediol, the presence of Valley Ridge Inflection (VRI) points at accessible energies cannot be excluded (actually, the results of the calculations carried out for this study suggest that one VRI point is encountered when the interconversion between the two Newman projections of fig. 2.2 is taken into account).

[b]In the case of 2,3-butanediol the conformer labeled as '$G_gC_{CH_3}C_{CH_3}$' were not considered in the list of the most populated conformers becasue of (i) its symmetry (which lower its population with respect to conformers which pertain to the C_1 symmetry point

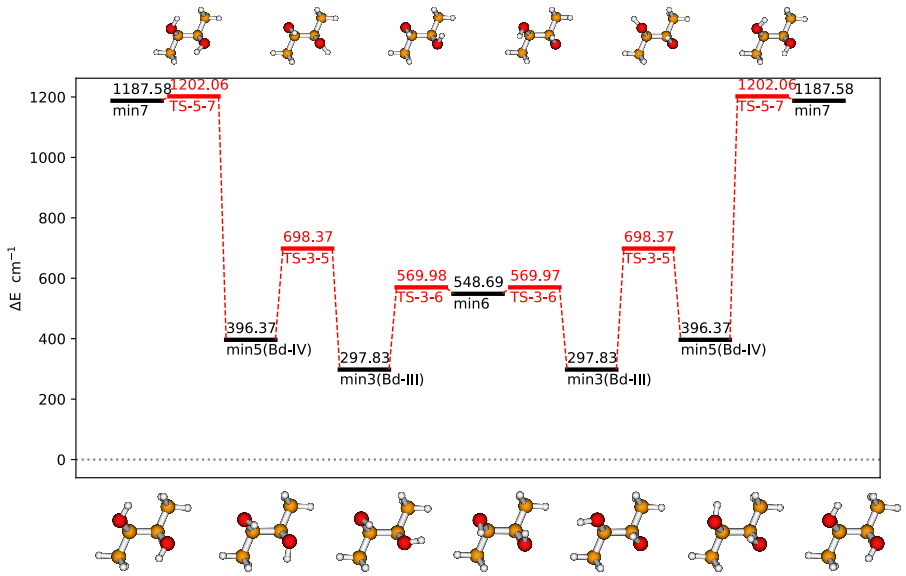

Figure 2.4: Structures and relative energies (in cm^{-1}) for low-energy conformers (in black) of 2*R*,3*R*-butanediol and for transition states (in red) governing their interconversion. The computational protocol is provided in the caption of fig. 2.1. All the structures shown in this figure correspond to the Newman projection II (see fig. 2.2b).

The next step was to evaluate the relative stabilities of the selected conformers at higher level of theory. A reliable description of the relative stabilities is a crucial step that can substantially influence the final results because the simulated spectrum can be very sensitive to the Boltzmann population. Therefore, the geometries of the most stable conformers obtained at B3LYP/jul-cc-pVDZ level of theory were re-optimized at B2PLYP/jun-cc-pVTZ level.[a] The results are provided in table 2.6. For both molecules, the conformers taken into account for the simulation of iR and VCD spectra represent more than 95% of the total Boltzmann populations at room temperature.

IR and VCD spectra: experimental and computational results Experimental IR and VCD spectra are displayed in figure 2.6 in four spectroscopic regions for the two optically active enantiomers of 2,3-butanediol and the two enantiomers of *trans*-1,2-cyclohexanediol. Very good-to-excellent

group) and (ii) energy and structure close to two transition states (i.e. the conformer corresponds to a minimum at B3LYP/jul-cc-pVDZ level of theory, but could be a TS if the calculation is performed at another level of theory), see table 2.5 and fig. 2.3.

[a]There are extremely small differences between the optimized molecular structures obtained with the two level of theory. Therefore, images of the most stable conformers (fig. 2.5) and labels can be employed for the results obtained at both the level of theory.

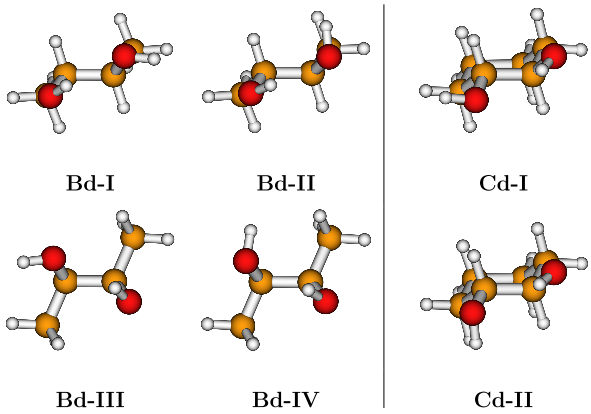

Figure 2.5: Structures of the most stable conformers of 2*R*,3*R*-butanediol (left side of the figure) and *trans*-1*R*,2*R*-cyclohexanediol (right side of the figure).

conformer	B3LYP/jul-cc-pVDZ			B2PLYP/jun-cc-pVTZ			
	$\Delta(E+ZPE)$	ΔG_{vac}	ΔG_{PCM}	$\Delta(E+ZPE)$	ΔG_{vac}	ΔG_{PCM}	pop.
Bd-I	0	0	0	0	0	0	47.1%
Bd-II	0.54	0.80	0.53	0.90	1.14	0.85	33.5%
Bd-III	3.04	2.81	3.48	2.91	2.84	3.51	11.5%
Bd-IV	4.33	4.13	4.09	4.42	4.46	4.42	7.9%
Cd-I	0	0	0	0	0	0	58.0%
Cd-II	0.72	1.03	0.47	1.11	1.36	0.80	42.0%

Table 2.6: Relative energies (in kJmol^{-1}) associated to the most populated conformers of 2*R*,3*R*-butanediol and *trans*-1*R*,2*R*-cyclohexanediol. Grimme's empirical dispersions (with Becke-Johnson damping) were employed in conjunction with B3LYP and B2PLYP methods. Solvent effects were taken into account with PCM with a single-point calculation performed on the geometry of the isolated molecule (optimized in vacuum, *without* the inclusion of solvation effects).

mirror image spectra have been obtained in all regions for the enantiomeric species even employing the rather diluted solutions required to avoid (or at least to minimize) intermolecular hydrogen bonding. This gives us confidence in testing high-level calculated spectra to compare to the experimental ones.

Wang and Polavarapu reported the IR and VCD spectra of 2R,3R-butanediol in the mid-IR region.[165] Both spectra are essentially identical to those reported in fig. 2.6 for the spectral region under evaluation. IR and VCD spectra in the region of fundamental OH stretchings can be easily found in literature, and the previous findings are in substantial agreement with the results shown in fig. 2.6 for *trans*-1,2-cyclohexanediol and 2,3-butanediol.

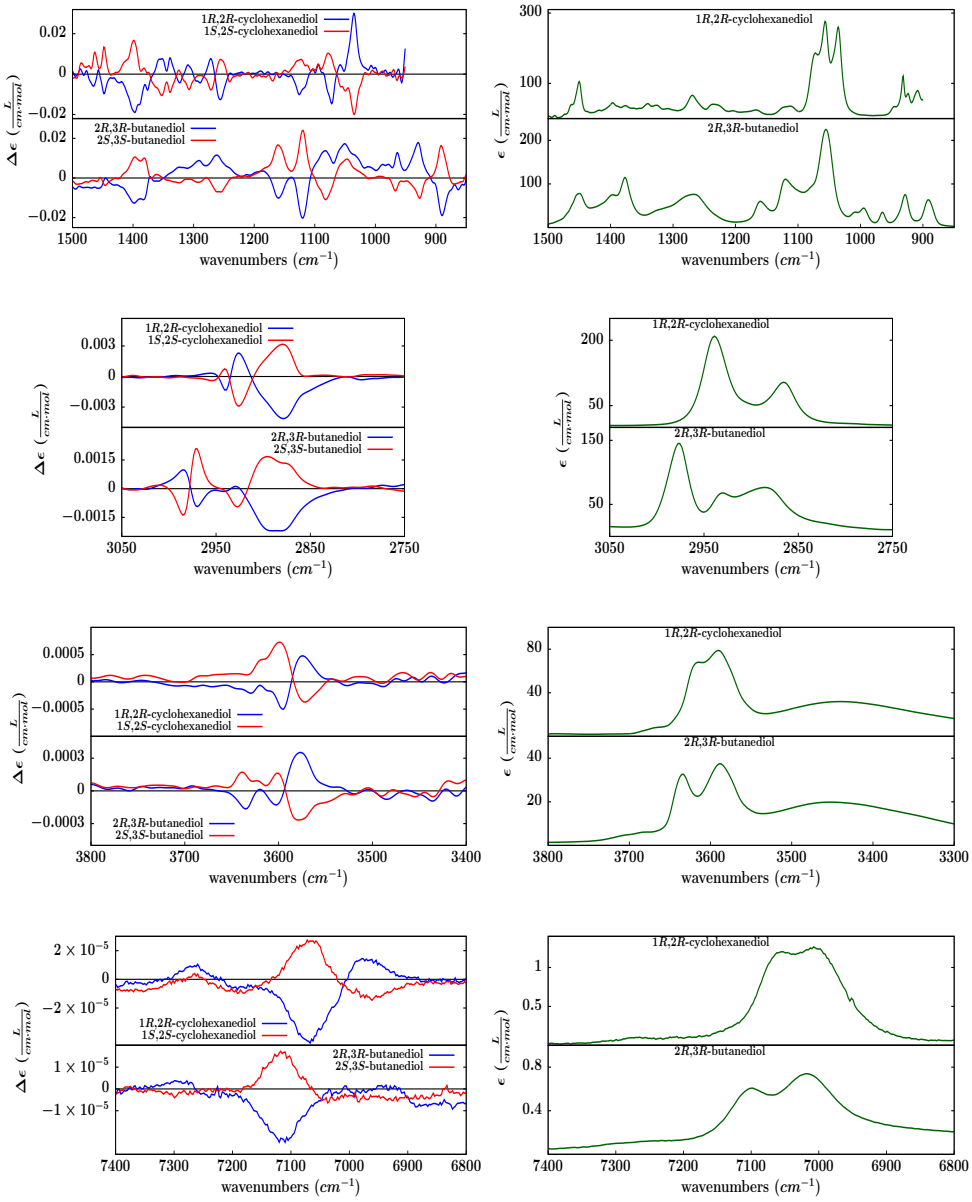

Figure 2.6: Experimental VCD (left column) and IR (right column) spectra of *trans*-1,2-cyclohexanediol (enantiomers 1*R*,2*R* and 1*S*,2*S*) and 2,3-butanediol (enantiomers 2*R*,3*R* and 2*S*,3*S*). From the top, mid-IR (850-1500 cm^{-1}), CH stretchings (2750-3050 cm^{-1}), fundamental OH stretchings (3300-3800 cm^{-1}), and NIR (6800-7400 cm^{-1}) spectroscopic regions are reported. The spectra have been recorded in diluted solutions, with $CDCl_3$ (in the case of *trans*-1,2-cyclohexanediol) and CCl_4 (in the case of 2,3-butanediol). For these data, the collaboration of Giuseppe Mazzeo (university of Brescia) is gratefully acknowledged.

To the best of our knowledge, the spectra reported for the fundamental CH stretching region and for the NIR region in fig. 2.6 are new.

IR and VCD spectra of *trans*-1,2-cyclohexanediol and 2,3-butanediol show several similarities in shape and intensity. On the basis of molecular structures of the two enantiomeric pairs, a relationship between common structural motifs and similar spectral features can be guessed.

In the mid-IR region both compounds show a strong IR band at ca. 1050 cm^{-1} and in the same region of the spectrum (between 1000 and 1200 cm^{-1}) the VCD spectra of both compounds exhibit a similar pattern (going from higher to lower wavenumbers, a "−,−,+" triplet for the *R*,*R* configuration and a "+,+,−" triplet for the *S*,*S* configuration, between 1050 and 1200 cm^{-1} in the case of *trans*-1,2-cyclohexanediol and between 1000 and 1150 cm^{-1} in the case of 2,3-butanediol, see fig. 2.6). Such a spectral region host normal mode transitions having contributions from CO-stretchings.

For what concerns IR spectra in the region of fundamental OH stretchings, a doublet is observed between 3550 and 3650 cm^{-1} and a broad IR band below 3500 cm^{-1} for both compounds; in ref. 172, the broad IR band below 3500 cm^{-1} in the spectrum of *trans*-1,2-cyclohexanediol is interpreted as the signature of aggregation of two (or even three) molecules promoted by the formation of intermolecular hydrogen bonds: it is tempting to explain analogously the observation of the same feature in the spectrum of 2,3-butanediol, but to confirm this hypothesis more data are needed.[a] In the same region, the VCD spectrum of *trans*-1,2-cyclohexanediol exhibits a doublet (a "−,+" in the case of the *R*,*R* configuration, with the negative feature weaker than the positive one), while the VCD spectrum of 2,3-butanediol shown a triplet (a "−,−,+" in the case of *R*,*R* configuration, again with the negative features weaker and at higher frequency than the positive one).[b]

For the first-overtone region (of OH stretchings) a NIR absorption doublet is observed in both cases, while a VCD doublet is observed only for *trans*-1,2-cyclohexanediol molecular system (with pattern "−,+" for the *R*,*R* configuration, from higher to lower wavenumbers) and a singlet (negative, in the case of *R*,*R* configuration) is observed for the VCD spectrum of 2,3-butanediol.

The observed anisotropy ratio (also called *g*-factor) for the various signals of the spectra reported in fig. 2.6 is between 10^{-4} and 10^{-5} in the mid-IR region, about 10^{-5} in the CH stretchings region, between 10^{-6} and 10^{-5} for the fundamental OH stretchings transitions, and about 10^{-5} for the first OH

[a] For example, IR spectra in the region of fundamental OH stretchings at various concentrations.

[b] For what concerns the VCD spectrum of the enantiomeric pair (*R*,*R*) and (*S*,*S*) of 2,3-butanediol, the results shown in fig. 2.6 are in agreement with the experimental VCD spectrum previously observed by Siligardi. The pattern suggested in this study is slightly different from the pattern suggested in ref. 164 (which is a doublet "−,+" for the *R*,*R* configuration).

stretchings overtones (the values for *trans*-1,2-cyclohexanediol and the chiral forms of 2,3-butanediol are similar).

A more detailed description of the experimental spectra can be found in the original article.

In what follows, the computational simulation of the IR and VCD spectra reported in fig. 2.6 is presented and discussed. All the calculated spectra reported in this paragraph were obtained as average spectra of the two most populated conformers (corresponding to the two lowest energy minima of the global PES) for 1*R*,2*R*-cyclohexanediol (see fig. 2.1 and tables 2.4 and 2.6) and of the four most populated conformers for 2*R*,3*R*-butanediol (see figs. 2.3 and 2.4 and tables 2.5 and 2.6).

The normal modes related to the LAMs investigated in the previous paragraph (HOCC torsions associated with the two hydroxyl groups) were removed from the VPT2 treatment, together with low energy modes involving methyl rotations or butane torsions (in the case of 2*R*,3*R*-butanediol) or ring deformations (in the case of 1*R*,2*R*-cyclohexanediol). The LAMs excluded from the VPT2 treatment are listed and depicted for each conformer (in section 5.2 of the SI of the original article).

Despite some discrepancies, the agreement between experimental and computational results is generally satisfying.

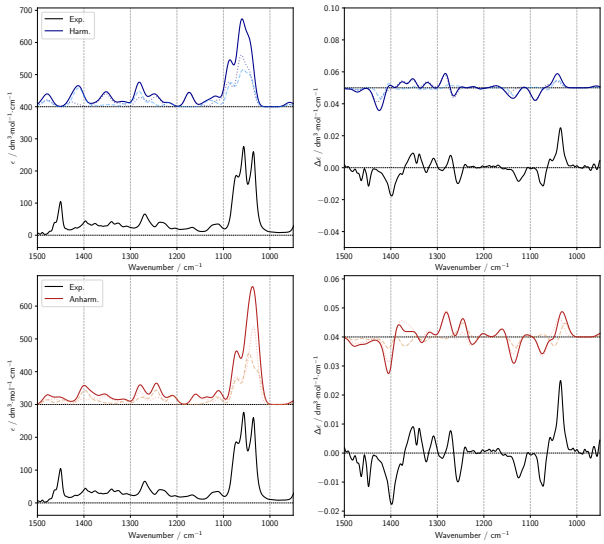

Figure 2.7: Comparison of experimental spectra of 1*R*,2*R*-cyclohexanediol with harmonic (top images) and anharmonic (bottom images) calculations of IR and VCD spectra in the mid-IR region. The spectra of each conformer were weighted with their respective Boltzmann population based on B2PLYP harmonic energy. The spectra were simulated assigning Gaussian distribution functions of 10 cm^{-1} half-width at half-maximum.

Harmonic and bare anharmonic results in the mid-IR region are provided for 1*R*,2*R*-cyclohexanediol (fig. 2.7) and 2*R*,3*R*-butanediol (fig. 2.8). In this

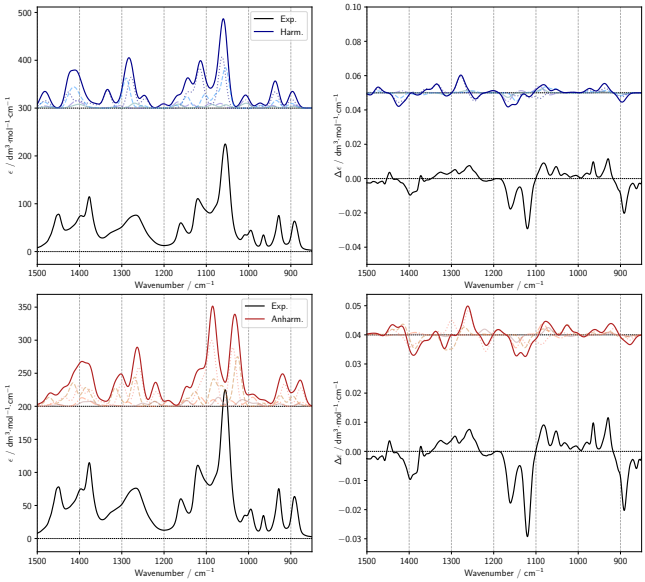

Figure 2.8: Comparison of experimental spectra of 2*R*,3*R*-butanediol with harmonic (top images) and anharmonic (bottom images) calculations of IR and VCD spectra in the mid-IR region. The spectra of each conformer were weighted with their respective Boltzmann population based on B2PLYP harmonic energy. The spectra were simulated assigning Gaussian distribution functions of 10 cm^{-1} half-width at half-maximum.

region, the agreement between experimental and scaled harmonic results is better than the agreement obtained between experimental and bare anharmonic (GVPT2) results (this statement is confirmed by the corresponding similarity indexes,[186–188] given in table 2.7).

In the case of the CH-stretching region, the anharmonic calculations were performed with DVPT2 and GVPT2 model.[a] Scaled harmonic and bare anharmonic[b] results are in satisfying agreement with the experimental spectra.

IR and VCD spectra in the region of fundamental OH-stretching are displayed in figs. 2.9 and 2.10 together with the results for the CH-stretching region. In this case, calculations carried out with VPT2 and local mode approximations are provided (see fig. 2.11). For what concerns the comparison between experimental and computed IR absorption spectra at anharmonic level, a satisfying agreement can be observed for both molecular systems (and with both approximations, VPT2 and local mode models). Substantial discrepancies are observed when the same comparison is extended to

[a] The DVPT2 model was employed for *trans*-1,2-cyclohexanediol (see fig. 2.9), while the GVPT2 model was adopted for the chiral species of 2,3-butanediol.

[b] Actually, the anharmonic calculations were performed with both anharmonic models (i.e. GVPT2 and DVPT2), but only the more satisfying results obtained for each species are shown in this paragraph (a quantitative comparison based on similarity indices is provided in table 2.7).

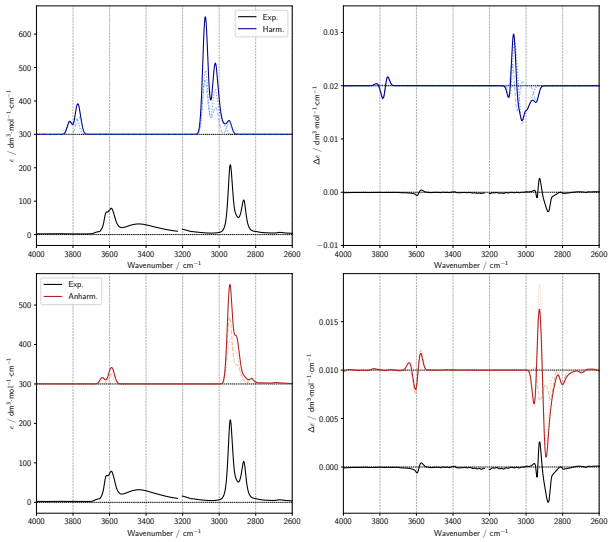

Figure 2.9: Comparison of experimental spectra of 1*R*,2*R*-cyclohexanediol with harmonic (top images) and anharmonic (bottom images) calculations of IR and VCD spectra in the region of fundamental OH stretching transitions ($\Delta\nu = 1$) and CH stretching region. The spectra of each conformer were weighted with their respective Boltzmann population based on B2PLYP harmonic energy. The spectra were simulated assigning Gaussian distribution functions of 15 cm^{-1} half-width at half-maximum.

the VCD spectra, particularly in the case of local mode approximation. When the GVPT2 approximation is employed, a better reproduction of the experimental VCD spectrum of *trans*-1,2-cyclohexanediol is obtained (in the region of fundamental OH-stretching): the "−, +" experimental VCD doublet of 1*R*,2*R*-cyclohexanediol corresponds to the "+,−, +" triplet predicted by the GVPT2 calculation, taking into account that the first "+" feature of the triplet is weak with respect to the other two (see figs. 2.9 and 2.11). The "−,−,+" structure observed in the experimental VCD spectrum of 2*R*,3*R*-butanediol is not correctly predicted by GVPT2 calculations[a]. In this region of the spectrum the transition frequencies are well reproduced with the local mode[b] and GVPT2 approximations, while the intensities (especially in the case of VCD spectra) can be considered satisfactory[c] for the calculations performed with the GVPT2 approximation and not entirely satisfactory for the calculations performed with the local mode approximation. The effects of intra- and intermolecular hydrogen bonding are fairly evident (in calculated and experimental spectra) and are similar for *trans*-1,2-cyclohexanediol and the chiral forms of 2,3-butanediol: thus, the two observed features, one just

[a] The discrepancy is due to the wrong sign predicted for the first feature, at higher wavenumbers: the pattern obtained in the case of the GVPT2 calculation is "+,−,+".

[b] Although a minor discrepancy can be observed in the spectrum of 2*R*,3*R*-butanediol, see fig. 2.11.

[c] Although future improvements are desirable.

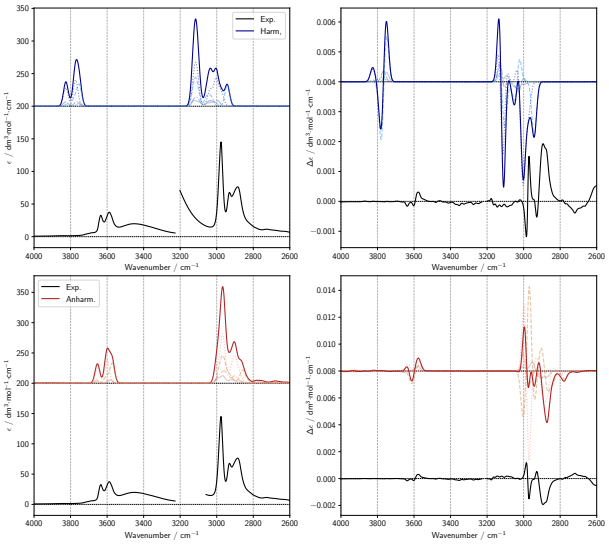

Figure 2.10: Comparison of experimental spectra of 2*R*,3*R*-butanediol with harmonic (top images) and anharmonic (bottom images) calculations of IR and VCD spectra in the region of fundamental OH stretching transitions ($\Delta\nu = 1$) and CH stretching region. The spectra of each conformer were weighted with their respective Boltzmann population based on B2PLYP harmonic energy. The spectra were simulated assigning Gaussian distribution functions of 15 cm^{-1} half-width at half-maximum.

below and the other just above 3600 cm^{-1}, can be assigned to the stretching modes of the donor and acceptor OH bonds, respectively, involved in an intramolecular hydrogen bonding. Aggregation effects are neglected in the calculations provided in this paragraph, and this choice explain the absence of the broad band below 3500 cm^{-1} in the calculated spectra (see figs. 2.9 and 2.10).

The best agreement between anharmonic GVPT2 calculations and experimental data is obtained in the NIR region (see fig. 2.11).[a] It must be underlined that not only frequencies and relative intensities but also absolute intensities are well reproduced by the anharmonic GVPT2 calculations in this region. In this region, also the results obtained with the local mode approximation are in good agreement with the experimental results (especially in the case of *trans*-1,2-cyclohexanediol).

The evaluation of the agreement between experimental and computational data is usually based on graphical comparisons. In conjunction with graphical evaluations (presented in figs. 2.7-2.11), two quantitative indexes[b] were adopted in this study: the aim is to complement a qualitative notion (the agreement between the graphical representations of two sets of data) with a quantitative measurement which is not subject to the (potentially

[a] A discrepancy related to the positive band in the NIR-VCD spectra of the 2*R*,3*R*-butanediol must be pointed out.

[b] One is the so-called Similarity Index (SI) introduced in ref. 186. The numerical value

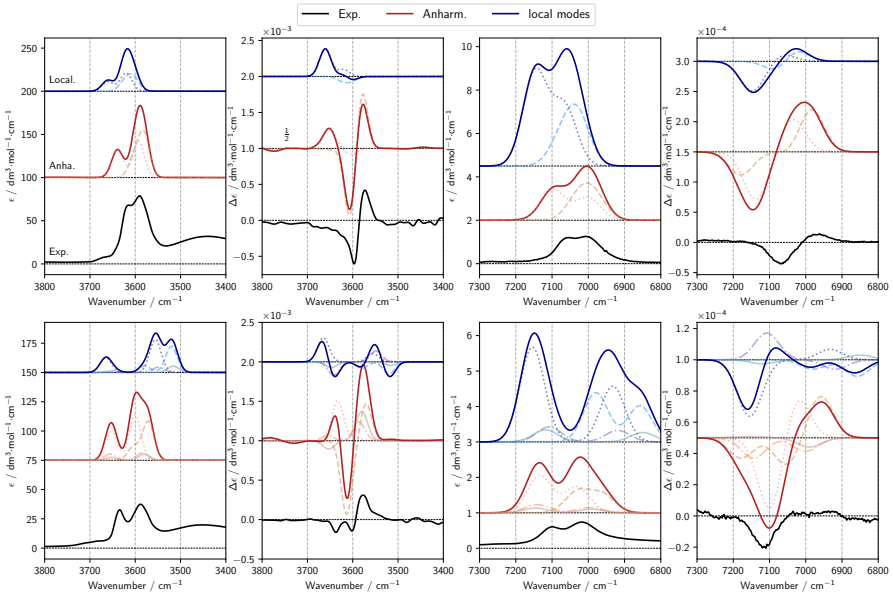

Figure 2.11: Comparison of experimental spectra of 1*R*,2*R*-cyclohexanediol (top images) and 2*R*,3*R*-butanediol (bottom images) with anharmonic calculations of IR and VCD spectra in the regions of fundamental OH stretching transitions ($\Delta\nu = 1$) in the left side of the figure and of first overtone OH stretching transitions ($\Delta\nu = 2$) in the right one. The spectra of each conformer were weighted with their respective Boltzmann population based on B2PLYP harmonic energy. The spectra were simulated assigning Gaussian distribution functions of 15 cm^{-1} half-width at half- maximum in $\Delta\nu = 1$ region and 40 half-width at half-maximum in $\Delta\nu = 2$ region

biased) author's judgement. The results are provided in table 2.7: comparing scaled harmonic and bare anharmonic results, an improvement between experimental and calculated data is obtained when the anharmonic calcu-

is obtained from the following overlap integral:

$$\mathrm{SI} = \frac{\int [f(\nu,\kappa)g(\nu)]d\nu}{\sqrt{\int [f^2(\nu,\kappa)]d\nu \int [g^2(\nu)]d\nu}}. \tag{2.57}$$

$g(\nu)$ and $f(\nu,\kappa)$ are functions associated, respectively, to experimental and calculated spectral intensities at each frequency ν; κ is the frequency scaling factor. The maximum value of SI (obtained when the spectra f and g are identical) is equal to 1, and the minimum tends to 0 for IR spectra and to -1 for VCD spectra (a value of -1 for the SI is obtained when the spectra are the opposite of each other). Eq. 2.57 can result in a division by zero (if either f or g is of zero strength). The values of another index (the so-called spectrum similarity, Sim) [187] are proposed in table 2.7. The numerical value of Sim are computed as follows:

$$\mathrm{Sim} = \frac{\int [f(\nu,\kappa)g(\nu)]d\nu}{\int [f^2(\nu,\kappa)]d\nu + \int [g^2(\nu)]d\nu - |\int [f(\nu,\kappa)g(\nu)]d\nu|} \tag{2.58}$$

Analogously to to the values of SI, the numerical values can assume values in the range $[0, 1]$ in the case of IR spectra and $[-1, 1]$ in the case of VCD spectra.

lations are carried out, with the exception of the mid-IR regions of both compounds.[a]

Molecule	Region	IR		VCD	
		SI	Sim	SI	Sim
2*R*,3*R*-butanediol	mid-IR harm. ($\kappa = 0.988$)	0.91	0.79	0.63	0.33
	mid-IR anharm. (GVPT2)	0.79	0.61	0.64	0.33
	CH-str. harm. ($\kappa = 0.955$)	0.53	0.27	0.46	0.26
	CH-str. anharm. (GVPT2)	0.93	0.86	0.71	0.42
	OH-str. harm. ($\kappa = 0.955$)	0.69	0.51	0.71	0.13
	OH-str. anharm. (GVPT2)	0.73	0.58	0.74	0.25
1*R*,2*R*-cyclohexanediol	mid-IR harm. ($\kappa = 0.988$)	0.94	0.89	0.74	0.52
	mid-IR anharm. (GVPT2)	0.90	0.79	0.60	0.39
	CH-str. harm. ($\kappa = 0.955$)	0.96	0.69	0.78	0.32
	CH-str. anharm. (GVPT2)	0.90	0.78	0.29	0.02
	CH-str. anharm. (DVPT2)	0.92	0.82	0.89	0.41
	OH-str. harm. ($\kappa = 0.955$)	0.74	0.56	0.30	0.09
	OH-str. anharm. (GVPT2)	0.80	0.61	0.67	0.27

Table 2.7: 2*R*,3*R*-butanediol and 1*R*,2*R*-cyclohexanediol: similarity indices (see eqs. 2.57 and 2.58) for IR and VCD experimental and calculated spectra. The spectra of each conformer were weighted with their respective Boltzmann population based on B2PLYP harmonic energy. In parentheses, we report the scaling factors (κ) employed in the harmonic approximation in the various spectroscopic regions. Computational spectra were simulated assigning the same gaussian distribution functions employed in figs. 2.7-2.11.

Conclusive remarks Besides the interest *per se*, the results presented in this subsection show strengths and limits of the different computational protocols employed for the anharmonic calculations.

The discrepancies between experimental and anharmonic calculations results raise an issue concerning the improvements of approximations and protocols employed in this study for the calculation of anharmonic spectra. The hypothesis proposed in this paragraph underlines the importance of LAMs in the anharmonic calculations of IR and VCD spectra, but it must be pointed

[a] And remembering that for the CH-stretching region of *trans*-1,2-cyclohexanediol (see fig. 2.9) the DVPT2 model was employed (the results obtained with the GVPT2 approach deteriorate the agreement between experimental and computational data with respect to the employment of the scaled harmonic results).

out that in order to give a satisfactory explanation of the discrepancies between experimental and anharmonic results other data would be extremely useful.

The exclusion of LAMs from the VPT2 treatment corresponds to the employment of a reduced dimensionality scheme to solve out the nuclear problem: the essential idea is to go beyond the harmonic approximation avoiding the inclusion of contributions which are not properly taken into account at VPT2 level. In practice, this approach is reliable if (in the real world) the contributions of the LAMs to the transitions[a] of interest is negligible. When these contributions are not negligible a computational procedure to properly take them into account is needed: therefore, in these cases the exclusion of the contributions related to LAMs can lead to discrepancies between experimental and computational results. The procedure chosen to account for the effects of LAMs relevantly affects the results of anharmonic calculations of *fundamental* transitions, while it is less important for what concerns *first overtone* transitions of OH-stretchings.[b]

An explanation of the discrepancies between experimental and anharmonic results based on the need of a proper inclusion of the contributions due to the LAMs can explain the excellent agreement between experimental and anharmonic results in the region of first overtone OH-stretching and the discrepancies observed in the other regions, where experimental signals due to *fundamental* transitions are measured. Moreover, analogous arguments can be extended to explain the better agreement of the computational results obtained with the local mode approximation in the case of first overtone transitions of OH-stretching modes.[c]

Although the explanation of the discrepancies between experimental and computational results proposed in this paragraph seems to be reasonable, it is only an hypothesis and should be verified with other calculations.

---

[a] More specifically, to transition frequencies, IR and VCD intensities.

[b] This statement was verified in the case of 2*R*,3*R*-butanediol, see the Supporting information of the original article.

[c] Another important approximation behind the local mode approach is the neglection of the interaction between the two OH stretchings simultaneously taking place in both the compounds considered in this study: each OH stretching has been treated assuming a fixed value (namely the value at the energy minimum) for all the internal degrees of freedoms (bond lengths, valence angles and dihedral angles) which does not define the position of the H or the O atoms directly involved in the OH stretching under investigation. To verify if reliable computational values of IR and VCD intensities can be obtained neglecting the interaction between the two OH moieties, the dependence of APTs and AATs from the length of both the OH bonds of the two most populated conformers of *trans*-1,2-cyclohexanediol was investigated: the results are provided in the Supporting Information of the original article, and support (at least partially, i.e. focusing on the more relevant terms) the reliability of the approximation adopted in this study (interaction between the local modes neglected).

2.4.2 IR and VCD spectra of organometallic compounds: the case of chiral ferrocenes *

The usefulness of IR and VCD spectroscopies for the characterization of organometallic compounds is well known. In this subsection, experimental and computational results obtained for a series of five chiral ferrocenes are presented and briefly discussed.

Ferrocene is a metallocene in which an iron divalent cation is sandwiched between cyclopentadienyl moieties. If one chiral pendant is attached to one cyclopentadienyl moiety[a] a chiral compound is obtained. The chemical interest of chiral ferrocenes (see, for example, ref. 189) motivates the investigation proposed in what follows.

An approach which combines the experimental measurements of IR and VCD spectra with their computational simulation is adopted.[b] The presence of a metal cation (Fe^{2+}) and the size of the molecular systems discussed in this subsection suggest a potentially challenging investigation, especially for what concerns the computational side. Therefore, special attention was devoted to the choice of the computational protocol (particularly to the compromise between computational cost and accuracy).

The molecular systems studied are depicted in figure 2.12. The synthesis of the two enantiomers of (from the left to the right of fig. 2.12) 1-acetoxyethylferrocene ([±]−**1**), 1-methoxyethylferrocene ([±]−**2**), 1-hydroxyethylferrocene ([±] − **3**) and 1,1′-bis(1-hydroxyethyl)ferrocene ([±] − **4**) was carried out by Angela Patti and Sonia Pedotti (Institute of Biomolecular Chemistry - Consiglio Nazionale delle Ricerche, Catania), while the synthesis of $\mathbf{5} - S_p$ and $\mathbf{5} - R_p$ (which are diastereoisomers) was carried out in the group of prof. Vladimir Dimitrov (Bulgarian academy of sciences).

Experimental and computational methods Details about the synthetic procedures employed for the synthesis of each enantiomers of **1**, **2**, **3** and **4** can be found in the original article. For what concerns the instrumentation employed to carry out VCD and IR measurements, the same apparatus utilized for the measurements presented in the previous section was used (FVS-6000 JASCO FTIR) and the spectra were measured in the regions of mid-IR, fundamental CH- and OH-stretching. In the original ar-

*Part of the results provided in this section (together with more details about experimental and computational methods) can be found in *Phys. Chem. Chem. Phys.*, **2019**, 21, 9419-9432.

[a]Or two different substituents (chiral or not) are attached to the same cyclopentadienyl moiety.

[b]To the best of the author's knowledge, the first *ab-initio* calculation of the VCD spectrum of an organometallic molecule was published in ref. 190. Since then, the combination of experiments and *ab-initio* calculations (usually at harmonic level) has been employed for the elucidation and the assignment of VCD spectra of organometallic molecules (see, for example, refs. 191–193).

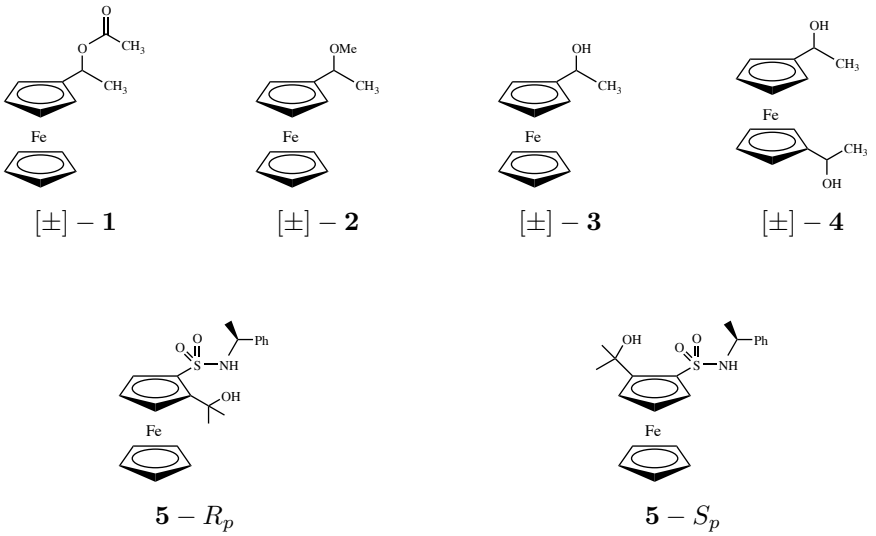

$[\pm] - \mathbf{1}$ $[\pm] - \mathbf{2}$ $[\pm] - \mathbf{3}$ $[\pm] - \mathbf{4}$

$\mathbf{5} - R_p$ $\mathbf{5} - S_p$

Figure 2.12: Structures of the chiral ferrocenes discussed in this section. The configuration in correspondence of the asymmetric center (the carbon atom directly bonded to the cyclopentadienyl ring) is not specified in the structures **1**, **2**, **3** and **4**. For what concerns the molecular system **4** only the two optically active enantiomers (*R*,*R*) and (*S*,*S*) are discussed in this work and not the *meso*-form (*R*,*S*). The structures $\mathbf{5} - R_p$ and $\mathbf{5} - S_p$ are diastereoisomers.

ticle more details about instrumentation, samples, experimental conditions and protocols may be found.

For what concerns the computational protocol, two issues must be addressed: (i) the lack of widely adopted and validated quantum chemical methods for the study of organometallic complexes and (ii) the availability of a limited (although significant) amount of computational resources. Some DFT-methods were tested in a previous work,[194] suggesting the employment of B3PW91 as exchange-correlation functional and Def2TZVP[195] as basis set. The tests provided in ref. 194 are limited to harmonic and anharmonic calculations of IR spectra (this is due to the lack of chirality of the investigated systems) and do not consider the effects of substituents on one of the two cyclopentadienyl moieties: despite these weak points (at least for this study), the quality of the results obtained at anharmonic levels at B3PW91/Def2TZVP level of theory supports the adoption of the same computational protocol for this work. A number of tests (with different exchange-correlation functionals and different basis sets) were carried out in order to verify the sensitivity of the computed VCD spectra to the level of theory employed, at least at harmonic level. The results of these tests (not shown in this thesis) make us conclude that the employment of the B3PW91/Def2TZVP level of theory for the calculations of IR and VCD spectra of the molecular systems shown in fig. 2.12 is a good choice.

All the calculations were performed with the Gaussian suite of pro-

grams.[12] For what concerns geometry optimizations, force fields and transition moments the protocols provided in the previous section (for the study of 2,3-butanediol and *trans*-1,2-cyclohexanediol) were employed. Solvent effects were included with the PCM model.

IR and VCD spectra were computed at harmonic level for all the molecular systems showed in fig. 2.12, while the anharmonic calculations were performed only for the molecular systems labeled with **1**, **2** and **3**.[a]

For what concerns anharmonic calculations, LAMs and resonances were treated with a procedure similar to the one introduced in the previous section. LAMs were identified with apreliminar analysis and excluded from the VPT2 treatement. The effects of resonances were taken into account for both energy and property calculation: FRs and DDRs affecting transition frequencies were identified with the two-step procedure implemented in Gaussian (with default Gaussian thresholds); FRs affecting intensities were identified by the operator and manually added to the input file of the final anharmonic calculation. Anharmonic spectra were computed with the GVPT2 approach.

Most populated conformers (with their geometries and populations) of molecular systems **1**, **2**, **3** and **4** are described and depicted in the original article. Anharmonic IR and VCD spectra provided in the next paragraph are calculated weighing with their respective Boltzmann population the spectra of the most populated conformers.

In the case of $\mathbf{5}-R_p$ and $\mathbf{5}-S_p$, the preliminary conformational analysis was performed as follows: dihedral angles associated to internal rotations with low-energy barriers [b] and to the umbrella inversion of the three groups directly bonded to the nitrogen atom (see fig. 2.12) were employed to generate a set of reliable guesses for the geometries of the various conformers. These initial geometries were optimized at B3LYP/TZVP level of theory[c]: the most stable geometries obtained at the end of this procedure were re-optimized at B3PW91/Def2TZVP level of theory, with the inclusion of solvent effects (as already mentioned).

IR and VCD spectra: experimental and computational results Experimental IR and VCD spectra of the molecular systems labeled with **1**, **2**, **3** and **4** are reported in fig. 2.13. The experimental spectra obtained in the regions of mid-IR, fundamental CH- and OH-stretching are reported for both

[a] The reason are (i) the high computational cost associated to the calculations of the anharmonic force-fields in the cases of $\mathbf{5}-R_p$ and $\mathbf{5}-S_p$ and (ii) the experimental evidence of a dimerization in which the molecules with the structure labeled with **4** in fig. 2.12 are involved (in other words, the reason is the high computational cost for what concerns the calculation of the anharmonic force-field of the dimer).

[b] $C_{Cp1\&CS}$—C_{Cp1}—C—O, C_{Cp1}—C—O—H, C_{Cp1}—$C_{Cp1\&CS}$—S—N,$C_{Cp1\&CS}$—S—N—C^* and S—N—C^*—H.

[c] Without the inclusion of solvent effects.

enantiomers of each investigated molecular systems.[a] Experimental IR and VCD spectra of $\mathbf{5}-R_p$ and $\mathbf{5}-S_p$ in the mid-IR region are shown in fig. 2.15.

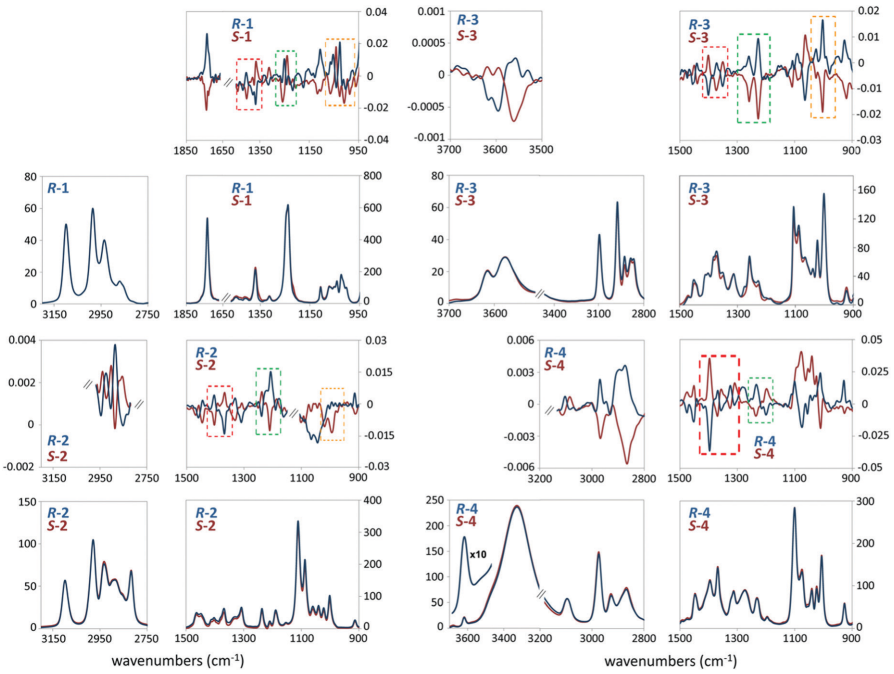

Figure 2.13: Experimental IR and VCD spectra of both the enantiomers of **1**, **2**, **3** and **4** measured in CCl_4 solutions. Spectral features which were found to be affected by significant experimental errors are omitted. Intensities are reported in units of ϵ (IR spectra) and $\Delta\epsilon$ (VCD spectra). The figure is taken from the original article. For these data, the collaboration of Giuseppe Mazzeo (university of Brescia) is gratefully acknowledged.

g-factors of the order of 10^{-4} in the mid-IR region of **3**, **4**, $\mathbf{5}-R_p$ and $\mathbf{5}-S_p$ (and in the C=O stretching region for the molecular system **1**) are observed (see figs. 2.13 and 2.15). In the regions of fundamental CH- and OH-stretching a g-factor of the order of 10^{-5} is observed for all the cases shown in fig. 2.13. A g-factor of the order of 10^{-5} is observed in the fingerprint region of **1** and **2** (see fig. 2.13).

Analysis of the results based exclusively on the experimental data shown in figs. 2.13 and 2.15 is not straightforward. Despite a common structural motif (the ferrocene moiety) the molecular systems considered in this subsection exhibit IR and VCD spectra with different features and patterns. Nevertheless, useful pieces of information can be inferred from the analysis of

[a]The experimental VCD spectra in the region of CH-stretching for the compounds **1** and **3** and in the region of fundamental OH-stretching for the compound **4** are not reported because the signals were found small and hardly reproducible. The experimental VCD and IR spectra in the region of fundamental OH-stretching are not reported for the molecular systems **1** and **2** for obvious reasons (absence of relevant signals due to the absence of hydroxyl moieties in the molecular structure).

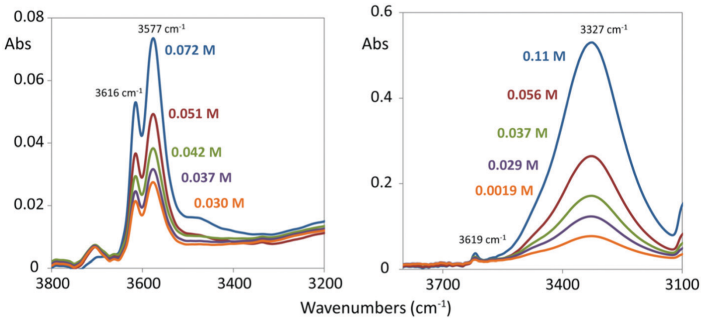

Figure 2.14: Experimental IR spectra of **3** (left side) and **4** (right side) in the OH-stretching region. Concentrations of the spectra are provided in the figure, while y values give the absorbance value. For these data, the collaboration of Giuseppe Mazzeo (university of Brescia) is gratefully acknowledged.

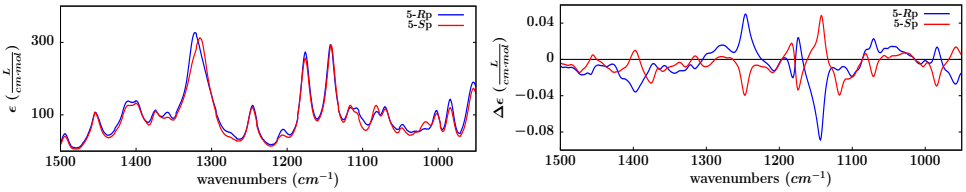

Figure 2.15: Experimental IR and VCD spectra of $\mathbf{5}-R_p$ and $\mathbf{5}-S_p$ in the mid-IR region measured in CCl_4. It must be underlined that $\mathbf{5}-R_p$ and $\mathbf{5}-S_p$ are *diastereoisomers*, not *enantiomers*. For these data, the collaboration of Giuseppe Mazzeo (university of Brescia) is gratefully acknowledged.

the spectra of **3** and **4** in the region of fundamental OH-stretching. For what concerns the molecule **3**, two signals of comparable intesities were observed at 3616 cm^{-1} and 3577 cm^{-1} in the IR spectrum: this observation suggests the simultaneous presence of at least two significantly populated conformers in the CCl_4 solution of **3**, since only one hydroxyl moiety is involved in the structure of **3**.[a] Turning to the signals observed in the OH-stretching region of the IR spectrum of **4** a feature at 3619 cm^{-1} (whose intensity is comparable to the two signals observed in the same region of the IR spectrum of **3**) and a broad and intense signal at 3327 cm^{-1} are observed. In order to verify whether or not the signal at 3327 cm^{-1} observed in the IR spectrum of **4** can be ascribed to the presence of inter-molecular H-bonds, the dependence of the absorbance value (associated to the signals observed in the OH-stretching region of the IR spectra of **3** and **4**) from the concentration of the CCl_4 solution was studied. The results are showed in figure 2.14. The band at 3327 cm^{-1} exhibits a concentration dependence which is ascribed to a dimeric structure (which is the result of the aggregation between two

[a]The structure is confirmed by the assignment of the ^{1}H-NMR spectrum reported in the SI of the original article (figure SI 47).

monomers of **4**).[a]

An attempt to relate the VCD signals of **1**, **2**, **3** and **4** was carried out. The features enclosed in red dashed squares (1450-1300 cm^{-1}, see fig. 2.13) exhibit an analogous pattern ("+,−" for the R enantiomers) for the molecular systems **1** and **2**, while a different motif ("−,+,−,+" for the R enantiomers with the first signal[b] at least slightly more intense than the others) is observed for the molecular systems **3** and **4**. Other two regions with some degree of similarity between the spectra of different molecules are enclosed in green and yellow dashed squares. The lack of a common spectral pattern in the fingerprint region of the VCD spectra of the molecular systems considered in this subsection is not surprising, and is due to the differences in the substituents attached to the cyclopentadienyl moiety (or moieties, in the case of **4**) which leads to entirely different VCD spectra (despite the presence of the ferrocene moiety as common structural motif).

For the assignment of the most intense vibrational transitions observed in IR and VCD spectra of figs. 2.13 and 2.15 a comparison between calculated and experimental spectra is extremely useful. Calculated spectra (at harmonic and anharmonic levels) are compared with their experimental counterparts in figs. 2.16, 2.17 and 2.18. Agreement between experimental and computational data are generally satisfactory for transition frequencies and relative intensities (in most of the cases considered in this subsection the absolute intensities are underestimated).

In the case of the molecular system labeled with **1**, calculated IR and VCD spectra[c] at the harmonic level are in good agreement with their experimental counterparts (in the mid-IR region and in the C=O stretching region), although the transition frequencies are systematically higher[d] than their experimental counterparts. At the anharmonic level, experimental and calculated transition frequencies are closer (but in the mid-IR region the correction to the transition frequencies seems to be slightly overestimated with the GVPT2 approach), particularly in the C=O stretching region. A redistribution of relative intensities (switching from the harmonic to the anharmonic level) is observed, which is not associated to an overall improve-

[a] These results are further confirmed by NMR data reported in the original article. Another possible explanation based on the presence of an intramolecular H-bond is not convincing due to the dependence from the concentration of the absorbance value of the band at 3327 cm^{-1}.

[b] Which is similar to the signal observed at ca. 1400 cm^{-1} for the molecule $\mathbf{5} - R_p$, see fig. 2.15.

[c] Only the averaged calculated spectra are reported in fig. 2.16. For what concerns the harmonic spectra, the contribution of all the 9 conformers found for the molecular system **1** were included. In the case of the anharmonic spectra (which requires computationally more demanding calculations), only the contributions of the four most populated conformers were included.

[d] Slightly higher in the case of the mid-IR region. The shift to higher frequencies due to the lack of anharmonic contributions is more pronounced for transitions characterized by an higher fundamental frequency.

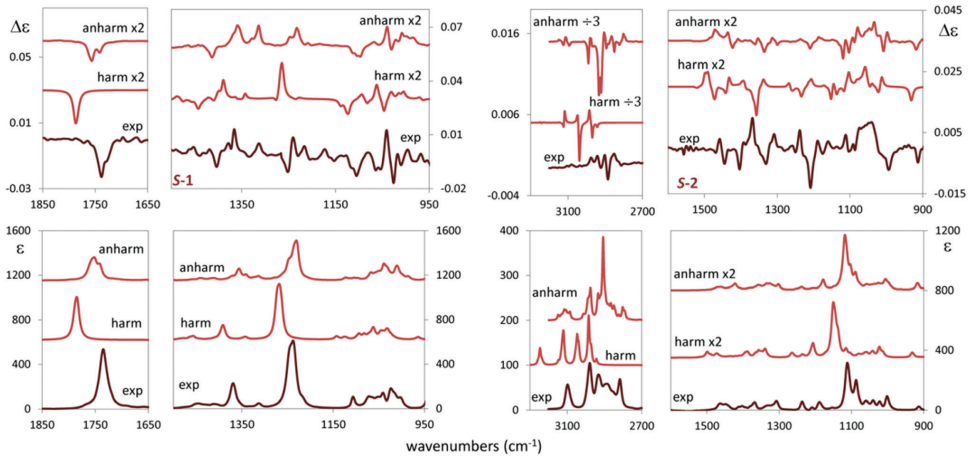

Figure 2.16: Comparison between experimental and calculated spectra of **1** (left side) and **2** (right side). IR and VCD spectra calculated at harmonic and anharmonic levels are reported. Experimental VCD spectra of the *S* enantiomers are provided as semi-differences of the VCD spectra provided in fig. 2.13. Lorentzian bandshapes (with bandwidths of 10 cm^{-1}) are assumed for the calculated spectra.

ment in the agreement between experimental and calculated spectra. The sign of the VCD singlet ("−" for the *S* enantiomer) experimentally probed in the C=O stretching region is correctly reproduced already at harmonic level.[a] The assignment of the harmonic signals due to the most populated conformer of **1** was performed and provided in the SI of the original article,[b] and suggests the assignment of the most intense IR signal of the mid-IR region of **1** (between 1200 and 1250 cm^{-1}) to a normal mode which involves the acetoxyethyl-substituent (particularly the bending of the C*—H bond) and the substituted cyclopentadienyl moiety.[c]

For what concerns **2**, the agreement between calculated and experimental spectra can be considered satisfactory, although some features of the experimental spectra are not well-reproduced.[d] In the mid-IR region, calculated IR spectra (at harmonic and anharmonic levels) are in good agreement with their experimental counterparts (although in the harmonic spectrum transition frequencies are slightly overestimated), while some discrepancies are found in the calculated VCD spectra: nevertheless, a comparison of the ex-

[a] It should be underlined (see the SI of the original article, particularly figure SI 11) that the sign of this specific VCD signal is not equal for all the conformers.

[b] See table SI 1 of the original article.

[c] The relative intensity associated with this normal mode is the highest of the IR spectrum in the mid-IR region for the four most populated conformers of **1**.

[d] The averaged calculated spectra are shown in fig. 2.16. The contributions of all the conformers (9) found for the molecular system **2** were included for the calculation of the harmonic spectrum. For what concerns the anharmonic spectra, only the contributions of the five most populated conformers were included.

perimentally probed with the calculated VCD spectrum of **2** in the mid-IR region allows the assignment of the absolute configuration (even if only the harmonic results are available). In the CH-stretching region, the transition frequencies are clearly overestimated at the harmonic level: this overestimation disappears when the anharmonic effects are taken into account with the GVPT2 model, but on the other hand the redistribution of the transition intensities increases the discrepancies between experimental and calculated intensities (even in the case of the IR spectrum). The most intense signal of the IR spectrum in the mid-IR region can be assigned to the stretchings of the two C—O bonds in which is involved the oxygen atom of the molecular system **2** (this assignment is based on the features of the normal mode associated to the most intense harmonic transition of the most populated conformers).[a]

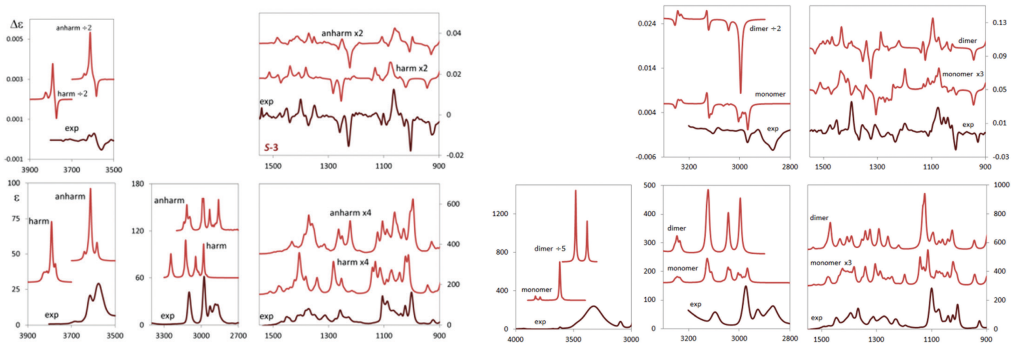

Figure 2.17: Comparison between experimental and calculated spectra of **3** (left side) and **4** (right side). IR and VCD spectra calculated at harmonic and anharmonic levels are reported for **3**, while IR and VCD spectra of **4** were calculated only at harmonic level. Experimental VCD spectra of the *S* enantiomers are provided as semi-differences of the VCD spectra provided in fig. 2.13. Lorentzian bandshapes (with bandwidths of 10 cm^{-1}) are assumed for the calculated spectra.

Good agreement between calculated and experimental spectra is found also in the case of **3**,[b] at least for transition frequencies and relative intensities (the absolute intensities are systematically underestimated in the mid-IR region). As expected, harmonic transition frequencies systematically overestimate the experimental results, while the introduction of the anharmonic contributions with the GVPT2 model leads to calculated values closer to the experimental ones.[c] For what concerns relative intensities, despite a gener-

[a] See table SI 3 and figure SI 23 in the SI of the original article.

[b] As for the molecular systems previously discussed, the contributions of all the 9 conformers found for the molecular system **2** were included in the Boltzmann average performed for the calculation of the harmonic spectrum. In the case of the anharmonic spectra, only the contributions of the six most populated conformers were included.

[c] This statement seems to be not valid in the region between 1200 and 1500 cm^{-1} (see fig. 2.17), where the introduction of anharmonic corrections leads to a systematic *under-*

ally good agreement between experimental and computational results some discrepancies should be pointed out. In the OH-stretching region the VCD spectrum exhibit a pattern "+,−" (for the S enantiomer, from higher to lower wavenumbers) which is correctly reproduced in the calculated spectra (at harmonic and anharmonic levels), but the ratio of the intensities associated to the "+" and to the "−" signals in the calculated spectrum is higher than the ratio found in the experimental one.[a] In the IR spectrum measured in the same region two close signals (with the signal at higher wavenumbers slightly less intense) were detected, while the calculated spectra reveal a different picture, with the signal at higher wavenumbers more than two (in the anharmonic case more than three) times more intense than the other signal. In the mid-IR region the VCD spectrum is particularly well-reproduced (at least with respect to the other cases considered in this section). The two negative signals experimentally probed between 1200 and 1300 cm^{-1} (see the signals enclosed in the dashed green square, spectrum on the top right of fig. 2.13) are highly diagnostic for the assignment of the absolute configuration and computationally well-reproduced (especially at harmonic level):[b] on the basis of the features of the normal modes associated to the two harmonic transitions, the two negative signals can be assigned[c] to the bending of C*—H (signal at higher wavenumbers) and to a combination of in plane bendings of the CH of the substituted cyclopentadienyl moiety, OH bending and C*—C_{Cp} stretching[d] (signal at lower wavenumbers).

In the case of **4**, the need of taking into account the dimer significantly complicates the picture. Anharmonic calculations were not performed because of the size of the dimer. Therefore, for the comparison between calculated and experimental spectra only the harmonic calculations are shown (see fig. 2.17). The partial agreement between experimental and calculated spectra can be employed to clarify the nature of the IR signals experimentally probed in the OH-stretching region (see figs. 2.13 and 2.14). First of all, it must be underlined that the harmonic spectra of the monomer and the dimer are quite similar (despite some differences) in the mid-IR and in the CH-stretching regions (see fig. 2.17). The agreement between the harmonic spectra of the dimer and the experimental values is slightly more satisfactory[e] than the agreement of the experimental values with the harmonic spectra of

estimation of the transition frequencies (this is particularly evident in the IR spectrum).

[a] Moreover, it must be noticed that the intensity associated to the "+" signal in the calculated spectrum is too high with respect to the experimental one.

[b] This feature is due to the harmonic VCD spectrum of the most populated conformer, see fig. SI 39 in the SI of the original article.

[c] See table 2 in the original article.

[d] In other words, ferrocene moiety and hydroxyethyl substituent are both involved in the transition.

[e] In light of the concentration of the experimentally probed CCl_4 solution of **4**, this is not surprising.

the monomer.[a] However, the two hydroxyl groups of the monomers are directly involved in the two intermolecular H-bonds which allow the formation of the dimer: therefore, substantial differences are expected (and are observed, see fig. 2.17) between the harmonic spectra of the monomer and the dimer. The outstanding intensities associated to the two transitions found in the harmonic IR spectrum of the dimer (one associated to the symmetric stretching of the four OH bonds, the other to the antisymmetric one) accounts for the band experimentally probed at 3327 cm^{-1}. The signals in the OH-stretching region of the harmonic IR spectrum of the monomer are associated, respectively, to the stretching of the donor OH group (i.e. the stretching of the OH group in which the hydrogen atom is involved in the H-bond) and to the stretching of the acceptor OH group (i.e. the OH group in which the oxygen is involved in the H-bond). The higher intensity associated to the stretching of the donor OH group (with transition frequencies in the interval between 3630 and 3641 cm^{-1}) is a feature common to the various conformers of the monomer with an intramolecular H-bond,[b] while the other (by far less intense) signals at higher wavenumbers (transition frequencies in the interval between 3760 and 3815 cm^{-1}) can be assigned to the stretching of acceptor OH bonds or to OH bonds not involved in an H-bond. On the basis of the negative frequency shift due to the introduction of anharmonic corrections, it is possible to put forward an additional hypothesis: also the transitions due to the stretching of the donor OH groups of the three conformers of the monomer with an intramolecular H-bond (and not only the two transitions associated to the dimer) account for the experimental band at 3327 cm^{-1}. As a consequence, the small experimental signal at 3619 cm^{-1} (see fig. 2.14) can be associated or to the stretching of OH groups not involved in a H-bond or (more probably) to the stretching of acceptor OH groups involved in an H-bond in the monomer of **4**. Moreover, it must be noticed that (in contrast with the other molecular systems treated in this paragraph) the dimer and two of the five conformers of the monomer pertains to the C_2 symmetry point group (and not to the C_1): this aspect was taken into account when the Boltzmann averages were carried out.

The molecular systems $\mathbf{5}-R_p$ and $\mathbf{5}-S_p$ involve 52 atoms each: therefore, anharmonic calculations are computationally very expensive. For this reason, the anharmonic analysis is not carried out; moreover, also the conformational analysis is cumbersome. The number of conformers which are characterized in this work is 5 for both the diastereoisomers. The analysis provided in this paragraph is based on a comparison of the experimental IR and VCD spectra (see fig. 2.15 or fig. 2.18) with computational results obtained at harmonic

[a] This is particularly evident for the IR spectra, especially in the CH-stretching region and in the interval between 950 and 1150 cm^{-1} of the mid-IR spectra.

[b] Five conformers of the monomer of **4** were included in the calculation: three of these five are characterized by an intramolecular H-bond (see figs. SI 51 - SI 55 in the SI of the original article).

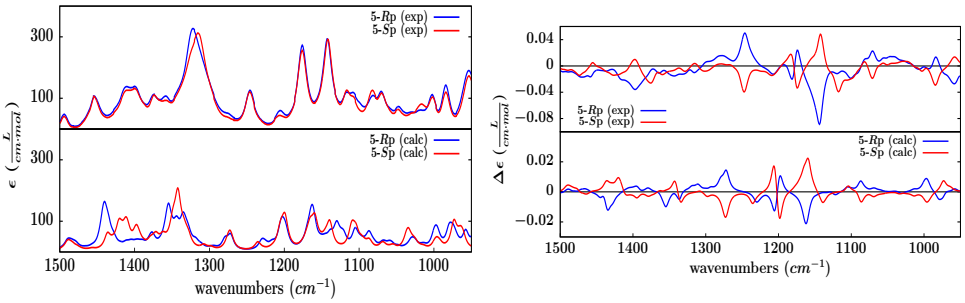

Figure 2.18: Comparison between experimental and calculated spectra of $\mathbf{5}-R_p$ and $\mathbf{5}-S_p$. IR and VCD spectra were calculated at harmonic level. Boltzmann average were performed on the 5 most populated conformers of each species. Lorentzian bandshapes (with bandwidths of 10 cm^{-1}) are assumed for the calculated spectra.

level. In contrast with the results provided in this paragraph for the other substituted chiral ferrocenes, experimental and computational data on $\mathbf{5}-R_p$ and $\mathbf{5}-R_p$ have not been published yet. Therefore, structures, populations and harmonic spectra of each of the most populated conformers must be provided for completeness (these additional data can be found in section B.7 of appendix B). A comparison between experimental and calculated spectra is provided in figure 2.18. It must be underlined (again) that $\mathbf{5}-R_p$ and $\mathbf{5}-S_p$ are diastereoisomers, and *not* enantiomers. In light of the flexibility of the substituents attached to one of the cyclopentadienyl moieties, the remarkably agreement observed between experimental and computational spectra suggests the reliability of (i) the B3PW91/Def2TZVP level of theory (for the computational characterization of this kind of systems) and of (ii) the preliminary conformational analysis (for the selection of the most populated conformers). The structures of the most populated conformers are characterized by the H-bond between the hydroxyl group of one of the substituents with one of the oxygen atoms (both bonded to a sulfur atom) of the other substituent. The harmonic results can be employed to assign the VCD patterns experimentally probed in the interval 1100-1300 cm^{-1}. For what concerns the molecular system $\mathbf{5}-R_p$, the following pattern is experimentally measured (and computationally reproduced)[a]: "+,−,−,+,−"[b] (from higher to lower wavenumbers, from 1280 to 1150 cm^{-1}). This portion of the calculated VCD spectra is similar to the harmonic spectrum of the most populated conformers, but the contributions of the harmonic VCD spectra of other four conformers improve the agreement between experimental and computed VCD spectra.[c] Some of the normal modes associated

[a] Transition frequencies are slightly overestimated at harmonic level.

[b] See figs. 2.18 and 2.19. The last negative signal is the most intense of the five. The other two negative signals are less intense than the two positive signals.

[c] For example, the second negative signal in the pattern "+,−,−,+,−" is almost absent in the harmonic VCD spectrum of the most populated conformer and clearly distinguish-

to the transitions which determine the pattern experimentally observed for the VCD spectrum in the interval 1280-1150 cm^{-1} are highly delocalized, and therefore their assignment to a specific group of atoms involved in the structure of the molecular system is not straightforward. However, only the atoms of the substituted cyclopentadienyl moiety and the atoms of the two substituents (i.e. the two substituents attached to the ferrocene moiety) are involved in these normal modes. More specifically, the most intense negative sign (the last signal of the VCD motif here considered, at about 1160 cm^{-1} in the calculated harmonic spectrum) is mainly due to a normal mode which involves the symmetric combination of the two S=O stretching,[a] the signal between 1190 and 1200 cm^{-1} (in the calculated harmonic spectrum) is prevalently due to the in-plane CH bending of the substituted cyclopentadienyl moiety and the negative signal at about 1205 cm^{-1} is the result of the superposition of two transitions prevalently associated to the in-plane CH bending of the phenyl group (see table B.2). In the case of the molecular system $\mathbf{5} - S_p$, the following experimental pattern is observed in the VCD spectrum:"−,−,+,−,+"[b] (from higher to lower wavenumbers, from 1280 to 1150 cm^{-1}). In this region, the pattern exhibited by the calculated VCD spectra obtained through a Boltzmann average is essentially the same found for the most abundant conformer (see fig. B.1). Similarly to what was observed in the case of $\mathbf{5} - R_p$, only the atoms of the substituted cyclopentadienyl moiety and the atoms of the two substituents are involved in these normal modes. The positive signal at about 1160 cm^{-1} (in the calculated harmonic spectrum) is due to a normal mode which involve the symmetric combination of the two S=O stretching, and this data can be particularly useful: for each of the conformers taken into account for the calculation of the VCD spectra of $\mathbf{5} - R_p$ and $\mathbf{5} - S_p$, a VCD signal was calculated at about 1160 cm^{-1}, of negative sign in the case of the conformers of $\mathbf{5} - R_p$ and of positive sign for the conformers of $\mathbf{5} - S_p$ (see fig. B.1). These results suggest the possibility of assign the planar chirality (R_p or S_p) on the basis of the sign of the VCD signal associated to the symmetric combination of the two S=O stretching for this kind of substituted chiral ferrocenes (see tables B.2 and B.3). To verify the correctness (and the extent) of this hypothesis, more experimental and computational data would be extremely useful.

The comparison of the VCD patterns found in the experimental (and reproduced by the calculated) spectra of $\mathbf{5} - R_p$ (pattern "+,−,−,+,−") and $\mathbf{5} - S_p$ (pattern "−,−,+,−,+") are *almost*, but not *exactly* opposite: the second, negative signal is the same in both the patterns (see fig. 2.19).

able in both the experimental and the calculated VCD spectra (which is obtained as Boltzmann average of the harmonic VCD spectra of the five conformers, see fig. B.1), see figs. 2.18 and 2.19.

[a] This negative signal can be observed in the harmonic spectra of all the conformers taken into account for the calculation of the VCD spectrum of $\mathbf{5} - R_p$, see fig. B.1.

[b] See figs. 2.18 and 2.19.

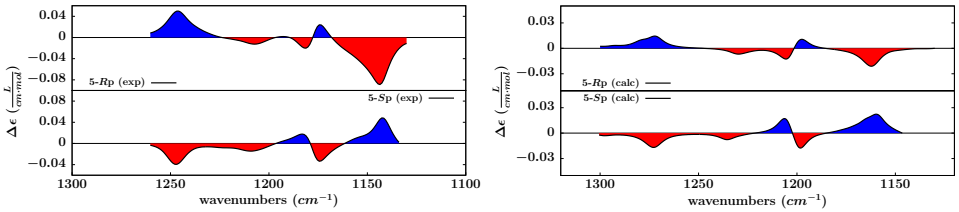

Figure 2.19: Experimental (left side) and calculated (right side) VCD patterns of $\mathbf{5}-R_p$ (top) and $\mathbf{5}-S_p$ (bottom). Areas enclosed by positive VCD signals are highlighted with the blue colour, while areas enclosed by negative VCD signals are highlighted with the red colour. Experimental patterns of $\mathbf{5}-R_p$ ("+,−,−,+,−") and $\mathbf{5}-S_p$ ("−,−,+,−,+") VCD spectra are correctly reproduced by the calculations.

This is not surprising, because $\mathbf{5}-R_p$ and $\mathbf{5}-S_p$ are diastereoisomers, not enantiomers. The opposite planar chirality is responsible of many opposite VCD features (see fig. 2.18), but the small negative signal (at ca. 1225-1230 cm^{-1}) with the same sign for both the compounds is associated to a normal mode localized on the sulfamidic substituent. This normal mode involves a C*—H bending and a C*—C stretching (see tables B.2 and B.3), i.e. it is prevalently localized in the neighbourhood of the asymmetric carbon atom which has exactly the same configuration in both the molecular systems considered here.

Conclusive remarks The results provided in this section strongly support the usefulness of a combined approach for the study of IR and VCD spectra of substituted chiral ferrocenes.

Among the various results, from a chemical point of view one of the most interesting ones is the existence (in diluted CCl_4 solutions) of the dimer of **4**. Worth of mention is the reliability of the comparison between calculated (at harmonic level) and experimental VCD spectra for the assignment of the absolute configuration of the substituted chiral ferrocene considered in this study.

For what concerns the usefulness of the anharmonic corrections introduced through the GVPT2 model, the improved agreement of calculated and experimental transition frequencies after the introduction of the anharmonic corrections is evident. An improvement in the agreement between calculated and experimental transition intensities (relative intensities) is not always observed after the introduction of the anharmonic corrections. However, despite some discrepancies the results obtained at anharmonic level can be considered satisfying. The importance of FRs and DDRs in molecular systems of this size cannot be overestimated, and a reliable, effective and automatic computational procedure for the treatment of resonances would be desirable in order to improve the results of anharmonic calculations performed on these systems.

Chapter 3

Calculation of energies and properties: dealing with two electronic states

The computational modeling of the transition between two electronic states is an issue of pivotal importance. Excitation ($A \rightarrow A^*$) or ionization ($A \rightarrow A^+$) of a molecular system are examples of processes which involve a transition between two electronic states, as well as the transitions between two different excited states with equal or different (this is the case of an intersystem crossing) spin multiplicity. There is ample computational and experimental evidence of the observable effects due to nuclear motions when a transition between two electronic states occurs. This chapter is devoted to the computational simulation of UPS spectra: more specifically, in section 3.1 the computational approach employed for the solution of the electronic problems associated to the ionization of the investigated molecular systems is introduced; the time-independent approach to the calculation of the vibrational signatures associated to an electronic transition is described in section 3.2; in the last section of this chapter (3.3) some original applications of the computational approaches considered in sections 3.1 and 3.2 of this chapter are provided: the results are discussed through a comparison with the experimental UPS spectra available in literature.

3.1 Electron propagator theory

The reformulation of differential equations (together with their boundary conditions) as integral equations by means of Green's functions is often advantageous. In the context of quantum chemistry, this reformulation unveils a physical picture which is transparent and computationally fruitful. In this

section the discussion is limited to one-electron Green's functions,[a] which can be employed to systematically improve the ionization energies obtained by means of Koopmans' Theorem (KT).[200] When an approach based on one electron Green's functions is employed to solve out the electronic problem associated to a ionization process $A \rightarrow A^+$ (or to an electron attachment, $A \rightarrow A^-$), the following expression gives the elements of the electron propagator matrix:

$$G_{pq}(E) = \lim_{\eta \to +0} \left[\sum_n \frac{\left\langle \phi_0^{N_{el}} \middle| a_p^\dagger \middle| \phi_n^{N_{el}-1} \right\rangle \left\langle \phi_n^{N_{el}-1} \middle| a_q \middle| \phi_0^{N_{el}} \right\rangle}{E + E_n^{N_{el}-1} - E_0^{N_{el}} - i\eta} + \sum_n \frac{\left\langle \phi_0^{N_{el}} \middle| a_q \middle| \phi_n^{N_{el}+1} \right\rangle \left\langle \phi_n^{N_{el}+1} \middle| a_p^\dagger \middle| \phi_0^{N_{el}} \right\rangle}{E - E_n^{N_{el}+1} + E_0^{N_{el}} + i\eta} \right]. \tag{3.1}$$

In eq. 3.1, p and q are spin orbital indices, $a_p^\dagger$ and a_q are known as, respectively, creation and destruction operators; $\phi_0^{N_{el}}$ labels the electronic ground state of the N_{el}-electron system (with energy equals to $E_0^{N_{el}}$), while $\phi_n^{N_{el}-1}$ and $\phi_n^{N_{el}+1}$ label an electronic state n of, respectively, the $(N_{el}-1)$-electron system (with an energy value of $E_n^{N_{el}-1}$) and the $(N_{el}+1)$-electron system (with energy equals to $E_n^{N_{el}+1}$). Poles of eq. 3.1 are values of E which correspond to a singularity[b], i.e. $E = E_0^{N_{el}} - E_n^{N_{el}-1}$ (when E equals an ionization energy) or $E = E_n^{N_{el}+1} - E_0^{N_{el}}$ (when E equals an electron affinity).

Introducing the following abbreviated notation for the matrix elements given in eq. 3.1:

$$G_{pq}(E) = \langle\langle a_p^\dagger; a_q \rangle\rangle_E, \tag{3.2}$$

[a] A textbook which provides an introduction to the use of Green's functions in the context of quantum chemistry is ref. 196 (for what concerns the aspects introduced in this section, see in particular the beginning of chapter 4 and chapter 9); a review focused on the electron propagator theory can be found in ref. 197; a bridge between the pictorial and the algebraic views of the theory of Green's functions is provided in ref. 198; an introduction to the subject which completely omits a discussion about the time-dependent aspects of the Green's functions theory is given in the last chapter of ref. 1; for a concise historical account of the early works concerning the development and the employment of the electron propagator theory to molecular problems, see ref. 199.

[b] In what follows, E can assume only real values and the complex factors of the denominators in eq. 3.1 are dropped; the infinitesimal positive value η guarantees the convergence of the Fourier transform for the time-dependent expression: more specifically, the time dependent expression of the propagator is multiplied for $e^{-\eta(t_2-t_1)}$ where $\eta(t_2-t_1) = 0$ if $t_2 - t_1$ (and therefore $e^{-\eta(t_2-t_1)} = 1$) has a finite value and $\eta(t_2-t_1) = \infty$ if $t_2 - t_1 = \infty$ (and therefore $e^{-\eta(t_2-t_1)} = 0$, assuring the desired convergence; see pages 40 and 41 of ref. 198 for a more detailed discussion).

and remembering the following simple relationships[a]:

$$\frac{1}{A-B} = \frac{1}{A} + \frac{B}{A(A-B)}, \tag{3.3}$$

$$\sum_n \left\langle \phi_0^{N_{el}} \middle| a_p^\dagger \middle| \phi_n^{N_{el}-1} \right\rangle \left\langle \phi_n^{N_{el}-1} \middle| a_q \middle| \phi_0^{N_{el}} \right\rangle = \left\langle \phi_0^{N_{el}} \middle| a_p^\dagger a_q \middle| \phi_0^{N_{el}} \right\rangle, \tag{3.4}$$

$$\sum_n \left\langle \phi_0^{N_{el}} \middle| a_q \middle| \phi_n^{N_{el}+1} \right\rangle \left\langle \phi_n^{N_{el}+1} \middle| a_p^\dagger \middle| \phi_0^{N_{el}} \right\rangle = \left\langle \phi_0^{N_{el}} \middle| a_q a_p^\dagger \middle| \phi_0^{N_{el}} \right\rangle, \tag{3.5}$$

$$\left\langle \phi_n^{N_{el}-1} \middle| a_q \middle| \phi_0^{N_{el}} \right\rangle \left(E_0^{N_{el}} - E_n^{N_{el}-1} \right) = \left\langle \phi_n^{N_{el}-1} \middle| \left[a_q, H \right]_- \middle| \phi_0^{N_{el}} \right\rangle, \tag{3.6}$$

$$\left\langle \phi_0^{N_{el}} \middle| a_q \middle| \phi_n^{N_{el}+1} \right\rangle \left(E_n^{N_{el}+1} - E_0^{N_{el}} \right) = \left\langle \phi_0^{N_{el}} \middle| \left[a_q, H \right]_- \middle| \phi_n^{N_{el}+1} \right\rangle, \tag{3.7}$$

eq. 3.1 can be developed[b]:

$$\begin{aligned}
E\langle\langle a_p^\dagger; a_q \rangle\rangle_E = & \sum_n \left[\left\langle \phi_0^{N_{el}} \middle| a_p^\dagger \middle| \phi_n^{N_{el}-1} \right\rangle \left\langle \phi_n^{N_{el}-1} \middle| a_q \middle| \phi_0^{N_{el}} \right\rangle \left(1 + \frac{E_0^{N_{el}} - E_n^{N_{el}-1}}{E + E_n^{N_{el}-1} - E_0^{N_{el}}} \right) \right] \\
& + \sum_n \left[\left\langle \phi_0^{N_{el}} \middle| a_q \middle| \phi_n^{N_{el}+1} \right\rangle \left\langle \phi_n^{N_{el}+1} \middle| a_p^\dagger \middle| \phi_0^{N_{el}} \right\rangle \left(1 + \frac{E_n^{N_{el}+1} - E_0^{N_{el}}}{E - E_n^{N_{el}+1} + E_0^{N_{el}}} \right) \right] = \\
& \left\langle \phi_0^{N_{el}} \middle| \left[a_p^\dagger, a_q \right]_+ \middle| \phi_0^{N_{el}} \right\rangle + \sum_n \left[\frac{\left\langle \phi_0^{N_{el}} \middle| a_p^\dagger \middle| \phi_n^{N_{el}-1} \right\rangle \left\langle \phi_n^{N_{el}-1} \middle| \left[a_q, H \right]_- \middle| \phi_0^{N_{el}} \right\rangle}{E + E_n^{N_{el}-1} - E_0^{N_{el}}} \right] \\
& + \sum_n \left[\frac{\left\langle \phi_0^{N_{el}} \middle| \left[a_q, H \right]_- \middle| \phi_n^{N_{el}+1} \right\rangle \left\langle \phi_n^{N_{el}+1} \middle| a_p^\dagger \middle| \phi_0^{N_{el}} \right\rangle}{E - E_n^{N_{el}+1} + E_0^{N_{el}}} \right] = \\
& \left\langle \phi_0^{N_{el}} \middle| \left[a_p^\dagger, a_q \right]_+ \middle| \phi_0^{N_{el}} \right\rangle + \left\langle\langle a_p^\dagger; \left[a_q, H \right]_- \right\rangle\rangle_E .
\end{aligned} \tag{3.8}$$

The last term provided in eq. 3.8 can be expanded in the same manner:

[a] The relationships given in eqs. 3.4 and 3.5 imply that the sums over n are assumed to be complete.

[b] See eq. 14 of ref. 201.

$$E\langle\langle a_p^\dagger; \left[a_q, H\right]_-\rangle\rangle_E = \left\langle \phi_0^{N_{el}} \middle| \left[a_p^\dagger, \left[a_q, H\right]_-\right]_+ \middle| \phi_0^{N_{el}} \right\rangle + \langle\langle a_p^\dagger; \left[\left[a_q, H\right]_-, H\right]_-\rangle\rangle_E \tag{3.9}$$

Employing eqs. 3.8 and 3.9, the matrix element pq of the electron propagator can be given as a series:

$$\begin{aligned}\langle\langle a_p^\dagger; a_q\rangle\rangle_E = {} & E^{-1} \left\langle \phi_0^{N_{el}} \middle| \left[a_p^\dagger, a_q\right]_+ \middle| \phi_0^{N_{el}} \right\rangle \\ & + E^{-2} \left\langle \phi_0^{N_{el}} \middle| \left[a_p^\dagger, \left[a_q, H\right]_-\right]_+ \middle| \phi_0^{N_{el}} \right\rangle \\ & + E^{-3} \left\langle \phi_0^{N_{el}} \middle| \left[a_p^\dagger, \left[\left[a_q, H\right]_-, H\right]_-\right]_+ \middle| \phi_0^{N_{el}} \right\rangle \\ & + \ldots \ .\end{aligned} \tag{3.10}$$

The Introduction of the concept of a linear space of field operators and the definition of suitable superoperators acting on this space[202] allow a more compact formulation of the result obtained in eq. 3.8 and of the approximation introduced in this section.

For any two operators X and Y in the linear space of field operators mentioned above a scalar product $(X|Y)$ is defined as follows:

$$(X|Y) = \left\langle \phi_0^{N_{el}} \middle| \left[X^\dagger, Y\right]_+ \middle| \phi_0^{N_{el}} \right\rangle \tag{3.11}$$

and the identity and Hamiltonian superoperators are defined, respectively, by:

$$\mathcal{I}X = X; \tag{3.12}$$

$$\mathcal{H}X = \left[X, H\right]_-. \tag{3.13}$$

Eq. 3.10 can be rewritten (employing eqs. 3.11, 3.12 and 3.13) in the following manner:

$$\langle\langle a_p^\dagger; a_q\rangle\rangle_E = E^{-1}(a_p|a_q) + E^{-2}(a_p|\mathcal{H}a_q) + E^{-3}(a_p|\mathcal{H}^2 a_q) + \ldots \ . \tag{3.14}$$

The series provided in eq. 3.14 converges;[a] therefore, a compact formulation of eq. 3.14 can be written as follows:

$$G_{pq}(E) = \langle\langle a_p^\dagger; a_q\rangle\rangle_E = (a_p|(E\mathcal{I} - \mathcal{H})^{-1} a_q); \tag{3.15}$$

[a] more specifically, $\sum_{i=0}^{\infty} a x^i = \frac{a}{1-x}$, for $|x| < 1$.

if the simple annihilation operators are gathered in a single vector ($\mathbf{a} = [a_1 a_2 ... a_R]$, where R is the dimension of the employed spin-orbital basis), the formulation given in eq. 3.15 can be easily extended to the entire electron propagator matrix:

$$\mathbf{G}(E) = (\mathbf{a}|(E\mathcal{I} - \mathcal{H})^{-1}\mathbf{a}). \tag{3.16}$$

To provide a formulation of the electron propagator matrix which is suitable for actual calculations, a basis of electron field operators can be constructed employing the set of field operator products that change the number of electrons by 1. This set includes products of k creators and $k+1$ annihilators (for $k \in \mathbb{N}$)[a] and can be employed to construct a vector $\mathbf{h}$ which spans the full space of ionization operators. Through an inner projection (more details are provided in section C.1 of appendix C), it is possible to write:

$$\mathbf{G}(E) = (\mathbf{a}|\mathbf{h})(\mathbf{h}|(E\mathcal{I} - \mathcal{H})\mathbf{h})^{-1}(\mathbf{h}|\mathbf{a}). \tag{3.17}$$

The manifold of field operator products involved in the inner projection can be partitioned in two orthogonal sets: the primary space of simple annihilators $\mathbf{a}$ and an additional orthogonal space of products of creation and annihilation operators ($\mathbf{f}$), i.e. triple ($a_k^\dagger a_l a_m$), quintuple ($a_j^\dagger a_k^\dagger a_l a_m a_n$) and higher products:

$$\mathbf{G}(E) = \begin{bmatrix}(\mathbf{a}|\mathbf{a}) & (\mathbf{a}|\mathbf{f})\end{bmatrix} \begin{bmatrix}(\mathbf{a}|(E\mathcal{I} - \mathcal{H})\mathbf{a}) & (\mathbf{a}|(E\mathcal{I} - \mathcal{H})\mathbf{f}) \\ (\mathbf{f}|(E\mathcal{I} - \mathcal{H})\mathbf{a}) & (\mathbf{f}|(E\mathcal{I} - \mathcal{H})\mathbf{f})\end{bmatrix}^{-1} \begin{bmatrix}(\mathbf{a}|\mathbf{a}) \\ (\mathbf{a}|\mathbf{f})\end{bmatrix}. \tag{3.18}$$

The following relationship is an immediate consequence of eq. 3.11:[b]

$$(\mathbf{a}|\mathbf{a}) = \mathbf{I}_{a\times a}; \tag{3.19}$$

The orthogonality between $\mathbf{a}$ and $\mathbf{f}$ imply the following results:[c]

$$(\mathbf{a}|\mathbf{f}) = \mathbf{0}_{a\times f}; \tag{3.20}$$

$$(\mathbf{f}|\mathbf{a}) = \mathbf{0}_{f\times a}. \tag{3.21}$$

[a] If $k = 0$ the set of simple annihilators (arrayed in the vector $\mathbf{a}$) is obtained; k cannot assume any positive integer value: this limitation is due to the finite dimension of the spin-orbital basis which determines the maximum value assumed by k to set up the full space of ionization operators.

[b] Because $(a_p|a_q) = \delta_{pq}$.

[c] The assumptions behind eqs. 3.20, 3.21 and 3.22 are not trivial: the operator basis $\mathbf{f}$ and the wavefunction $\phi_0^{N_{el}}$ (see eq. 3.11) must be chosen in order to ensure the validity of these relationships (see, for example, ref. 203); otherwise, suitable overlap terms $S_{x,y} = (x|y)$ are defined: these terms enter in the square matrix given in the RHS of eq. 3.23 (assuming eqs. 3.20, 3.21 and 3.22, $S_{x,y} = \delta_{xy}$ and eq. 3.23 is found).

Another relationship which is assumed in what follows is:

$$(\mathbf{f}|\mathbf{f}) = \mathbf{I}_{f\times f}; \tag{3.22}$$

Eq. 3.18 can be rewritten employing eqs. 3.19-3.22:

$$\mathbf{G}(E) = \begin{bmatrix}\mathbf{I}_{a\times a} & \mathbf{0}_{a\times f}\end{bmatrix} \begin{bmatrix} E\mathbf{I} - (\mathbf{a}|\mathcal{H}\mathbf{a}) & -(\mathbf{a}|\mathcal{H}\mathbf{f}) \\ -(\mathbf{f}|\mathcal{H}\mathbf{a}) & E\mathbf{I} - (\mathbf{f}|\mathcal{H}\mathbf{f})\end{bmatrix}^{-1} \begin{bmatrix}\mathbf{I}_{a\times a} \\ \mathbf{0}_{a\times f}\end{bmatrix}. \tag{3.23}$$

To compute the poles of $\mathbf{G}(E)$ in eq. 3.23, two different approaches can be adopted. The first is based on the partitioning technique for the calculation of an inverse matrix, which lead to the following result:[a]

$$\mathbf{G}(E) = \Big\{E\mathbf{I} - (\mathbf{a}|\mathcal{H}\mathbf{a}) - (\mathbf{a}|\mathcal{H}\mathbf{f})\big[E\mathbf{I} - (\mathbf{f}|\mathcal{H}\mathbf{f})\big]^{-1}(\mathbf{f}|\mathcal{H}\mathbf{a})\Big\}^{-1}. \tag{3.26}$$

Another approach[205] is based on the solution of the eigenvalue problem associated to the superoperator hamiltonian matrix:

$$\begin{bmatrix}(\mathbf{a}|\mathcal{H}\mathbf{a}) & (\mathbf{a}|\mathcal{H}\mathbf{f}) \\ (\mathbf{f}|\mathcal{H}\mathbf{a}) & (\mathbf{f}|\mathcal{H}\mathbf{f})\end{bmatrix} \begin{bmatrix}\mathbf{U}_{a,n} \\ \mathbf{U}_{f,n}\end{bmatrix} = \begin{bmatrix}\mathbf{U}_{a,n} \\ \mathbf{U}_{f,n}\end{bmatrix} \Omega_n. \tag{3.27}$$

A pole of the electron propagator occurs when the value of E equals an eigenvalue Ω_n of the superoperator hamiltonian matrix. Eq. 3.27 can be written in the following, more compact form:

$$\boldsymbol{\mathcal{H}}\mathbf{U} = \mathbf{U}\boldsymbol{\Omega}; \tag{3.28}$$

with:

$$\mathbf{U}^\dagger\mathbf{U} = \mathbf{I}; \tag{3.29}$$

[a] An heuristic approach to derive eq. 3.26 from eq. 3.23 can be found in ref. 197: the construction of an extension ($\mathbf{g}_{fa}$) of the electron propagator matrix is employed to write the following matrix equation:

$$\begin{bmatrix} E\mathbf{I} - (\mathbf{a}|\mathcal{H}\mathbf{a}) & -(\mathbf{a}|\mathcal{H}\mathbf{f}) \\ -(\mathbf{f}|\mathcal{H}\mathbf{a}) & E\mathbf{I} - (\mathbf{f}|\mathcal{H}\mathbf{f})\end{bmatrix} \begin{bmatrix}\mathbf{G}(E) \\ \mathbf{g}_{fa}\end{bmatrix} = \begin{bmatrix}\mathbf{I}_{a\times a} \\ \mathbf{0}_{a\times f}\end{bmatrix}. \tag{3.24}$$

The previous matrix equation can be exploited to write two simultaneous equations: one is used to obtain an explicit expression for $\mathbf{g}_{fa}$ and the other to derive the desired result.

Analogously, eq. 3.26 can be obtained as a particular case of the mathematical result that follows (see, for example, section 2.8 of ref. 204, particularly page 108): if $\mathbf{D}$ and $\mathbf{A} - \mathbf{B}\mathbf{D}^{-1}\mathbf{C}$ are nonsingular, then:

$$\begin{bmatrix}\mathbf{A} & \mathbf{B} \\ \mathbf{C} & \mathbf{D}\end{bmatrix}^{-1} = \begin{bmatrix} (\mathbf{A} - \mathbf{B}\mathbf{D}^{-1}\mathbf{C})^{-1} & -(\mathbf{A} - \mathbf{B}\mathbf{D}^{-1}\mathbf{C})^{-1}\mathbf{B}\mathbf{D}^{-1} \\ -\mathbf{D}^{-1}\mathbf{C}(\mathbf{A} - \mathbf{B}\mathbf{D}^{-1}\mathbf{C})^{-1} & \mathbf{D}^{-1} + \mathbf{D}^{-1}\mathbf{C}(\mathbf{A} - \mathbf{B}\mathbf{D}^{-1}\mathbf{C})^{-1}\mathbf{B}\mathbf{D}^{-1}\end{bmatrix} \tag{3.25}$$

The upper left block of eq. 3.25 is the desired result.

employing eqs. 3.28 and 3.29, the electron propagator matrix can be rewritten as follows:

$$\mathbf{G}(E) = \begin{bmatrix}\mathbf{I}_{a\times a} & \mathbf{0}_{a\times f}\end{bmatrix}\left[\mathbf{U}(E\mathbf{I}-\boldsymbol{\Omega})^{-1}\mathbf{U}^{\dagger}\right]\begin{bmatrix}\mathbf{I}_{a\times a}\\ \mathbf{0}_{a\times f}\end{bmatrix}. \tag{3.30}$$

Previous equations provide the general framework to obtain vertical energies associated with electron attachment ($A \rightarrow A^{-}$) or detachment ($A \rightarrow A^{+}$) processes. The remaining part of this section is devoted to the approximations which are needed to carry out numerical calculations aiming at the study of real molecular systems.

The level of approximation adopted is affected by various factors: among them, the choice of the reference state (or of the reference ensemble), which enters in the definition of the superoperator metric (see eq. 3.11), is an aspect of pivotal importance. The Hartree-Fock (HF) ground state is often employed as reference state, but other choices are possible, such as Kohn-Sham (KS) reference states[206], grand-canonical HF reference ensembles (allowing fractional occupation numbers of the molecular orbitals)[207] or HF reference states improved employing amplitudes from Coupled Cluster singles and doubles (CCSD) calculations[208]. A relevant approximation concerns the manifold of field operator products: in actual calculations, only a portion of the full space of ionization operators is spanned by the vector $\mathbf{h}$. A trivial choice is $\mathbf{h} = \mathbf{a}$: in this case, only the space of simple field operators is spanned by $\mathbf{h}$. The choice most frequently employed is to restrict $\mathbf{h}$ to the space of simple field operators and their triple products ($\{\mathbf{a}, \mathbf{f}_3\}$).[a]

3.1.1 The Dyson's equation

The formulation of the electron propagator matrix provided in eq. 3.26 is the Dyson's equation. Eq. 3.26 can be employed to formulate an eigenvalue problem: in this way, it is possible to give a transparent physical meaning to the terms on the RHS of eq. 3.26.

A pole of the electron propagator matrix occurs when $det[\mathbf{G}(E)]$ diverges. This condition is fulfilled if $det[\mathbf{G}^{-1}(E)] = 0$, namely a pole of the electron propagator matrix occurs when an eigenvalue of the inverse of the electron propagator matrix $\mathbf{G}^{-1}(E)$ is equal to zero. Defining the energy dependent self-energy matrix:

$$\boldsymbol{\sigma}(E) = (\mathbf{a}|\mathcal{H}\mathbf{f})\big[E\mathbf{I} - (\mathbf{f}|\mathcal{H}\mathbf{f})\big]^{-1}(\mathbf{f}|\mathcal{H}\mathbf{a}), \tag{3.31}$$

and a generalized Fock matrix:

$$\mathbf{F}^{gen} = (\mathbf{a}|\mathcal{H}\mathbf{a}), \tag{3.32}$$

[a] Extensions of $\mathbf{h}$ to the space of more complicated products of field operators have been proposed in literature.[203,209]

the inverse of the electron propagator matrix can be written as follows:

$$\mathbf{G}^{-1}(E) = E\mathbf{I} - \mathbf{F}^{gen} - \boldsymbol{\sigma}(E), \tag{3.33}$$

and a solution of the eigenvalue problem with an eigenvalue equal to zero can be formulated in the following manner:

$$\mathbf{G}^{-1}\mathbf{C}(E_{pole}) = 0\mathbf{C}(E_{pole}), \tag{3.34}$$

or, by means of eq. 3.33:

$$[E_{pole}\mathbf{I} - \mathbf{F}^{gen} - \boldsymbol{\sigma}(E_{pole})]\mathbf{C}(E_{pole}) = 0\mathbf{C}(E_{pole}). \tag{3.35}$$

Eq. 3.35 is equivalent to the following one:

$$[\mathbf{F}^{gen} + \boldsymbol{\sigma}(E_{pole})]\mathbf{C}(E_{pole}) = E_{pole}\mathbf{C}(E_{pole}); \tag{3.36}$$

in other words, a pole of the electron propagator matrix occurs when one of the eigenvalues (of the operator on the LHS of eq. 3.36) equals the energy which enters in the energy-dependent self-energy matrix $\boldsymbol{\sigma}(E)$. Therefore, the problem can be solved requiring self-consistency between one of the eigenvalues of the following eigenvalue problem and the value of E which is employed for the calculation of $\boldsymbol{\sigma}(E)$:

$$[\mathbf{F}^{gen} + \boldsymbol{\sigma}(E)]\mathbf{C} = \mathbf{C}\mathbf{E}. \tag{3.37}$$

A more explicit formulation of the elements of the generalized Fock matrix $\mathbf{F}^{gen}$ can be provided:[a]

$$F^{gen}_{rs} = (a_s|\mathcal{H}a_r) = h_{rs} + \sum_{tu}\langle rt||su\rangle\rho_{tu}. \tag{3.38}$$

In eq. 3.38, h_{rs} is a matrix element of the monoelectronic operator of the many-body hamiltonian, $\langle rt||su\rangle$ is a compact notation which is equal to $\langle rt|su\rangle - \langle rt|us\rangle$ (Coulomb minus exchange contributions) and give the contribution of Coulomb and exchange bielectronic integrals; $\boldsymbol{\rho}$ is the reference state's one-electron density matrix, with elements:

$$\rho_{tu} = \left\langle \phi_0^{N_{el}} \middle| a_t^\dagger a_u \middle| \phi_0^{N_{el}} \right\rangle. \tag{3.39}$$

The relationship between $\mathbf{F}^{gen}$ and $\mathbf{F}$ (the customary Fock matrix) can be easily found if $\boldsymbol{\rho}$ is partitioned as follows:

$$\boldsymbol{\rho} = \boldsymbol{\rho}^{HF} + \boldsymbol{\rho}^{corr} \tag{3.40}$$

and eq. 3.38 is rewritten in the canonical, HF orbital basis:

[a] The derivation of eq. 3.38 requires the evaluation of the elements of the $(\mathbf{a}|\mathcal{H}\mathbf{a})$ block of the superoperator hamiltonian matrix, and is provided in section C.2 of appendix C.

$$F_{rs}^{gen} = \varepsilon_r \delta_{rs} + \sum_{tu} \langle rt||su\rangle \rho_{tu}^{corr}. \tag{3.41}$$

Therefore, if $\boldsymbol{\rho} = \boldsymbol{\rho}^{HF}$ (which means that $\boldsymbol{\rho}^{corr} = 0$) the relationship $F_{rs}^{gen} = \varepsilon_r \delta_{rs} = F_{rs}$ holds. $\boldsymbol{\rho}^{corr}$ is the correlation contribution to the one-electron density matrix and accounts for non-vanishing contributions to off-diagonal elements of the $\mathbf{F}^{gen}$ matrix and for corrections to the HF orbital energies (ε_r) in the diagonal elements. If the elements of the energy-independent (or constant) contribution to the total self-energy matrix $\boldsymbol{\Sigma}(\infty)$ are defined in the following manner:[a]

$$\Sigma_{rs}(\infty) = \sum_{tu} \langle rt||su\rangle \rho_{tu}^{corr}, \tag{3.42}$$

Defining the total self-energy matrix as the sum of the constant (eq. 3.42) and the energy-dependent (eq. 3.31) contributions previously defined:

$$\boldsymbol{\Sigma}(E) = \boldsymbol{\Sigma}(\infty) + \boldsymbol{\sigma}(E), \tag{3.43}$$

eq. 3.37 can be written as a function of the customary Fock matrix $\mathbf{F}$ and of the total self-energy matrix $\boldsymbol{\Sigma}(E)$:

$$[\mathbf{F} + \boldsymbol{\Sigma}(E)]\mathbf{C} = \mathbf{CE}. \tag{3.44}$$

A possible route to the calculation of the poles of the electron propagator matrix is immediately suggested by eq. 3.44: the Fock matrix $\mathbf{F}$ can be employed in conjunction with a suitable approximation of the total self-energy matrix (an approach of this kind is discussed in the next subsection).

It can be noticed from eq. **??** that a value of $\boldsymbol{\rho}^{corr}$ which differs from zero can be employed to provide orbital energies which takes partially into account the effects of the electron correlation. In other words, writing eq. **??** in terms of occupation numbers:

$$F_{rs}^{gen} = (a_r|\mathcal{H}a_s) = h_{rs} + \sum_{t} \langle rt||st\rangle n_t, \tag{3.45}$$

an element of the customary Fock matrix F_{rs} is obtained if 1 and 0 are the occupation numbers associated, respectively, to occupied and virtual orbitals;[b] another set of occupation numbers correspond to a choice of the one-electron density matrix which differs from $\boldsymbol{\rho}^{HF}$. To improve the results obtained from the calculation of the ionization energies of a molecule, the

[a] The symbol ∞ is used to label the constant contribution to the self energy matrix because in the limit of extremely high values of E the contribution of the energy dependent part to the total self-energy matrix decrease dramatically (see eq. 3.31), i.e. if $E \to \infty$ then $\boldsymbol{\sigma}(E) \to 0$; this means that electron attachment poles at very high energies approach the eigenvalues of $\mathbf{F}^{gen}$.

[b] This choice is equivalent to the assumption $\boldsymbol{\rho} = \boldsymbol{\rho}^{HF}$

employment of the so-called transition operator method has been suggested: the set of occupation numbers employed for the customary HF equations is modified for a single occupied spin-orbital, for which an occupation number of 0.5 is adopted. Reference density matrices which are suitable to the description of this kind of "transition spin-orbital" with a fractional occupation number correspond to ensembles, and not to pure states: to carry out this kind of calculations the grand-canonical HF (GCHF) theory can be exploited. For each final state, a single GCHF calculation is carried out employing an occupation number of 0.5 for a single spin-orbital. The energy of a transition spin-orbital calculated with the transition operator method provide an initial estimate of the ionization energy which is especially useful for core electrons: this is due to the inclusion of relaxation and correlation effects which are not taken into account at zeroth-order when the customary estimate based on the Koopmans' theorem (KT) is employed.

3.1.2 Diagonal approximations of the self-energy matrix: the Outer Valence Green's Function method

The brief discussion provided in the previous subsection allows the definition of a zeroth-order electron propagator $\mathbf{G}^{(0)}(E)$:

$$\mathbf{G}^{(0)}(E) = (E\mathbf{I} - \mathbf{F})^{-1}. \tag{3.46}$$

The orbital energies of the HF approximation are the poles of $\mathbf{G}^{(0)}(E)$ (because $F_{rs} = \varepsilon_r \delta_{rs}$). Employing eqs. 3.41, 3.42, 3.43 and 3.46, it is possible to rewrite eq. 3.33 as follows:

$$\mathbf{G}^{-1}(E) = [\mathbf{G}^{(0)}(E)]^{-1} - \mathbf{\Sigma}(E). \tag{3.47}$$

Multiplying from the left $\mathbf{G}^{(0)}(E)$ and from the right $\mathbf{G}(E)$ with eq. 3.47, another formulation of the Dyson's equation is obtained:

$$\mathbf{G}(E) = \mathbf{G}^{(0)}(E) + \mathbf{G}^{(0)}(E)\mathbf{\Sigma}(E)\mathbf{G}(E). \tag{3.48}$$

Eq. 3.48 is a starting point for a perturbative treatment,[a] i.e. the total self-energy can be expanded in a perturbation series. The derivations of second and third-order contributions[b] to the total self-energy are not provided in this thesis, but their final expressions are reported for completeness.

[a] Perturbation series and recursive definitions are provided in ref. 210 (see section II A of ref. 210, more specifically eqs. 15-23).

[b] The zeroth-order contribution to the total self-energy is zero by definition,[210] and all the first-order contribution vanishes (see the beginning of chapter 9 of ref. 196, particularly eq. 9.18), i.e. $\Sigma^{(1)}_{rs}(E) = 0$.

The matrix elements of the second-order contribution to the total self-energy matrix can be written as follows:[a]

$$\Sigma^{(2)}_{rs}(E) = \overbrace{\frac{1}{2}\sum_{a,i,j}\left[\frac{\langle ra||ij\rangle\langle ij||sa\rangle}{E+\varepsilon_a-\varepsilon_i-\varepsilon_j}\right]}^{2hp} + \overbrace{\frac{1}{2}\sum_{i,a,b}\left[\frac{\langle ri||ab\rangle\langle ab||si\rangle}{E+\varepsilon_i-\varepsilon_a-\varepsilon_b}\right]}^{2ph}. \quad (3.49)$$

In eq. 3.49, r and s denote orbitals with unspecified occupancy, i and j denote occupied orbitals and a and b denote virtual orbitals; the terms collected in the first summation (over two occupied and one virtual indices) on the RHS of eq. 3.49 provide the so-called two holes - one particle ($2hp$) contribution, while the terms collected in the second summation (over two virtual and one occupied indices) provide the two particles - one hole ($2ph$) contribution.

In the case of outer-valence binding energies and electron affinities of closed-shell molecules a diagonal approximation to the total self-energy matrix is often adopted (i.e. the off-diagonal elements of the total self-energy matrix are neglected). This approximation reduces the pole search to a solution of the following simplified form of eq. 3.47:[b]

$$G^{-1}_{rr}(E) = E - \varepsilon_r - \Sigma_{rr}(E) = 0, \quad (3.50)$$

or, equivalently:

$$E = \varepsilon_r + \Sigma_{rr}(E). \quad (3.51)$$

Eq. 3.51 can be iterated with respect to E in order to calculate a pole.

The results obtained employing eq. 3.51 are affected by the level of approximation chosen for the diagonal elements of $\mathbf{\Sigma}(E)$. If $\Sigma_{rr}(E) \approx \Sigma^{(2)}_{rr}(E)$ in eq. 3.51, the so-called second-order diagonal approximation (D2) is found. Analogously, when $\Sigma_{rr}(E) \approx \Sigma^{(3)}_{rr}(E)$ the third-order diagonal approximation (D3) is adopted. The third-order contribution to the diagonal elements of the total self-energy matrix can be formulated in the following manner:[c]

[a] A derivation of eq. 3.49 based on superoperator algebra can be found at the beginning of chapter 9 (see in particular eqs. 9.19-9.27) of ref. 196; for the diagrammatic derivation see section II B of ref. 210: in the same reference[210] (see appendix A1) a purely algebraic (and extensible to any order) derivation is explicitly provided.

[b] Avoiding the solution of the eigenvalue problem introduced in eqs. 3.37 and 3.44.

[c] An attempt to include all the corrections up to the third order for electron affinities and ionization potentials in the context of the so-called equation of motion method (closely related to the approaches based on one electron Green's functions) can be found in ref. 211; the final expression given in ref. 211 was integrated with other terms in a communication by Purvis and Öhrn[212] in which the complete result is provided for the first time; a general (and lengthy) expression for $\Sigma^{(3)}_{rs}(E)$ (the matrix element of the third-order contribution to $\mathbf{\Sigma}(E)$) is provided (to the best of the author's knowledge, for the first time) in ref. 213;

$$\Sigma^{(3)}_{rr}(E) = \overbrace{\sum_{aij}\left[\frac{(W_{raij}+\frac{1}{2}Y_{raij}(E))\langle ra||ij\rangle}{E+\varepsilon_a-\varepsilon_i-\varepsilon_j}\right]}^{2hp} + \underbrace{\sum_{iab}\left[\frac{(W_{riab}+\frac{1}{2}Y_{riab}(E))\langle ri||ab\rangle}{E+\varepsilon_i-\varepsilon_a-\varepsilon_b}\right]}_{2ph} + \Sigma^{(3)}_{rr}(\infty), \tag{3.52}$$

where:

$$W_{raij} = \langle ra||ij\rangle + \frac{1}{2}\sum_{bc}\left[\frac{\langle ra||bc\rangle\langle bc||ij\rangle}{\varepsilon_i+\varepsilon_j-\varepsilon_b-\varepsilon_c}\right] + (1-\hat{P}_{ij})\sum_{bk}\left[\frac{\langle rk||bi\rangle\langle ba||jk\rangle}{\varepsilon_j+\varepsilon_k-\varepsilon_a-\varepsilon_b}\right], \tag{3.53}$$

$$Y_{raij}(E) = -\frac{1}{2}\sum_{kl}\left[\frac{\langle ra||kl\rangle\langle kl||ij\rangle}{E+\varepsilon_a-\varepsilon_k-\varepsilon_l}\right] - (1-\hat{P}_{ij})\sum_{bk}\left[\frac{\langle rb||jk\rangle\langle ak||bi\rangle}{E+\varepsilon_b-\varepsilon_j-\varepsilon_k}\right], \tag{3.54}$$

$$W_{riab} = \langle ri||ab\rangle + \frac{1}{2}\sum_{jk}\left[\frac{\langle ri||jk\rangle\langle jk||ab\rangle}{\varepsilon_j+\varepsilon_k-\varepsilon_a-\varepsilon_b}\right] + (1-\hat{P}_{ab})\sum_{jc}\left[\frac{\langle rc||ja\rangle\langle ji||bc\rangle}{\varepsilon_i+\varepsilon_j-\varepsilon_b-\varepsilon_c}\right], \tag{3.55}$$

$$Y_{riab}(E) = \frac{1}{2}\sum_{cd}\left[\frac{\langle ri||cd\rangle\langle cd||ab\rangle}{E+\varepsilon_i-\varepsilon_c-\varepsilon_d}\right] + (1-\hat{P}_{ab})\sum_{jc}\left[\frac{\langle rj||bc\rangle\langle ic||ja\rangle}{E+\varepsilon_j-\varepsilon_b-\varepsilon_c}\right], \tag{3.56}$$

$$\Sigma^{(3)}_{rr}(\infty) = \sum_{tu}\langle rt||ru\rangle\rho^{(2)}_{tu}; \tag{3.57}$$

$\hat{P}_{ab}$ and $\hat{P}_{ij}$ are spin-orbital permutation operators. Eq. 3.52 includes (through the first term on the RHS of eqs. 3.53 and 3.55) the second-order contribution to the diagonal elements of the self-energy ($\Sigma^{(2)}_{rr}(E)$) and an approximation to the diagonal elements of the constant self-energy contribution (eq. 3.57) which requires the knowledge of the second-order corrections to the one-electron density matrix ($\rho^{(2)}_{tu}$).

the compact formulation adopted in this thesis to account for the third order corrections in the diagonal terms of $\mathbf{\Sigma}(E)$ is provided in ref. 214 (see in particular eq. 4.2 of ref. 214).

The physical meaning of the contributions to $\Sigma_{rr}^{(2)}(E)$ and $\Sigma_{rr}^{(3)}(E)$ can be recovered in terms of relaxation and correlation contributions to the estimation of the ionization energy provided by the KT.

For what concern closed shell molecules, poles calculated by means of eq. 3.51 generally overestimate corrections to HF orbital energies when the D2 approximation is employed and underestimate these corrections when the D3 approximation is chosen. Therefore, computational results obtained employing D2 and D3 approximations generally bracket the experimental results: this observation has been employed to devise an improved approximation of $\Sigma_{rr}(E)$ without requiring a relevant, additional computational effort. The essential idea behind the Outer Valence Green's Function (OVGF) method[a] is to scale the third-order corrections to the diagonal terms of $\mathbf{\Sigma}(E)$: in this way, fourth and higher order contributions to the self-energy can be approximately recovered.

The A version of the OVGF method approximate $\Sigma_{rr}(E)$ with the RHS of the following equation:

$$\Sigma_{rr}^{OVGF(A)}(E) = \Sigma_{rr}^{(2)}(E) + \frac{1}{1 + X_r^A}\left[\Sigma_{rr}^{(3)}(E) - \Sigma_{rr}^{(2)}(E)\right], \tag{3.58}$$

where the scaling factor X_r^A is defined as follows:

$$X_r^A = -2\left[\overbrace{\frac{1}{2}\sum_{aij}\left(\frac{\langle ra||ij\rangle W_{raij}}{E + \varepsilon_a - \varepsilon_i - \varepsilon_j}\right)}^{2hp} + \overbrace{\frac{1}{2}\sum_{iab}\left(\frac{\langle ri||ab\rangle W_{riab}}{E + \varepsilon_i - \varepsilon_a - \varepsilon_b}\right)}^{2ph}\right]\left[\Sigma_{rr}^{(2)}(E)\right]^{-1}. \tag{3.59}$$

Despite its usefulness, eq. 3.58 depends on the value assumed by the scaling factor X_r^A: if $|X_r^A| < 1$, the multiplicative factor in the second term of the RHS of eq. 3.58 is the result of a geometric convergent series; otherwise eq. 3.58 can lead to unreliable results. Generally the condition $|X_r^A| < 1$ is fulfilled, because the second-order contribution to the self-energy is greater than the third-order one. However, when the second-order contribution is particularly small[b] an alternative formulation to eq. 3.58 is needed.

In the B version of the OVGF method two distinct scaling factors (instead of one) are employed:

[a] This method was formulated in ref. 215 and explicit formulas are given in appendix C of ref. 216; it must be underlined that in the formulas for second- and third-order corrections to the self-energy provided in appendix C of ref. 216 the summation over the spins (differently from what has been done in this thesis and in other references) is already carried out (for a closed shell system, the convention adopted in appendix C of ref. 216 is often preferred).

[b] For example, this is possible when KT provides a result in excellent agreement with the experimental value.

$$\Sigma_{rr}^{OVGF(B)}(E) = \Sigma_{rr}^{(2)}(E) + \Sigma_{rr}^{(3)}(\infty) + \frac{\Sigma_{rr}^{(3-2hp)}(E) - \Sigma_{rr}^{(2-2hp)}(E)}{1 + X_r^{2hp}} + \frac{\Sigma_{rr}^{(3-2ph)}(E) - \Sigma_{rr}^{(2-2ph)}(E)}{1 + X_r^{2ph}}, \tag{3.60}$$

where:

$$X_r^{2hp} = -\left[\sum_{aij}\left(\frac{\langle ra||ij\rangle W_{raij}}{E + \varepsilon_a - \varepsilon_i - \varepsilon_j}\right)\right]\left[\Sigma_{rr}^{(2-2hp)}(E)\right]^{-1}, \tag{3.61}$$

$$X_r^{2ph} = -\left[\sum_{iab}\left(\frac{\langle ri||ab\rangle W_{riab}}{E + \varepsilon_i - \varepsilon_a - \varepsilon_b}\right)\right]\left[\Sigma_{rr}^{(2-2ph)}(E)\right]^{-1}. \tag{3.62}$$

In eq. 3.60, the three components $\Sigma_{rr}^{(3)}(\infty)$, $2hp$ and $2ph$ of the third-order contribution to the self-energy are treated separately. $2hp$ and $2ph$ components are scaled (with two different scaling factors), while the energy independent component is left unscaled.[a] Despite the partition of the third-order contribution to the self-energy and the energy independent component left unaltered, the reliability of eq. 3.60 depends on conditions similar to the one already encountered in the analysis of eq. 3.58: $|X_r^{2hp}| < 1$ and $|X_r^{2ph}| < 1$. If the $2hp$ and $2ph$ components of $\Sigma_{rr}^{(2)}(E)$ are (each one individually) too small, an alternative formulation (the C version of the OVGF method) can be employed:

$$\Sigma_{rr}^{OVGF(A)}(E) = \Sigma_{rr}^{(2)}(E) + \frac{1}{1 + X_r^C}\left[\Sigma_{rr}^{(3)}(E) - \Sigma_{rr}^{(2)}(E)\right], \tag{3.63}$$

where:

$$X_r^C = \frac{X_r^{2hp}\left[\Sigma_{rr}^{(3-2hp)}(E) - \Sigma_{rr}^{(2-2hp)}(E)\right] + X_r^{2ph}\left[\Sigma_{rr}^{(3-2ph)}(E) - \Sigma_{rr}^{(2-2ph)}(E)\right]}{\left[\Sigma_{rr}^{(3-2hp)}(E) - \Sigma_{rr}^{(2-2hp)}(E)\right] + \left[\Sigma_{rr}^{(3-2ph)}(E) - \Sigma_{rr}^{(2-2ph)}(E)\right]}. \tag{3.64}$$

Eq. 3.63 is formally equivalent to eq. 3.58: the only difference between the two formulations lies in the definition of the scaling factors.[b].

[a] An energy independent component is absent in the second-order contribution, i.e. $\mathbf{\Sigma}^{(2)}(E) = \boldsymbol{\sigma}^{(2)}(E)$.

[b] It must be noticed that the definition of the scaling factor X_r^C provided in ref. 197 is wrong; the formulation provided in this thesis is the correct one (as can be easily verified from other references, see for example eq. C.30 of ref. 216).

A selection procedure[217] based on a series of numerical criteria[a] was devised with the aim of select the best version of the OVGF method for the calculation of each pole. This selection procedure was implemented in the Gaussian[12] suite of programs and has been employed for the calculation of the results provided in section 3.3 of this chapter.

The reliability of the results calculated with the OVGF method are often evaluated on the basis of the derivative of the corresponding diagonal element of $\mathbf{\Sigma}(E)$ with respect to the energy; this quantity enters in the definition of the pole strength which can be written as follows:

$$\mathscr{P}_r = \left[1 - \frac{d\Sigma_{rr}(E)}{dE}\right]^{-1}. \tag{3.65}$$

A value of $\mathscr{P}_r$ which is greater than 0.85 has been proposed[218] as an approximate standard of validity for the calculation of ionization energies (or electron affinities) when the OVGF method is employed.[b] $\mathscr{P}_r$ can be also employed as an estimate of the relative intensities of the transitions experimentally probed through the measurement of UPS spectra.

3.1.3 The non-diagonal renormalized second-order approximation

The limited computational cost of the diagonal approximations introduced in the previous subsection have boosted their employment for the calculation of ionization energies and electron affinities, particularly for what concerns the OVGF method.[c] Despite the success of this approach, the employment of the diagonal approximation leads to the assumption of a quasiparticle picture[d] which is known to be unable to account for some experimental signals, even qualitatively.[222,223] To deal with the breakdown of the molecular orbital picture, a non-diagonal approximation must be employed.

When a non-diagonal approximation is employed, poles of the electron propagator matrix are generally calculated solving the eigenvalue problem associated to the superoperator hamiltonian matrix $\boldsymbol{\mathcal{H}}$ (see eq. 3.28). In contrast with other non-diagonal approximations such as the ADC(3) (third-order algebraic diagrammatic construction),[216] in the non-diagonal, renor-

[a] These criteria involves the magnitude of each scaling factor, the magnitude of the second-order contribution to the diagonal elements of $\mathbf{\Sigma}(E)$ and the calculated value of the pole.

[b] A value of $\mathscr{P}_r \geqslant 0.85$ corresponds to an absolute value of $\frac{d\Sigma_{rr}(E)}{dE}$ which is extremely small (these values are always negatives): the essential point is that the self-energy itself has poles, and the assumptions behind the OVGF method are valid only far from those poles (as is the case when the absolute value of $\frac{d\Sigma_{rr}(E)}{dE}$ is small).[216]

[c] These methods are widely employed by many experimentalists for the assignment of UPS experimental spectra (see, for example, refs. 219–221), due to their implementation in a popular commercial software.[12]

[d] In other words, the molecular orbital picture is retained.

malized second-order (NR2)[224] approximation[a] the third-order terms in $\mathbf{\Sigma}(E)$ are only partially retained. The search of a good compromise between accuracy and efficiency leads to an inclusion of the third-order contribution which is limited to the corrections needed to provide a reliable estimate of the observables of interest.

In the NR2 approximation, for the calculation of ionization energies the following superoperator metric is adopted:[b]

$$(X|Y) = \left\langle \phi_{HF}^{N_{el}} \middle| \left[X^\dagger, Y\right]_+ (1 + T_2^{(1)}) \middle| \phi_{HF}^{N_{el}} \right\rangle . \tag{3.66}$$

In eq. 3.66, $T_2^{(1)}$ stands for the first-order correction in the Rayleigh-Schröedinger perturbation theory (RSPT).[c] Only the portion $\{\mathbf{a}, \mathbf{f}_3\}$ of the full space of field operators is employed, i.e. the operator manifold is restricted to h (hole), p (particle), $2hp$ (shakeup) and $2ph$ (shakeon) operators. $\boldsymbol{\mathcal{H}}$ can be written as follows (in the canonical, HF basis):

$$\begin{aligned} \boldsymbol{\mathcal{H}} &= \begin{bmatrix} (\mathbf{a}_h|\mathcal{H}\mathbf{a}_h) & (\mathbf{a}_h|\mathcal{H}\mathbf{a}_p) & (\mathbf{a}_h|\mathcal{H}\mathbf{a}_{2hp}) & (\mathbf{a}_h|\mathcal{H}\mathbf{a}_{2ph}) \\ (\mathbf{a}_p|\mathcal{H}\mathbf{a}_h) & (\mathbf{a}_p|\mathcal{H}\mathbf{a}_p) & (\mathbf{a}_p|\mathcal{H}\mathbf{a}_{2hp}) & (\mathbf{a}_p|\mathcal{H}\mathbf{a}_{2ph}) \\ (\mathbf{a}_{2hp}|\mathcal{H}\mathbf{a}_h) & (\mathbf{a}_{2hp}|\mathcal{H}\mathbf{a}_p) & (\mathbf{a}_{2hp}|\mathcal{H}\mathbf{a}_{2hp}) & (\mathbf{a}_{2hp}|\mathcal{H}\mathbf{a}_{2ph}) \\ (\mathbf{a}_{2ph}|\mathcal{H}\mathbf{a}_h) & (\mathbf{a}_{2ph}|\mathcal{H}\mathbf{a}_p) & (\mathbf{a}_{2ph}|\mathcal{H}\mathbf{a}_{2hp}) & (\mathbf{a}_{2ph}|\mathcal{H}\mathbf{a}_{2ph}) \end{bmatrix} \\ &\approx \begin{bmatrix} \varepsilon\delta_{ij} & 0 & \boldsymbol{\mathcal{H}}^{(1)}_{h,2hp} & \boldsymbol{\mathcal{H}}^{(1)}_{h,2ph} \\ 0 & \varepsilon\delta_{ab} & \boldsymbol{\mathcal{H}}^{(1)}_{p,2hp} & \boldsymbol{\mathcal{H}}^{(1)}_{p,2ph} \\ \boldsymbol{\mathcal{H}}^{(2)}_{2hp,h} & \boldsymbol{\mathcal{H}}^{(1)}_{2hp,p} & \boldsymbol{\mathcal{H}}^{(1)}_{2hp,2hp} & 0 \\ \boldsymbol{\mathcal{H}}^{(1)}_{2ph,h} & \boldsymbol{\mathcal{H}}^{(1)}_{2ph,p} & 0 & \boldsymbol{\mathcal{H}}^{(0)}_{2ph,2ph} \end{bmatrix} . \end{aligned} \tag{3.67}$$

When the NR2 approximation is employed, the matrix $\boldsymbol{\mathcal{H}}$ is not hermitian. Therefore, the ionization energies are obtained as eigenvalues of the matrix $\frac{1}{2}(\boldsymbol{\mathcal{H}} + \boldsymbol{\mathcal{H}}^\dagger)$. The energy-independent contribution $\mathbf{\Sigma}(\infty)$ vanishes in eq. 3.67, because $\mathbf{\Sigma}(\infty)$ arises from correlation terms in the primary-primary block $(\mathbf{a}|\mathcal{H}\mathbf{a})$ which are neglected in the NR2 approximation.[d] More generally, the final expression provided in eq. 3.67 is complete (and hermitian) for what concerns the second-order contribution, while the third-order corrections are limited to the terms $\boldsymbol{\mathcal{H}}^{(2)}_{2hp,h}$ and $\boldsymbol{\mathcal{H}}^{(1)}_{2hp,2hp}$. The elements of eq. 3.67

[a] The NR2 approximation is a non-diagonal counterpart of the Partial third-order (P3) method.[225]

[b] For the calculation of electron affinities, a different superoperator metric is employed (in order to provide the second-order contribution of the block $(\mathbf{a}_{2ph}|\mathcal{H}\mathbf{a}_p)$ and the first-order contribution of the block $(\mathbf{a}_{2hp}|\mathcal{H}\mathbf{a}_h)$, in contrast with the final result provided in eq. 3.67 and used for the calculation of ionization energies, in which the opposite choice is done).

[c] The subscript stands for the contribution of the double excitations to the first-order correction.

[d] The derivation of the contributions to the block $(\mathbf{a}|\mathcal{H}\mathbf{a})$ in the framework of the NR2 approximation is provided in section C.2 of appendix C.

which pertains to the blocks $(\mathbf{a}|\mathcal{H}\mathbf{f}_3)$, $(\mathbf{f}_3|\mathcal{H}\mathbf{a})$ and $(\mathbf{f}_3|\mathcal{H}\mathbf{f}_3)$ are provided in ref. 224.[a] Details about the implementation of non-diagonal approximations to the calculation of poles of the electron propagator matrix can be found elsewhere.[226]

Assessments[227] of the results obtained when the NR2 approximation is employed in conjunction with various basis sets suggest the usefulness of this approximation for the calculation of valence vertical ionization energy of closed-shell molecules.[b]

When a non-diagonal approximation is employed, the knowledge of the eigenvectors of $\boldsymbol{\mathcal{H}}$ allows the calculation of the pole strength $\mathscr{P}_n$ associated to a specific ionization energy. The definition of $\mathscr{P}_n$ given in eq. 3.65 can be generalized as follows:[c]

$$\mathscr{P}_n = \sum_r |U_{nr}|^2 \tag{3.68}$$

When a non-diagonal approximation is employed, the calculation of $\mathscr{P}_n$ must be performed with the definition provided in eq. 3.68 (more general than the simplified one given in eq. 3.65, which is correct if a diagonal approximation is assumed). Analogously to the case of a diagonal approximation, $\mathscr{P}_n$ can be related to the intensity associated to a specific ionization energy.

3.2 Vibronic transitions: the time-independent approach

In order to reproduce the band shapes observed when an electronic transition is experimentally probed, the nuclear motion of the molecular system under investigation must be taken into account. This means that a suitable approximation to the following transition integral must be employed:

$$\langle \boldsymbol{\mathscr{T}} \rangle_{IF}^{if} = \frac{\left\langle \psi_{Ii} \middle| \hat{\boldsymbol{\mathscr{T}}}(\mathbf{r}) \middle| \psi_{Ff} \right\rangle}{\sqrt{\langle \psi_{Ii} \,|\, \psi_{Ii} \rangle \langle \psi_{Ff} \,|\, \psi_{Ff} \rangle}}. \tag{3.69}$$

Eq. 3.69 is a generalization of eq. 2.35 to the case $I \neq F$ (when $I = F$, eq. 2.35 is recovered). I and F (i and f) label the electronic (nuclear) states. Defining $\boldsymbol{\mathscr{T}}_{IF}^{e}$ as follows:

[a] More specifically, elements and formulae for all the blocks of eq. 3.67 are given in table I of ref. 224, where a typographical error should be pointed out: the term $\boldsymbol{\mathcal{H}}^{(2)}_{2hp,p}$ given in table I of ref. 224 is actually the term $\boldsymbol{\mathcal{H}}^{(2)}_{2hp,h}$ (the contribution of the block $(\mathbf{a}_{2hp}|\mathcal{H}\mathbf{a}_p)$ is included only at first-order in the NR2 approximation).

[b] Improvements of the original NR2 approximation to treat particularly challenging systems have been proposed[228] (one of this improvements is based on the retainment of the second-order contribution to the block $(\mathbf{a}_{2hp}|\mathcal{H}\mathbf{a}_{2hp})$, i.e. on the substitution of $\boldsymbol{\mathcal{H}}^{(1)}_{2hp,2hp}$ with $\boldsymbol{\mathcal{H}}^{(2)}_{2hp,2hp}$ in eq. 3.67).

[c] U_{nr} is a component of the n-th eigenvector of $\boldsymbol{\mathcal{H}}$, see eq. 3.28.

$$\boldsymbol{\mathscr{T}}^{e}_{IF}(\mathbf{r}) = \left\langle \phi_I \left| \hat{\boldsymbol{\mathscr{T}}}(\mathbf{r}) \right| \phi_F \right\rangle, \tag{3.70}$$

and if the orthonormality of the electronic wavefunctions is assumed, eq. 3.69 can be rewritten in the following manner:

$$\langle \boldsymbol{\mathscr{T}} \rangle^{if}_{IF} = \frac{\left\langle \chi_{Ii} \left| \boldsymbol{\mathscr{T}}^{e}_{IF}(\mathbf{r}) \right| \chi_{Ff} \right\rangle}{\sqrt{\langle \chi_{Ii} \,|\, \chi_{Ii} \rangle \langle \chi_{Ff} \,|\, \chi_{Ff} \rangle}}. \tag{3.71}$$

The nuclear wavefunctions of each electronic state are orthonormal if the harmonic approximation is assumed; translations and (assuming an Eckart frame) rotations can be factored out; therefore, at harmonic level eq. 3.71 can be furtherly simplified:

$$\langle \boldsymbol{\mathscr{T}} \rangle^{if}_{IF} = \left\langle \chi_{Ii} \left| \boldsymbol{\mathscr{T}}^{e}_{IF}(\mathbf{r}) \right| \chi_{Ff} \right\rangle. \tag{3.72}$$

In what follows, the calculation of $\langle \boldsymbol{\mathscr{T}} \rangle^{if}_{IF}$ (the transition probability between two vibrational levels) is addressed, assuming the availability of a method to perform the calculation of $\boldsymbol{\mathscr{T}}^{e}_{IF}$ at a specific molecular geometry. With an efficient method for the calculation of $\langle \boldsymbol{\mathscr{T}} \rangle^{if}_{IF}$, the vibrational signature of the electronic transition $I \rightarrow F$ can be easily recovered from the spectral lineshape $L(\nu)$. If a time-independent (TI) approach is adopted, $L(\nu)$ is provided by the following sum-over-states (SOS) expression:

$$L(\nu) = \sum_i \sum_f \rho_{Ii}(T) |\langle \boldsymbol{\mathscr{T}} \rangle^{if}_{IF}|^2 \delta\left(\nu - \frac{E^f_F - E^i_I}{\hbar} \right), \tag{3.73}$$

where $\rho_{Ii}(T)$ is the Boltzmann population of the vibrational state χ_{Ii}. In this section, an efficient computational procedure for the calculation of $L(\nu)$ is briefly outlined and discussed.

3.2.1 Calculation of $L(\nu)$

Normal coordinates can be employed for the description of vibrational motions of a molecular system. If two different electronic states are taken into account, two different sets of normal coordinates can be adopted (because the optimized geometry and the corresponding harmonic force field depend on the electronic state). Nevertheless, two different sets of normal coordinates (pertaining to the same molecule with different minimum geometries and harmonic force fields) can be related through a linear transformation (due to Duschinsky):[229]

$$\overline{\mathbf{Q}} = \mathbf{J}\overline{\overline{\mathbf{Q}}} + \mathbf{K}. \tag{3.74}$$

In eq. 3.74, $\mathbf{J}$ is a square matrix of dimensions $(3N-6) \times (3N-6)$ (the Duschinsky matrix), $\mathbf{K}$ is a vector with $3N-6$ elements (the shift vector),

$\overline{\mathbf{Q}}$ and $\overline{\overline{\mathbf{Q}}}$ are the normal coordinates obtained for, respectively, the initial and the final (I and F) electronic states. The vibrational subspace spanned by a set of $3N-6$ normal modes depends on the optimized geometry of the molecular system, which in turn depends on the electronic state. As a consequence, vibrational subspaces spanned by $\overline{\mathbf{Q}}$ and $\overline{\overline{\mathbf{Q}}}$ are different,[a] and therefore the relationship given in eq. 3.74 is an approximation.[230,231] In practice, eq. 3.74 is a good approximation for semi-rigid molecular systems[b] but can be inadequate when applied to the study of flexible ones. Eq. 3.74 is also affected by the choice of the coordinate system.[c]

Suitable approximations of the PESs of initial and final electronic states must be chosen in order to define $\mathbf{J}$ and $\mathbf{K}$ in eq. 3.74. In this chapter, the harmonic expansion is employed for both the PESs. This assumption provides reliable results for semi-rigid molecular systems. Four approximations have been devised:

- Adiabatic hessian (AH) model: in this case, the expansion of both the PESs is performed about their own minima. Given the following definitions for the two sets of normal coordinates:[d]

$$\overline{\mathbf{Q}} = \overline{\mathbf{L}}(\mathbf{r} - \overline{\mathbf{r}}_{eq}), \tag{3.75}$$

$$\overline{\overline{\mathbf{Q}}} = \overline{\overline{\mathbf{L}}}(\mathbf{r} - \overline{\overline{\mathbf{r}}}_{eq}), \tag{3.76}$$

  The following relationship can be easily obtained employing eqs. 3.75 and 3.76:[e]

$$\overline{\mathbf{Q}} = \overline{\mathbf{L}}\overline{\overline{\mathbf{L}}}^{T}\overline{\overline{\mathbf{Q}}} + \overline{\mathbf{L}}(\overline{\overline{\mathbf{r}}}_{eq} - \overline{\mathbf{r}}_{eq}). \tag{3.77}$$

[a] because the two sets of normal coordinates pertain to two different electronic states, whose minima are associated with different geometries.

[b] Because the differences between the optimized geometries of the two electronic states are expected to be small.

[c] In two ways; firstly, because the choice of the reference coordinates affects the coupling between rotations and vibrations: in the applications given in the next section, the Eckart frame has been adopted for the equilibrium geometry of the initial electronic state I, while the equilibrium geometry of the final electronic state F has been oriented in order to maximize the overlap with the first one; secondly, the coordinate system adopted for the definition of the two sets of normal coordinates affects the computational results even at harmonic level in the case of vibronic transitions: in this thesis, cartesian-based normal coordinates are employed, but the definition of normal coordinates in terms of a set of curvilinear, internal coordinates has been proposed, implemented and tested and improves the reliability of the computational results when flexible molecular systems are investigated.

[d] The normal coordinates $\mathbf{Q}$ are mass-weighted, therefore in eqs. 3.75 and 3.76 the RHS contain a multiplication with $\mathbf{M}^{1/2}$ which is left implicit.

[e] The following relationship holds: $\mathbf{L}^T\mathbf{L} = \mathbf{I}$; see ref. 34.

The definition of $\mathbf{J}$ and $\mathbf{K}$ in the AH model can be obtained through comparison of eqs. 3.74 and 3.77:

$$\mathbf{J} = \overline{\mathbf{L}}\overline{\overline{\mathbf{L}}}^{T}, \tag{3.78}$$

$$\mathbf{K} = \overline{\mathbf{L}}(\overline{\overline{\mathbf{r}}}_{eq} - \overline{\mathbf{r}}_{eq}). \tag{3.79}$$

The AH model provides a good description of the final state's PES in the neighborhood of the minimum, but the most intense transitions are localized in the neighborhood of the initial state's minimum. Therefore, a model focused on the description of both the PESs in the neighborhood of the initial state's minimum can improve the accuracy of the computational results if the equilibrium geometries of the initial and the final electronic states differ significantly.

- Adiabatic Shift (AS) model: in this approximation, the definition of $\mathbf{K}$ is the same provided for the AH model (see eq. 3.79); for what concerns $\mathbf{J}$, in the AS model the assumption $\mathbf{J} = \mathbf{I}$ is done: this simplifying assumption is particularly useful when the analytic second derivatives of the energy with respect to the nuclear coordinates are not available for the final electronic state; therefore, the additional assumption of the AS model is the retainment of vibrational energies and normal mode's displacements calculated for the initial electronic state as approximations of vibrational energies and normal mode's displacements for the final electronic state.

- Vertical Hessian (VH) model: in this approach, the PES of the final electronic state is expanded at the equilibrium geometry of the initial electronic state. To derive the formulations of $\mathbf{J}$ and $\mathbf{K}$, the harmonic expansion of the final state's PES at its minimum is formulated as follows:

$$\overline{\overline{V}}(\overline{\overline{\mathbf{Q}}}) = \frac{1}{2}\overline{\overline{\mathbf{Q}}}^{T}\overline{\overline{\boldsymbol{\omega}}}^{2}\overline{\overline{\mathbf{Q}}} + E^{0}_{I-F} \tag{3.80}$$

where E^{0}_{I-F} is the difference between the minimum energies of the initial and the final electronic states and $\overline{\overline{\boldsymbol{\omega}}}$ is a diagonal matrix whose elements are the harmonic frequencies of the final electronic state. Eq. 3.80 can be rewritten as a function of $\overline{\mathbf{Q}}$ employing eq. 3.74:[a]

$$\overline{\overline{V}}(\overline{\mathbf{Q}}) = \frac{1}{2}\overline{\mathbf{Q}}^{T}\mathbf{J}\overline{\overline{\boldsymbol{\omega}}}^{2}\mathbf{J}^{T}\overline{\mathbf{Q}} - \mathbf{K}^{T}\mathbf{J}\overline{\overline{\boldsymbol{\omega}}}^{2}\mathbf{J}^{T}\overline{\mathbf{Q}} + \frac{1}{2}\mathbf{K}^{T}\mathbf{J}\overline{\overline{\boldsymbol{\omega}}}^{2}\mathbf{J}^{T}\mathbf{K} + E^{0}_{I-F} \tag{3.81}$$

[a] The Duschinsky matrix $\mathbf{J}$ is an orthogonal matrix, therefore $\mathbf{J}^{T}\mathbf{J} = \mathbf{I}$ and eq. 3.74 can be written as follows: $\mathbf{J}^{T}\overline{\mathbf{Q}} - \mathbf{J}^{T}\mathbf{K} = \overline{\overline{\mathbf{Q}}}$.

To connect $\mathbf{J}$ and $\mathbf{K}$ to the energy derivatives of the final state's PES at the equilibrium geometry of the initial state, the following expansion of $\overline{\overline{V}}$ with respect to $\overline{\mathbf{Q}}$ is employed:

$$\begin{aligned}\overline{\overline{V}}(\overline{\mathbf{Q}}) =& \overline{\overline{V}}(\overline{\mathbf{Q}}_{eq}) + \left(\frac{\partial \overline{\overline{V}}}{\partial \overline{\mathbf{Q}}}\right)^T \overline{\mathbf{Q}} + \frac{1}{2}\overline{\mathbf{Q}}^T \frac{\partial^2 \overline{\overline{V}}}{\partial \overline{\mathbf{Q}}^2}\overline{\mathbf{Q}} \\ =& \overline{\overline{V}}(\overline{\mathbf{Q}}_{eq}) + \overline{\overline{\mathbf{g}}}^T \overline{\mathbf{Q}} + \frac{1}{2}\overline{\mathbf{Q}}^T \overline{\overline{\mathbf{H}}}\overline{\mathbf{Q}},\end{aligned} \tag{3.82}$$

where $\overline{\overline{\mathbf{g}}}$ and $\overline{\overline{\mathbf{H}}}$ are, respectively, the gradient and the hessian of the final state's PES. Comparing eqs. 3.81 and 3.82, the following relationships can be obtained:

$$\overline{\overline{\mathbf{g}}} = -\mathbf{K}^T \mathbf{J} \overline{\overline{\boldsymbol{\omega}}}^2 \mathbf{J}^T \Longrightarrow \mathbf{K} = -\mathbf{J}\left[\overline{\overline{\boldsymbol{\omega}}}\right]^{-2} \mathbf{J}^T \overline{\overline{\mathbf{g}}}, \tag{3.83}$$

$$\overline{\overline{\mathbf{H}}} = \mathbf{J} \overline{\overline{\boldsymbol{\omega}}}^2 \mathbf{J}^T \Longrightarrow \overline{\overline{\mathbf{H}}}\mathbf{J} = \mathbf{J}\overline{\overline{\boldsymbol{\omega}}}^2. \tag{3.84}$$

In other words, $\mathbf{J}$ can be obtained from the eigenvalue problem associated to $\overline{\overline{\mathbf{H}}}$[a] and $\mathbf{K}$ can be calculated from $\overline{\overline{\mathbf{H}}}$ and $\overline{\overline{\mathbf{g}}}$.[b] The main drawback of the VH model lie in the evaluation of $\overline{\overline{\mathbf{H}}}$ at an extrapolated minimum of the final electronic state which is not the real one.[c] The evaluation of $\overline{\overline{\mathbf{H}}}$ at a non-stationary point can lead to unreliable (even negative) values of $\overline{\overline{\boldsymbol{\omega}}}^2$ and to inaccuracies in the components of $\mathbf{J}$. For what concerns these aspects, the AH model introduced above is clearly more reliable.

- Vertical gradient (VG) model: as for the AS model introduced above, the Duschinsky matrix $\mathbf{J}$ is assumed to be equal to the identity matrix ($\mathbf{J} = \mathbf{I}$). The PES of the final electronic state is expanded at the equilibrium geometry of the initial electronic state, as in the VH model. For what concerns the shift vector $\mathbf{K}$ the definition given in eq. 3.83 is employed, assuming $\mathbf{J} = \mathbf{I}$ and $\overline{\overline{\boldsymbol{\omega}}} = \overline{\boldsymbol{\omega}}$. Despite its limits, this model can be useful when neither second nor first derivatives of the energy with respect to the nuclear coordinates are available for the final electronic state.

[a] If the nuclear coordinates are described in terms of the normal modes of the initial electronic states $\overline{\mathbf{Q}}$.

[b] As for $\overline{\overline{\mathbf{H}}}$, if the nuclear coordinates are described in terms of $\overline{\mathbf{Q}}$.

[c] The approximation provided by the quadratic extrapolation employed in the VH model is exact in the limit of an harmonic final state's PES, which is not the case in the real world.

The definitions of **J** and **K** can be employed to perform the calculation of the transition probability between two vibrational levels. The starting point is the Taylor expansion of the transition property $\boldsymbol{\mathscr{T}}^{e}_{IF}$ with respect to a set of normal coordinates. Expanding $\boldsymbol{\mathscr{T}}^{e}_{IF}$, the RHS of eq. 3.72 can be written as follows:

$$\begin{aligned}\left\langle \overline{\chi_i} \middle| \boldsymbol{\mathscr{T}}^{e}_{IF} \middle| \overline{\overline{\chi_f}} \right\rangle = \boldsymbol{\mathscr{T}}^{e}_{IF}(\overline{\mathbf{Q}}_{eq}) \left\langle \overline{\chi_i} \middle| \overline{\overline{\chi_f}} \right\rangle + \\ \sum_{k=1}^{3N-6} \left[\left(\frac{\partial \boldsymbol{\mathscr{T}}^{e}_{IF}}{\partial \overline{Q}_k} \right)_{eq} \left\langle \overline{\chi_i} \middle| \overline{Q}_k \middle| \overline{\overline{\chi_f}} \right\rangle \right] + \\ \sum_{k=1}^{3N-6} \sum_{l=1}^{3N-6} \left[\left(\frac{\partial^2 \boldsymbol{\mathscr{T}}^{e}_{IF}}{\partial \overline{Q}_k \partial \overline{Q}_l} \right)_{eq} \left\langle \overline{\chi_i} \middle| \overline{Q}_k \overline{Q}_l \middle| \overline{\overline{\chi_f}} \right\rangle \right] + \dots \quad .\end{aligned} \tag{3.85}$$

In the Franck-Condon (FC) approximation,[232,233] the transition probability between two vibrational states is approximated with the zeroth-order term of the Taylor expansion provided in the RHS of eq. 3.85.[a] The FC approximation usually provides reliable results for calculations performed on fully-allowed transitions, but when weakly-allowed transitions or chiroptical transition properties are considered the first-order contributions should be retained. The sum of the first-order contributions to eq. 3.85[b] is the so-called Herzberg-Teller (HT)[234] term.

In the applications provided in the next section, the VG model is assumed for the calculation of **J** and **K** and the FC approximation is employed for the calculation of $\langle \boldsymbol{\mathscr{T}} \rangle^{if}_{IF}$. Therefore, suitable expressions and derivations for the inclusion of the HT term in the expansion given in eq. 3.85 are considered beyond the scope of this thesis and are not treated in what follows.

For the calculation of $\langle \boldsymbol{\mathscr{T}} \rangle^{if}_{IF}$ at FC level, an effective procedure to compute the FC overlap integrals $\left\langle \overline{\chi_i} \middle| \overline{\overline{\chi_f}} \right\rangle$ is needed. If the harmonic approximation is employed, analytical expressions for the FC overlap integrals are available in literature.[235,236] However, the direct employment of the analytical expressions to the computation of FC overlap integrals is not practical for a general implementation, because for each class of integrals a different expression must be implemented. A more practical route is based on the employment of recursion formulas:[237–239] in this case, only the analytical expression for the overlap integral of the vibrational ground states of the initial and the final electronic states $\left\langle \overline{\mathbf{0}} \middle| \overline{\overline{\mathbf{0}}} \right\rangle$ is needed. All the other FC overlap integrals can be derived with two recursion formulas. In the most general cases:

[a] i.e. only the first term on the RHS of eq. 3.85 is retained.
[b] second term on the RHS of eq. 3.85.

$$\begin{aligned}\left\langle \overline{\boldsymbol{v}} \middle| \overline{\overline{\boldsymbol{v}}} + \overline{\overline{1}}_i \right\rangle = &\sum_j \left[f_1(i,j,v_i,v_j) \left\langle \overline{\boldsymbol{v}} - \overline{1}_j \middle| \overline{\overline{\boldsymbol{v}}} \right\rangle \right] \\ &+ \sum_j \left[f_2(i,j,v_i,v_j) \left\langle \overline{\boldsymbol{v}} \middle| \overline{\overline{\boldsymbol{v}}} - \overline{\overline{1}}_j \right\rangle \right] \\ &+ f_3(i,v_i) \left\langle \overline{\boldsymbol{v}} \middle| \overline{\overline{\boldsymbol{v}}} \right\rangle ,\end{aligned} \tag{3.86}$$

$$\begin{aligned}\left\langle \overline{\boldsymbol{v}} + \overline{1}_i \middle| \overline{\overline{\boldsymbol{v}}} \right\rangle = &\sum_j \left[f_4(i,j,v_i,v_j) \left\langle \overline{\boldsymbol{v}} \middle| \overline{\overline{\boldsymbol{v}}} - \overline{\overline{1}}_j \right\rangle \right] \\ &+ \sum_j \left[f_5(i,j,v_i,v_j) \left\langle \overline{\boldsymbol{v}} - \overline{1}_j \middle| \overline{\overline{\boldsymbol{v}}} \right\rangle \right] \\ &+ f_6(i,v_i) \left\langle \overline{\boldsymbol{v}} \middle| \overline{\overline{\boldsymbol{v}}} \right\rangle .\end{aligned} \tag{3.87}$$

In eqs. 3.86 and 3.87, v_i and v_j label the number of quanta in, respectively, the modes i and j; $|\overline{\boldsymbol{v}}\rangle$ and $\left|\overline{\overline{\boldsymbol{v}}}\right\rangle$ denote products of harmonic functions in coordinates $\overline{\mathbf{Q}}$ and $\overline{\overline{\mathbf{Q}}}$, with quantum numbers given by the vectors $\overline{\boldsymbol{v}}$ and $\overline{\overline{\boldsymbol{v}}}$. Simplifications of eqs. 3.86 and 3.87 are obtained for the special (and relevant) case of the ground vibrational wavefunction of the initial electronic state $\left|\overline{\mathbf{0}}\right\rangle$.[a] Derivations of eqs. 3.86 and 3.87, as well as of an analytical expression for the $\left\langle \overline{\mathbf{0}} \middle| \overline{\overline{\mathbf{0}}} \right\rangle$ overlap integral can be found elsewhere.[b]

When the calculation of the lineshape $L(\nu)$ is performed in the TI approach, a double summation over the vibrational states of the electronic states I and F must be carried out (see eq. 3.73). The number of elements included in the two summations in a given energy range $\Delta E = E_F^f - E_I^i$ is finite: therefore, a simple computational procedure for the calculation of $L(\nu)$ can be based on the selection and calculation of all the FC overlap integrals in a preselected energy range ΔE. This procedure has been employed,[c] but lead to the evaluation of a number of overlap integrals which rise steeply with the size of the molecular system. Other strategies have been proposed:[241–244] for the applications provided in the next section of this thesis, the computational protocol implemented in the Gaussian[12] suite of programs has been employed for the selection of the FC overlap integrals. This protocol is briefly outlined in what follows.[243]

A partition of the manifold of vibrational states $\left|\overline{\overline{\boldsymbol{v}}}\right\rangle$ in different classes is introduced. Each vibrational state is assigned to a specific class on the basis of the number of oscillators whose quantum number differ from zero. The

[a] For example, in the special case $\left\langle \overline{\mathbf{0}} \middle| \overline{\overline{\boldsymbol{v}}} + \overline{\overline{1}}_i \right\rangle$ the first term on the RHS of eq. 3.86 vanishes.

[b] See, for example, refs. 237 and 238; particularly clear and easy to follow is the derivation provided in ref. 239.

[c] See, for example, ref. 240.

class of the states with n excited oscillators among the $3N-6$ normal modes of the molecular system studied is labeled C_n.[a] If the quantum number of each oscillator is limited to w,[b] the total number of states belonging to the class C_n is equal to $\mathscr{N}(N,n)\cdot w^n$, where $\mathscr{N}(N,n)$ is the number of distinguishable combinations of n oscillators (from an ensemble of $3N-6$). Each element of the various classes C_n can be associated to a FC overlap integral of the type $\langle \overline{\mathbf{0}} \,|\, \overline{\overline{\boldsymbol{v}}} \rangle$. If temperature effects are not taken into account,[c] all the non-vanishing FC overlap integrals are of the type $\langle \overline{\mathbf{0}} \,|\, \overline{\overline{\boldsymbol{v}}} \rangle$. The computation of the overlap integrals associated to the classes C_1 and C_2 up to a quantum number large enough to discard only the negligible overlap integrals is computationally cheap (the number of these overlap integrals is limited), but the number of elements pertaining to a single class increases dramatically with n: therefore, in order to limit the computational burden an effective criterium to select the overlap integrals of larger classes[d] is needed. In practice, three user-defined pre-screening factors are employed: the maximum quantum number adopted for the calculation of the overlap integrals of the class C_1, the maximum quantum number reached by both the excited modes of the overlap integrals of the class C_2, an approximate maximum of overlap integrals to be computed for a class C_n with n>2. The selection of the overlap integrals pertaining to a class C_n with $n > 2$ is performed through an estimation of their transition probability, computed with an algorithm which employs the FC overlap integrals already computed for the classes C_1 and C_2. A detailed description of the algorithm and of the entire computational protocol can be found in ref. 243. [e]

The computational protocol introduced above for the selection of the FC overlap integrals needed for the calculation of $L(\nu)$ is efficient and reliable for the study of semi-rigid molecular systems, but is somewhat arbitrary: to evaluate the reliability of the calculation performed a criterium to evaluate the convergence of the computation is needed. When the FC approximation is adopted, the convergence can be evaluated trivially on the basis of the following equation:

$$\sum_i \sum_f |\left\langle \overline{\chi_i} \,\middle|\, \overline{\overline{\chi_f}} \right\rangle|^2 = 1, \tag{3.88}$$

[a] In other words, in the manifold of vibrational states of the final electronic state F the class C_1 collects fundamentals and overtones, the class C_2 corresponds to 2-modes combinations and so on.

[b] Without fixing a maximum number of quanta for each oscillator, the number of states pertaining to a specific class C_n would be infinite.

[c] i.e. only $|\overline{\mathbf{0}}\rangle$ (the ground vibrational state of the initial electronic state) is populated; this assumption corresponds to $T = 0K$.

[d] i.e. associated to classes C_n with $n > 2$

[e] More specifically, the selection of the FC overlap integrals for $T = 0K$ is discussed in section IV of ref. 243; an extension of the algorithm to the case of finite temperatures is provided in ref. 244.

Where $|\langle\overline{\chi_i}|\overline{\overline{\chi_f}}\rangle|^2$ is the so-called Franck-Condon Factor (FCF). In other words, the sum of FCFs must tend to 1. Details and discussions about the implementation available in the Gaussian suite of programs (and employed for the calculations presented in the next section) can be found in refs. 245 and 246.

3.2.2 Calculation of relative intensities

The knowledge of the spectral lineshape $L(\nu)$ associated to an electronic transition $I \rightarrow F$ allows the calculation of the intensity[a] of the vibronic transition. For the comparison between experimental and computational results discussed in the next section, only relative values are needed.[b] The following formulation is employed:

$$\mathscr{I}(\nu) = \alpha\nu L(\nu) = \alpha\nu \sum_i \sum_f \rho_{Ii}(T) \left[\boldsymbol{\mathscr{T}}^e_{IF}(\overline{\mathbf{Q}}_{eq})\right]^2 |\langle\overline{\chi_i}|\overline{\overline{\chi_f}}\rangle|^2 \delta\left(\nu - \frac{E^f_F - E^i_I}{\hbar}\right) \tag{3.89}$$

In eq. 3.89, for the formulation of $L(\nu)$ the TI approach and the FC approximation are employed. α is a fixed proportionality constant.[c] The value of $\left[\boldsymbol{\mathscr{T}}^e_{IF}(\overline{\mathbf{Q}}_{eq})\right]^2$ is obtained from the electronic calculations, and depends on the phenomenon of interest.

It must be underlined that the theoretical framework introduced in this section is general, i.e. not limited to absorption/emission or photoionization spectroscopies: with a suitable choice of $\left[\boldsymbol{\mathscr{T}}^e_{IF}(\overline{\mathbf{Q}}_{eq})\right]^2$, the vibrational signatures associated to the electronic transition $I \rightarrow F$ can be computationally simulated with eq. 3.89.[d]

3.3 Applications ¶

The computational protocols introduced in the previous sections of this chapter can be employed to reproduce vibrationally resolved UPS spectra of semi-rigid molecular systems.

[a] The word 'intensity' is employed in the context of absorption/emission spectroscopies. In the case of photoionization, the word 'cross-section' is usually employed.

[b] The experimental photoionization cross-sections are taken from the literature and are given in arbitrary units.

[c] For what concerns the results provided in the next section, the values of α were chosen in order to reproduce the experimental results (because only relative experimental cross-sections are available for the molecular systems shown in figures 3.1-3.6).

[d] This *does not mean* that the validity of eq. 3.89 is *completely general*: If the assumptions behind the formulation proposed for $L(\nu)$ are *not* valid, eq. 3.89 must be replaced with other, more suitable formulations.

¶ The results provided in this section were published in *J. Chem. Theory Comput.*, **2020**, 16, 8, 5218-5226.

molecule	symmetry point group	chiral?	structure
tricyclo[3.3.0.$0^{3,7}$]octane-2,6-dione (2,6-STDO)	D_2	yes	fig. 3.1
2,6-dimethylenetricyclo[3.3.$0^{1,5}$.$0^{3,7}$]octane (2,6-STDE)	D_2	yes	fig. 3.2
6-methylenetricyclo[3.3.0.$0^{3,7}$]octan-2-one (2,6-STEO)	C_2	yes	fig. 3.3
2-oxotricyclo[3.3.0.$0^{3,7}$]octane-6-thione (2,6-STOT)	C_2	yes	fig. 3.4
tricyclo[3.3.0.$0^{3,7}$]octane-2,4-dione (2,4-STDO)	C_s	no	fig. 3.5
4-methylenetricyclo[3.3.0.$0^{3,7}$]octan-2-one (2,4-STEO)	C_1	yes	fig. 3.6

Table 3.1: names, symmetry point groups and chirality of the six molecular systems discussed in section 3.3

In what follows, assignment and computational reproduction of the UPS spectra of the six molecular systems shown in figures 3.1-3.6 is discussed; names (and abbreviations), chirality and symmetry point groups of these molecular systems are given in table 3.1.

A feature shared by the six compounds shown in figures 3.1-3.6 is the presence of two π-bonds separated by a rigid σ-scaffold. Interactions between two π-bonds embedded in the same molecular system and separated by a rigid σ-scaffold (i.e. not conjugated π-bonds, with fixed orientations and distance) have been investigated to unveil their features in connection with long-range electron and excitation transfer between chromophores. Therefore, a full characterization of compounds with the same σ-scaffold which differ for the orientation of the π-bonds (and for the moieties linked to the σ-scaffold through the two double bonds) can have an interest.

UPS spectroscopy provides useful experimental data related to the structure of the neutral molecular system and its ionized counterparts: pieces of information about the electronic structures of the neutral and ionized forms of the molecule (as well as about nuclear dynamics and electronic structures) are intertwined in the experimental data, and the employment of suitable computational tools is an invaluable support for rationalization and analysis of experimental results.

Synthesis[a] and experimental UPS spectra[250,251] of the six compounds considered in this section have been reported in literature. The available computational results do not take into account the vibrational signatures of the electronic transitions associated to low-energy ionizations.

The main purposes of this study are (i) the integration of the computational results already available in literature, particularly for what concerns the characterization of the vibrational progressions observed in the experimental spectra and (ii) the validation of a computational protocol which has been devised to combine methods based on one-electron Green's functions

[a]The synthesis of 2,4-STEO was published in ref. 247, while the synthesis of 2,6-STEO and 2,6-STDO were reported in ref. 248. The synthesis of 2,6-STDE is described in ref. 249. To the best of the author's knowledge, the synthesis of 2,4-STDO and 2,6-STOT were detailed for the first time in ref. 250 (The UPS spectra of the two compounds provided in this thesis are taken from the same article).

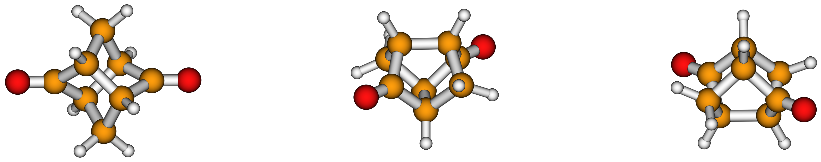

Figure 3.1: Structure of 2,6-STDO from three different perspectives.

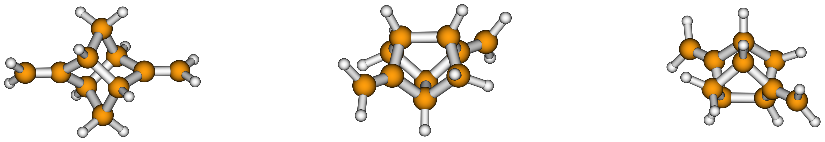

Figure 3.2: Structure of 2,6-STDE from three different perspectives.

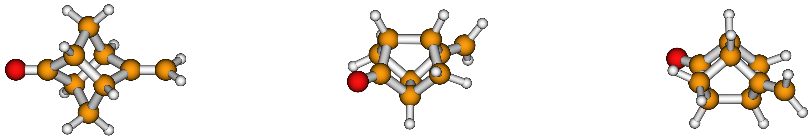

Figure 3.3: Structure of 2,6-STEO from three different perspectives.

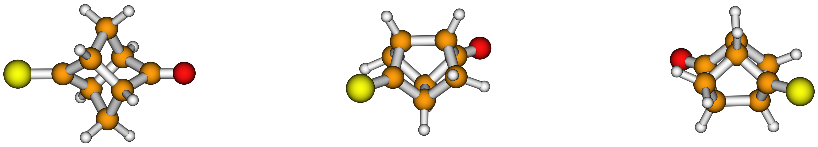

Figure 3.4: Structure of 2,6-STOT from three different perspectives.

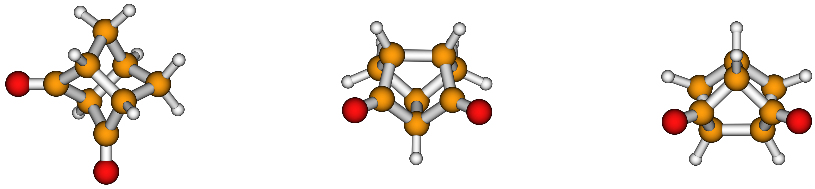

Figure 3.5: Structure of 2,4-STDO from three different perspectives.

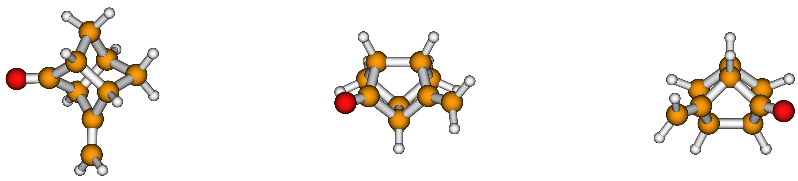

Figure 3.6: Structure of 2,4-STEO from three different perspectives.

for the calculation of ionization potentials (IPs) with a characterization of ground electronic states obtained with DFT-based methods.

3.3.1 Vibrational signatures in UPS spectra: a brief overview

In the framework of the BO approximation, in order to reproduce the vibrational signature associated to an electronic transition reliable approximations of the PESs of the electronic states involved in the electronic transition are needed (see section 3.2 and references therein). The usefulness of methods based on one-electron Green's functions for what concerns the calculation of vertical IPs is well recognized (see section 3.1 and references therein), but the vertical IP corresponds to the energy difference between two PESs at a specific nuclear configuration (the equilibrium geometry of the neutral molecular system): therefore, to approximate the PESs of neutral and ionized states other pieces of information are needed.

In principle, methods based on one-electron Green's functions can provide reliable approximations of PESs: indeed, the connection between the one-electron Green's function and the ground state energy is well-known.[a] Although the exploration of a PES can be carried out with a direct search method,[b] a more effective procedure employing derivative-based optimization methods in conjunction with analytic gradients of the energies of initial and final states is desirable (see section 1.1.1). Second-order many body perturbation theory (MBPT2) can be recovered from a second-order approximation to the one-electron Green's function:[254] therefore, the MBPT2 expression of the ground state energy can be employed and hence the analytic gradients of the ground state energy can be obtained from the MBPT2 treatment. For what concerns the analytic gradients of the ionized state energy, analytic gradients of electron propagator poles are needed: these expressions are available for the second-order approximation to the self-energy matrix[c] and for some higher-order extensions.[d] Thanks to the advancements just mentioned, geometry optimizations of neutral and ionized electronic states with methods based on one-electron Green's functions are nowadays possible.

The first calculations of the vibrational signatures associated to electronic transitions computed by means of methods based on electron prop-

[a] See, for example, section 6 of ref. 201.

[b] These methods are based on energy-only algorithms and do not require the knowledge of the derivatives of the energy with respect to nuclear coordinates: therefore, knowledge of a computational procedure which provides the ground state energy and the energy difference between the ionized electronic states and the neutral one allows the employment of a direct search method without requiring other pieces of information.

[c] For the derivation, see refs. 252 and 253 (the result is the same but is obtained following two different routes); the expressions of the analytic gradients obtained for the second-order approximation to the self-energy matrix were implemented and some applications were provided.[254–256]

[d] This is the case of the NR2 approximation: the analytic gradients are derived in ref. 253.

agator theory can be traced back to the works of Cederbaum et al.,[257–259] and since then many other contributions can be found.[a] Other approaches (i.e. approaches which do not employ the electron propagator theory for the calculation of electronic transitions) have been proposed and successfully applied to the calculation of vibrationally resolved UPS spectra.[b]

In this study, a pragmatic approach has been employed:[c] the PES of the neutral form of a molecular system is approximated with DFT-based methods, while the energy difference between a ionized form and the neutral form of the same molecular system is computed with methods based on the electron propagator theory.

3.3.2 Computational details

All the calculations have been performed with a development version of the Gaussian suite of programs. Geometry optimization and harmonic force field of the ground (neutral) electronic state have been carried out with DFT, employing B3LYP[176–178] as exchange-correlation functional combined with maug-cc-pVTZ basis set.[68,69] The calculation of vertical IPs has been performed employing two different approximations of the electron propagator matrix: the OVGF method[215–217] (which is computationally cheap and retains the quasi-particle picture, see section 3.1.2) and the NR2 method[224] (a non-diagonal approximation which is computationally more demanding than the OVGF method but cheaper than other non-diagonal approaches, see section 3.1.3) combined with maug-cc-pVTZ basis set.

For what concerns the calculation of the vibrational signatures of the first two (or three, in the case of the 2,6-STOT molecule) ionized electronic states, the VG model has been employed in conjunction with the FC approximation (see section 3.2). In the VG model, the derivatives of the differences of the final (ionized) and the initial (neutral) state PESs with respect to the normal coordinates of the initial state (evaluated at the equilibrium geometry of the initial state) are needed. A formulation of the analytic gradients of the final (ionized) states in the framework of the NR2 approximation is available in literature[253] but has not been implemented: therefore, in the vibronic calculations the band positions (which are given by the vertical IPs) have been calculated with the NR2 approximation and the calculation of the gradients has been performed numerically with the (computationally less demanding) OVGF method. The numerical calculation of the gradient is performed with an external python script, employing the following expression:

[a] See, for example, ref. 260 (with caution for what concerns the conclusions).

[b] See, for example, refs. 261 and 262.

[c] This approach has been devised to provide a good compromise between computational cost and accuracy despite the lack of analytic gradients for the ionized states.

$$g_i^{IP} = \frac{E^{IP}(+\delta_i) - E^{IP}(-\delta_i)}{2\delta_i}, \tag{3.90}$$

where g_i^{IP} is the i-th cartesian component of the gradient $\mathbf{g}^{IP}$ expressed in cartesian coordinates, $E^{IP}(+\delta_i)$ and $E^{IP}(-\delta_i)$ are the vertical IPs calculated with displacements from the equilibrium geometry (of the initial, neutral electronic state) of, respectively, $+\delta$ and $-\delta$ along the i-th cartesian coordinate. In this study, the value of δ has been set equal to 0.001Å. It must be noticed that $\overline{\overline{\mathbf{g}}}$ (and not $\mathbf{g}^{IP}$) is needed for the calculation of the shift vector $\mathbf{K}$ in the VG model (see eq. 3.83).[a] However, the following relationship holds:

$$\overline{\overline{g}}_x = \overline{g}_x + g_x^{IP}. \tag{3.91}$$

In eq. 3.91, the subscript x indicates a generic coordinate system. The numerical differentiation is performed at the equilibrium geometry of the initial (neutral) electronic state, and therefore $\overline{\mathbf{g}} = 0$: the direct consequence is that $\overline{\overline{\mathbf{g}}} = \mathbf{g}^{IP}$ and the calculation of the components of $\overline{\overline{\mathbf{g}}}$ can be carried out with eq. 3.90.[b] The prescreening protocol described in section 3.2.1 has been employed to select the most relevant FC overlap integrals: in this study, the values $C_1^{max} = 20$, $C_2^{max} = 13$ and $N_i^{max} = 10^8$ have been adopted (if not otherwise specified) for the three user-defined prescreening factors.

3.3.3 Results

In what follows, the computational results obtained for the six molecular systems listed in table 3.1 are presented and discussed. In figure 3.7, experimental UPS spectra (taken from refs. 251 and 250) are compared with computational ones (calculated in this study, at NR2/maug-cc-pVTZ and OVGF/maug-cc-pVTZ level of theory). Intensities are given in arbitrary units, and therefore the absolute intensity is not meaningful (it is adjusted

[a] In the VG model, for the calculation of $\mathbf{K}$ the following assumptions are employed in eq. 3.83: $\mathbf{J} = \mathbf{I}$ and $\overline{\overline{\boldsymbol{\omega}}} = \overline{\boldsymbol{\omega}}$

[b] The coordinate system adopted for the nuclear coordinates is important. In eq. 3.90 a cartesian coordinate system is assumed for the nuclear coordinates, while in eqs. 3.83 and 3.84 gradient $\overline{\overline{\mathbf{g}}}$ and hessian $\overline{\overline{\mathbf{H}}}$ are provided in terms of normal coordinates of the initial electronic state $\overline{\mathbf{Q}}$. The gradient given in one coordinate system can be easily obtained in another coordinate system, and conversely; useful equations are provided in section A.1 of appendix A: when normal coordinates are employed as non redundant coordinates, eq. A.2 is exact (and hence all the elements of $\mathbf{B}'$ are zero) and the dependence from the mass is left implicit. In practice, in this study the gradient is numerically computed in cartesian coordinates with eq. 3.90; this vector is provided to the Gaussian software, which takes into account the coordinate system in which the gradient is expressed for the calculation of the shift vector $\mathbf{K}$: essentially, $\mathbf{K}$ is computed with eq. 8.67 of ref. 263 (see eq. 8.62 of ref. 263 in which the masses are explicitly taken into account in the relationship which is used to transform the gradient between the two coordinate systems).

in order to reproduce the experimental results). However, a comparison of the relative intensities is still possible and meaningful. Each pole of the electron propagator matrix corresponds to a transition energy and its pole strength to the intensity of the same transition. Gaussian functions are employed to reproduce broadening effects in the computational results.

Detailed assignments of the transition energies are provided in tables C.1, C.3, C.5, C.6, C.8 and C.10 (section C.3 of appendix C). The assignments proposed in this study can be compared with the assignments reported in table 1 of ref. 251 and table 1 of ref. 250. For what concerns 2,6-STDO and 2,6-STDE another computational study is available in literature:[264] the computational results reported in ref. 264 are listed in tables C.1 and C.3 together with the results of the calculations discussed in this section.

Transition energies of an UPS spectrum are usually assigned to the electron binding energy of a specific Molecular Orbital (MO) i.e. the validity of the quasiparticle picture is assumed: when the diagonal approximation is adopted,[a] this assumption is valid; however, when a non-diagonal approximation is employed this assumption must be verified.[b] For the molecular systems investigated in this study, the transition energies obtained with the OVGF and the NR2 approximations are (at least qualitatively) similar (see figure 3.7), and in the case of the (non-diagonal) NR2 approximation the contributions to a single DO are dominated by a single MO. Therefore, in section C.3 and in what follows each electronic transition energy is associated with a specific molecular orbital (also in the case of the non-diagonal NR2 approximation).[c]

Calculated transition energies assigned to outer valence MOs are in good agreement with the experimental values, for both the approximations of the electron propagator matrix employed in this study (see fig. 3.7 and the tables of section C.3 already mentioned), with the exception of the 2,6-STEO molecule: in this case, the agreement of the NR2 results with the experimental values is more satisfying than the results obtained when the OVGF approximation is employed (see figure 3.7c). All the outer valence MOs (and therefore all the transition energies) are mainly (but not exclusively) related to the lone pairs of the chalcogens (oxygen and sulfur atoms) or to the π-bonds of the six compounds investigated. Nevertheless, a partial delocalization of the outer valence MOs on the central σ-scaffold (which is the central molecular unit common to each of the molecular systems considered

[a] This is the case of the OVGF method and of the values obtained by means of the KT.

[b] When a diagonal approximation is employed, Dyson orbitals (DOs) are proportional to MOs; in the case of a non-diagonal approximation, DOs are obtained (in general) as linear combination of MOs: in practice, in most cases (for a closed-shell molecule) the linear combination is dominated by a single MO, and therefore the transition energies can be still assigned to a specific MO.

[c] In tables C.1, C.3, C.5, C.6, C.8 and C.10, it has been reported whether other contributions (besides the contribution of the dominant MO) to a specific DO are relevant for a non-diagonal approximation.

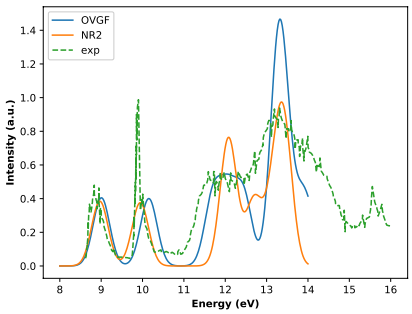

(a) UPS spectra of 2,6-STDO

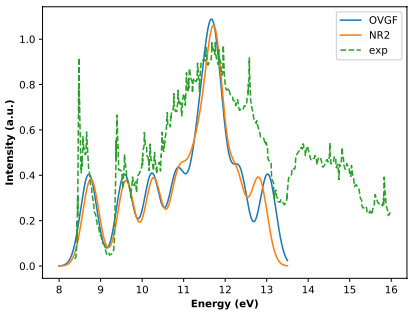

(b) UPS spectra of 2,6-STDE

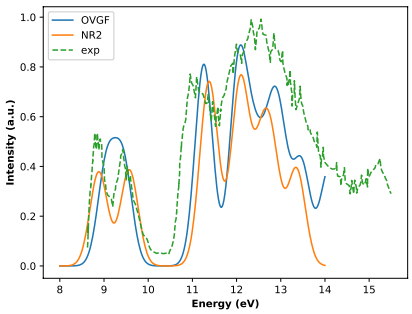

(c) UPS spectra of 2,6-STEO

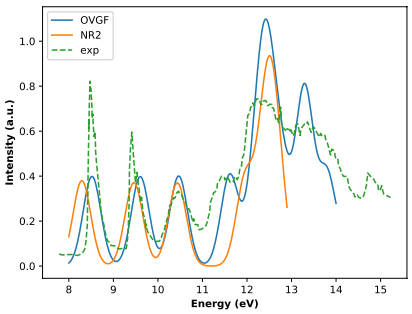

(d) UPS spectra of 2,6-STOT

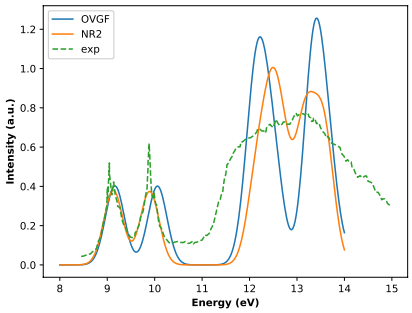

(e) UPS spectra of 2,4-STDO

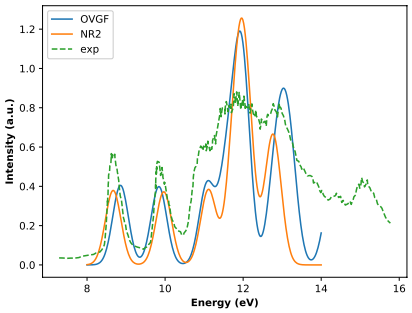

(f) UPS spectra of 2,4-STEO

Figure 3.7: UPS spectra of the six molecular systems listed in table 3.1; Intensities are given in arbitrary units and transition energies are provided in electronvolt (eV); the experimental spectra (dashed green lines) are taken from the literature (see the text).

in this work) is observed for MOs related to the oxygen lone pairs:[a] this is the case for $7b_2$ and $6b_3$ MOs of 2,6-STDO, $12b$ MO of 2,6-STEO, $11b$ MO

[a] for what concerns 2,4-STDO and 2,4-STEO, this phenomenon was already recognized in ref. 250 (see figure 2 of ref. 250).

of 2,6-STOT, 11a'' and 15a' MOs of 2,4-STDO.[a]

The effects of the orientation of π-bonds on the strength of the coupling between two lone pairs or two π-bonds were discussed in ref. 250. The experimental trend[250] which suggests a coupling between the lone pairs of the oxygen atoms in 2,6-STDO stronger (greater difference between the first two transition energies) than the coupling observed in the case of 2,4-STDO is confirmed by the calculations performed for this study (both OVGF and NR2 results are in agreement with the experimental trend, see tables C.1 and C.8), and an agreement between the experimental trend and the calculated values given in this study is found also if a comparison between the transition energies associated to the outer valence MOs of 2,6-STEO and 2,4-STEO is considered (in this case, the coupling experimentally probed is stronger in the case of 2,4-STEO molecule). All the assignments proposed in refs. 251 and 250 are confirmed: this is not surprising, because only the first, well-separated experimental bands were assigned in refs. 251 and 250; moreover, a diagonal approximation to the electron propagator matrix provides results which are even quantitatively in agreement with the experimental values in almost all the cases considered in this study. However, it must be noticed that corrections to the KT results are needed in order to correctly reproduce (even qualitatively) the experimental results.[b]

As mentioned above, the discrepancy between the experimental values and the OVGF results for the transition energies referred to the outer valence MOs (13b and 12b) of the 2,6-STEO molecular system is removed when the NR2 approximation is adopted (see fig. 3.7c). Since the corresponding DOs are dominated by the contributions of the MOs 13b and 12b (see table C.5) when the NR2 approximation is employed, the importance of the non-diagonal contribution to the improvement of the calculated results has been verified as follows: a single point calculation (at the equilibrium geometry) with the diagonal counterpart of the NR2 approximation (the so-called P3 method)[225] has been carried out (employing the basis set maug-cc-pVTZ) and the difference between the transition energies associated to the MOs 13b and 12b obtained at P3/maug-cc-pVTZ level of theory are compared with the same difference obtained at OVGF/maug-cc-pVTZ and NR2/maug-cc-pVTZ levels. For the P3 method, the difference is equal to 0.51, while for OVGF and NR2 approximations the results are, respectively, equal to 0.38 and 0.69 eV: these values suggest that the discrepancy (between experimental and calculated transition energies observed for the 2,6-STEO molecule) can be removed (at least partially) retaining the diagonal approximation.

[a] This phenomenon can be observed also in the case of 2,4-STEO (see table C.10), but in this specific case the (approximate) identification of the DOs with the MOs seems to be particularly problematic for what concerns the outer valence MOs.

[b] For example, KT do not provides qualitatively reliable results for the first transitions of 2,6-STEO and 2,6-STOT (see tables C.5 and C.6), as was already recognized in refs. 251 and 250.

The results showed in fig. 3.7 and reported in tables C.1, C.3, C.5, C.6, C.8 and C.10 suggest a good agreement between experimental and calculated results for electron binding energies lower than about 14 eV. For what concerns the six compounds studied, the results calculated with NR2 and OVGF approximations in most of the cases are similar (in the case of the 2,6-STOT molecule the OVGF results are even closer to the experimental results than the NR2 ones). To obtain a better agreement between experimental and calculated values the vibronic structure must be taken into account.

In this work the vibronic structure has been computed for the lower electron binding energies, for which well-separated vibronic structures are available from refs. 251 and 250. The results are shown in fig. 3.8. The resolution of the experimental spectra provided in refs. 251 and 250 is limited; nevertheless, a fairly good agreement between experimental and computational results can be noticed with the exception of the vibronic structures computed for the 2,6-STEO molecule.

The assignment of the most intense vibronic transitions can be found in section C.3 of appendix C. For what concerns the five compounds for which the experimental spectra are in good agreement with the calculations presented in this work, the most intense vibronic transition is the $|0\rangle \rightarrow |0\rangle$ for each vibronic structure.[a]

For what concerns 2,6-STDO and 2,6-STDE, vibronic signatures characterized by intense $|0\rangle \rightarrow |0\rangle$ vibronic transitions (see tables C.2 and C.4) and a computational extrapolation of the final state geometry (based on the VG model) suggest equilibrium geometries (for the ionized states of interest) which are very similar to the equilibrium geometry calculated for the ground electronic state of the neutral molecule; moreover, the good agreement between experimental and calculated results (particularly evident in the case of 2,6-STDO) supports the reliability of the computational approach employed for this study.

Other intense vibronic transitions for the electronic transitions of interest of the molecules 2,6-STDO and 2,6-STDE are associated to the normal modes depicted in figures C.1 and C.2. The vibronic transitions associated to the symmetric stretching of the two double bonds[b] are of particular interest: despite the limited resolution of the available experimental spectra, the numerical results provided in this work for the 2,6-STDE molecule suggest the assignment of the vibronic features at 8.7 eV and at 9.6 eV to the vibronic transition $|0\rangle \rightarrow |47(1)\rangle$ (see fig. 3.8b, table C.4 and fig. C.2e); moreover, the results listed in table C.4 (and plotted in fig. 3.8b) suggests the possibility of

[a] this is particularly evident for the second electronic transition of the 2,6-STDO molecule (and was alerady recognized in ref. 251).

[b] Double bonds between a carbon and an oxygen atom in the case of 2,6-STDO and between two carbon atoms in the case of 2,6-STDE; the corresponding normal modes are the 40-th normal mode in the case of 2,6-STDO (see fig. C.1e) and the 47-th normal mode in the case of 2,6-STDE (see fig. C.2e).

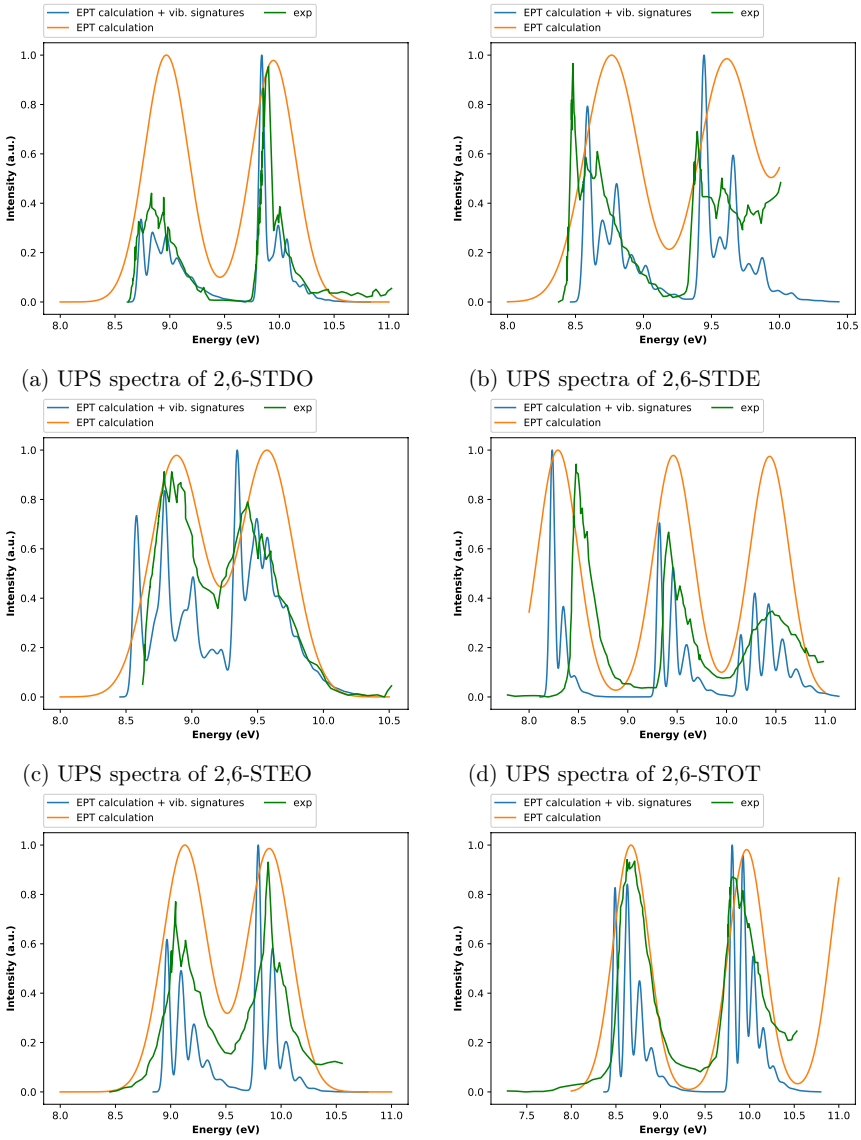

(a) UPS spectra of 2,6-STDO

(b) UPS spectra of 2,6-STDE

(c) UPS spectra of 2,6-STEO

(d) UPS spectra of 2,6-STOT

(e) UPS spectra of 2,4-STDO

(f) UPS spectra of 2,4-STEO

Figure 3.8: Vibronic structures of the transition energies associated to the outer valence electron binding energies for the six compounds listed in table 3.1; the experimental spectra (continuous green lines) are taken from the literature (see the text).

a direct observation of the vibronic transitions associated to the first overtone ($|0\rangle \rightarrow |47(2)\rangle$) of the symmetric stretching of the two double bonds in the 2,6-STDE molecule: to verify this hypothesis, the measurement of an high-resolution UPS spectra would be desirable. The other intense vibronic transitions listed in tables C.2 and C.4 involve one-photon excitation of CH

bendings (see figs. C.1b-C.1d and C.2b-C.2d) of the central σ-scaffold.[a]

In the cases of 2,6-STOT, 2,4-STDO and 2,4-STEO, the adoption of the computational protocol successfully employed for 2,6-STDO and 2,6-STDE leads to extrapolated equilibrium geometries (obtained in the framework of the VG model) for the ionized states which differ substantially from the equilibrium geometry of the neutral ground state.[b] The relevant changes in the equilibrium geometries are accompanied (not surprisingly) by exceedingly small FC overlap integrals for the $|0\rangle \rightarrow |0\rangle$ vibronic transitions: in the light of these results, the reliability of the adopted computational protocol can be questioned. In principle, to solve out the problem a better approximation of the final PES is needed: for example, other harmonic models for the description of the final state PES can be employed, or a computational approach suitable for the description of vibronic transitions in flexible molecular systems.[c] In practice, another route (computationally less demanding) can be employed, which is based on the combination of the computational protocol described in section 3.3.2 with a reduced-dimensionality scheme: in this case, the vibronic calculation is carried out on a fraction of the normal modes of the molecular system of interest, while the contributions of the other normal modes are neglected. In this study, the selection of the normal modes included in the vibronic calculation is based on the inspection of the components of the shift vector $\mathbf{K}$: too high values of the low-frequencies components of $\mathbf{K}$ are avoided by neglecting the contributions of the corresponding normal modes in the vibronic calculation. For what concerns the computational protocol, all the normal modes with a fundamental frequency below a certain user-defined value are neglected in the vibronic calculation: when the same user-defined value is chosen for all the electronic transitions of a specific molecular system, with this protocol the vibronic calculations are performed on a selection of normal modes which is exactly the same for all the electronic transitions of the molecular system of interest.[d] In order to ensure reproducibility of the computational results, the user-defined values employed for the calculations presented in this study are provided in section C.3 of appendix C.

With the employment of the reduced-dimensionality scheme mentioned

[a] With two exceptions: the vibronic transition $|0\rangle \rightarrow |8(1)\rangle$ for the 2,6-STDO molecule (a skeletal deformation is involved in the 8-th normal mode, see fig. C.1a) and the vibronic transition $|0\rangle \rightarrow |7(1)\rangle$ for the 2,6-STDE molecule (the CH bendings of the peripheral CH_2 units involved in the 7-th normal mode, see fig. C.2a).

[b] The conformational changes involve the orientation of the two π-bonds with respect to the central σ-scaffold and the related distortions of the central σ-scaffold.

[c] See, for example, ref. .

[d] On the other hand, with this protocol some normal modes which can be safely included in the vibronic calculation referred to a specific electronic transition can be excluded because a normal mode with an higher fundamental frequency does not allow a proper description (in the framework of the VG model) of the vibrational signature of another electronic transition of the same molecular system.

above, the computational results obtained for 2,6-STOT, 2,4-STDO and 2,4-STEO molecules are in good agreement with the experimental UPS spectrum (see figs. 3.8d-3.8f) and the extrapolated equilibrium geometry for the ionized states are very similar to the equilibrium geometry of the neutral ground state.[a]

Although (as mentioned above) the $|0\rangle \rightarrow |0\rangle$ vibronic transition is the most intense one for the three vibronic structures of 2,6-STOT investigated in this study, the vibronic band associated to the $|0\rangle \rightarrow |0\rangle$ vibronic transition is not necessarily the most intense of the vibronic structure calculated (and observed) for a certain electronic transition; more specifically, in fig. 3.8d the vibronic band which corresponds to the transition $|0\rangle \rightarrow |0\rangle$ is the most intense one for the vibronic structures of the first (between 8 and 9 eV) and the second (between 9 and 10 eV) electronic transitions, but the same is not true for the vibronic structure of the third electronic transition (between 10 and 11 eV): indeed, a single vibronic band can result from the contributions of several vibronic transitions.[b] Besides the $|0\rangle \rightarrow |0\rangle$ transition, the other most relevant contributions (identified in table C.7) involve the bending of CH bonds of the central σ-scaffold (see figs. C.3a-C.3i) and the stretchings of CO (fig. C.3k) and CS (fig. C.3j) bonds; moreover, the relative intensity of the $|0\rangle \rightarrow |0\rangle$ transitions and the vibrational progressions for the three vibronic structures reported in fig. 3.8d and assigned in table C.7 is consistent with the assigments proposed in table C.6 for the three electronic transitions.[c]

The two vibronic structures computed for the two outer valence ionization transitions of 2,4-STDO are similar: the first (and most intense) vibronic band (assigned to the $|0\rangle \rightarrow |0\rangle$ transition) is followed by vibronic bands of decreasing intensity (the assignment is provided in table C.9); these vibronic structures are similar to the vibronic structure calculated for the electronic transition associated with the MO $11b$ of 2,6-STOT. The contribution (to the first vibronic structure) of the vibronic transitions associated with the symmetric (see fig. C.4j) and the antisymmetric (see fig. C.4i) CO stretchings is worth of mention (see table C.9).[d]

For what concerns 2,4-STEO molecule, assignment of the vibronic struc-

[a] In the case of the 2,4-STEO molecule, the extrapolated equilibirum structures (for the two ionized states of interest) for the fragment $C(sp^2)$=$C(sp^2)H_2$ (which is planar in the neutral ground state) are slightly bent: this is consistent with the assignment of a partial π_{CC} character for the outer valence MOs $26a$ and $25a$ (proposed in table C.10).

[b] This is a consequence of the finite bandwidth of each vibronic transition.

[c] The less intense $|0\rangle \rightarrow |0\rangle$ transition pertains to the electronic transition assigned to the removal of one electron from the π_{CS} MO, while the other two vibronic transitions of interest are assigned to n_O and n_S MOs; moreover, the MO $11b$ is partially delocalized on the σ-scaffold: this is consistent with a vibronic progression which is not dominated by (and almost reduced to) the $|0\rangle \rightarrow |0\rangle$ transition (as in the case of the first electronic transition, assigned to the n_S MO).

[d] The other intense vibronic transitions (besides the $|0\rangle \rightarrow |0\rangle$) are assigned to the CH bendings of the central σ-scaffold, see figs. C.4a-C.4h.

tures are provided in table C.11. Besides the $|0\rangle \rightarrow |0\rangle$ transition and the transitions involving the CH bendings of the central σ-scaffold, a vibronic transition of relevant intensity is associated with the CC stretching (fig. C.5n).

An attempt to explain the disagreement between experimental and computational results in the case of 2,6-STEO (see fig. 3.8c) is provided in what follows. At first glance, the VG model seems to work well (the extrapolated equilibrium geometries for the ionized states are very similar to the equilibrium geometry of the ground state of the neutral molecular system), while the absolute intensities of the vibronic bands are significantly lower than their counterparts in the other computed spectra discussed in this work.[a] Therefore, a first attempt to go beyond the FC approximation retaining the first order contributions to the transition properties (so-called HT term, see section 3.2.1, particularly eq. 3.85) has been done, without significant improvements in the computational results. Probably the agreement between computational and experimental results can be improved employing other harmonic models (for example, the AH model) and avoiding the approximation $\mathbf{J} = \mathbf{I}$: an attempt in this direction would benefit from the implementation of an analytical formulation of the gradient for the ionized states, in order to limit the required computational effort. Serious concerns about the anharmonicity of the ionized states PESs or about the reliability of cartesian-based normal coordinates seems to be unmotivated (in the light of the semi-rigid nature of the molecular system), but cannot be excluded. On the basis of the low agreement between computational and experimental results for what concerns purely electronic calculations at OVGF/maug-cc-pVTZ level of theory (see fig. 3.7c and table C.5) the reliability of the OVGF method for the numerical calculation of the gradient can be questioned. As mentioned above, the discrepancy between experimental and computational results turned out at OVGF/maug-cc-pVTZ level of theory does not imply (at least not necessarily) the failure of the diagonal approximation to the electron propagator matrix. In order to verify whether the partial inclusion of the third order corrections is (at least partially) responsible for the observed discrepancies[b], an attempt to compute the numerical gradients at D2/maug-cc-pVTZ level of theory[c] has been done: again, the disagreement between computational and experimental results remains evident. Another issue is the adequacy of the basis set: despite the good results obtained in this work for the other molecular systems studied, an improvement of the

[a] This is not clear from the spectra displayed in fig. 3.8 because the intensities are reported in arbitrary units (i.e. only the relative intensities in the same spectrum can be compared).

[b] The OVGF method is based on a partial inclusion of the third-order corrections to the diagonal elements of the electron propagator matrix; for more details, see section 3.1.2.

[c] I.e. only the second-order correction to the diagonal elements of the electron propagator matrix are retained; for more details, see section 3.1.2.

results with the employment of other basis (for example, the aug-cc-pVTZ basis set) cannot be excluded. Other calculations are left for future studies, for which the availability of an implementation of the analytic gradients for the ionized states and a more resolved experimental UPS spectrum would be extremely useful.

Conclusions and perspectives

In the light of the results provided in this thesis, the usefulness of the computational approaches introduced and discussed in the previous chapters should be recognized. However, the comparison between computational results and experimental observables shows limitations that should be explicitly mentioned.

The computational protocols introduced in chapter 1 for the construction of PESs (in other words, for the approximation of the potential energy term in the nuclear hamiltonian) can be regarded as an essential instrument in the toolkit of quantum chemists. The limitations of these protocols are mainly due to the growth of the computational cost associated to (i) the lack of analytical gradients and hessians for certain electronic calculation method and (ii) to the increase of the global PES dimensions with the number of atoms of the molecular system investigated. The applications discussed in section 1.3 support the usefulness of carefully devised curvilinear coordinate systems for the dimensionality reduction of global PESs. The results provided in section 1.3 can be employed to construct a nuclear hamiltonian: in this manner, a direct comparison between the energy levels (which are the solutions of the associated TINSE) and the experimental transitions (probed by high resolution spectroscopies, e.g. microwave or far infrared spectroscopies) could be carried out. For the construction of such a nuclear hamiltonian, a formulation of the kinetic energy operator in curvilinear coordinates is needed (see section 2.1).

Solutions of the TINSE were calculated and discussed in the previous chapters (see sections 2.4 and 3.3): a good agreement between experimental and calculated transition energies was obtained for almost all the molecular systems investigated. In order to reproduce an experimental spectrum, the computational reproduction of transition energies must be combined with a reliable simulation of the intensities. For what concerns intensities, in certain cases the agreement between the computational results and the experimental data is poor. Some of the possible reasons of these discrepancies were already pointed out. In particular, the computational approaches introduced in chapters 2 and 3 (see sections 2.2, 2.3 and 3.2) are not suitable to take into account the contributions of flexible motions to the overall spectra. In the group of prof. Barone, some efforts are devoted to overcome this limitation

(see, for example, ref. 265).

Limits and discrepancies briefly summarized above should not be underestimated. However, some interesting achievements should be mentioned. More specifically, the accurate calculation of VCD spectra of organometallic molecules is not a trivial task, especially at anharmonic level. The very good agreement between experimental and calculated VCD spectra of $\mathbf{5}-R_p$ and $\mathbf{5}-S_p$ (see subsection 2.4.2) is an outstanding achievement. Another relevant achievement is the validation (for semi-rigid molecular systems) of a computational protocol for the calculation of vibrationally resolved UPS spectra (see section 3.3).

In conclusion, in this thesis a series of computational approaches to the simulation of vibrational signatures in molecular spectroscopy were discussed. Strength and limitations were outlined and verified through a comparison of a number of calculated data with their experimental counterparts. The results provided in this thesis definitely support the need of taken into account the effects of nuclear motions for an accurate reproduction of high resolution molecular spectra.

Appendix A

A.1 Specify nuclear positions: the choice of the coordinate system

The choice of the coordinate system employed to deal with the positions of nuclei is a technical aspect of pivotal importance. A concise discussion of this aspect is provided due to its relevance for a number of topics treated in this thesis (e.g. optimization procedures and PESs representations, see chapter 1). The nuclei of a molecular system are treated as a system of points with masses (specified by the corresponding atom type), and in principle several coordinate systems can be employed to specify their positions. In practice, the choice of the coordinate system affects computational procedures (such as the number of single point calculations needed for the convergence of an optimization algorithm, see Sections 1.1.1 and 1.2.1) and their mathematical formulations.

- If a cartesian coordinate system is chosen, the positions of the nuclei are specified with a number of $3N$ coordinates (3 for each nucleus, N is the total number of atoms). Despite its simplicity, this coordinate system has a number of relevant drawbacks: it is not the natural choice for the description of molecular motions and contains redundant information about an isolated molecular system (the position of the origin, fixed with 3 coordinates, and the orientation of the molecular system, fixed with other 3 coordinates). However, many useful mathematical and physical quantities obtained with electronic structure calculations are almost always given in terms of cartesian coordinate system. Furthermore, the employment of a cartesian coordinate system can be still useful in the context of molecular structure optimizations (an example is the optimization of complex polycyclic molecular systems), although the employment of carefully devised redundant internal coordinate systems can further increase the efficiency of commonly used optimization algorithms;

- The employment of an internal coordinate system is advantageous in

many cases. Several types of internal coordinate systems have been devised, and here only a brief account of the most popular and common ones is given. The relation between internal and cartesian coordinates can be written as a Taylor series:

$$\begin{aligned} s_i = &\sum_{j=1}^{N}\sum_{\alpha=1}^{3}\frac{\partial s_i}{\partial r_{j\alpha}}(r_{j\alpha}-r_{j\alpha}^{eq}) \\ &+\sum_{j,k=1}^{N}\sum_{\alpha,\beta}^{3}\frac{\partial^2 s_i}{\partial r_{j\alpha}\partial r_{k\beta}}(r_{j\alpha}-r_{j\alpha}^{eq})(r_{k\beta}-r_{k\beta}^{eq})+O[(\mathbf{r}-\mathbf{r}^{eq})^2] \end{aligned} \tag{A.1}$$

In eq. A.1, the second-order expansion is reported. The internal coordinates are set to 0 in correspondence of the equilibrium structure of the molecular system. In literature the first derivatives $\frac{\partial s_i}{\partial r_{j\alpha}}$ are gathered into a matrix $\mathbf{B}$ called the Wilson's $\mathbf{B}$ matrix[34].

The specific internal coordinate system chosen determines the dimensions of the $\mathbf{B}$ matrix and the number of elements s_i employed to specify the structure of the molecular system (and gathered in a vector $\mathbf{s}$). The minimum number of elements needed to completely specify the structure of the molecular system is equal to $3N-6$. A set of linearly independent internal coordinates $\mathbf{s}$ with $3N-6$ elements is a non-redundant internal coordinate system: example of non-redundant internal coordinates are the normal coordinates $\mathbf{Q}$[a] and the so-called Z-matrix type coordinates, constructed by means of a limited number of bond lengths, valence angles and dihedral angles (the so-called primitive internal coordinates). When a set of internal coordinates $\mathbf{s}$ with more than $3N-6$ elements is employed, a certain degree of redundancy is introduced and the set constitutes a redundant internal coordinate system (for example, the set of all the primitive internal coordinates for a polyatomic molecule is intrinsically redundant). The normal coordinate system is an example of internal coordinate system that is related to the cartesian coordinate system by a simple linear transformation (i.e. the relation between cartesian and internal coordinates is defined with a truncation to the first-order of the series given in equation A.1). This kind of coordinate systems are called rectilinear internal coordinate systems, with $\mathbf{s}$ given in matrix notation by:[b]

$$\mathbf{s} = \mathbf{B}(\mathbf{r}-\mathbf{r}^{eq}). \tag{A.2}$$

[a] This coordinate system is introduced and extensively discussed in ref. 34

[b] In the case of the normal coordinate system, the coordinates $\mathbf{r}$ are mass-weighted (see ref. 34).

The internal coordinate systems which cannot be related exactly to a cartesian framework with a simple linear transformation are called curvilinear internal coordinate systems (eq. A.2 is adopted also for curvilinear internal coordinate systems, but should be considered an approximation which is rigorously valid only for small displacements[a]). Z-matrix type coordinates or the Cremer-Pople ring puckering coordinates employed in this thesis (see Chapter 1) are examples of curvilinear internal coordinates.

Direct and inverse transformation of the set of nuclear positions $\mathbf{r}$, of the gradient $\mathbf{g}$[b] and of the hessian $\mathbf{H}$[c] between two coordinate systems deserves some comments.

Gradients and hessians in cartesian coordinates ($\mathbf{g}_r$ and $\mathbf{H}_r$) can be obtained in a straightforward manner (if the $\mathbf{B}$ matrix and its derivatives with respect to the cartesian coordinates $\mathbf{B}'$[d] are known):

$$\mathbf{g}_r = \mathbf{B}^T \mathbf{g}_s \tag{A.3}$$

$$\mathbf{H}_r = \mathbf{B}^T \mathbf{H}_s \mathbf{B} + \mathbf{B}'^T \mathbf{g}_s \tag{A.4}$$

Where $\mathbf{g}_s$ and $\mathbf{H}_s$ are, respectively, gradient and hessian expressed in internal coordinates; eqs. A.3 and A.4 can be easily derived from the definitions of $\mathbf{g}$ and $\mathbf{H}$ and from eq. A.1[e].

For what concerns the inverse transformations the mathematical formulation is more complicated. For a transformation of $\mathbf{g}$ and $\mathbf{H}$ from cartesian to internal *non redundant* coordinates the mathematical problem is the inversion of the $\mathbf{B}^T$ matrix, which is rectangular and therefore not invertible:[f] the solution[30] lies in the existence of a set of matrices labeled with $(\mathbf{B}^T)^{-1}$ which satisfy the following relation:

---

[a] This approximation is employed and discussed for primitive internal coordinates in ref. 34; see ref. 266 for the first article (to the best of the author's knowledge) in which this approximation is presented and exploited.

[b] this quantity is a vectorial function of the coordinates of the nuclei, the elements of which are defined (in cartesian coordinates) as $g_{i\alpha} = \frac{\partial E_m}{\partial r_{i\alpha}}$.

[c] $\mathbf{H}$ can be represented as a square matrix (its dimensions depend on the coordinate system adopted) with elements defined (in cartesian coordinates) as $H_{i\alpha,j\beta} = \frac{\partial^2 E_m}{\partial r_{i\alpha} \partial r_{j\beta}}$.

[d] The elements of $\mathbf{B}'$ are the factors $\frac{\partial^2 s_i}{\partial r_{j\alpha} \partial r_{k\beta}}$ of eq. A.1.

[e] For the derivation of eq. A.4, see also eq. 5 of ref. 24 and its explanation; another clear presentation of eqs. A.3 and A.4 can be found at the beginning of Section II of ref. 267, where $\mathbf{B}$ and $\mathbf{B}'$ are recognized and labeled as, respectively, a jacobian matrix and its derivatives.

[f] From the physical point of view, the problem is a consequence of the lack of uniqueness of the transformation from internal, non-redundant coordinates to cartesian, redundant coordinates. An interesting discussion about the inversion of this kind of rectangular matrices can be found in ref. 268.

$$(\mathbf{B}^T)^{-1}\mathbf{B}^T = \mathbf{I} \tag{A.5}$$

where I is the square, unit matrix. A matrix satisfying eq. A.5 can be used in the following relations, which provides $\mathbf{g}_{s(nr)}$ and $\mathbf{H}_{s(nr)}$ i.e. the gradient and the hessian in internal, non redundant coordinates[a]:

$$\mathbf{g}_{s(nr)} = (\mathbf{B}^T)^{-1}\mathbf{g}_r \tag{A.6}$$

$$\mathbf{H}_{s(nr)} = (\mathbf{B}^T)^{-1}(\mathbf{H}_r - \mathbf{g}^T_{s(nr)}\mathbf{B}')[(\mathbf{B}^T)^{-1}]^T \tag{A.7}$$

The matrix $(\mathbf{B}^T)^{-1}$ can be obtained calculating the Moore-Penrose inverse[30], which is the pseudoinverse computed with the following expression:

$$(\mathbf{B}^T)^{-1} = (\mathbf{B}\mathbf{u}\mathbf{B}^T)^{-1}\mathbf{B}\mathbf{u} = \mathbf{G}^{-1}\mathbf{B}\mathbf{u} \tag{A.8}$$

Where $\mathbf{u}$ must be a square matrix of suitable dimensions (various choices are possible[24,26,30]: it can be set equal to the unit matrix[24,26]). If the matrix $\mathbf{u}$ is chosen to be a diagonal matrix with triplets of the inverse mass of each of the nuclei pertaining to the molecular system under investigation the square matrix $\mathbf{G}$ is equal to the spectroscopic $\mathbf{G}$ matrix[34].

In the case of the transformation of $\mathbf{g}$ and $\mathbf{H}$ from cartesian to internal *redundant* coordinates an additional problem arise; in this case, the diagonalization of the $\mathbf{G}$ matrix introduced in eq. A.8 can be easily accomplished:

$$\mathbf{G}\begin{bmatrix}\mathbf{U} & \mathbf{R}\end{bmatrix} = \begin{bmatrix}\mathbf{U} & \mathbf{R}\end{bmatrix}\begin{bmatrix}\lambda & \mathbf{0} \\ \mathbf{0} & \mathbf{0}\end{bmatrix}. \tag{A.9}$$

Eq. A.9 is an eigenvalue equation: $\mathbf{U}$ (which is a matrix of dimensions $(n+r)\times n$) is the set of n nonredundant eigenvectors (where in the general polyatomic case $n = 3N-6$) corresponding to nonzero eigenvalues ($\lambda > 0$), while $\mathbf{R}$ (with dimensions $(n+r)\times r$) is the set of r redundant eigenvectors corresponding to zero eigenvalues ($\lambda = 0$). In this case (i.e. when a diagonal matrix has elements of the diagonal equal to zero), the $\mathbf{G}$ has no inverse. The devised solution is the definition of a *generalized inverse*[26], often labeled as $\mathbf{G}^-$ and obtained in the following manner[24,26]:

$$\begin{bmatrix}\mathbf{U}^T \\ \mathbf{R}^T\end{bmatrix}\mathbf{G}\begin{bmatrix}\mathbf{U} & \mathbf{R}\end{bmatrix} = \begin{bmatrix}\lambda & \mathbf{0} \\ \mathbf{0} & \mathbf{0}\end{bmatrix} \tag{A.10}$$

$$\mathbf{G}^- = \begin{bmatrix}\mathbf{U} & \mathbf{R}\end{bmatrix}\begin{bmatrix}\lambda^{-1} & \mathbf{0} \\ \mathbf{0} & \mathbf{0}\end{bmatrix}\begin{bmatrix}\mathbf{U}^T \\ \mathbf{R}^T\end{bmatrix} \tag{A.11}$$

[a] see, for example, eqs. 5a and 5b of ref. 54

In eq. A.10, the diagonalization of **G** is accomplished[a]: the generalized inverse $\mathbf{G}^{-}$ is obtained inverting the diagonal elements of the diagonalized **G** matrix and transforming it back (eq. A.11). This solution has opened the possibility of performing a geometry optimization directly in redundant internal coordinates: $\mathbf{g}_{s(r)}$ and $\mathbf{H}_{s(r)}$, which label, respectively, the gradient and the hessian in internal, redundant coordinates are given in the following two equations:

$$\mathbf{g}_{s(r)} = \mathbf{G}^{-}\mathbf{B}\mathbf{u}\mathbf{g}_r \tag{A.12}$$

$$\mathbf{H}_{s(r)} = \mathbf{G}^{-}\mathbf{B}\mathbf{u}(\mathbf{H}_r - \mathbf{g}_{s(r)}^{T}\mathbf{B}')\mathbf{u}^{T}\mathbf{B}^{T}\mathbf{G}^{-}. \tag{A.13}$$

Another relevant point is the transformation of the nuclear positions of a molecular system given in internal coordinates **s** in a set of nuclear positions **r** given in cartesian coordinates: a brief account of this problem is provided at the end of Section 1.1.1 (see in particular eq. 1.20) due to its importance for geometry optimization procedures.

[a]It is worthwhile to remember the validity of the following relation, which is a consequence of the spectral theorem: $\mathbf{G} = \mathbf{P}^{-1}\mathbf{D}\mathbf{P} = \mathbf{P}^{T}\mathbf{D}\mathbf{P}$, where **G** is a symmetric matrix (i.e. a matrix which is equal to its transpose matrix, $\mathbf{G} = \mathbf{G}^{T}$), **D** is a diagonal matrix and **P** is an orthogonal matrix (i.e. with a transpose matrix which is equal to the inverse, $\mathbf{P}^{T} = \mathbf{P}^{-1}$).

Appendix B

B.1 Additional remarks on the formulation of kinetic energy operators in curvilinear coordinates

Various implicit formulations (i.e. formulations which do not specify explicitly the relation between generalized internal and cartesian coordinates) of the KEO in curvilinear coordinates are available in literature. A short account of these formulations is provided here for the interested reader.

As starting point, it can be useful the overview given in ref. 126, in which the equivalence of the different formulations and their dependence on a series of arbitrary choices (i.e. normalization convention adopted for the wavefunction and the choices related to the momentum operators) are shown and discussed.

The derivation of the formulation provided in chapter 2 (see eqs. 2.14, 2.15 and 2.16) of this thesis can be found in chapter 6 of ref. 3 where the existence of two refuses must be pointed out. In the right hand side of eqs. 6.73 and 6.76 of ref. 3 the following term:

$$\sum_{i=1}^{3N} G^{ij}(\mathbf{q})\Big(\frac{\partial \ln J(\mathbf{q})}{\partial q^i} + \frac{\partial G^{ij}(\mathbf{q})}{\partial q^i}\Big) \tag{B.1}$$

must be replaced with:

$$\sum_{i=1}^{3N} \Big[G^{ij}(\mathbf{q})\Big(\frac{\partial \ln J(\mathbf{q})}{\partial q^i}\Big) + \frac{\partial G^{ij}(\mathbf{q})}{\partial q^i}\Big] \tag{B.2}$$

Adopting B.2 instead of B.1 the formulation given in eqs. 6.74, 6.75 and 6.76 of ref. 3 is perfectly equivalent to the formulation given in eqs. 5, 6 and 7 of ref. 125 and in this thesis[a]. Moreover, the reorganization of $\hat{T}$ presented

[a] in this thesis $g(\mathbf{q})$ is employed in place of the jacobian $J(\mathbf{q})$; between the two quantities the following relation exists: $J = \sqrt{g}$; therefore $\ln J = \frac{1}{2}\ln g$; it should be noticed that in ref. 126 a different convention is adopted: in that case $g = J^{-2}$ instead of the most popular $g = J^2$ adopted in almost all the other references.

in eq. 6.72 of ref. 3 is perfectly equivalent[a] to eq. 2.33 of ref. 126.

All the formulations of the KEO in curvilinear coordinates cited and provided until now (eqs. 2.14, 2.15 and 2.16 in chapter 2 of this thesis, ref. 125, subsection 6.2.1 of ref. 3 and section 2 of ref. 126) are constructed to act on a wavefunction normalized with the help of the euclidean volume element $d\tau^{(c)} = dr_{11}dr_{12}dr_{13}dr_{21}...dr_{N3}$.

In another formulation of the KEO in curvilinear coordinates (due to Meyer and Günthard)[269] a different normalization convention is adopted, with the volume element $d\tau^{(i)} = dq_1dq_2dq_3...dq_{3N}$ adopted for the normalization of the wavefunction[b]. The vibrational part of the KEO in curvilinear coordinates can be written, according to Meyer and Günthard, as follows[c]:

$$\hat{T}^{(i)} = -\frac{1}{2}\hbar^2 \sum_{i=1}^{3N-6}\sum_{j=1}^{3N-6}\left[\left(\frac{\partial}{\partial q_i} + \frac{1}{4}\frac{\partial \ln g}{\partial q_i}\right)G^{ij}\left(\frac{\partial}{\partial q_j} - \frac{1}{4}\frac{\partial \ln g}{\partial q_j}\right)\right] \tag{B.3}$$

Where all the terms have been already defined (see section 2.1). Eq. B.3 can be developed in the following manner:

$$\begin{aligned}
\hat{T}^{(i)} =& -\frac{1}{2}\hbar^2 \sum_{i=1}^{3N-6}\sum_{j=1}^{3N-6}\left[\frac{\partial}{\partial q_i}\left(G^{ij}\frac{\partial}{\partial q_j}\right) - \frac{1}{4}\frac{\partial}{\partial q_i}\left(G^{ij}\frac{\partial \ln g}{\partial q_j}\right) + \right.\\
&\left. + \frac{1}{4}\left(\frac{\partial \ln g}{\partial q_i}\right)G^{ij}\frac{\partial}{\partial q_j} - \frac{1}{16}\left(\frac{\partial \ln g}{\partial q_i}\right)G^{ij}\left(\frac{\partial \ln g}{\partial q_j}\right)\right] =\\
=& -\frac{1}{2}\hbar^2 \sum_{i=1}^{3N-6}\sum_{j=1}^{3N-6}\left[\frac{\partial}{\partial q_i}\left(G^{ij}\frac{\partial}{\partial q_j}\right) - \frac{1}{4}\left(\frac{\partial G^{ij}}{\partial q_i}\right)\left(\frac{\partial \ln g}{\partial q_j}\right) + \right.\\
&- \frac{1}{4}G^{ij}\frac{\partial^2 \ln g}{\partial q_i \partial q_j} - \frac{1}{4}\left(\frac{\partial \ln g}{\partial q_j}\right)G^{ij}\frac{\partial}{\partial q_i} + \frac{1}{4}\left(\frac{\partial \ln g}{\partial q_i}\right)G^{ij}\frac{\partial}{\partial q_j} +\\
&\left. - \frac{1}{16}\left(\frac{\partial \ln g}{\partial q_i}\right)G^{ij}\left(\frac{\partial \ln g}{\partial q_j}\right)\right] = -\frac{1}{2}\hbar^2 \sum_{i=1}^{3N-6}\sum_{j=1}^{3N-6}\left[\frac{\partial}{\partial q_i}\left(G^{ij}\frac{\partial}{\partial q_j}\right) + \right.\\
&\left. - \frac{1}{4}\left(\frac{\partial G^{ij}}{\partial q_i}\right)\left(\frac{\partial \ln g}{\partial q_j}\right) - \frac{1}{4}G^{ij}\frac{\partial^2 \ln g}{\partial q_i \partial q_j} - \frac{1}{16}\left(\frac{\partial \ln g}{\partial q_i}\right)G^{ij}\left(\frac{\partial \ln g}{\partial q_j}\right)\right].
\end{aligned} \tag{B.4}$$

[a] taking into account a slight rearrangement and avoiding an evident refuse (two plus signs instead of one), in eq. 6.72 of ref. 3.

[b] In other words, the coordinate dependence of the jacobian is included in the wavefunction; indeed, the euclidean volume element can be written in the following manner: $d\tau^{(c)} = dr_{11}dr_{12}dr_{13}dr_{21}...dr_{N3} = J(\mathbf{q})dq_1dq_2dq_3...dq_{3N}$

[c] There is a wrong index in the last equation (3.29) of the original article[269]: the term $\left(\frac{\partial}{\partial S_{k'}} - \frac{1}{4}\frac{\partial \ln g}{\partial S_k}\right)$ should be replaced with $\left(\frac{\partial}{\partial S_{k'}} - \frac{1}{4}\frac{\partial \ln g}{\partial S_{k'}}\right)$

When the normalization convention based on the volume element $d\tau^{(i)}$ is employed, a pseudo-potential term (which does not depend on momenta) can be defined:

$$\hat{V}'(\mathbf{q}) = \frac{1}{8}\hbar^2 \sum_{i=1}^{3N-6}\sum_{j=1}^{3N-6}\left[\left(\frac{\partial G^{ij}}{\partial q_i}\right)\left(\frac{\partial \ln g}{\partial q_j}\right)+G^{ij}\frac{\partial^2 \ln g}{\partial q_i \partial q_j}+\frac{1}{4}\left(\frac{\partial \ln g}{\partial q_i}\right)G^{ij}\left(\frac{\partial \ln g}{\partial q_j}\right)\right]. \tag{B.5}$$

Employing the pseudopotential defined in eq. B.5, the result of eq. B.4 can be written as follows:

$$\hat{T}^{(i)} = -\frac{1}{2}\hbar^2 \sum_{i=1}^{3N-6}\sum_{j=1}^{3N-6}\left[\frac{\partial}{\partial q_i}\left(G^{ij}\frac{\partial}{\partial q_j}\right)\right] + \hat{V}'. \tag{B.6}$$

Eqs. B.6 and B.5 are the same provided, respectively, in eqs. 15 and 20 of ref. 270.

The first formulation of the KEO for generalized coordinate systems (due to Podolski)[123] can be easily recovered employing the following relations:

$$\frac{\partial}{\partial q_i} + \frac{1}{4}\frac{\partial \ln g}{\partial q_i} = g^{-\frac{1}{4}}\frac{\partial}{\partial q_i}g^{\frac{1}{4}} \tag{B.7}$$

$$\frac{\partial}{\partial q_i} - \frac{1}{4}\frac{\partial \ln g}{\partial q_i} = g^{\frac{1}{4}}\frac{\partial}{\partial q_i}g^{-\frac{1}{4}} \tag{B.8}$$

With eqs. B.7 and B.8, the right hand side of eq. B.3 can be rearranged as follows:

$$\hat{T}^{(i)} = -\frac{1}{2}\hbar^2 \sum_{i=1}^{3N-6}\sum_{j=1}^{3N-6} g^{-\frac{1}{4}}\left[\frac{\partial}{\partial q_i}g^{\frac{1}{2}}G^{ij}\left(\frac{\partial}{\partial q_j}g^{-\frac{1}{4}}\right)\right]. \tag{B.9}$$

Eq. B.9 is exactly the formulation suggested by Podolski[123] when the volume element $d\tau^{(i)}$ is adopted for the normalization of the wavefunction. This formulation can be easily partitioned: eq. B.6 is obtained, exactly as in the case of the formulation of Meyer and Günthard. The pseudopotential given in eq. B.5 can be further manipulated:

$$\hat{V}'(\mathbf{q}) = \frac{1}{8}\hbar^2 \sum_{i=1}^{3N-6}\sum_{j=1}^{3N-6}\left[\left(\frac{\partial G^{ij}}{\partial q_i}\right)\left(\frac{\partial \ln g}{\partial q_j}\right) + G^{ij}\frac{\partial^2 \ln g}{\partial q_i \partial q_j} + \frac{1}{4}\left(\frac{\partial \ln g}{\partial q_i}\right)G^{ij}\left(\frac{\partial \ln g}{\partial q_j}\right)\right]$$
$$= \frac{1}{8}\hbar^2 \sum_{i=1}^{3N-6}\sum_{j=1}^{3N-6}\left[\frac{1}{g}\left(\frac{\partial G^{ij}}{\partial q_i}\frac{\partial g}{\partial q_j}\right) + G^{ij}\frac{\partial}{\partial q_i}\left(\frac{1}{g}\frac{\partial g}{\partial q_j}\right) + \frac{G^{ij}}{4g^2}\left(\frac{\partial g}{\partial q_i}\right)\left(\frac{\partial g}{\partial q_j}\right)\right]$$
$$= \frac{1}{8}\hbar^2 \sum_{i=1}^{3N-6}\sum_{j=1}^{3N-6}\left[\frac{1}{g}\left(\frac{\partial G^{ij}}{\partial q_i}\frac{\partial g}{\partial q_j}\right) + \frac{G^{ij}}{g}\left(\frac{\partial^2 g}{\partial q_i \partial q_j}\right) - \frac{G^{ij}}{g^2}\left(\frac{\partial g}{\partial q_i}\right)\left(\frac{\partial g}{\partial q_j}\right) + \right.$$
$$\left. + \frac{G^{ij}}{4g^2}\left(\frac{\partial g}{\partial q_i}\right)\left(\frac{\partial g}{\partial q_j}\right)\right] = \frac{1}{8}\hbar^2 \sum_{i=1}^{3N-6}\sum_{j=1}^{3N-6}\left[\frac{1}{g}\left(\frac{\partial G^{ij}}{\partial q_i}\frac{\partial g}{\partial q_j}\right) + \frac{G^{ij}}{g}\left(\frac{\partial^2 g}{\partial q_i \partial q_j}\right) + \right.$$
$$\left. - \frac{3G^{ij}}{4g^2}\left(\frac{\partial g}{\partial q_i}\right)\left(\frac{\partial g}{\partial q_j}\right)\right]. \tag{B.10}$$

Some authors (see, for example, eq. 3.6 of ref. 129) provide the pseudopotential $\hat{V}'(\mathbf{q})$ with the formulation given in the last term of eq. B.10. A simple prescription can be employed to modify the KEO in curvilinear coordinates when the normalization convention is changed[a]:

$$\hat{T}^{(i)} = g^{\frac{1}{4}}\hat{T}^{(c)}g^{-\frac{1}{4}} \tag{B.11}$$

For example, applying the prescription to eq. B.9, the following expression of the KEO in curvilinear coordinates for a wavefunction normalized with the euclidean volume element will be obtained [123,129]:

$$\hat{T}^{(c)} = -\frac{1}{2}\hbar^2 \sum_{i=1}^{3N-6}\sum_{j=1}^{3N-6} g^{-\frac{1}{2}}\left(\frac{\partial}{\partial q_i}g^{\frac{1}{2}}G^{ij}\frac{\partial}{\partial q_j}\right). \tag{B.12}$$

With simple manipulations, the vibrational part of the formulation given in eq. 2.14 can be easily recovered from eq. B.12.

B.2 The perturbative formulation of the nuclear hamiltonian

In a formulation based on perturbative theory, the terms involved in the hamiltonian matrix are expanded in order of importance with the help of an arbitrary ordering parameter:

[a] See, for example, ref. 123, subsection 6.2.2 of ref. 3 and section 4 of ref. 126; instead of applying the prescription to the KEO, it is possible to obtain the same results applying the same prescription to the single momentum operators appearing in the expression of the kinetic energy.

$$\hat{H} = \hat{H}^0 + \lambda\hat{H}' + \lambda\hat{H}'' + ... \tag{B.13}$$

If the parameter λ is set equal to 1 and the expansion is truncated at second order, eq. B.13 can be written as follows:

$$\hat{H} = \hat{H}^0 + \hat{H}' + \hat{H}'' \tag{B.14}$$

In eqs. B.13 and B.14, $\hat{H}^0$ is the harmonic hamiltonian given in eq. 2.17:

$$\hat{H}^0 = \frac{1}{2}\left(\sum_{k=1}^{3N-6}\hat{P}_k + \sum_{i=1}^{3N-6}\lambda_k\hat{Q}_k^2\right) \tag{B.15}$$

The expression given in eq. B.15 can be formulated in terms of dimensionless operators employing the following transformations and remembering that $\lambda_k = (2\pi c\omega_k)^2$:

$$q_k = \left(\frac{\lambda_k}{\hbar^2}\right)^{\frac{1}{4}}\hat{Q}_k; \tag{B.16}$$

$$p_k = \left(\frac{1}{\lambda_k\hbar^2}\right)^{\frac{1}{4}}\hat{P}_k; \tag{B.17}$$

Where $\hat{Q}_k$ is mass-weighted (with dimensions $[M]^{\frac{1}{2}}[L]$) and $\hat{P}_k$ is defined according to eq. 2.9 (and therefore with dimensions $[M]^{\frac{1}{2}}[L][T]^{-1}$). Employing eqs. B.16 and B.17, $\hat{H}^0$ can be written as follows:

$$\hat{H}^0 = \frac{1}{2}hc\left\{\sum_{k=1}^{3N-6}\omega_k(p_k^2 + q_k^2)\right\} \tag{B.18}$$

Again, exploiting eq. B.16 the Taylor expansion of the potential energy given in eq. 1.21 can be written in the following manner:

$$\hat{V} = hc\left\{\frac{1}{2}\sum_{i=1}^{3N-6}\omega_i q_i^2 + \frac{1}{3!}\sum_{ijr}^{3N-6}\phi_{ijr}q_iq_jq_r + \frac{1}{4!}\sum_{ijrs}^{3N-6}\phi_{ijrs}q_iq_jq_rq_s\right\}. \tag{B.19}$$

ϕ_{ijr} and ϕ_{ijrs} are respectively the cubic and quartic force constants (referred to a potential expanded with non-restrictive summations, see Section 2 of ref. 137 and appendix 1 of ref. 271 for more details). The term $\hat{H}'$ on the right hand side of eq. B.14 is constructed with the cubic contributions to the potential energy of eq. B.19:

$$\hat{H}' = hc\left\{\frac{1}{3!}\sum_{ijr}^{3N-6}\phi_{ijr}q_iq_jq_r\right\}. \tag{B.20}$$

For what concerns the term $\hat{H}''$, it is important to remember that vibrational and rotational wavefunctions are not completely separable. If the vibro-rotational coupling is taken into account, it turns out (see ref. 137 for the derivation) that an additional contribution to the quartic contributions to the potential energy must be included in the expression of $\hat{H}''$, which is the vibrational angular momentum term. Therefore, $\hat{H}''$ can be written as follows:

$$\hat{H}'' = hc\left\{\frac{1}{4!}\sum_{ijrs}^{3N-6}\phi_{ijrs}q_iq_jq_rq_s + \frac{1}{2}\sum_{\alpha\beta}^{3}\mu_{\alpha\beta}\hat{\pi}_\alpha\hat{\pi}_\beta\right\}. \tag{B.21}$$

Equation 2.18 is obtained inserting eqs. B.18, B.20 and B.21 in eq. B.14.

B.3 Separability of the wavefunction beyond the Born-Oppenheimer approximation

In what follows, a generalization of the Born-Oppenheimer (BO) hamiltonian is presented[a]. A brief derivation is provided, and the separability of the first order expansion of its solutions is demonstrated. The eigenfunctions of the hamiltonian adopted in this section are suitable for the calculation of the electronic contribution to the magnetic transition dipole moment, which is equal to zero in the framework of the BO approximation (because $\langle\phi_G \,|\, \hat{\boldsymbol{m}}^{el} \,|\, \phi_G\rangle = 0$ if the BO approximation is employed).

The hamiltonian and the eigenvalue problem The BO approximation can be briefly summarized with eqs. 7-9. The pivotal assumption behind the BO approximation is the commutative property between $\hat{T}_n$ and ϕ_e, namely the equality $\hat{T}_n\phi_e = \phi_e\hat{T}_n$. In other words, the terms of the type[b] $-\frac{1}{2}\frac{\partial^2\phi_e}{\partial\boldsymbol{r}_a^2}$ and $-(\frac{\partial\phi_e}{\partial\boldsymbol{r}_a})\frac{\partial}{\partial\boldsymbol{r}_a}$ are omitted in the BO approximation,[272] and the molecular hamiltonian can be written as follows:

$$\begin{aligned}\hat{H}^{BO}\phi_e(\boldsymbol{\xi};\boldsymbol{r})\chi_{ev}(\boldsymbol{r}) &= [\hat{H}_{el}(\boldsymbol{r}) + \hat{T}_n]\phi_e(\boldsymbol{\xi};\boldsymbol{r})\chi_{ev}(\boldsymbol{r}) \approx \\ &\approx \phi_e(\boldsymbol{\xi};\boldsymbol{r})[E_e(\boldsymbol{r}) + T_n]\chi_{ev}(\boldsymbol{r}) = E_e^v\phi_e(\boldsymbol{\xi};\boldsymbol{r})\chi_{ev}(\boldsymbol{r}).\end{aligned} \tag{B.22}$$

A correction of the first order to the BO approximation can be easily obtained retaining the terms of $\hat{T}_n$ which contain the first order derivatives of ϕ_e (which are omitted in eq. B.22)[c]:

[a] In essence, the derivation proposed in this subsection is based on the material provided in sections 4.1.2 and 4.1.3 of ref. 150.

[b] The following relation holds: $\hat{T}_n\phi_e = -\frac{1}{2}\frac{\partial^2\phi_e}{\partial\boldsymbol{r}_a^2} - (\frac{\partial\phi_e}{\partial\boldsymbol{r}_a})\frac{\partial}{\partial\boldsymbol{r}_a} - \phi_e\frac{1}{2}\frac{\partial^2}{\partial\boldsymbol{r}_a^2}$.

[c] hereafter in this section, the Planck constant is explicitly written (in atomic units, $\hbar = 1$ and therefore can be omitted).

$$\hat{H}^{NBO} = \hat{H}^{BO} - \sum_{j}^{N}\sum_{\alpha}^{3}\left[\frac{\hbar^2}{m_j}\left(\frac{\partial}{\partial r_{j\alpha}}\right)_{el}\left(\frac{\partial}{\partial r_{j\alpha}}\right)_{nucl}\right]. \tag{B.23}$$

In general, the solution of eq. B.23 is a wavefunction which cannot be partitioned to give the product of nuclear and electronic wavefunctions. If the last derivative of eq. B.23 is converted and treated as a classical nuclear velocity coordinate (and not as a quantum mechanical operator), a new parametric dependence is added to the electronic wavefunction and the separability of the solution in a product of nuclear and electronic wavefunctions is retained[273]. Employing the relationship $(\frac{\partial}{\partial r_{j\alpha}})_{nucl} = im_j\frac{\dot{r}_{j\alpha}}{\hbar}$ the molecular hamiltonian can be written in the following manner:

$$\hat{H}^{CA} = \hat{H}^{BO} - i\hbar\sum_{j}^{N}\sum_{\alpha}^{3}\left[\left(\frac{\partial}{\partial r_{j\alpha}}\right)_{el}\dot{r}_{j\alpha}\right]. \tag{B.24}$$

The hamiltonian given in eq. B.24 is often called Complete Adiabatic (CA) Hamiltonian. The electronic part of the CA hamiltonian is the following:

$$\hat{H}^{CA}_{el}(\boldsymbol{r},\dot{\boldsymbol{r}}) = \hat{H}^{BO}_{el}(\boldsymbol{r}) - i\hbar\frac{\partial}{\partial \boldsymbol{r}}\dot{\boldsymbol{r}}. \tag{B.25}$$

The CA electronic wavefunctions are solutions of the eigenvalue problem associated to the hamiltonian operator given in eq. B.25:

$$\hat{H}^{CA}_{el}(\boldsymbol{r},\dot{\boldsymbol{r}})\phi^{CA}_{e}(\boldsymbol{\xi};\boldsymbol{r},\dot{\boldsymbol{r}}) = E^{CA}_{e}(\boldsymbol{r},\dot{\boldsymbol{r}})\phi^{CA}_{e}(\boldsymbol{\xi};\boldsymbol{r},\dot{\boldsymbol{r}}). \tag{B.26}$$

The dependence of the CA electronic wavefunctions on both nuclear positions and velocities is parametric (the parametric variable $\dot{\boldsymbol{r}}$ of eq. B.26 can be converted into the corresponding quantum operator when an integration over the nuclear coordinates is performed, after the determination of the CA electronic wavefunction).

The CA eigenfunctions To show the separability of the CA eigenfunctions, the first order expansion of the CA wavefunctions can be written combining the lowest order of the nonadiabatic BO correction terms[a] and an Herzberg-Teller (HT) expansion . Through the HT expansion the nuclear positions dependence of the electronic wavefunction is taken into account[b]:

[a] Actually, to show the separability of the first order expansion of the CA eigenfunctions only the development of the nonadiabatic BO correction terms is needed (eqs. B.31-B.35).

[b] The superscript 0 for electronic wavefunctions and energies (and the subscript 0 for derivatives) is referred to the nuclear positions

$$\phi_e(\boldsymbol{\xi};\boldsymbol{r}) \approx \phi_e^0(\boldsymbol{\xi}) - \sum_j^N \sum_\alpha^3 \sum_{s\neq e} \left[\frac{\left\langle \phi_s^0 \left| \left(\frac{\partial \hat{H}_{el}^{BO}(\boldsymbol{r})}{\partial r_{j\alpha}} \right)_0 \right| \phi_e^0 \right\rangle}{E_s^0 - E_e^0} \phi_s^0(\boldsymbol{\xi}) r_{j\alpha} \right]. \quad \text{(B.27)}$$

Eq. B.27 can be rewritten in the following manner:

$$\phi_e(\boldsymbol{\xi};\boldsymbol{r}) \approx \phi_e^0(\boldsymbol{\xi}) + \sum_j^N \sum_\alpha^3 \left[\left(\frac{\partial \phi_e(\boldsymbol{\xi})}{\partial r_{j\alpha}} \right)_0 r_{j\alpha} \right]. \quad \text{(B.28)}$$

To derive eq. B.28 starting from eq. B.27, the following relationship has been exploited (see, for example, eq. 6 of ref. 274):

$$\left(\frac{\partial \phi_e(\boldsymbol{\xi})}{\partial r_{j\alpha}} \right)_0 = - \sum_{s\neq e} \left[\frac{\left\langle \phi_s^0 \left| \left(\frac{\partial \hat{H}_{el}^{BO}(\boldsymbol{r})}{\partial r_{j\alpha}} \right)_0 \right| \phi_e^0 \right\rangle}{E_s^0 - E_e^0} \phi_s^0(\boldsymbol{\xi}) \right]. \quad \text{(B.29)}$$

Another expression of the HT expansion (equivalent to eqs. B.27 and B.28) is the following[a]:

$$\phi_e(\boldsymbol{\xi};\boldsymbol{r}) \approx \phi_e^0(\boldsymbol{\xi}) + \sum_{s\neq e} \sum_j^N \sum_\alpha^3 \left[\left\langle \phi_s^0 \left| \left(\frac{\partial \phi_e(\boldsymbol{\xi})}{\partial r_{j\alpha}} \right)_0 \right\rangle r_{j\alpha} \phi_s^0(\boldsymbol{\xi}) \right]. \quad \text{(B.30)}$$

To take into account the nonadiabatic BO correction terms, the term $-\sum_j^N \sum_\alpha^3 \left[\frac{\hbar^2}{m_j} \left(\frac{\partial}{\partial r_{j\alpha}} \right)_{el} \left(\frac{\partial}{\partial r_{j\alpha}} \right)_{nucl} \right]$ (part of the nuclear kinetic energy terms omitted in the BO approximation) is used as perturbation operator:

$$\psi_{ev}^{NBO}(\boldsymbol{\xi},\boldsymbol{r}) \approx \phi_e(\boldsymbol{\xi},\boldsymbol{r}) \chi_{ev}(\boldsymbol{r}) + \\ + \sum_{su\neq ev} \sum_j^N \sum_\alpha^3 \left[\frac{\hbar^2}{m_j} \frac{\left\langle \phi_s \left| \frac{\partial}{\partial r_{j\alpha}} \right| \phi_e \right\rangle \left\langle \chi_{su} \left| \frac{\partial}{\partial r_{j\alpha}} \right| \chi_{ev} \right\rangle}{E_s^u - E_e^v} \phi_s(\boldsymbol{\xi},\boldsymbol{r}) \chi_{su}(\boldsymbol{r}) \right] \quad \text{(B.31)}$$

Although $\psi_{ev}^{NBO}(\boldsymbol{\xi},\boldsymbol{r})$ is a non-separable wavefunction, the RHS of eq. B.31 can be written in the following manner[b]:

[a] To derive eq. B.30 from eqs. B.27-B.29, the relationships $\sum_e \left| \phi_e^0 \right\rangle \left\langle \phi_e^0 \right| = 1$ and $\left\langle \phi_e^0 \left| \left(\frac{\partial \phi_e(\boldsymbol{\xi})}{\partial r_{j\alpha}} \right)_0 \right\rangle = 0$ have been employed (see eq. 2.83 of ref. 150).

[b] the relationship $\left(\frac{\partial}{\partial r_{j\alpha}} \right)_{nucl} = i m_j \frac{\dot{r}_{j\alpha}}{\hbar}$ is used to convert the quantum operator $\left(\frac{\partial}{\partial r_{j\alpha}} \right)_{nucl}$ into its classical analogue.

$$\phi_e(\boldsymbol{\xi},\boldsymbol{r})\chi_{ev}(\boldsymbol{r})+ \\ +i\hbar\sum_{su\neq ev}\sum_{j}^{N}\sum_{\alpha}^{3}\left[\frac{\left\langle\phi_s\left|\frac{\partial}{\partial r_{j\alpha}}\right|\phi_e\right\rangle\langle\chi_{su}\,|\,\chi_{ev}\rangle\,\dot{r}_{j\alpha}}{E_s^u-E_e^v}\phi_s(\boldsymbol{\xi},\boldsymbol{r})\chi_{su}(\boldsymbol{r})\right] \tag{B.32}$$

The energy denominator can be decomposed and approximated[a] as follows[272,273]:

$$\frac{1}{E_s^u-E_e^v}=\frac{1}{E_s^0-E_e^0}-\frac{E_s^u-E_e^v-(E_s^0-E_e^0)}{(E_s^u-E_e^v)(E_s^0-E_e^0)}\approx\frac{1}{E_s^0-E_e^0}. \tag{B.33}$$

Adopting the approximation provided in eq. B.33, the vibronic details of the excited states are neglected and therefore the summation over the excited vibrational states can be carried out with the relationship $\sum_u|\chi_{su}\rangle\langle\chi_{su}|=1$. The expression of eq. B.32 can be rewritten in the following manner:

$$\phi_e(\boldsymbol{\xi},\boldsymbol{r})\chi_{ev}(\boldsymbol{r})+ \\ +i\hbar\sum_{s\neq e}\sum_{j}^{N}\sum_{\alpha}^{3}\left[\frac{\left\langle\phi_s\left|\frac{\partial\phi_e}{\partial r_{j\alpha}}\right\rangle\dot{r}_{j\alpha}\right.}{E_s^0-E_e^0}\phi_s(\boldsymbol{\xi},\boldsymbol{r})\right]\chi_{ev}(\boldsymbol{r}). \tag{B.34}$$

Taking into account eqs. B.31-B.34, the first order expansion of the CA wavefunction (with respect to the nuclear velocities) can be easily written:

$$\psi_{ev}^{CA}(\boldsymbol{\xi},\boldsymbol{r},\dot{\boldsymbol{r}})\approx\left\{\phi_e(\boldsymbol{\xi},\boldsymbol{r})+i\hbar\sum_{s\neq e}\sum_{j}^{N}\sum_{\alpha}^{3}\left[\frac{\left\langle\phi_s^0\left|\left(\frac{\partial\phi_e}{\partial r_{j\alpha}}\right)_0\right\rangle\dot{r}_{j\alpha}\right.}{E_s^0-E_e^0}\phi_s^0(\boldsymbol{\xi})\right]\right\}\chi_{ev}(\boldsymbol{r}). \tag{B.35}$$

If the first term of the RHS of eq. B.35 is expanded (employing the HT expansion, eq. B.30), the first order expansion of the CA wavefunction with respect to nuclear velocities and positions is obtained:

$$\psi_{ev}^{CA}(\boldsymbol{\xi},\boldsymbol{r},\dot{\boldsymbol{r}})\approx\left\{\phi_e^0(\boldsymbol{\xi})+ \right. \\ \left.+\sum_{s\neq e}\sum_{j}^{N}\sum_{\alpha}^{3}\left[\left\langle\phi_s^0\left|\left(\frac{\partial\phi_e}{\partial r_{j\alpha}}\right)_0\right\rangle\phi_s^0(\boldsymbol{\xi})\left(r_{j\alpha}+\frac{i\dot{r}_{j\alpha}}{E_s^0-E_e^0}\right)\right]\right\}\chi_{ev}(\boldsymbol{r}). \tag{B.36}$$

[a] The approximation provided in eq. B.33 is not valid if a molecular system with low-lying electronic states is considered. An extension valid for molecular systems with low-lying electronic states can be found in ref. 275 (and is summarized in appendix C of ref. 150).

In eqs. B.35 and B.36 the separability of the first order expansion of the CA wavefunction in a product of nuclear and elecronic wavefunctions is evident.

The CA eigenvalues The calculation of the CA electronic eigenvalues can be performed employing eq. B.26:

$$E_e^{CA}(\boldsymbol{r},\dot{\boldsymbol{r}}) = \left\langle \phi_e^{CA}(\boldsymbol{\xi};\boldsymbol{r},\dot{\boldsymbol{r}}) \left| \hat{H}_{el}^{CA}(\boldsymbol{r},\dot{\boldsymbol{r}}) \right| \phi_e^{CA}(\boldsymbol{\xi};\boldsymbol{r},\dot{\boldsymbol{r}}) \right\rangle . \tag{B.37}$$

The influence of the velocity perturbation on $E_e^{CA}(\boldsymbol{r},\dot{\boldsymbol{r}})$ can be estimated through first order in perturbation theory[a]:

$$\begin{aligned} &E_e^{CA}(\boldsymbol{r},\dot{\boldsymbol{r}}) \approx \left\langle \phi_e(\boldsymbol{\xi};\boldsymbol{r}) \left| (\hat{H}_{el}^{BO}(\boldsymbol{r}) - i\hbar\frac{\partial}{\partial \boldsymbol{r}}\dot{\boldsymbol{r}}) \right| \phi_e(\boldsymbol{\xi};\boldsymbol{r}) \right\rangle = \\ &\left\langle \phi_e(\boldsymbol{\xi};\boldsymbol{r}) \left| \hat{H}_{el}^{BO}(\boldsymbol{r}) \right| \phi_e(\boldsymbol{\xi};\boldsymbol{r}) \right\rangle - i\hbar \left\langle \phi_e(\boldsymbol{\xi};\boldsymbol{r}) \left| \frac{\partial \phi_e}{\partial \boldsymbol{r}} \right\rangle \dot{\boldsymbol{r}} = \\ &\left\langle \phi_e(\boldsymbol{\xi};\boldsymbol{r}) \left| \hat{H}_{el}^{BO}(\boldsymbol{r}) \right| \phi_e(\boldsymbol{\xi};\boldsymbol{r}) \right\rangle = E_e(\boldsymbol{r}). \end{aligned} \tag{B.38}$$

In eq. B.38, the relationship $\left\langle \phi_e \left| \frac{\partial \phi_e}{\partial r_{j\alpha}} \right\rangle = 0$ has been employed. Therefore, $E_e^{CA}(\boldsymbol{r},\dot{\boldsymbol{r}}) = E_e(\boldsymbol{r})$ through first order in $\dot{\boldsymbol{r}}$: as a consequence, at this level of approximation the CA description does not affect the equilibrium conformational structure, nor the electronic or vibrational energy levels.

B.4 Application of the Magnetic Field Perturbation Theory to the calculation of the electronic contribution to the magnetic transition dipole moment

In what follows the first order approximation of the CA wavefunction derived in the previous section (B.3) is employed to evaluate the transition integral which involves the operator $\hat{\boldsymbol{m}}^{el}$. The Magnetic Field Perturbation Theory (MFPT) proposed by Stephens[276] is exploited in order to avoid the explicit sum over the excited electronic states introduced in the CA wavefunction (see eqs. B.35 and B.36).

Taking into account eq. B.35, the following first order expansions can be written:

$$\psi_{Gg}^{CA} \approx \left[\phi_G + \sum_{i\neq G} C_{G,i}\phi_i\right]\chi_{Gg}; \tag{B.39}$$

[a] See eqs. 10 and 11 of ref. 273.

$$\psi_{Ge}^{CA} \approx \left[\phi_G + \sum_{i\neq G} C_{G,i}\phi_i\right]\chi_{Ge}; \tag{B.40}$$

where:

$$C_{G,i} = i\hbar \sum_j^N \sum_\alpha^3 \left[\frac{\left\langle \phi_i \left| \left(\frac{\partial \phi_G}{\partial r_{j\alpha}}\right)\right\rangle \dot{r}_{j\alpha}}{E_i^0 - E_G^0}\right] = \sum_j^N \sum_\alpha^3 \left[\frac{\hbar^2}{m_j}\frac{\left\langle \phi_i \left| \left(\frac{\partial \phi_G}{\partial r_{j\alpha}}\right)\right\rangle}{E_i^0 - E_G^0}\frac{\partial}{\partial r_{j\alpha}}\right]. \tag{B.41}$$

Employing the CA wavefunction for the evaluation of the transition integral involving the operator $\hat{\boldsymbol{m}}^{el}$ and expanding the CA wavefunction through first order perturbation theory (eqs. B.39-B.41), the transition integral can be developed as follows:

$$\begin{aligned}
&\left\langle \psi_{Gg}^{CA} \left| \hat{\boldsymbol{m}}^{el} \right| \psi_{Ge}^{CA} \right\rangle \approx \left\langle \phi_G\chi_{Gg} \left| \hat{\boldsymbol{m}}^{el} \right| \phi_G\chi_{Ge} \right\rangle + \sum_{i\neq G}\left[C_{G,i}\left\langle \phi_G\chi_{Gg} \left| \hat{\boldsymbol{m}}^{el} \right| \phi_i\chi_{Ge} \right\rangle\right] \\
&+ \sum_{i\neq G}\left[C_{G,i}^*\left\langle \phi_i\chi_{Gg} \left| \hat{\boldsymbol{m}}^{el} \right| \phi_G\chi_{Ge} \right\rangle\right] + \sum_{i\neq G}\sum_{j\neq G}\left[C_{G,i}^* C_{G,j}\left\langle \phi_i\chi_{Gg} \left| \hat{\boldsymbol{m}}^{el} \right| \phi_j\chi_{Ge} \right\rangle\right] = \\
&\sum_{i\neq G}\left[C_{G,i}\left\langle \phi_G\chi_{Gg} \left| \hat{\boldsymbol{m}}^{el} \right| \phi_i\chi_{Ge} \right\rangle\right] + \sum_{i\neq G}\left[C_{G,i}^*\left\langle \phi_i\chi_{Gg} \left| \hat{\boldsymbol{m}}^{el} \right| \phi_G\chi_{Ge} \right\rangle\right] = \\
&\sum_{i\neq G}\left[C_{G,i}\left\langle \phi_G\chi_{Gg} \left| \hat{\boldsymbol{m}}^{el} \right| \phi_i\chi_{Ge} \right\rangle\right] - \sum_{i\neq G}\left[C_{G,i}^*\left\langle \phi_G\chi_{Ge} \left| \hat{\boldsymbol{m}}^{el} \right| \phi_i\chi_{Gg} \right\rangle\right]
\end{aligned} \tag{B.42}$$

In eq. B.42, the term which involves the double summation has been omitted (it is a second order term, while the first order terms only are needed for the purposes here considered) and the BO term vanishes[a]. The results of eq. B.42 are the starting point of a treatment based on the MFPT[276] (the approximation provided in eq. B.33 is often introduced in a later stage, while in the derivation given in this thesis has been already introduced for the construction of the CA wavefunction).

The essential step of the MFPT is the recognition[276] in the results of eq. B.42 (more specifically, in the summation over the excited states) of a first order perturbative term due to a magnetic field $\boldsymbol{\mathcal{B}}$. Employing the interaction operator $-\hat{\boldsymbol{m}}^{el}\cdot\boldsymbol{\mathcal{B}}$ the following result can be easily obtained through first order perturbation theory:

$$\frac{\partial \phi_G}{\partial \boldsymbol{\mathcal{B}}} = \sum_{i\neq G}\frac{\left\langle \phi_i \left| \hat{\boldsymbol{m}}^{el} \right| \phi_G \right\rangle}{E_i^0 - E_G^0}\phi_i. \tag{B.43}$$

[a] the operator $\hat{\boldsymbol{m}}^{el}$ is hermitian and purely imaginary; therefore, if the electronic and nuclear wavefunctions are real, the following properties hold (both employed in eq. B.42): $\left\langle \phi_G\chi_{Gg} \left| \hat{\boldsymbol{m}}^{el} \right| \phi_G\chi_{Ge} \right\rangle = 0$ and $\left\langle \phi_i\chi_{Gg} \left| \hat{\boldsymbol{m}}^{el} \right| \phi_G\chi_{Ge} \right\rangle = -\left\langle \phi_G\chi_{Ge} \left| \hat{\boldsymbol{m}}^{el} \right| \phi_i\chi_{Gg} \right\rangle$.

The derivation provided in what follows is close to the one given in section II D of ref. 157. The aim is to provide a formulation suitable for the calculation of anharmonic VCD intensities. The first term after the last equality of eq. B.42 can be rewritten in the following manner:

$$\begin{aligned}
&\sum_{i\neq G}\left[C_{G,i}\left\langle\phi_G\chi_{Gg}\left|\,\hat{\boldsymbol{m}}^{el}\,\right|\phi_i\chi_{Ge}\right\rangle\right]=\left\langle\chi_{Gg}\left|\sum_{i\neq G}\left[C_{G,i}\left\langle\phi_G\left|\,\hat{\boldsymbol{m}}^{el}\,\right|\phi_i\right\rangle\right]\right|\chi_{Ge}\right\rangle=\\
&\left\langle\chi_{Gg}\left|\sum_{j}^{N}\sum_{\alpha}^{3}\left[\frac{\hbar^2}{m_j}\sum_{i\neq G}\frac{\left\langle\phi_G\left|\,\hat{\boldsymbol{m}}^{el}\,\right|\phi_i\right\rangle\left\langle\phi_i\left|\left(\frac{\partial\phi_G}{\partial r_{j\alpha}}\right)\right.\right\rangle}{E_i^0-E_G^0}\frac{\partial}{\partial r_{j\alpha}}\right]\right|\chi_{Ge}\right\rangle=\\
&-\left\langle\chi_{Gg}\left|\sum_{j}^{N}\sum_{\alpha}^{3}\left[\frac{\hbar^2}{m_j}\sum_{i\neq G}\frac{\left\langle\left(\frac{\partial\phi_G}{\partial r_{j\alpha}}\right)\right|\left.\phi_i\right\rangle\left\langle\phi_i\left|\,\hat{\boldsymbol{m}}^{el}\,\right|\phi_G\right\rangle}{E_i^0-E_G^0}\frac{\partial}{\partial r_{j\alpha}}\right]\right|\chi_{Ge}\right\rangle=\\
&-\left\langle\chi_{Gg}\left|\sum_{j}^{N}\sum_{\alpha}^{3}\left[\frac{\hbar^2}{m_j}\left\langle\frac{\partial\phi_G}{\partial r_{j\alpha}}\right|\left.\frac{\partial\phi_G}{\partial\boldsymbol{\mathcal{B}}}\right\rangle\frac{\partial}{\partial r_{j\alpha}}\right]\right|\chi_{Ge}\right\rangle=\\
&-\left\langle\chi_{Gg}\left|\sum_{j}^{N}\sum_{\alpha}^{3}\left[\frac{\hbar^2}{m_j}\boldsymbol{\mathcal{A}}_{j\alpha}\frac{\partial}{\partial r_{j\alpha}}\right]\right|\chi_{Ge}\right\rangle.
\end{aligned}\tag{B.44}$$

$\boldsymbol{\mathcal{A}}$ is the symbol of the electronic part of the AAT, which is defined as $\boldsymbol{\mathcal{A}}_{j\alpha\beta}=\left\langle\frac{\partial\phi_G}{\partial r_{j\alpha}}\right|\left.\frac{\partial\phi_G}{\partial\mathcal{B}_\beta}\right\rangle$. In eq. B.44, the nature of $\hat{\boldsymbol{m}}^{el}$ (purely imaginary and hermitian) and of ϕ (the electronic wavefunctions are assumed to be real)[a] have been employed together with the relationship given in eq. B.43. An analogous procedure can be employed for the development of the second term after the last equality of eq. B.42:[b]

$$\sum_{i\neq G}\left[C_{G,i}^{*}\left\langle\phi_G\chi_{Ge}\left|\,\hat{\boldsymbol{m}}^{el}\,\right|\phi_i\chi_{Gg}\right\rangle\right]=-\left\langle\chi_{Ge}\left|\sum_{j}^{N}\sum_{\alpha}^{3}\left[\frac{\hbar^2}{m_j}\boldsymbol{\mathcal{A}}_{j\alpha}\frac{\partial}{\partial r_{j\alpha}}\right]\right|\chi_{Gg}\right\rangle.\tag{B.45}$$

If the results given in eqs. B.44 and B.45 are inserted in eq. B.42, the following expression is obtained:

[a] The following relations are consequences of these properties: $\left\langle\phi_i\chi_{Gg}\left|\,\hat{\boldsymbol{m}}^{el}\,\right|\phi_G\chi_{Ge}\right\rangle=-\left\langle\phi_G\chi_{Ge}\left|\,\hat{\boldsymbol{m}}^{el}\,\right|\phi_i\chi_{Gg}\right\rangle$ and $\left\langle\phi_i\left|\left(\frac{\partial\phi_G}{\partial r_{j\alpha}}\right)\right.\right\rangle=\left\langle\left(\frac{\partial\phi_G}{\partial r_{j\alpha}}\right)\right|\left.\phi_i\right\rangle$.

[b] The purely quantum mechanical form of $C_{G,i}$ is real (see eq. B.41) and therefore $C_{G,i}^{*}=C_{G,i}$.

$$\left\langle \psi_{Gg}^{CA} \middle| \hat{\boldsymbol{m}}^{el} \middle| \psi_{Ge}^{CA} \right\rangle \approx \sum_{j}^{N} \sum_{\alpha}^{3} \left[\frac{\hbar^2}{m_j} \left(\left\langle \chi_{Ge} \middle| \boldsymbol{\mathcal{A}}_{j\alpha} \frac{\partial}{\partial r_{j\alpha}} \middle| \chi_{Gg} \right\rangle - \left\langle \chi_{Gg} \middle| \boldsymbol{\mathcal{A}}_{j\alpha} \frac{\partial}{\partial r_{j\alpha}} \middle| \chi_{Ge} \right\rangle \right) \right]. \tag{B.46}$$

In the formulation of the electronic contribution to the vibrational magnetic transition dipole moment provided in eq. B.46 (and derived employing first order perturbation theory)[a] the AAT depends on the nuclear positions. In the original formulation based on MFPT the elements of the AAT $\mathcal{A}_{j\alpha\beta}(\boldsymbol{r})$ are approximated by their values at the equilibrium geometry of the molecular system investigated ($\mathcal{A}^0_{j\alpha\beta}$). With this approximation, the original formulation can be easily recovered[b] as showed in section II F of ref. 157:

$$\begin{aligned} &\sum_{j}^{N} \sum_{\alpha}^{3} \left[\frac{\hbar^2}{m_j} \left(\left\langle \chi_{Ge} \middle| \boldsymbol{\mathcal{A}}_{j\alpha}(\boldsymbol{r}) \frac{\partial}{\partial r_{j\alpha}} \middle| \chi_{Gg} \right\rangle - \left\langle \chi_{Gg} \middle| \boldsymbol{\mathcal{A}}_{j\alpha}(\boldsymbol{r}) \frac{\partial}{\partial r_{j\alpha}} \middle| \chi_{Ge} \right\rangle \right) \right] \approx \\ &\sum_{j}^{N} \sum_{\alpha}^{3} \left[\frac{\hbar^2 \boldsymbol{\mathcal{A}}^0_{j\alpha}}{m_j} \left(\left\langle \chi_{Ge} \middle| \frac{\partial}{\partial r_{j\alpha}} \middle| \chi_{Gg} \right\rangle - \left\langle \chi_{Gg} \middle| \frac{\partial}{\partial r_{j\alpha}} \middle| \chi_{Ge} \right\rangle \right) \right] = \\ &- \sum_{j}^{N} \sum_{\alpha}^{3} \left[\frac{2\hbar^2 \boldsymbol{\mathcal{A}}^0_{j\alpha}}{m_j} \left\langle \chi_{Gg} \middle| \frac{\partial}{\partial r_{j\alpha}} \middle| \chi_{Ge} \right\rangle \right]. \end{aligned} \tag{B.47}$$

The result of eq. B.47 is equal to the electronic part of eq. 40 of ref. 157.

B.5 More details on the local mode approximation

In what follows the protocols employed to calculate the quantities involved in the expressions of energies (eq. 2.30) and intensities (IR, eq. 2.53, and VCD, eq. 2.54) are briefly summarized.

[a] To the best of the authors' knowledge, the first derivation of a general formulation explicitly taking into account the dependence of the AAT values from the nuclear positions is given in ref. 157; the formulation given in ref. 157 (and in this thesis) was employed in ref. 145 for what concerns local mode approximation and in ref. 149 to provide a formulation of VCD intensities based on VPT2 method (and extended to two quanta vibrational transitions, in contrast with the formulation given in ref. 157 which is suitable only for fundamental vibrational transitions).

[b] Bearing in mind that the operator $\frac{\partial}{\partial r_{j\alpha}}$ (which is not hermitian) is antysimmetric for what concerns the exchange of wavefunctions (see section II of ref. 272 or section II of ref. 273), i.e. $\left\langle \chi_{Ge} \middle| \frac{\partial}{\partial r_{j\alpha}} \middle| \chi_{Gg} \right\rangle = - \left\langle \chi_{Gg} \middle| \frac{\partial}{\partial r_{j\alpha}} \middle| \chi_{Ge} \right\rangle$.

The evaluation of ω_l and χ_{ll} is performed numerically. A series of calculations is performed, each one corresponding to a different value of the X—H internuclear distance z: quadratic ($\frac{\partial^2 V}{\partial z^2}$, labeled as ϕ_{ll}), cubic ($\frac{\partial^3 V}{\partial z^3}$, labeled as ϕ_{lll}) and quartic ($\frac{\partial^4 V}{\partial z^4}$, labeled as ϕ_{llll}) force constants are evaluated by a polynomial fitting of the energy associated to the different value of z. The key assumption is the description of the energy dependence on the internuclear distance z through a Morse potential; with this assumption, ω_l can be easily obtained from ϕ_{ll}[a]:

$$\omega_l = \frac{1}{2\pi c}\sqrt{\frac{\phi_{ll}}{\mu_{XH}}}, \tag{B.48}$$

while χ_{ll} is calculated employing ϕ_{ll}, ϕ_{lll} and ϕ_{llll}:[b]

$$\chi_{ll} = -\frac{h}{64\pi^2 \mu_{XH} c}\left(\frac{5}{3}\frac{\phi_{lll}^2}{\phi_{ll}^2} - \frac{\phi_{llll}}{\phi_{ll}}\right) \tag{B.49}$$

For what concerns the intensities, $\mathbf{\Pi}^0$ and $\boldsymbol{\mathcal{A}}^0$ can be easily extracted from the output of an harmonic frequency calculation[c], while the first derivatives (the so-called electrical and magnetic anharmonicities) of their xz, yz and zz components (for atoms X and H) can be easily obtained from the first-order terms of a polynomial interpolation of these components versus the internuclear distance z.

B.6 Identification and treatment of resonances

The reliability of calculations based on VPT2 approximation depend on the availability of a computational protocol to identify and treat resonances. Effects of resonances can be particularly relevant: this is the case of the anharmonic corrections for molecular systems with an high number of atoms.[d] In what follows, a brief account of this topic is provided for the interested reader.

Identification of resonances The following account is focused on FRs. The simplest protocol which can be employed to identify two resonant states is based on the numerical value of Δ (with $\Delta = |2\omega_i - \omega_j|$ for FRs of type 1 and $\Delta = |\omega_i + \omega_k - \omega_j|$ for FRs of type 2). If Δ is smaller than a certain threshold (chosen by the operator) the states are classified as resonant,

[a] see eq. 14 of ref. 147 and eq. 6 of ref. 277.

[b] See eq. 7 of ref. 277; see also section 2 of ref. 147.

[c] the implicit assumption is the employment of a quantum chemical software which provides the numerical values needed to set up $\mathbf{\Pi}$ and $\boldsymbol{\mathcal{A}}$ (this is the case of the Gaussian [12] suite of programs).

[d] And therefore with an high number of internal degrees of freedom.

otherwise not. This simple criterium provides a numerical estimation of potentially divergent terms of diagonal and off-diagonal anharmonicity constants (see eqs. 2.23 and 2.24). However, this estimation is based uniquely on the magnitude of the denominator. An additional test to identify resonant states was proposed by Martin and coworkers.[139] In this section, an account of the Martin's test for FRs of type 1 is provided.[a]

Given a potential FR of type 1 ($2\omega_i \approx \omega_j$), the first step is the calculation of the numerical difference between full (χ_{ii} and χ_{ij}) and deperturbed (χ^*_{ii} and χ^*_{ij}) anharmonicity constants:[b]

[a] The conceptual framework of the Martin's test can be employed also for the identification of FRs of type 2 (see appendix A of ref. 139).

[b] To write the expression of χ^*_{ii} and χ^*_{ij}, eqs. 2.23 and 2.24 can be employed. In the case of χ_{ii}, eq. 2.23 can be easily rewritten as follows:[139]

$$\chi_{ii} = \frac{\phi_{iiii}}{16} - \sum_{j=1}^{3N-6} \frac{(8\omega_i^2 - 3\omega_j^2)\phi_{iij}^2}{16\omega_j(4\omega_i^2 - \omega_j^2)}; \tag{B.50}$$

where the second term on the RHS side of eq. 2.23 is included in the summation of the last term on the RHS of eq. B.50 (which is not restricted to $j \neq i$, in contrast with eq. 2.23). The term involved in the summation (RHS of eq. B.50) can be factored in the following manner:

$$\frac{(8\omega_i^2 - 3\omega_j^2)\phi_{iij}^2}{16\omega_j(4\omega_i^2 - \omega_j^2)} = \frac{\phi_{iij}^2}{32}\left(\frac{1}{2\omega_i + \omega_j} + \frac{4}{\omega_j} - \frac{1}{2\omega_i - \omega_j}\right); \tag{B.51}$$

where the last term on the RHS of eq. B.51 is the potentially divergent term (the denominator approaches zero when $2\omega_i \approx \omega_j$). The expression of χ^*_{ii} is equal to the expression of χ_{ii}, except for the last term on the RHS of eq. B.51 (the potentially divergent term), which is removed from the expression of χ^*_{ii}.

χ_{ij} can be rewritten in the following manner:

$$\begin{aligned}\chi_{ij} =& \frac{\phi_{iijj}}{4} - \sum_{r=1}^{3N-6} \frac{\phi_{iir}\phi_{jjr}}{4\omega_r} + \sum_{r=1}^{3N-6}\left[\frac{\omega_r(\omega_i^2 + \omega_j^2 - \omega_r^2)\phi_{ijr}^2}{2\Delta_{ijr}}\right] \\ &+ \frac{(\omega_i^2 + \omega_j^2)}{\omega_i\omega_j} \sum_{\alpha=a,b,c} B_\alpha^{eq}\{\zeta_{ij}^\alpha\}^2;\end{aligned} \tag{B.52}$$

where second and third terms on the RHS of eq. 2.24 are collected in the sum of the third term on the RHS of eq. B.52; similarly, fourth and fifth terms on the RHS of eq. 2.24 are collected in the sum of the second term on the RHS of eq. B.52 (in eq. A2 of ref. 139 the sign of the third term on the RHS is different, because $\Delta_{ijr} = -\Omega_{ijr}$). The terms involved in the summation (third term on the RHS of eq. B.52) can be factored as follows:

$$\begin{aligned}-\frac{2\omega_r(\omega_i^2 + \omega_j^2 - \omega_r^2)\phi_{ijr}^2}{2\Delta_{ijr}} =& \frac{\phi_{ijr}^2}{8}\left(\frac{1}{\omega_i + \omega_j + \omega_r} + \frac{1}{-\omega_i + \omega_j + \omega_r}\right. \\ &\left. + \frac{1}{\omega_i - \omega_j + \omega_r} - \frac{1}{\omega_i + \omega_j - \omega_r}\right);\end{aligned} \tag{B.53}$$

where the potentially divergent term is explicitly provided. As for the diagonal anharmonicity constants, χ^*_{ij} is equal to χ_{ij} except for the absence of the potentially divergent term (the third one on the RHS of eq. B.53).

$$\chi_{ii} - \chi^*_{ii} = \frac{\phi^2_{iij}}{32}\left(\frac{1}{2\omega_i - \omega_j}\right) = \frac{\phi^2_{iij}}{32\Delta}; \tag{B.54}$$

$$\chi_{ij} - \chi^*_{ij} = -\frac{\phi^2_{iji}}{8}\left(\frac{1}{\omega_i - \omega_j + \omega_i}\right) = -\frac{\phi^2_{iij}}{8\Delta}. \tag{B.55}$$

Eqs. B.54 and B.55 can be employed to calculate the following differences between standard and deperturbed anharmonic transition frequencies:

$$[2\nu_i] - [2\nu_i]^* = 6(\chi_{ii} - \chi^*_{ii}) + (\chi_{ij} - \chi^*_{ij}) = \frac{\phi^2_{iij}}{16\Delta}; \tag{B.56}$$

$$\nu_j - \nu^*_j = \frac{1}{2}(\chi_{ij} - \chi^*_{ij}) = -\frac{\phi^2_{iij}}{16\Delta}. \tag{B.57}$$

With eqs. B.56 and B.57, the numerical contribution of the potentially divergent terms in the framework of second order perturbation theory (Δ_{PT2}) can be written as follows (for FRs of type 1):[a]

$$2\Delta_{PT2} = \Big([2\nu_i] - \nu_j\Big) - \Big([2\nu_i]^* - \nu^*_j\Big) = \frac{\phi^2_{iij}}{8\Delta}. \tag{B.58}$$

The essential idea behind the Martin's test is to compare the numerical contribution of potentially divergent terms in the perturbative framework (Δ_{PT2}) with the numerical contribution Δ_{var} obtained with a variational treatment. To obtain Δ_{var}, a simple hamiltonian is constructed:[b]

$$\begin{bmatrix} [2\nu_i]^* & K_{ij} \\ K_{ij} & \nu^*_j \end{bmatrix} = \begin{bmatrix} \overline{\nu}^* + \Delta^* & K_{ij} \\ K_{ij} & \overline{\nu}^* - \Delta^* \end{bmatrix}; \tag{B.59}$$

where $\overline{\nu}^*$ is the average frequency of the deperturbed states $[2\nu_i]^*$ and ν^*_j, Δ^* is their separation from the average value ($\Delta^* = \frac{|[2\nu_i]^* - \nu^*_j|}{2}$). The eigenvalues of the matrix B.59 can be easily written:

$$\nu_\pm = \overline{\nu}^* \pm \Delta^* \sqrt{1 + \frac{K^2_{ij}}{\Delta^{*2}}}. \tag{B.60}$$

Eq. B.60 can be easily developed with a Taylor series:

$$\overline{\nu}^* \pm \Delta^* \sqrt{1 + \frac{K^2_{ij}}{\Delta^{*2}}} \approx \overline{\nu}^* \pm \Delta^* \pm \frac{K^2_{ij}}{2\Delta^*} \mp \frac{K^4_{ij}}{8\Delta^{*3}} + \dots. \tag{B.61}$$

With the following two assumptions:

[a] Actually, in eq. B.58 the numerical contribution of the potentially divergent terms is referred to two different states ($[2\nu_i]$ and ν_j). Therefore, the result is equal to $2\Delta_{PT2}$.

[b] In eq. B.59, $[2\nu_i]^*$ and ν^*_j states interact between them but not with other states.

$$2\Delta^* \approx \Delta; \tag{B.62}$$

$$K_{ij} = \sqrt{\frac{\phi_{iij}^2}{16}} = \frac{\phi_{iij}}{4}; \tag{B.63}$$

eq. B.60 can be rewritten and developed as follows:

$$\begin{aligned} \nu_{\pm} = \overline{\nu}^* \pm \Delta^* \sqrt{1 + \frac{K_{ij}^2}{\Delta^{*2}}} = \overline{\nu}^* \pm \frac{\Delta}{2} \sqrt{1 + \frac{\phi_{iij}^2}{4\Delta^2}} \approx \\ \overline{\nu}^* \pm \frac{\Delta}{2} \pm \frac{\phi_{iij}^2}{16\Delta} \mp \frac{\phi_{iij}^4}{256\Delta^3} + \dots . \end{aligned} \tag{B.64}$$

Δ_{var} can be defined in the following manner:

$$\nu_{\pm} = \overline{\nu}^* \pm \frac{\Delta}{2} \pm \Delta_{var} \approx \overline{\nu}^* \pm \frac{\Delta}{2} \pm \frac{\phi_{iij}^2}{16\Delta} \mp \frac{\phi_{iij}^4}{256\Delta^3} + \dots . \tag{B.65}$$

To estimate the magnitude of the resonance, eqs. B.58 and B.65 can be employed. More specifically, the Martin's test evaluate the magnitude of the following difference:

$$|\Delta_{var} - \Delta_{PT2}| \approx \frac{\phi_{iij}^4}{256\Delta^3}. \tag{B.66}$$

In other words, to evaluate whether or not a resonance should be explicitly included in a subsequent variational procedure[a] the following conditions can be employed:

$$\Delta < t_1; \tag{B.67}$$

$$|\Delta_{var} - \Delta_{PT2}| > t_2; \tag{B.68}$$

where t_1 and t_2 are parameters chosen by the operator. In the Gaussian suite of programs, this computational protocol is the default one for the identification of resonances.

Despite its usefulness, the computational protocol based on inequalities B.67 and B.68 have two important limitations. The first is the need of two parameters (t_1 and t_2) which are somewhat arbitrary. To overcome this limitation, another computational protocol (proposed by Truhlar and coworkers)[278] can be employed.[b] The second limitation is the limited reliability of eq. B.68 to estimate the impact of FRs on IR and VCD intensities: a

[a] And therefore excluded from the perturbative treatment.

[b] Far from resonances, the reliability of the computational protocol proposed in ref. 278 is limited.

FR which has a little impact on transition frequencies (and therefore do not satisfy the inequality B.68) can have a relevant effect on IR and VCD intensities. In order to address this problem, a computational protocol to estimate the impact of resonances on dipole and rotational strengths was proposed in ref. 162 (and employed for the simulation of IR and VCD spectra provided in section 2.4.1 of this thesis).

Treatment of identified resonances An explicit treatment of resonances can be performed in different ways. For simplicity, in this paragraph only the correction of anharmonic transition frequencies is addressed. A possible solution is the removal of the resonant terms from the anharmonicity constants: this simple procedure is known as Deperturbed VPT2 (DVPT2).[279] An alternative is the systematic replacement of all potentially resonant terms with a correction devised to assure the non-resonant formulation of $\boldsymbol{\chi}$.[278] This protocol is known as Degeneracy-corrected PT2 (DCPT2). Another approach was proposed in ref. 280: the idea is to combine the best of DCPT2 and VPT2 approaches. More specifically, the VPT2 protocol is employed far from resonances, while the DCPT2 approach is employed for the correction of resonant terms. This approach is known as Hybrid DCPT2 (HDCPT2).

The approach employed for almost all the anharmonic calculations presented in this thesis (see section 2.4) is known as Generalized VPT2 (GVPT2). The idea behind this approach is simple. Resonant terms are identified through a suitable computational protocol[a] and removed from the perturbative treatment: therefore, the first step is a DVPT2 calculation. After this first step, the DVPT2 results and the contributions due to the resonant terms are employed to build a matrix. This matrix has the following structure: DVPT2 energies are included in the diagonal positions and the interaction terms (due to resonances) are inserted in the off-diagonal positions.[b] The diagonalization of this matrix (i.e. a variational step) lead to the GVPT2 energies.[c]

[a] For example, the Martin's test introduced in the previous paragraph.

[b] For the sake of clearness, the following one is an example:

$$\begin{bmatrix}
\ddots & \vdots & \vdots & \vdots & \vdots & \vdots & \vdots & \iddots \\
\dots & \epsilon^{DVPT2}_{\nu_i} & 0 & \dots & 0 & \dots & K_{i,m} & \dots \\
\dots & 0 & \epsilon^{DVPT2}_{\nu_j} & \dots & K_{j,kl} & \dots & 0 & \dots \\
\dots & \vdots & \vdots & \ddots & \dots & \dots & \dots & \dots \\
\dots & 0 & K_{j,kl} & \vdots & \epsilon^{DVPT2}_{[\nu_k \nu_l]} & \dots & 0 & \dots \\
\dots & \vdots & \vdots & \vdots & \vdots & \ddots & \dots & \dots \\
\dots & K_{i,m} & 0 & \vdots & 0 & \vdots & \epsilon^{DVPT2}_{[2\nu_m]} & \dots \\
\iddots & \vdots & \vdots & \vdots & \vdots & \vdots & \vdots & \ddots
\end{bmatrix}; \tag{B.69}$$

where a FR of type 1 ($2\omega_m \approx \omega_i$) and a FR of type 2 ($\omega_k + \omega_l \approx \omega_j$) were previously identified.

[c] For an early example of this approach, see ref. 281.

B.7 More details on the computational characterization of $\mathbf{5}-R_p$ and $\mathbf{5}-S_p$

For what concerns molecular systems **1**, **2**, **3** and **4** additional data (not given in this thesis) can be easily found in the original article. This is not the case of $\mathbf{5}-R_p$ and $\mathbf{5}-S_p$, because experimental and computational data concerning IR and VCD spectra of these compounds have not been published yet. Therefore, in what follows structures (figs. B.2-B.11), populations (table B.1), IR and VCD spectra (fig. B.1, see tables B.2 and B.3 for their assignment) of the five most populated conformers of $\mathbf{5}-R_p$ and $\mathbf{5}-S_p$ are provided.

conformer	population	conformer	population
I_{R_p}	35.67%	I_{S_p}	35.14%
II_{R_p}	32.43%	II_{S_p}	23.74%
III_{R_p}	14.90%	III_{S_p}	23.07%
IV_{R_p}	12.35%	IV_{S_p}	11.30%
V_{R_p}	4.65%	V_{S_p}	6.74%

Table B.1: populations of the relevant conformers calculated through Boltzmann distribution (employing free energies and assuming a temperature of 298 K); structures optimized at B3PW91/Def2TZVP level of theory; frequencies calculated at B3PW91/Def2TZVP level of theory; solvent effects taken into account with PCM.

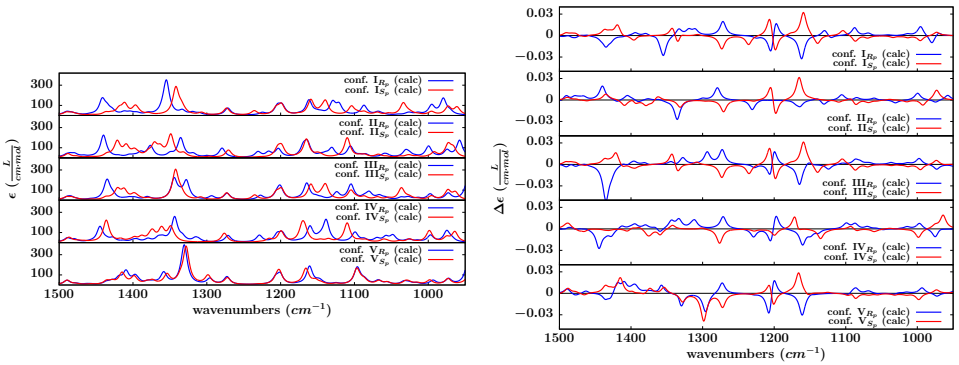

Figure B.1: IR and VCD spectra of the five most populated conformers of $\mathbf{5}-R_p$ and $\mathbf{5}-S_p$, calculated at harmonic level with Lorentzian bandshapes (with bandwidths of 10 cm^{-1}). Level of theory: B3PW91/Def2TZVP. Solvent effects taken into account with PCM.

nor. mo.	conf. I_{Rp} (pop. 35.67%)				nor. mo.	conf. II_{Rp} (pop. 32.43%)			
	E(cm^{-1})	D[1]	R[2]	description		E(cm^{-1})	D[1]	R[2]	description
88	1151.11	44.5	5.6	mainly OH bending (IprOH[3])	89	1163.73	315.9	-46.7	mainly symmetric SO stretchings
89	1161.65	355.5	-198.6	mainly symmetric SO stretchings	90	1169.23	225.3	-21.8	skeletal deformations and CH bendings (sCp[4], IprOH[3])
90	1175.06	14.0	-4.0	skeletal deformations and CH bendings (sCp[4], IprOH[3])	91	1177.51	0.2	0.1	in plane CH bendings (ph[5])
91	1178.25	0.2	-0.3	in plane CH bendings (ph[5])	92	1201.24	1.3	-0.4	in plane CH bendings (ph[5])
92	1197.97	195.3	168.5	skeletal deformations and CH bendings (sCp[4], IprOH[3])	93	1203.14	193.2	0.2	skeletal deformations and CH bendings (sCp[4], IprOH[3])
93	1203.80	95.8	-98.2	mainly in plane CH bendings (ph[5])	94	1216.36	110.3	5.9	skeletal deformations and CH bendings (sCp[4], IprOH[3])
94	1204.59	98.9	-86.7	mainly in plane CH bendings (ph[5])	95	1230.65	123.2	-77.5	C*H bending, C*C stretching and in plane CH bendings (ph[5])
95	1224.86	51.5	-16.1	C*H bending and C*C stretching	96	1279.31	203.7	89.4	skeletal deformations and CH bendings (sCp[4], IprOH[3])
96	1271.60	158.3	108.6	skeletal deformations and CH bendings (sCp[4], IprOH[3])	97	1279.73	1.8	5.8	in plane CH bendings (uCp[6])
97	1281.88	0.3	0.9	in plane CH bendings (uCp[6])	98	1299.89	23.0	12.5	C*H bending, NH bending and in plane CH bendings (ph[5])

Table B.2: Transition frequencies, dipole strengths and rotational strengths of the most populated conformers of $\mathbf{5} - R_p$.

nor. mo.	conf. I_{Sp} (pop. 35.14%)				nor. mo.	conf. II_{Sp} (pop. 23.75%)			
	E(cm^{-1})	D[1]	R[2]	description		E(cm^{-1})	D[1]	R[2]	description
88	1152.50	7.2	7.6	mainly OH bending and symmetric SO stretchings	89	1165.09	438.4	190.8	mainly OH bending and symmetric SO stretchings
89	1159.15	359.9	198.4	mainly OH bending and symmetric SO stretchings	90	1174.76	12.6	0.9	skeletal deformations, CH and OH bendings (sCp[4], IprOH[3])
90	1176.48	0.6	0.8	in plane CH bendings (ph[5])	91	1178.58	0.1	0.2	in plane CH bendings (ph[5])
91	1176.60	16.0	11.7	skeletal deformations, CH and OH bendings (sCp[4], IprOH[3])	92	1198.69	229.2	-190.8	skeletal deformations and CH bendings (sCp[4], IprOH[3])
92	1195.69	5.0	3.6	in plane CH bendings (ph[5])	93	1200.40	3.1	1.5	in plane CH bendings (ph[5])
93	1198.97	231.4	-181.4	skeletal deformations and CH bendings (sCp[4], IprOH[3])	94	1204.02	181.4	179.4	skeletal deformations, CH and OH bendings (sCp[4], IprOH[3])
94	1205.94	144.6	189.2	skeletal deformations and CH bendings (sCp[4], IprOH[3])	95	1228.28	7.5	-11	C*H bending, C*C stretching, in plane CH bendings (ph[5])
95	1235.67	96.3	-72.3	C*H bending, C*C stretching, in plane CH bendings (ph[5])	96	1270.71	166.1	-90.6	skeletal deformations and CH bendings (sCp[4], IprOH[3])
96	1273.17	155.8	-102.1	skeletal deformations and CH bendings (sCp[4], IprOH[3])	97	1282.01	0.4	-1.1	in plane CH bendings (uCp[6])
97	1281.76	0.2	-1.6	in plane CH bendings (uCp[6])	98	1296.32	18.1	-4.6	C*H bending, NH bending and in plane CH bendings (ph[5])

Table B.3: Transition frequencies, dipole strengths and rotational strengths of the most populated conformers of $\mathbf{5} - S_p$.

[1] Dipole strength in electrostatic units ($10^{-40} \cdot esu^2 \cdot cm^2$).

[2] Rotational strength in electrostatic units ($10^{-44} \cdot esu^2 \cdot cm^2$ respectively).

[3] 'IprOH' stands for isopropanol group.

[4] 'sCp' stands for substituted cyclopentadienyl moiety.

[5] 'ph' stands for phenyl group.

[6] 'uCp' stands for unsubstituted cyclopentadienyl moiety.

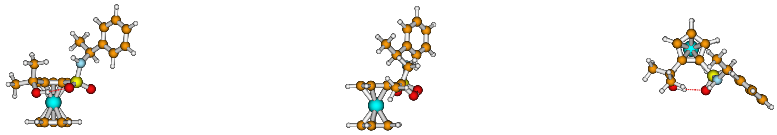

Figure B.2: structure of conformer I_{R_p} from different perspectives

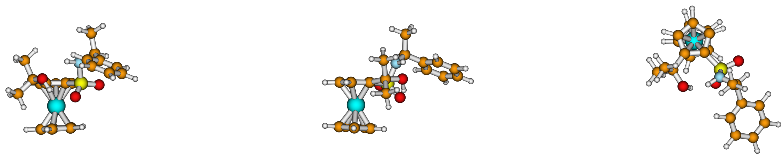

Figure B.3: structure of conformer II_{R_p} from different perspectives

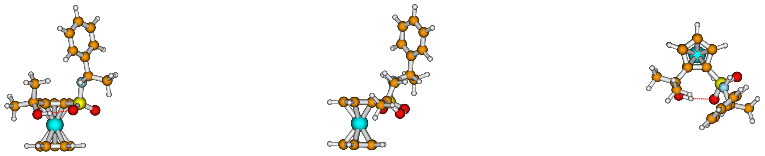

Figure B.4: structure of conformer III_{R_p} from different perspectives

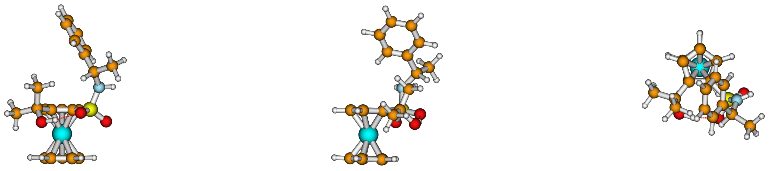

Figure B.5: structure of conformer IV_{R_p} from different perspectives

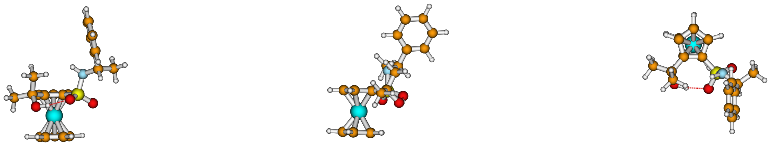

Figure B.6: structure of conformer V_{R_p} from different perspectives

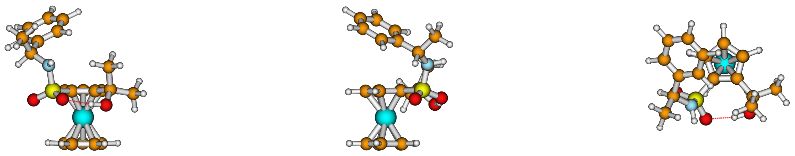

Figure B.7: structure of conformer I_{S_p} from different perspectives

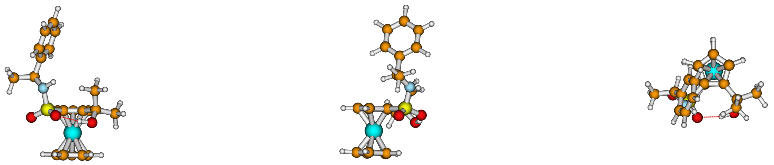

Figure B.8: structure of conformer II_{S_p} from different perspectives

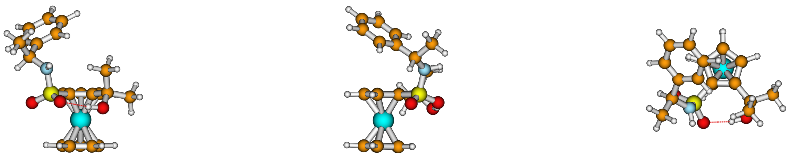

Figure B.9: structure of conformer III_{S_p} from different perspectives

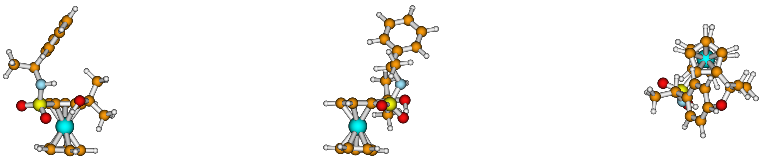

Figure B.10: structure of conformer IV_{S_p} from different perspectives

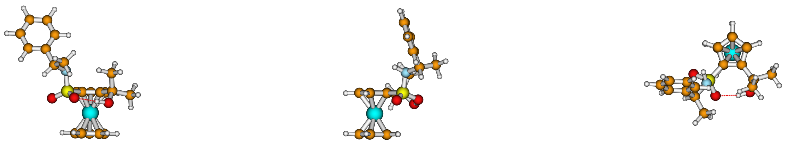

Figure B.11: structure of conformer V_{S_p} from different perspectives

Appendix C

C.1 Some remarks on projection operators

In quantum chemistry, the pivotal importance of projection operators is well known. In this appendix, the distinction between outer and inner projections is briefly introduced. This distinction allows a full understanding of the method employed to construct eq. 3.17. The following treatment is based on the classic article of Löwdin.[282]

Given a projection operator $\hat{O}$ which is idempotent ($\hat{O}^2 = \hat{O}$) and self-adjoint ($\hat{O}^\dagger = \hat{O}$) and a self-adjoint operator $\hat{A}$,[a] the outer projection $\hat{A}'$ of the operator $\hat{A}$ can be written as follows:

$$\hat{A}' = \hat{O}\hat{A}\hat{O}. \tag{C.1}$$

In order to provide a general definition of the projection operator $\hat{O}$ associated with a manifold X_n, a set of n linearly independent vectors $\mathbf{o} \equiv \{o_1, o_2, ..., o_n\}$ spanning the manifold X_n is employed to define a metric matrix $\mathbf{\Delta}$ (with elements $\Delta_{ij} = \langle o_i \,|\, o_j \rangle$). In this manner, the projection operator is defined as follows:[b]

[a] A rigorous mathematical treatment of projection operators is beyond the scope of this appendix, which is devoted to a concise introduction of the distinction between outer and inner projections. However, it must be underlined the importance of the mathematical features of the operators $\hat{O}$ and $\hat{A}$: these features determine validity and limits of the formulations provided in what follows. In this treatment the mathematical hypothesis implicitly and explicitly assumed in ref. 282 are employed. Therefore, for the construction of the outer projection of the operator $\hat{A}$ we assume (analogously to ref. 282) that $\hat{A}$ is bounded from below.

[b] There is an important mathematical consequence which follows from the rules of vector product. To clarify this aspect, two finite column vectors $\mathbf{a}$ and $\mathbf{b}$ are employed (for simplicity the n elements of these vectors are assumed to be real, i.e. $\mathbf{a}^\dagger = \mathbf{a}^T$). If the *inner* product is performed, the result is the following one:

$$\langle \mathbf{a} \,|\, \mathbf{b} \rangle = \mathbf{a}^T\mathbf{b} = \begin{bmatrix} a_1 & \dots & a_n \end{bmatrix} \cdot \begin{bmatrix} b_1 \\ \vdots \\ b_n \end{bmatrix} = [\dots]_{1\times 1}; \tag{C.2}$$

i.e. the result is a *number*; on the other hand, if the *outer* product is performed the

$$\hat{O} = \mathbf{o}\boldsymbol{\Delta}^{-1}\mathbf{o}^{\dagger} = \sum_{ij} |o_i\rangle \, (\Delta^{-1})_{ij} \, \langle o_j| \, . \tag{C.4}$$

If the set $\mathbf{o}$ is infinite and complete, then $\hat{O} \equiv \hat{I}$. The expression of the projection operator can be simplified if an orthonormal basis is chosen, for example $\mathbf{x} \equiv \{x_1, x_2, ..., x_n\}$ with $\langle x_i \,|\, x_j \rangle = \delta_{ij}$. In this case, eq. C.4 can be rewritten in the following manner:

$$\hat{O} = \mathbf{x}\mathbf{x}^{\dagger} = \sum_{i} |x_i\rangle \, \langle x_i| \, . \tag{C.5}$$

In the context of quantum chemistry, the expression provided in eq. C.5 for the projection operator is probably the best known. Employing eq. C.5 the outer projection $\hat{A}'$ can be written as the n-order matrix with elements $A_{ij} = \left\langle x_i \middle| \hat{A} \middle| x_j \right\rangle$, i.e. the outer projection is the result of the truncation of the infinite-order matrix associated to $\hat{A}$.

An alternative projection can be defined for the self-adjoint operator $\hat{A}$[a], which is called an inner projection. The inner projection $\hat{A}''$ of the operator $\hat{A}$ is defined by the following relationship:

$$\hat{A}'' = \hat{A}^{\frac{1}{2}} \hat{O} \hat{A}^{\frac{1}{2}} ; \tag{C.6}$$

where the inequality $0 < \hat{A}'' < \hat{A}$ holds.[b] More explicitly, the inner projection on a linear manifold X_n can be written as follows (employing eq. C.4):

$$\hat{A}'' = \hat{A}^{\frac{1}{2}} \mathbf{o}\boldsymbol{\Delta}^{-1}\mathbf{o}^{\dagger} \hat{A}^{\frac{1}{2}} . \tag{C.7}$$

Another form of eq. C.7 can be obtained if the substitution $\mathbf{o} = \hat{A}^{-\frac{1}{2}}\mathbf{h}$ is employed;[283] with this substitution, eq. C.7 can be rewritten in the following manner:

$$\hat{A}'' = \mathbf{h}\boldsymbol{\Delta}^{-1}\mathbf{h}^{\dagger} = |\mathbf{h}\rangle \left\langle \mathbf{h} \middle| \hat{A}^{-1} \middle| \mathbf{h} \right\rangle^{-1} \langle \mathbf{h}| \, ; \tag{C.8}$$

---

application of the same rules leads to the following result:

$$|\mathbf{a}\rangle \, \langle \mathbf{b}| = \mathbf{a}\mathbf{b}^{T} = \begin{bmatrix} a_1 \\ \vdots \\ a_n \end{bmatrix} \cdot \begin{bmatrix} b_1 & \dots & b_n \end{bmatrix} = \begin{bmatrix} a_1 b_1 & \dots & a_n b_1 \\ \vdots & \ddots & \vdots \\ a_1 b_n & \dots & a_n b_n \end{bmatrix}_{n \times n} ; \tag{C.3}$$

i.e. the result is a *matrix*: the result of an outer product is an operator which can act on other vectors. The results provided in eqs. C.2 and C.3 are straightforward, but are worth of mention in this appendix due to their importance.

[a] An additional requirement is the positive definiteness of $\hat{A}$, see ref. 282.

[b] The inequality is easily proved in ref. 282.

where $\mathbf{\Delta} = \mathbf{h}^\dagger \hat{A}^{-1}\mathbf{h} = \left\langle \mathbf{h} \middle| \hat{A}^{-1} \middle| \mathbf{h} \right\rangle$. The expression introduced in eq. C.8 can be used to construct eq. 3.17.

C.2 Derivation of the primary-primary block of the superoperator hamiltonian

In order to provide an explicit derivation of the elements $(a_i|\mathcal{H}a_j)$ of the superoperator hamiltonian matrix, the electronic hamiltonian is written with the second quantization formalism:[a]

$$H = \overbrace{\sum_{r,s} h_{rs} a_r^\dagger a_s}^{H_{mono}} + \overbrace{\frac{1}{4}\sum_{r,s,t,u} \langle rs||tu\rangle a_r^\dagger a_t^\dagger a_u a_s}^{H_{int}} \tag{C.9}$$

In what follows, the derivation is carried out employing the fundamental relationships of creation and annihilation operators. The superoperator metric is not completely specified in the first part of the derivation.[b] However, the choice of the superoperator metric affects the final result. Therefore, in the last part of the derivation the results corresponding to different choices of the superoperator metric are provided.

The starting point is the development of an element $(a_i|\mathcal{H}a_j)$ of the superoperator hamiltonian matrix:

$$\begin{aligned}(a_i|\mathcal{H}a_j) = \left\langle \left| \left[a_i^\dagger, \left[a_j, H\right]_-\right]_+ \right| \right\rangle = \left\langle \left| a_i^\dagger \left[a_j, H\right]_- \right| \right\rangle + \left\langle \left| \left[a_j, H\right]_- a_i^\dagger \right| \right\rangle = \\ \left\langle \left| a_i^\dagger a_j H \right| \right\rangle - \left\langle \left| a_i^\dagger H a_j \right| \right\rangle + \left\langle \left| a_j H a_i^\dagger \right| \right\rangle - \left\langle \left| H a_j a_i^\dagger \right| \right\rangle .\end{aligned} \tag{C.10}$$

The contribution due to the component H_{mono} of the full electronic hamiltonian can be easily derived from the last term of eq. C.10:

[a] The formulation of H in eq. C.9 depends on the convention adopted. In this appendix, the same convention adopted in ref. 207 are employed, i.e. $\langle rs||tu\rangle = \langle rs|tu\rangle - \langle ru|ts\rangle$ and $H_{int} = \frac{1}{4}\sum_{r,s,t,u}\langle rs||tu\rangle a_r^\dagger a_t^\dagger a_u a_s$ with a superoperator metric defined by eqs. 3.11, 3.12 and 3.13. In section 3.1.1 of this thesis a different convention is employed ($\langle rt||su\rangle = \langle rt|su\rangle - \langle rt|us\rangle$ and $H'_{int} = \frac{1}{4}\sum_{r,s,t,u}\langle rt||su\rangle a_r^\dagger a_t^\dagger a_u a_s$), which is the convention adopted in ref. 197 and specified at the beginning of chapter 4 of ref. 196.

[b] The notation $\langle\,|\ldots|\,\rangle$ is employed. The reference state is specified later in this section.

$$\left\langle \left| a_i^\dagger a_j H_{mono} \right| \right\rangle - \left\langle \left| a_i^\dagger H_{mono} a_j \right| \right\rangle + \left\langle \left| a_j H_{mono} a_i^\dagger \right| \right\rangle - \left\langle \left| H_{mono} a_j a_i^\dagger \right| \right\rangle =$$
$$\left\langle \left| a_i^\dagger a_j \sum_{r,s} h_{rs} a_r^\dagger a_s \right| \right\rangle - \left\langle \left| a_i^\dagger \sum_{r,s} h_{rs} a_r^\dagger a_s a_j \right| \right\rangle +$$
$$\left\langle \left| a_j \sum_{r,s} h_{rs} a_r^\dagger a_s a_i^\dagger \right| \right\rangle - \left\langle \left| \sum_{r,s} h_{rs} a_r^\dagger a_s a_j a_i^\dagger \right| \right\rangle =$$
$$\sum_{r,s} h_{rs} \left\langle \left| a_i^\dagger a_j a_r^\dagger a_s - a_i^\dagger a_r^\dagger a_s a_j + a_j a_r^\dagger a_s a_i^\dagger - a_r^\dagger a_s a_j a_i^\dagger \right| \right\rangle = {}^{a}$$
$$\sum_{r,s} h_{rs} \left\langle \left| a_i^\dagger a_r^\dagger a_s a_j + \delta_{rj} a_i^\dagger a_s - a_i^\dagger a_r^\dagger a_s a_j + a_j a_r^\dagger a_s a_i^\dagger - a_r^\dagger a_s a_j a_i^\dagger \right| \right\rangle =$$
$$\sum_{r,s} h_{rs} \left\langle \left| \delta_{rj} a_i^\dagger a_s + a_j a_r^\dagger a_s a_i^\dagger - a_r^\dagger a_s a_j a_i^\dagger \right| \right\rangle = {}^{b}$$
$$\sum_{r,s} h_{rs} \left\langle \left| \delta_{rj} a_i^\dagger a_s + a_r^\dagger a_s a_j a_i^\dagger + \delta_{rj} a_s a_i^\dagger - a_r^\dagger a_s a_j a_i^\dagger \right| \right\rangle =$$
$$\sum_{r,s} h_{rs} \left\langle \left| \delta_{rj} (a_i^\dagger a_s + a_s a_i^\dagger) \right| \right\rangle = \sum_{r,s} h_{rs} \left\langle \left| \delta_{rj} \delta_{si} \right| \right\rangle = h_{ji}. \tag{C.11}$$

The contribution of the component H_{int} can be derived in analogous manner:

$$\left\langle \left| a_i^\dagger a_j H_{int} \right| \right\rangle - \left\langle \left| a_i^\dagger H_{int} a_j \right| \right\rangle + \left\langle \left| a_j H_{int} a_i^\dagger \right| \right\rangle - \left\langle \left| H_{int} a_j a_i^\dagger \right| \right\rangle =$$
$$\left\langle \left| a_i^\dagger a_j \frac{1}{4} \sum_{r,s,t,u} \langle rs||tu\rangle a_r^\dagger a_t^\dagger a_u a_s \right| \right\rangle - \left\langle \left| a_i^\dagger \frac{1}{4} \sum_{r,s,t,u} \langle rs||tu\rangle a_r^\dagger a_t^\dagger a_u a_s a_j \right| \right\rangle +$$
$$\left\langle \left| a_j \frac{1}{4} \sum_{r,s,t,u} \langle rs||tu\rangle a_r^\dagger a_t^\dagger a_u a_s a_i^\dagger \right| \right\rangle - \left\langle \left| \frac{1}{4} \sum_{r,s,t,u} \langle rs||tu\rangle a_r^\dagger a_t^\dagger a_u a_s a_j a_i^\dagger \right| \right\rangle. \tag{C.12}$$

The terms written in the previous equation can be collected and developed as follows:

[a] The following relationship holds:
$a_i^\dagger a_j a_r^\dagger a_s = -a_i^\dagger a_r^\dagger a_j a_s + a_i^\dagger \delta_{rj} a_s = a_i^\dagger a_r^\dagger a_s a_j + \delta_{rj} a_i^\dagger a_s$.

[b] The following relationship holds:
$a_j a_r^\dagger a_s a_i^\dagger = -a_r^\dagger a_j a_s a_i^\dagger + \delta_{rj} a_s a_i^\dagger = a_r^\dagger a_s a_j a_i^\dagger + \delta_{rj} a_s a_i^\dagger$.

$$
\begin{aligned}
&\frac{1}{4}\sum_{r,s,t,u}\langle rs||tu\rangle\left\langle\left|\, a_i^\dagger a_j a_r^\dagger a_t^\dagger a_u a_s - a_i^\dagger a_r^\dagger a_t^\dagger a_u a_s a_j + a_j a_r^\dagger a_t^\dagger a_u a_s a_i^\dagger - a_r^\dagger a_t^\dagger a_u a_s a_j a_i^\dagger \,\right|\right\rangle \\
&= {}^{a}\frac{1}{4}\sum_{r,s,t,u}\langle rs||tu\rangle\left\langle\left|\, \delta_{jr} a_i^\dagger a_t^\dagger a_u a_s - \delta_{tj} a_i^\dagger a_r^\dagger a_u a_s + a_j a_r^\dagger a_t^\dagger a_u a_s a_i^\dagger - a_r^\dagger a_t^\dagger a_u a_s a_j a_i^\dagger \,\right|\right\rangle \\
&= {}^{b}\frac{1}{4}\sum_{r,s,t,u}\langle rs||tu\rangle\left\langle\left|\, \delta_{jr} a_i^\dagger a_t^\dagger a_u a_s - \delta_{tj} a_i^\dagger a_r^\dagger a_u a_s + \delta_{jr} a_t^\dagger a_u a_s a_i^\dagger - \delta_{tj} a_r^\dagger a_u a_s a_i^\dagger \,\right|\right\rangle \\
&= {}^{c}\frac{1}{4}\sum_{r,s,t,u}\langle rs||tu\rangle\left\langle\left|\, \delta_{jr}\delta_{is} a_t^\dagger a_u - \delta_{jr}\delta_{iu} a_t^\dagger a_s + \delta_{tj}\delta_{iu} a_r^\dagger a_s - \delta_{tj}\delta_{is} a_r^\dagger a_u \,\right|\right\rangle \\
&= \frac{1}{4}\sum_{t,u}\langle ji||tu\rangle\left\langle\left|\, a_t^\dagger a_u \,\right|\right\rangle - \frac{1}{4}\sum_{s,t}\langle js||ti\rangle\left\langle\left|\, a_t^\dagger a_s \,\right|\right\rangle + \\
&\quad \frac{1}{4}\sum_{r,s}\langle rs||ji\rangle\left\langle\left|\, a_r^\dagger a_s \,\right|\right\rangle - \frac{1}{4}\sum_{r,u}\langle ri||ju\rangle\left\langle\left|\, a_r^\dagger a_u \,\right|\right\rangle = \\
&= \frac{1}{4}\sum_{r,s}\langle ji||rs\rangle\left\langle\left|\, a_r^\dagger a_s \,\right|\right\rangle - \frac{1}{4}\sum_{r,s}\langle js||ri\rangle\left\langle\left|\, a_r^\dagger a_s \,\right|\right\rangle + \\
&\quad \frac{1}{4}\sum_{r,s}\langle rs||ji\rangle\left\langle\left|\, a_r^\dagger a_s \,\right|\right\rangle - \frac{1}{4}\sum_{r,s}\langle ri||js\rangle\left\langle\left|\, a_r^\dagger a_s \,\right|\right\rangle = {}^{d} \\
&\quad \sum_{r,s}\langle ji||rs\rangle\left\langle\left|\, a_r^\dagger a_s \,\right|\right\rangle = \sum_{r,s}\langle ji||rs\rangle\rho_{rs}
\end{aligned}
\tag{C.13}
$$

Combining the results of eqs. C.11 and C.13, the expression of an element of the generalized Fock matrix (already provided in eq. 3.38) can be written:[e]

$$
F_{ji}^{gen} = (a_i|\mathcal{H}a_j) = h_{ji} + \sum_{r,s}\langle ji||rs\rangle\rho_{rs}. \tag{C.14}
$$

To further specify the elements of the primary-primary block of the superoperator Hamiltonian, the superoperator metric must be completely speci-

[a] The following relationship holds:
$a_i^\dagger a_j a_r^\dagger a_t^\dagger a_u a_s = -a_i^\dagger a_r^\dagger a_j a_t^\dagger a_u a_s + \delta_{jr} a_i^\dagger a_t^\dagger a_u a_s = a_i^\dagger a_r^\dagger a_t^\dagger a_j a_u a_s + \delta_{jr} a_i^\dagger a_t^\dagger a_u a_s - \delta_{tj} a_i^\dagger a_r^\dagger a_u a_s = a_i^\dagger a_r^\dagger a_t^\dagger a_u a_s a_j + \delta_{jr} a_i^\dagger a_t^\dagger a_u a_s - \delta_{tj} a_i^\dagger a_r^\dagger a_u a_s.$

[b] The following relationship holds:
$a_j a_r^\dagger a_t^\dagger a_u a_s a_i^\dagger = -a_r^\dagger a_j a_t^\dagger a_u a_s a_i^\dagger + \delta_{jr} a_t^\dagger a_u a_s a_i^\dagger = a_r^\dagger a_t^\dagger a_j a_u a_s a_i^\dagger + \delta_{jr} a_t^\dagger a_u a_s a_i^\dagger - \delta_{tj} a_r^\dagger a_u a_s a_i^\dagger = a_r^\dagger a_t^\dagger a_u a_s a_j a_i^\dagger + \delta_{jr} a_t^\dagger a_u a_s a_i^\dagger - \delta_{tj} a_r^\dagger a_u a_s a_i^\dagger.$

[c] The following relationships hold:
$a_i^\dagger a_t^\dagger a_u a_s = -a_t^\dagger a_i^\dagger a_u a_s = a_t^\dagger a_u a_i^\dagger a_s - \delta_{iu} a_t^\dagger a_s = -a_t^\dagger a_u a_s a_i^\dagger - \delta_{iu} a_t^\dagger a_s + \delta_{is} a_t^\dagger a_u;$
$a_i^\dagger a_r^\dagger a_u a_s = -a_r^\dagger a_i^\dagger a_u a_s = a_r^\dagger a_u a_i^\dagger a_s - \delta_{iu} a_r^\dagger a_s = -a_r^\dagger a_u a_s a_i^\dagger + \delta_{is} a_r^\dagger a_u - \delta_{iu} a_r^\dagger a_s.$

[d] It must be pointed out that $\langle ji||rs\rangle = \langle rs||ji\rangle$ and $\langle ji||rs\rangle = -\langle js||ri\rangle$ (see, for example, eq. 4 of ref. 207).

[e] Differences between eqs. 3.38 and C.14 are due to the different notation adopted to label bielectronic integrals.

fied. In what follows, three examples are provided. In the first one, the Hartree-Fock ground state is employed as reference state:

$$\begin{aligned} F_{ji}^{gen} =&(a_i|\mathcal{H}a_j) = h_{ji}\left\langle \phi_{HF}^{N_{el}} \middle| \phi_{HF}^{N_{el}} \right\rangle + \sum_{r,s}\langle ji||rs\rangle \left\langle \phi_{HF}^{N_{el}} \middle| a_r^\dagger a_s \middle| \phi_{HF}^{N_{el}} \right\rangle = \text{[a]} \\ & h_{ji} + \sum_r \langle ji||rr\rangle \rho_{rr}^{HF} = \delta_{ji}\varepsilon_j = F_{ji} \end{aligned} \tag{C.15}$$

The result of eq. C.15 is equal to the RHS of eq. 3.41 when $\boldsymbol{\rho}^{corr} = 0$.

In the second example, the primary-primary block for the NR2 approximation is derived. In this case, the superoperator metric is specified in eq. 3.66; in the framework of RSPT, first-order corrections involve only double excitations:[284,b]

$$T_2^{(1)} \left|\phi_{HF}^{N_{el}}\right\rangle = \sum_{a,b,x,y} K_{xy}^{ab} a_a^\dagger a_x a_b^\dagger a_y \left|\phi_{HF}^{N_{el}}\right\rangle = \sum_{a,b,x,y} K_{xy}^{ab} \left|\phi_{xy\to ab}^{N_{el}}\right\rangle. \tag{C.16}$$

Values of K_{xy}^{ab} are specified in ref. 284.[c] Employing the notation of eq. C.16 and the superoperator metric specified in eq. 3.66, and taking into account that $\left\langle \phi_{HF}^{N_{el}} \middle| \phi_{xy\to ab}^{N_{el}} \right\rangle = 0$ and $\left\langle \phi_{HF}^{N_{el}} \middle| a_r^\dagger a_s \middle| \phi_{xy\to ab}^{N_{el}} \right\rangle = 0$:

$$\begin{aligned} F_{ji}^{gen} =&(a_i|\mathcal{H}a_j) = h_{ji}\Big(\left\langle \phi_{HF}^{N_{el}} \middle| \phi_{HF}^{N_{el}} \right\rangle + \sum_{a,b,x,y} K_{xy}^{ab} \left\langle \phi_{HF}^{N_{el}} \middle| \phi_{xy\to ab}^{N_{el}} \right\rangle \Big) + \\ & \sum_{r,s}\langle ji||rs\rangle \Big(\left\langle \phi_{HF}^{N_{el}} \middle| a_r^\dagger a_s \middle| \phi_{HF}^{N_{el}} \right\rangle + \sum_{a,b,x,y} K_{xy}^{ab} \left\langle \phi_{HF}^{N_{el}} \middle| a_r^\dagger a_s \middle| \phi_{xy\to ab}^{N_{el}} \right\rangle \Big) \\ & = h_{ji} + \sum_r \langle ji||rr\rangle \rho_{rr}^{HF} = \delta_{ji}\varepsilon_j = F_{ji} \end{aligned} \tag{C.17}$$

The result of eq. C.17 (which is equal to the result of eq. C.15) provides the primary-primary block of the superoperator hamiltonian matrix in the NR2 approximation (see subsection 3.1.3).

In the third example, the reference state of the transition operator method is employed. The following ensemble:[207,d]

---

[a] Remember that $\left\langle \phi_{HF}^{N_{el}} \middle| a_r^\dagger a_s \middle| \phi_{HF}^{N_{el}} \right\rangle = 0$ if $r \neq s$.

[b] In the notation employed in eq. C.16 x and y are occupied orbitals and a and b are unoccupied orbitals in the HF ground state.

[c] The values of K_{xy}^{ab} are not needed for the derivation and therefore in this thesis are not specified.

[d] The notation $\left|\phi_{HF}^{N_{el}-1(x)}\right\rangle$ employed for the ionized state specify the orbital x from which the electron is removed.

$$\left|\phi_{GCHF}^{N_{el}-\frac{1}{2}}\right\rangle = \frac{1}{\sqrt{2}}\left|\phi_{HF}^{N_{el}}\right\rangle + \frac{1}{\sqrt{2}}\left|\phi_{HF}^{N_{el}-1(x)}\right\rangle, \tag{C.18}$$

is employed in the superoperator metric:

$$(X|Y) = \left\langle \phi_{GCHF}^{N_{el}-\frac{1}{2}} \middle| \left[X^\dagger, Y\right]_+ \middle| \phi_{GCHF}^{N_{el}-\frac{1}{2}} \right\rangle \tag{C.19}$$

Taking into account eqs. C.18 and C.19, the generalized Fock matrix can be derived as follows:

$$\begin{aligned}
F_{ji}^{gen} =& (a_i|\mathcal{H}a_j) = \frac{1}{2}h_{ji}\Big(\left\langle \phi_{HF}^{N_{el}} \middle| \phi_{HF}^{N_{el}} \right\rangle + \left\langle \phi_{HF}^{N_{el}} \middle| \phi_{HF}^{N_{el}-1(x)} \right\rangle + \\
& \left\langle \phi_{HF}^{N_{el}-1(x)} \middle| \phi_{HF}^{N_{el}} \right\rangle + \left\langle \phi_{HF}^{N_{el}-1(x)} \middle| \phi_{HF}^{N_{el}-1(x)} \right\rangle \Big) + \\
& \sum_{r,s}\langle ji||rs\rangle \frac{1}{2}\Big(\left\langle \phi_{HF}^{N_{el}} \middle| a_r^\dagger a_s \middle| \phi_{HF}^{N_{el}} \right\rangle + \left\langle \phi_{HF}^{N_{el}} \middle| a_r^\dagger a_s \middle| \phi_{HF}^{N_{el}-1(x)} \right\rangle \\
& + \left\langle \phi_{HF}^{N_{el}-1(x)} \middle| a_r^\dagger a_s \middle| \phi_{HF}^{N_{el}} \right\rangle + \left\langle \phi_{HF}^{N_{el}-1(x)} \middle| a_r^\dagger a_s \middle| \phi_{HF}^{N_{el}-1(x)} \right\rangle \Big) = \\
& \frac{1}{2}h_{ji}\Big(\left\langle \phi_{HF}^{N_{el}} \middle| \phi_{HF}^{N_{el}} \right\rangle + \left\langle \phi_{HF}^{N_{el}-1(x)} \middle| \phi_{HF}^{N_{el}-1(x)} \right\rangle \Big) + \\
& \sum_{r,s}\langle ji||rs\rangle \frac{1}{2}\Big(\left\langle \phi_{HF}^{N_{el}} \middle| a_r^\dagger a_s \middle| \phi_{HF}^{N_{el}} \right\rangle + \left\langle \phi_{HF}^{N_{el}-1(x)} \middle| a_r^\dagger a_s \middle| \phi_{HF}^{N_{el}-1(x)} \right\rangle \Big) = \\
& h_{ji} + \sum_r \langle ji||rr\rangle \rho_{rr}^{TOM(ref)}.
\end{aligned} \tag{C.20}$$

In the case of the result of eq. C.20, $\boldsymbol{\rho}^{corr} \neq 0$. To clarify the physical meaning of $\rho_{rr}^{TOM(ref)}$, the result of eq. C.20 can be written in terms of occupation numbers:[a]

$$F_{ji}^{gen} = h_{ji} + \sum_r \langle ji||rr\rangle n_r. \tag{C.21}$$

In eq. C.21, n_r is equal to $\frac{1}{2}$ if $r = x$, otherwise n_r is equal to 0 for unoccupied orbitals and to 1 for occupied orbitals. The reference ensemble provided in eq. C.18 can be a useful starting point for the study of the ionization process associated to the orbital x.[285]

[a] Eq. C.21 is equivalent to eq. 3.45; the formal difference is due to the different notation adopted for the bielectronic integrals.

C.3 Assignment of UPS spectra

In what follows, computational and experimental values of transition energies for the six UPS spectra showed and discussed in section 3.3 are provided. For what concerns the assignment of the purely electronic transition energies, the quasiparticle picture is retained. The numeration of MOs do not take into account the core levels. The pole strength are provided in parenthesis. Values of the transition energies calculated by means of the OVGF method are provided for transition energies below 20 eV, while values calculated with the NR2 approximation are given only for transitions assigned to outer valence MOs. In the cases of 2,6-STDO (table C.1) and 2,6-STDE (table C.3), the computational results provided in ref. 264 are also reported.

The assignment of the vibronic transitions is carried out for five of the six compounds studied in this work. The analysis is not carried out for the 2,6-STEO molecule due to the distance between experimental and calculated values; in other words, in this case the analysis of the computed values do not have a counterpart in the real world and therefore is left out. Normal modes associated with the most intense vibronic transitions are depicted.

Only the most intense vibronic transitions are listed, although in most of the cases many other vibronic transitions should be taken into account in order to completely reproduce the vibronic signature of a specific electronic transition.

A reduced-dimensionality scheme has been employed for the calculation of vibronic transitions of 2,6-STOT, 2,4-STDO and 2,4-STEO. The protocol is based on the exclusion (from the vibronic calculation) of all the normal modes with a fundamental frequency below a user-defined threshold. These thresholds are 800 cm^{-1} in the case of 2,4-STDO and 850 cm^{-1} in the cases of 2,6-STOT and 2,4-STEO.

transition	method						experimental (UPS)
	KT (HF/maug-cc-pVTZ)	OVGF/maug-cc-pVTZ	OVGF/cc-pVTZ[1]	NR2/maug-cc-pVTZ	ADC(3)/cc-pVDZ[1]		
$7b_2$ [n $(+\sigma)$]	10.31	9.01 (0.899)	8.96 (0.901)	8.97 (0.876)	8.94 (0.897)	8.84^3	
$6b_3$ [n $(+\sigma)$]	11.61	10.15 (0.894)	10.09 (0.896)	9.95 $(0.866)^2$	10.02 (0.889)	9.90^3	
7a $[\sigma]$	13.05	11.70 (0.905)	11.64 (0.907)	12.06 (0.886)	11.92 (0.906)		
$6b_2$ $[\sigma(+n)]$	13.13	12.07 (0.893)	11.99 (0.894)	12.11 (0.864)	11.94 (0.883)		11.5-12.5[4]
$6b_1$ $[\sigma]$	13.80	12.45 (0.904)	12.40 (0.906)	12.70 (0.885)	12.62 (0.904)		
$5b_3$ $[\pi]$	14.39	13.49 (0.883)	13.36 (0.882)	13.21 (0.840)	13.11 (0.854)		
$5b_2$ $[\sigma(+n)]$	14.47	13.29 (0.897)	13.20 (0.899)	13.18 $(0.874)^2$	13.16 (0.891)		
$4b_2$ $[\sigma]$	14.80	13.27 (0.902)	13.21 (0.904)	13.44 $(0.873)^2$	13.40 (0.893)		13-14[4]
6a $[\sigma]$	15.03	13.29 (0.895)	13.20 (0.898)	13.41 (0.871)	13.41 (0.894)		
$5b_1$ $[\sigma]$	15.29	13.91 (0.906)	13.85 (0.907)	13.92 (0.883)	13.89 (0.901)		
$4b_3$ $[\sigma(+n)]$	16.17	14.48 (0.885)	14.37 (0.888)	-	14.27 (0.850)		14-14.5[4]
$3b_2$ $[\pi]$	16.42	14.71 (0.878)	14.58 (0.882)	-	14.48 (0.669)		
$3b_3$ $[\sigma]$	17.27	15.65 (0.893)	15.57 (0.893)	-	15.75 (0.811)		15.5[5]
$4b_1$ $[\sigma]$	18.11	16.09 (0.884)	15.99 (0.883)	-	15.96 (0.867)		
$2b_2$ $[\sigma(+n)]$	18.91	17.07 (0.883)	16.97 (0.883)	-	17.16 (0.761)		
5a $[\sigma]$	19.42	17.32 (0.881)	17.24 (0.880)	-	17.24 (0.828)		
$3b_1$ $[\sigma]$	20.13	18.02 (0.883)	17.96 (0.882)	-	18.02 (0.836)		
4a $[\sigma]$	20.58	18.43 (0.882)	18.36 (0.881)	-	18.41 (0.852)		

Table C.1: values and assignment of each electronic transition for 2,6-STDO molecule.

[1] taken from ref. 264
[2] slight contributions from other MOs
[3] taken from ref. 251
[4] our assignment
[5] taken from ref. 251; assignment proposed in ref. 264

transition	main contributions	energy (eV)	intensity (a. u.)
$7b_2$ [n $(+\sigma)$]	$\|0\rangle \rightarrow \|0\rangle$	8.737	$0.769 \cdot 10^{-3}$
	$\|0\rangle \rightarrow \|12(1)\rangle$	8.834	$0.518 \cdot 10^{-3}$
	$\|0\rangle \rightarrow \|24(1)\rangle$	8.874	$0.181 \cdot 10^{-3}$
	$\|0\rangle \rightarrow \|33(1)\rangle$	8.893	$0.188 \cdot 10^{-3}$
	$\|0\rangle \rightarrow \|40(1)\rangle$	8.967	$0.262 \cdot 10^{-3}$
	$\|0\rangle \rightarrow \|12(1), 40(1)\rangle$	9.064	$0.177 \cdot 10^{-3}$
$6b_3$ [n $(+\sigma)$]	$\|0\rangle \rightarrow \|0\rangle$	9.839	$0.205 \cdot 10^{-2}$
	$\|0\rangle \rightarrow \|8(1)\rangle$	9.915	$0.250 \cdot 10^{-3}$
	$\|0\rangle \rightarrow \|33(1)\rangle$	9.995	$0.425 \cdot 10^{-3}$
	$\|0\rangle \rightarrow \|40(1)\rangle$	10.069	$0.402 \cdot 10^{-3}$

Table C.2: energies, intensities and assignment of the main vibronic transitions for the first and the second bands of the spectrum of 2,6-STDO molecule.

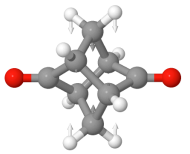

(a) 8-th normal mode

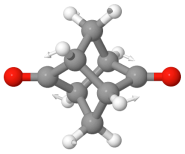

(b) 12-th normal mode

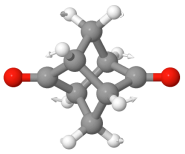

(c) 24-th normal mode

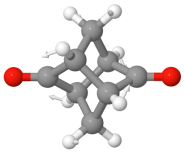

(d) 33-th normal mode

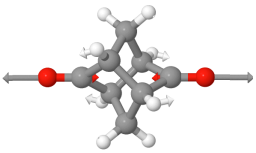

(e) 40-th normal mode

Figure C.1: Graphical representation of the normal modes of 2,6-STDO, numbered with respect to the associated fundamental frequency in ascending order; only the normal modes involved in the most intense vibronic transitions are reported (see table C.2).

transition	method					experimental (UPS)
	KT (HF/maug-cc-pVTZ)	OVGF/maug-cc-pVTZ	OVGF/cc-pVTZ[1]	NR2/maug-cc-pVTZ	ADC(3)/cc-pVDZ[1]	
$7b_2$ [π]	9.06	8.71 (0.898)	8.69 (0.899)	8.77 (0.874)	8.68 (0.885)	8.49[2]
$6b_3$ [π]	9.98	9.58 (0.896)	9.54 (0.897)	9.61 (0.866)	9.55 (0.879)	9.40[2]
$6b_2$ [σ]	11.35	10.23 (0.898)	10.20 (0.902)	10.27 (0.876)	10.32 (0.897)	10.05[2]
7a [σ]	11.96	10.84 (0.897)	10.81 (0.901)	10.87 (0.874)	10.96 (0.897)	10.9[3]
$5b_3$ [σ]	12.54	11.32 (0.897)	11.28 (0.901)	11.28 (0.875)	11.38 (0.896)	} 11.4[3]
$6b_1$ [σ]	12.81	11.63 (0.897)	11.59 (0.900)	11.59 (0.874)	11.70 (0.896)	
$5b_2$ [σ]	13.03	11.90 (0.896)	11.86 (0.899)	11.82 (0.870)	11.95 (0.890)	} 11.9[3]
6a [σ]	13.20	11.66 (0.891)	11.63 (0.895)	11.76 (0.868)	11.84 (0.893)	
$4b_2$ [σ]	13.72	12.35 (0.898)	12.32 (0.902)	12.27 (0.875)	12.41 (0.897)	} 12.5[4]
$5b_1$ [σ]	14.29	13.02 (0.898)	13.00 (0.900)	12.81 (0.873)	12.97 (0.892)	
$4b_3$ [σ]	15.57	14.29 (0.882)	14.25 (0.884)	-	14.12 (0.847)	
$3b_2$ [σ]	15.79	14.52 (0.876)	14.49 (0.878)	-	14.31 (0.805)	} 14-15[4]
$3b_3$ [σ]	16.29	14.86 (0.884)	14.81 (0.887)	-	14.79 (0.710)	
$4b_1$ [σ]	16.82	15.11 (0.887)	15.07 (0.887)	-	15.13 (0.871)	
$2b_2$ [σ]	17.65	15.91 (0.877)	15.86 (0.877)	-	16.01 (0.549)	15.9[4]
5a [σ]	18.52	16.70 (0.876)	16.66 (0.876)	-	16.60 (0.700)	
$3b_1$ [σ]	19.19	17.19 (0.875)	17.16 (0.875)	-	17.25 (0.736)	
4a [σ]	19.56	17.54 (0.874)	17.50 (0.874)	-	17.54 (0.785)	

Table C.3: values and assignment of each electronic transition for 2,6-STDE molecule.

[1] taken from ref. 264
[2] taken from ref. 251
[3] taken from ref. 251; assignment proposed in ref. 264
[4] our assignment

transition	main contributions	energy (eV)	intensity (a. u.)
$7b_2$ $[\pi]$	$\|0\rangle \rightarrow \|0\rangle$	8.588	$0.148 \cdot 10^{-1}$
	$\|0\rangle \rightarrow \|16(1)\rangle$	8.688	$0.367 \cdot 10^{-2}$
	$\|0\rangle \rightarrow \|31(1)\rangle$	8.728	$0.189 \cdot 10^{-2}$
	$\|0\rangle \rightarrow \|47(1)\rangle$	8.803	$0.698 \cdot 10^{-2}$
	$\|0\rangle \rightarrow \|16(1), 47(1)\rangle$	8.903	$0.173 \cdot 10^{-2}$
	$\|0\rangle \rightarrow \|47(2)\rangle$	9.019	$0.164 \cdot 10^{-2}$
$6b_3$ $[\pi]$	$\|0\rangle \rightarrow \|0\rangle$	9.445	$0.168 \cdot 10^{-1}$
	$\|0\rangle \rightarrow \|7(1)\rangle$	9.503	$0.178 \cdot 10^{-2}$
	$\|0\rangle \rightarrow \|23(1)\rangle$	9.559	$0.257 \cdot 10^{-2}$
	$\|0\rangle \rightarrow \|47(1)\rangle$	9.660	$0.879 \cdot 10^{-2}$
	$\|0\rangle \rightarrow \|23(1), 47(1)\rangle$	9.774	$0.134 \cdot 10^{-2}$
	$\|0\rangle \rightarrow \|47(2)\rangle$	9.876	$0.229 \cdot 10^{-2}$

Table C.4: energies, intensities and assignment of the main vibronic transitions for the first and the second bands of the spectrum of 2,6-STDE molecule.

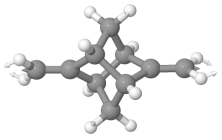

(a) 7-th normal mode

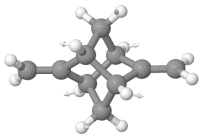

(b) 16-th normal mode

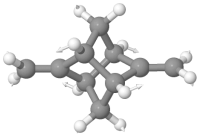

(c) 23-th normal mode

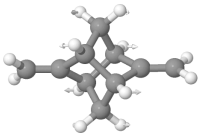

(d) 31-th normal mode

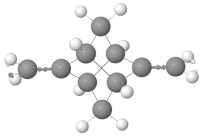

(e) 47-th normal mode

Figure C.2: Graphical representation of the normal modes of 2,6-STDE, numbered with respect to the associated fundamental frequency in ascending order; only the normal modes involved in the most intense vibronic transitions are reported (see table C.4).

transition	method			experimental (UPS)[1]
	KT (HF/maug-cc-pVTZ)	OVGF/maug-cc-pVTZ	NR2/maug-cc-pVTZ	
13b [π]	9.85	9.44 (0.900)	9.57 (0.878)	9.40[3]
12b [n($+\sigma$)]	10.33	9.06 (0.895)	8.88 (0.868)	8.85[3]
13a [σ]	12.48	11.25 (0.901)	11.43 (0.880)	10.95[3]
11b [σ(+n)]	12.55	11.27 (0.899)	11.32 (0.876)[2]	
10b [n($+\sigma$)]	13.14	12.07 (0.893)	12.04 (0.861)	
12a [σ]	13.29	12.02 (0.900)	12.13 (0.879)	
9b [$\pi(+\sigma)$]	14.02	13.00 (0.888)	12.72 (0.858)	12-13.5[4]
11a [σ]	14.05	12.42 (0.894)	12.56 (0.870)	
8b [σ]	14.23	12.78 (0.900)	12.81 (0.867)[2]	
10a [σ]	14.79	13.47 (0.901)	13.36 (0.878)	
7b [$\pi(+\sigma)$]	15.73	14.10 (0.882)	-	
6b [σ(+n)]	16.17	14.83 (0.877)	-	
5b [σ(+n)]	16.75	15.14 (0.890)	-	15.1[4]
9a [σ]	17.48	15.61 (0.885)	-	
4b [σ]	18.28	16.48 (0.880)	-	
8a [σ]	18.96	16.99 (0.878)	-	
7a [σ]	19.64	17.59 (0.879)	-	
6a [σ]	20.05	17.97 (0.878)	-	

Table C.5: values and assignment of each electronic transition for 2,6-STEO molecule.

[1] taken from ref. 251
[2] slight contributions from other MOs
[3] assignemnt proposed in ref. 251
[4] our assignment

transition	method			experimental (UPS)[1]
	KT (HF/maug-cc-pVTZ)	OVGF/maug-cc-pVTZ	NR2/maug-cc-pVTZ	
13b[n_S]	9.17	8.52 (0.892)	8.29 (0.87)	8.49[3]
12b[π_{CS}]	10.72	10.47 (0.894)	10.44 (0.859)	10.50[3]
11b[$n_O(+\sigma)$]	11.00	9.60 (0.891)	9.46 (0.861)[2]	9.45[3]
12a[σ]	13.04	11.62 (0.899)	11.96 (0.875)	11.40[3]
11a[σ]	13.58	12.21 (0.895)	12.40 (0.868)[2]	
10b[$\pi_{CO}(+\sigma)$]	13.61	12.44 (0.889)	12.49 (0.818)[2]	12-13[4]
10a[σ]	13.93	12.45 (0.896)	12.68 (0.872)[2]	
9b[$\sigma(+n_O)$]	14.22	12.78 (0.89)	-	
8b[$\pi_{CO}(+\sigma)$]	14.67	13.32 (0.887)	-	
7b[$\sigma(+n_O)$]	14.96	13.26 (0.888)	-	13-14.5[4]
9a[σ]	15.29	13.80 (0.900)	-	
6b[$\pi_{CO}(+\sigma)$]	16.22	14.45 (0.88)	-	
8a[σ]	16.82	15.05 (0.874)	-	15[4]
5b[$\sigma(+n_O)$]	17.23	15.52 (0.889)	-	
4b[σ]	18.75	16.85 (0.874)	-	
7a[σ]	19.01	16.87 (0.868)	-	
6a[σ]	20.08	17.91 (0.876)	-	
5a[σ]	20.51	18.33 (0.875)	-	

Table C.6: values and assignment of each electronic transition for 2,6-STOT molecule.

[1] taken from ref. 250
[2] slight contributions from other MOs
[3] assignment proposed in ref. 250
[4] our assignment

transition	main contributions	energy (eV)	intensity (a. u.)
13b[n_S]	$\|0\rangle \rightarrow \|0\rangle$	8.253	$0.269 \cdot 10^{-3}$
	$\|0\rangle \rightarrow \|16(1)\rangle$	8.362	$0.133 \cdot 10^{-4}$
	$\|0\rangle \rightarrow \|21(1)\rangle$	8.374	$0.116 \cdot 10^{-4}$
	$\|0\rangle \rightarrow \|23(1)\rangle$	8.387	$0.138 \cdot 10^{-4}$
	$\|0\rangle \rightarrow \|27(1)\rangle$	8.395	$0.107 \cdot 10^{-4}$
12b[π_{CS}]	$\|0\rangle \rightarrow \|0\rangle$	10.146	$0.502 \cdot 10^{-4}$
	$\|0\rangle \rightarrow \|19(1)\rangle$	10.259	$0.125 \cdot 10^{-4}$
	$\|0\rangle \rightarrow \|27(1)\rangle$	10.288	$0.182 \cdot 10^{-4}$
	$\|0\rangle \rightarrow \|28(1)\rangle$	10.289	$0.111 \cdot 10^{-4}$
	$\|0\rangle \rightarrow \|37(1)\rangle$	10.316	$0.115 \cdot 10^{-4}$
11b[$n_O(+\sigma)$]	$\|0\rangle \rightarrow \|0\rangle$	9.321	$0.154 \cdot 10^{-3}$
	$\|0\rangle \rightarrow \|21(1)\rangle$	9.441	$0.232 \cdot 10^{-4}$
	$\|0\rangle \rightarrow \|24(1)\rangle$	9.458	$0.351 \cdot 10^{-4}$
	$\|0\rangle \rightarrow \|29(1)\rangle$	9.470	$0.142 \cdot 10^{-4}$
	$\|0\rangle \rightarrow \|35(1)\rangle$	9.481	$0.136 \cdot 10^{-4}$
	$\|0\rangle \rightarrow \|40(1)\rangle$	9.550	$0.127 \cdot 10^{-4}$

Table C.7: energies, intensities and assignment of the main vibronic transitions for the first, the second and the third bands of the spectrum of 2,6-STOT molecule.

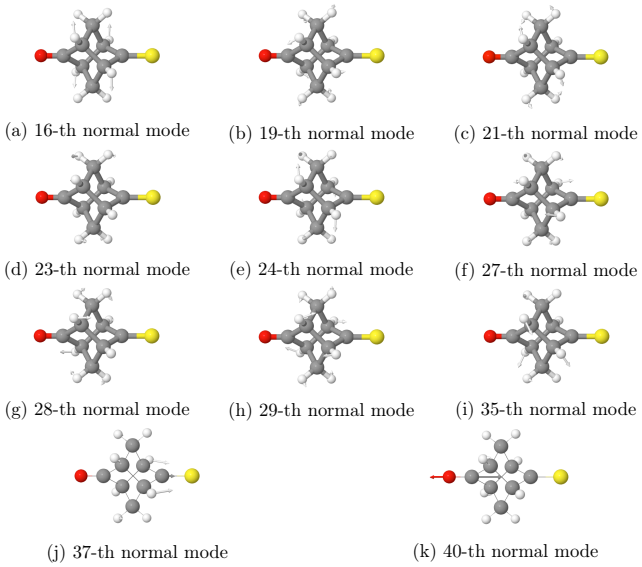

(a) 16-th normal mode (b) 19-th normal mode (c) 21-th normal mode

(d) 23-th normal mode (e) 24-th normal mode (f) 27-th normal mode

(g) 28-th normal mode (h) 29-th normal mode (i) 35-th normal mode

(j) 37-th normal mode (k) 40-th normal mode

Figure C.3: Graphical representation of the normal modes of 2,6-STOT, numbered with respect to the associated fundamental frequency in ascending order; only the normal modes involved in the most intense vibronic transitions are reported (see table C.7).

transition	method			experimental (UPS)[2]
	KT (HF/maug-cc-pVTZ)	OVGF/maug-cc-pVTZ	NR2/maug-cc-pVTZ	
11a″[$n(+\sigma)$]	10.51	9.16 (0.896)	9.13 (0.870)	9.04[3]
15a′[$n(+\sigma)$]	11.47	10.06 (0.895)	9.89 (0.864)	9.88[3]
10a″[$\sigma(+n)$]	13.28	12.03 (0.900)	12.14 (0.874)	
14a′[$\sigma(+n)$]	13.44	12.19 (0.901)	12.41 (0.872)[1]	
13a′[σ]	13.64	12.28 (0.902)	12.52 (0.879)[1]	
9a″[$\sigma(+n)$]	14.01	12.54 (0.900)	12.73 (0.877)	12-14[4]
8a″[π]	14.43	13.38 (0.885)	13.17 (0.836)	
12a′[$n(+\sigma)$]	14.55	13.28 (0.893)	13.16 (0.820)[1]	
11a′[$\sigma(+n)$]	14.80	13.45 (0.899)	13.49 (0.850)[1]	
7a″[σ]	15.00	13.69 (0.902)	13.62 (0.863)[1]	
10a′[$\pi(+\sigma)$]	16.18	14.47 (0.884)	-	
6a″[$\pi(+\sigma)$]	16.83	14.95 (0.876)	-	
9a′[σ]	17.76	15.91 (0.887)	-	
5a″[σ]	17.96	15.98 (0.884)	-	
8a′[σ]	18.76	16.94 (0.885)	-	
7a′[σ]	19.62	17.61 (0.883)	-	
4a″[σ]	20.48	18.18 (0.874)	-	
6a′[σ]	20.51	18.35 (0.880)	-	

Table C.8: values and assignment of each electronic transition for 2,4-STDO molecule.

[1] slight contributions from other MOs
[2] taken from ref. 250
[3] assignment proposed in ref. 250
[4] our assignment

transition	main contributions	energy (eV)	intensity (a. u.)
11a″[$n(+\sigma)$]	$\|0\rangle \rightarrow \|0\rangle$	8.966	$0.201 \cdot 10^{-1}$
	$\|0\rangle \rightarrow \|16(1)\rangle$	9.076	$0.597 \cdot 10^{-2}$
	$\|0\rangle \rightarrow \|20(1)\rangle$	9.084	$0.129 \cdot 10^{-2}$
	$\|0\rangle \rightarrow \|22(1)\rangle$	9.095	$0.160 \cdot 10^{-2}$
	$\|0\rangle \rightarrow \|25(1)\rangle$	9.105	$0.411 \cdot 10^{-2}$
	$\|0\rangle \rightarrow \|29(1)\rangle$	9.113	$0.133 \cdot 10^{-2}$
	$\|0\rangle \rightarrow \|33(1)\rangle$	9.124	$0.113 \cdot 10^{-2}$
	$\|0\rangle \rightarrow \|39(1)\rangle$	9.192	$0.105 \cdot 10^{-2}$
	$\|0\rangle \rightarrow \|40(1)\rangle$	9.197	$0.175 \cdot 10^{-2}$
	$\|0\rangle \rightarrow \|16(1);25(1)\rangle$	9.215	$0.122 \cdot 10^{-2}$
15a′[$n(+\sigma)$]	$\|0\rangle \rightarrow \|0\rangle$	9.793	$0.297 \cdot 10^{-1}$
	$\|0\rangle \rightarrow \|15(1)\rangle$	9.902	$0.711 \cdot 10^{-2}$
	$\|0\rangle \rightarrow \|22(1)\rangle$	9.922	$0.109 \cdot 10^{-2}$
	$\|0\rangle \rightarrow \|25(1)\rangle$	9.932	$0.631 \cdot 10^{-2}$
	$\|0\rangle \rightarrow \|27(1)\rangle$	9.934	$0.359 \cdot 10^{-2}$
	$\|0\rangle \rightarrow \|15(1);25(1)\rangle$	10.041	$0.151 \cdot 10^{-2}$

Table C.9: energies, intensities and assignment of the main vibronic transitions for the first and the second bands of the spectrum of 2,4-STDO molecule.

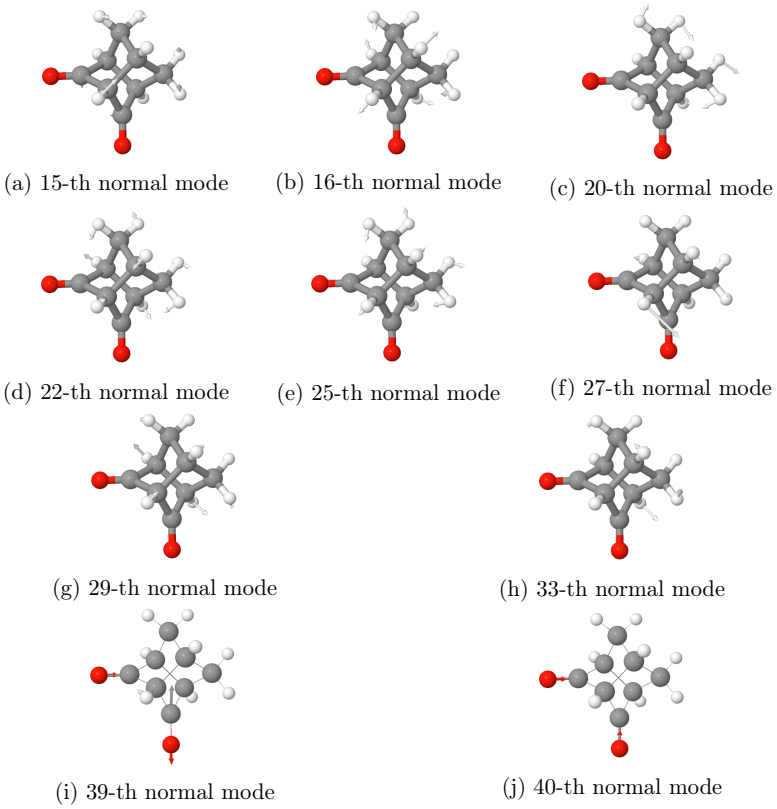

(a) 15-th normal mode (b) 16-th normal mode (c) 20-th normal mode

(d) 22-th normal mode (e) 25-th normal mode (f) 27-th normal mode

(g) 29-th normal mode (h) 33-th normal mode

(i) 39-th normal mode (j) 40-th normal mode

Figure C.4: Graphical representation of the normal modes of 2,4-STDO, numbered with respect to the associated fundamental frequency in ascending order; only the normal modes involved in the most intense vibronic transitions are reported (see table C.9).

transition	method			experimental (UPS)[4]
	KT (HF/maug-cc-pVTZ)	OVGF/maug-cc-pVTZ	NR2/maug-cc-pVTZ	
26a[$\pi_{CC}(+n+\sigma)$]	9.52	8.86 (0.899)	8.67 (0.870)[1]	8.65[5]
25a[$n(+\pi_{CC}+\sigma)$]	10.94	9.84 (0.892)	9.97 (0.862)[2]	9.77[5]
24a[$\sigma(+n)$]	12.22	11.07 (0.897)	11.11 (0.873)[3]	10.90[5]
23a[σ]	12.85	11.56 (0.899)	11.75 (0.878)	
22a[σ]	13.08	11.83 (0.900)	11.91 (0.878)[3]	11.5-12.5[6]
21a[σ]	13.20	12.01 (0.898)	12.03 (0.872)[3]	
20a[σ]	13.41	11.98 (0.897)	12.09 (0.874)	
19a[$\pi_{CO}(+\sigma)$]	14.09	13.04 (0.885)	12.70 (0.829)[3]	
18a[σ]	14.20	12.82 (0.900)	12.82 (0.838)[3]	12.5-13.5[6]
17a[σ]	14.47	13.21 (0.902)	-	
16a[$\pi_{CO}(+\sigma)$]	15.84	14.26 (0.880)	-	
15a[$\sigma(+n)$]	16.42	14.91 (0.873)	-	
14a[σ]	16.95	15.28 (0.889)	-	
13a[σ]	17.33	15.44 (0.884)	-	
12a[σ]	18.18	16.41 (0.883)	-	
11a[σ]	19.10	17.18 (0.880)	-	
10a[σ]	19.86	17.67 (0.869)	-	
9a[σ]	19.98	17.90 (0.877)	-	

Table C.10: values and assignment of each electronic transition for 2,4-STEO molecule.

[1] relevant contribution from MO 25a
[2] relevant contribution from MO 26a
[3] slight contributions from other MOs
[4] taken from ref. 250
[5] assignment proposed in ref. 250
[6] our assignment

transition	main contributions	energy (eV)	intensity (a. u.)
26a[$\pi_{CC}(+n+\sigma)$]	$\|0\rangle \rightarrow \|0\rangle$	8.491	$0.372 \cdot 10^{-1}$
	$\|0\rangle \rightarrow \|18(1)\rangle$	8.602	$0.193 \cdot 10^{-2}$
	$\|0\rangle \rightarrow \|21(1)\rangle$	8.605	$0.426 \cdot 10^{-2}$
	$\|0\rangle \rightarrow \|24(1)\rangle$	8.612	$0.244 \cdot 10^{-2}$
	$\|0\rangle \rightarrow \|25(1)\rangle$	8.620	$0.570 \cdot 10^{-2}$
	$\|0\rangle \rightarrow \|26(1)\rangle$	8.626	$0.394 \cdot 10^{-2}$
	$\|0\rangle \rightarrow \|27(1)\rangle$	8.628	$0.410 \cdot 10^{-2}$
	$\|0\rangle \rightarrow \|28(1)\rangle$	8.631	$0.710 \cdot 10^{-2}$
	$\|0\rangle \rightarrow \|29(1)\rangle$	8.634	$0.362 \cdot 10^{-2}$
	$\|0\rangle \rightarrow \|34(1)\rangle$	8.643	$0.309 \cdot 10^{-2}$
	$\|0\rangle \rightarrow \|37(1)\rangle$	8.651	$0.154 \cdot 10^{-2}$
	$\|0\rangle \rightarrow \|39(1)\rangle$	8.654	$0.247 \cdot 10^{-2}$
25a[$n(+\pi_{CC}+\sigma)$]	$\|0\rangle \rightarrow \|0\rangle$	9.805	$0.390 \cdot 10^{-1}$
	$\|0\rangle \rightarrow \|17(1)\rangle$	9.914	$0.153 \cdot 10^{-2}$
	$\|0\rangle \rightarrow \|21(1)\rangle$	9.919	$0.142 \cdot 10^{-1}$
	$\|0\rangle \rightarrow \|23(1)\rangle$	9.924	$0.449 \cdot 10^{-2}$
	$\|0\rangle \rightarrow \|24(1)\rangle$	9.926	$0.106 \cdot 10^{-1}$
	$\|0\rangle \rightarrow \|27(1)\rangle$	9.942	$0.287 \cdot 10^{-2}$
	$\|0\rangle \rightarrow \|34(1)\rangle$	9.957	$0.227 \cdot 10^{-2}$
	$\|0\rangle \rightarrow \|43(1)\rangle$	10.019	$0.526 \cdot 10^{-2}$
	$\|0\rangle \rightarrow \|21(2)\rangle$	10.033	$0.260 \cdot 10^{-2}$
	$\|0\rangle \rightarrow \|21(1);23(1)\rangle$	10.038	$0.164 \cdot 10^{-2}$
	$\|0\rangle \rightarrow \|21(1);24(1)\rangle$	10.040	$0.389 \cdot 10^{-2}$
	$\|0\rangle \rightarrow \|24(2)\rangle$	10.047	$0.145 \cdot 10^{-2}$
	$\|0\rangle \rightarrow \|21(1);43(1)\rangle$	10.133	$0.192 \cdot 10^{-2}$
	$\|0\rangle \rightarrow \|24(1);43(1)\rangle$	10.140	$0.144 \cdot 10^{-2}$

Table C.11: energies, intensities and assignments of the main vibronic transitions for the first and the second bands of the spectrum of 2,4-STEO molecule.

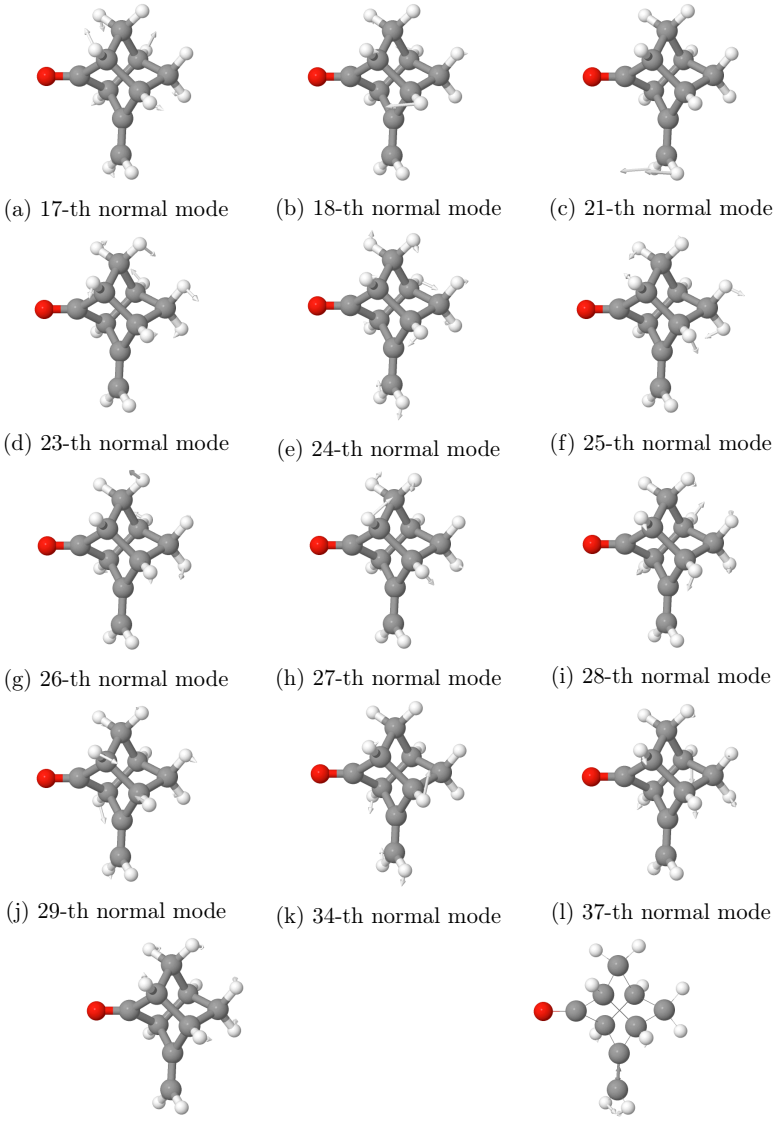

(a) 17-th normal mode (b) 18-th normal mode (c) 21-th normal mode

(d) 23-th normal mode (e) 24-th normal mode (f) 25-th normal mode

(g) 26-th normal mode (h) 27-th normal mode (i) 28-th normal mode

(j) 29-th normal mode (k) 34-th normal mode (l) 37-th normal mode

(m) 39-th normal mode (n) 43-th normal mode

Figure C.5: Graphical representation of the normal modes of 2,4-STEO, numbered with respect to the associated fundamental frequency in ascending order; only the normal modes involved in the most intense vibronic transitions are reported (see table C.11).

References

[1] A. Szabo and N. Ostlund. *Modern Quantum Chemistry: Introduction to Advanced Electronic Structure Theory*. Dover Books on Chemistry. Dover Publications, **1996**.

[2] D. Tannor. *Introduction to Quantum Mechanics. A Time-Dependent Perspective*. University Science Books, **2007**.

[3] F. Gatti, B. Lasorne, H. Meyer, and A. Nauts. *Applications of Quantum Dynamics in Chemistry*. Lecture Notes in Chemistry. Springer International Publishing, **2017**.

[4] B. T. Sutcliffe and R. G. Woolley. *Phys. Chem. Chem. Phys.*, 7:3664–3676, **2005**.

[5] E. Mátyus, J. Hutter, U. Müller-Herold, and M. Reiher. *Phys. Rev. A*, 83:052512, **2011**.

[6] E. Mátyus, J. Hutter, U. Müller-Herold, and M. Reiher. *J. Chem. Phys.*, 135(20):204302, **2011**.

[7] O. Christiansen. *Phys. Chem. Chem. Phys.*, 14:6672–6687, **2012**.

[8] H. B. Schlegel. *Wiley Interdiscip. Rev. Comput. Mol. Sci.*, 1(5):790–809, **2011**.

[9] R. M. Lewis, V. Torczon, and M. W. Trosset. *J. Comput. Appl. Math.*, 124(1):191 – 207, **2000**. Numerical Analysis 2000. Vol. IV: Optimization and Nonlinear Equations.

[10] U. García-Palomares and J. Rodríguez. *SIAM Journal on Optimization*, 13(1):79–96, **2002**.

[11] T. Kolda, R. Lewis, and V. Torczon. *SIAM Review*, 45(3):385–482, **2003**.

[12] M. J. Frisch, G. W. Trucks, H. B. Schlegel, G. E. Scuseria, M. A. Robb, J. R. Cheeseman, G. Scalmani, V. Barone, G. A. Petersson, H. Nakatsuji, X. Li, M. Caricato, A. V. Marenich, J. Bloino, B. G. Janesko,

R. Gomperts, B. Mennucci, H. P. Hratchian, J. V. Ortiz, A. F. Izmaylov, J. L. Sonnenberg, D. Williams-Young, F. Ding, F. Lipparini, F. Egidi, J. Goings, B. Peng, A. Petrone, T. Henderson, D. Ranasinghe, V. G. Zakrzewski, J. Gao, N. Rega, G. Zheng, W. Liang, M. Hada, M. Ehara, K. Toyota, R. Fukuda, J. Hasegawa, M. Ishida, T. Nakajima, Y. Honda, O. Kitao, H. Nakai, T. Vreven, K. Throssell, J. A. Montgomery, Jr., J. E. Peralta, F. Ogliaro, M. J. Bearpark, J. J. Heyd, E. N. Brothers, K. N. Kudin, V. N. Staroverov, T. A. Keith, R. Kobayashi, J. Normand, K. Raghavachari, A. P. Rendell, J. C. Burant, S. S. Iyengar, J. Tomasi, M. Cossi, J. M. Millam, M. Klene, C. Adamo, R. Cammi, J. W. Ochterski, R. L. Martin, K. Morokuma, O. Farkas, J. B. Foresman, and D. J. Fox. Gaussian 16 Revision A.03, **2016**. Gaussian Inc. Wallingford CT.

[13] X. Li and M. J. Frisch. *J. Chem. Theory Comput.*, 2(3):835–839, **2006**.

[14] J. Baker. *J. Comput. Chem.*, 14(9):1085–1100, **1993**.

[15] C. J. Cerjan and W. H. Miller. *J. Chem. Phys.*, 75(6):2800–2806, **1981**.

[16] A. Banerjee, N. Adams, J. Simons, and R. Shepard. *J. Phys. Chem.*, 89(1):52–57, **1985**.

[17] J. Baker. *J. Comput. Chem.*, 7(4):385–395, **1986**.

[18] J. Nichols, H. Taylor, P. Schmidt, and J. Simons. *J. Chem. Phys.*, 92(1):340–346, **1990**.

[19] P. Pulay. *Chem. Phys. Lett.*, 73(2):393 – 398, **1980**.

[20] P. Pulay. *J. Comput. Chem.*, 3(4):556–560, **1982**.

[21] P. Császár and P. Pulay. *J. Mol. Struct.*, 114:31 – 34, **1984**.

[22] K. N. Kudin, G. E. Scuseria, and E. Cancès. *J. Chem. Phys.*, 116(19):8255–8261, **2002**.

[23] Ö. Farkas and H. B. Schlegel. *Phys. Chem. Chem. Phys.*, 4:11–15, **2002**.

[24] C. Peng, P. Y. Ayala, H. B. Schlegel, and M. J. Frisch. *J. Comput. Chem.*, 17(1):49–56, **1996**.

[25] H. Bernhard Schlegel. *Theoretica chimica acta*, **1984**.

[26] P. Pulay and G. Fogarasi. *J. Chem. Phys.*, 96(4):2856–2860, **1992**.

[27] P. Pulay, G. Fogarasi, F. Pang, and J. E. Boggs. *J. Am. Chem. Soc.*, 101(10):2550–2560, **1979**.

[28] J. Baker, D. Kinghorn, and P. Pulay. *J. Chem. Phys.*, 110(11):4986–4991, **1999**.

[29] J. Gerratt and I. M. Mills. *J. Chem. Phys.*, 49(4):1719–1729, **1968**.

[30] P. Pulay. *Mol. Phys.*, 17(2):197–204, **1969**.

[31] J. A. Pople, P. M. Gill, and B. G. Johnson. *Chem. Phys. Lett.*, 199(6):557 – 560, **1992**.

[32] L. Han and M. Neumann. *Optimization Methods and Software*, 21(1):1–16, **2006**.

[33] A. R. Leach. A survey of methods for searching the conformational space of small and medium-sized molecules. In *Reviews in Computational Chemistry*, chapter 1, pages 1–55. John Wiley & Sons, Ltd, **1991**.

[34] E. B. Wilson, J. C. Decius, and P. C. Cross. *Molecular Vibrations: The Theory of Infrared and Raman Vibrational Spectra*. Dover Books on Chemistry. Dover Publications, New York, **1980**.

[35] J. F. Gaw, Y. Yamaguchi, H. F. Schaefer, and N. C. Handy. *J. Chem. Phys.*, 85(9):5132–5142, **1986**.

[36] S. M. Colwell, D. Jayatilaka, P. E. Maslen, R. D. Amos, and N. C. Handy. *Int. J. Quantum Chem.*, 40(2):179–199, **1991**.

[37] P. E. Maslen, D. Jayatilaka, S. M. Colwell, R. D. Amos, and N. C. Handy. *J. Chem. Phys.*, 95(10):7409–7417, **1991**.

[38] M. Ringholm, D. Jonsson, R. Bast, B. Gao, A. J. Thorvaldsen, U. Ekström, T. Helgaker, and K. Ruud. *J. Chem. Phys.*, 140(3):034103, **2014**.

[39] A. G. Császár. *Wiley Interdiscip. Rev. Comput. Mol. Sci.*, 2(2):273–289, **2012**.

[40] S. Carter, J. M. Bowman, and L. B. Harding. *Spectrochimica Acta Part A: Molecular and Biomolecular Spectroscopy*, 53(8):1179 – 1188, **1997**. Ab Initio and Ab Initio Derived Force Fields: State of the Science.

[41] G. Rauhut. *J. Chem. Phys.*, 121(19):9313–9322, **2004**.

[42] G. Rauhut and B. Hartke. *J. Chem. Phys.*, 131(1):014108, **2009**.

[43] B. J. Braams and J. M. Bowman. *Int. Rev. Phys. Chem.*, 28(4):577–606, **2009**.

[44] N. Sathyamurthy. *Comput. Phys. Rep.*, 3(1):1 – 69, **1985**.

[45] G. C. Schatz. *Rev. Mod. Phys.*, 61:669–688, **1989**.

[46] R. Jaquet. Interpolation and fitting of potential energy surfaces: Concepts, recipes and applications. In A. F. Sax, editor, *Potential Energy Surfaces*, pages 97–175, Berlin, Heidelberg, **1999**. Springer Berlin Heidelberg.

[47] J. Baker. *J. Comput. Chem.*, 13(2):240–253, **1992**.

[48] J. Baker and D. Bergeron. *J. Comput. Chem.*, 14(11):1339–1346, **1993**.

[49] R. H. Boyd and S. M. Breitling. *Macromolecules*, 5(1):1–7, **1972**.

[50] K. B. Wiberg and R. H. Boyd. *J. Am. Chem. Soc.*, 94(24):8426–8430, **1972**.

[51] B. van de Graaf, J. M. A. Baas, and A. van Veen. *Recueil des Travaux Chimiques des Pays-Bas*, 99(5):175–178, **1980**.

[52] B. van de Graaf and J. M. A. Baas. *J. Comput. Chem.*, 5(4):314–321, **1984**.

[53] J. Baker. *J. Comput. Chem.*, 18(8):1079–1095, **1997**.

[54] J. Baker, A. Kessi, and B. Delley. *J. Chem. Phys.*, 105(1):192–212, **1996**.

[55] D.-H. Lu, M. Zhao, and D. G. Truhlar. *J. Comput. Chem.*, 12(3):376–384, **1991**.

[56] D. Cremer and J. A. Pople. *J. Am. Chem. Soc.*, 97(6):1354–1358, **1975**.

[57] D. Cremer. *J. Phys. Chem.*, 94(14):5502–5509, **1990**.

[58] C. Altona and M. Sundaralingam. *J. Am. Chem. Soc.*, 94(23):8205–8212, **1972**.

[59] A. Wu, D. Cremer, A. A. Auer, and J. Gauss. *J. Phys. Chem. A*, 106(4):657–667, **2002**.

[60] D. Cremer. *Isr. J. Chem.*, 20(1-2):12–19, **1980**.

[61] D. Cremer. *Isr. J. Chem.*, 23(1):72–84, **1983**.

[62] S. Grimme. *J. Chem. Phys.*, 124(3):034108, **2006**.

[63] M. Biczysko, P. Panek, G. Scalmani, J. Bloino, and V. Barone. *J. Chem. Theory Comput.*, 6(7):2115–2125, **2010**.

[64] E. Penocchio, M. Piccardo, and V. Barone. *J. Chem. Theory Comput.*, 11(10):4689–4707, **2015**.

[65] C. Puzzarini and V. Barone. *Acc. Chem. Res.*, 51(2):548–556, **2018**.

[66] S. Grimme, S. Ehrlich, and L. Goerigk. *J. Comput. Chem.*, 32(7):1456–1465, **2011**.

[67] L. Goerigk and S. Grimme. *J. Chem. Theory Comput.*, 7(2):291–309, **2011**.

[68] E. Papajak, H. R. Leverentz, J. Zheng, and D. G. Truhlar. *J. Chem. Theory Comput.*, 5(5):1197–1202, **2009**.

[69] E. Papajak and D. G. Truhlar. *J. Chem. Theory Comput.*, 6(3):597–601, **2010**.

[70] T. H. Dunning. *J. Chem. Phys.*, 90(2):1007–1023, **1989**.

[71] R. A. Kendall, T. H. Dunning, and R. J. Harrison. *J. Chem. Phys.*, 96(9):6796–6806, **1992**.

[72] D. E. Woon and T. H. Dunning. *J. Chem. Phys.*, 98(2):1358–1371, **1993**.

[73] T. H. Dunning, K. A. Peterson, and A. K. Wilson. *J. Chem. Phys.*, 114(21):9244–9253, **2001**.

[74] W. J. Adams, H. J. Geise, and L. S. Bartell. *J. Am. Chem. Soc.*, 92(17):5013–5019, **1970**.

[75] L. E. Bauman and J. Laane. *J. Phys. Chem.*, 92(5):1040–1051, **1988**.

[76] E. J. Ocola, L. E. Bauman, and J. Laane. *J. Phys. Chem. A*, 115(24):6531–6542, **2011**.

[77] P. Kowalewski, H.-M. Frey, D. Infanger, and S. Leutwyler. *J. Phys. Chem. A*, 119(45):11215–11225, **2015**.

[78] W. Dong, H. Yang, Z. Qiu, and Y. Tang. *J. Electron Spectrosc. Relat. Phenom.*, 230:40 – 45, **2019**.

[79] W. J. Lafferty, D. W. Robinson, R. V. S. Louis, J. W. Russell, and H. L. Strauss. *J. Chem. Phys.*, 42(8):2915–2919, **1965**.

[80] H. Geise, W. Adams, and L. Bartell. *Tetrahedron Lett.*, 25(15):3045–3052, **1969**.

[81] G. G. Engerholm, A. C. Luntz, W. D. Gwinn, and D. O. Harris. *J. Chem. Phys.*, 50(6):2446–2457, **1969**.

[82] R. Meyer, J. C. López, J. L. Alonso, S. Melandri, P. G. Favero, and W. Caminati. *J. Chem. Phys.*, 111(17):7871–7880, **1999**.

[83] A. H. Mamleev, L. N. Gunderova, and R. V. Galeev. *J. Struct. Chem.*, **2001**.

[84] D. G. Melnik, S. Gopalakrishnan, T. A. Miller, and F. C. De Lucia. *J. Chem. Phys.*, 118(8):3589–3599, **2003**.

[85] T. Yang, G. Su, C. Ning, J. Deng, F. Wang, S. Zhang, X. Ren, and Y. Huang. *J. Phys. Chem. A*, 111(23):4927–4933, **2007**.

[86] A. Giuliani, P. Limão-Vieira, D. Duflot, A. R. Milosavljevic, B. P. Marinkovic, S. V. Hoffmann, N. Mason, J. Delwiche, and M.-J. Hubin-Franskin. *Eur. Phys. J. D*, **2009**.

[87] B. Cadioli, E. Gallinella, C. Coulombeau, H. Jobic, and G. Berthier. *J. Phys. Chem.*, 97(30):7844–7856, **1993**.

[88] S. J. Han and Y. K. Kang. *J. Mol. Struct.: THEOCHEM*, 369(1):157–165, **1996**.

[89] A. Wu and D. Cremer. *Int. J. Mol. Sci.*, 4(4):158–192, **2003**.

[90] V. M. Rayón and J. A. Sordo. *J. Chem. Phys.*, 122(20):204303, **2005**.

[91] P. Duffy, J. A. Sordo, and F. Wang. *J. Chem. Phys.*, 128(12):125102, **2008**.

[92] B. N. Z. Náhlovská and H. M. Seip. *Acta Chem. Scand.*, 23:3534–3540, **1969**.

[93] D. W. Wertz. *J. Chem. Phys.*, 51(5):2133–2136, **1969**.

[94] T. Smithson and H. Wieser. *J. Mol. Spectrosc.*, 99(1):159–166, **1983**.

[95] A. K. Mamleev and I. M. Pozdeev. *J. Struct. Chem.*, **1969**.

[96] L. Margulès, M. E. Sanz, S. Kassi, D. Petitprez, G. Wlodarczak, J. C. López, and J. E. Boggs. *Chem. Phys.*, 263(1):19–31, **2001**.

[97] D. J. Coughlin, R. S. Brown, and R. G. Salomon. *J. Am. Chem. Soc.*, 101(6):1533–1539, **1979**.

[98] T. Kondo, M. Tanimoto, M. Matsumoto, K. Nomoto, Y. Achiba, and K. Kimura. *Tetrahedron Lett. Letters*, 21(17):1649–1652, **1980**.

[99] Q. Shen, T. L. Mathers, T. Raeker, and R. L. Hilderbrandt. *J. Am. Chem. Soc.*, 108(22):6888–6893, **1986**.

[100] P. A. Baron and D. O. Harris. *J. Mol. Spectrosc.*, 49(1):70–81, **1974**.

[101] A. K. Mamleev, L. N. Gunderova, R. V. Galeev, and A. A. Shapkin. *J. Struct. Chem.*, **2002**.

[102] A. K. Mamleev, L. N. Gunderova, R. V. Galeev, and A. A. Shapkin. *J. Struct. Chem.*, **2004**.

[103] J. R. Durig and D. W. Wertz. *J. Chem. Phys.*, 49(2):675–679, **1968**.

[104] J. A. Greenhouse and H. L. Strauss. *J. Chem. Phys.*, 50(1):124–134, **1969**.

[105] D. Cremer and J. A. Pople. *J. Am. Chem. Soc.*, 97(6):1358–1367, **1975**.

[106] H. Fuhrer and H. H. Günthard. *Helv. Chim. Acta*, 45(6):2036–2042, **1962**.

[107] L. A. Sternson, D. A. Coviello, and R. S. Egan. *J. Am. Chem. Soc.*, 93(24):6529–6532, **1971**.

[108] F. S. Jørgensen and L. Carlsen. *Chem. Ber.*, 116(6):2374–2377, **1983**.

[109] S. J. Leibowitz, J. Laane, R. Verastegui, and J. R. Villarreal. *J. Chem. Phys.*, 96(10):7298–7305, **1992**.

[110] J. E. Kilpatrick, K. S. Pitzer, and R. Spitzer. *J. Am. Chem. Soc.*, 69(10):2483–2488, **1947**.

[111] D. J. Wilkins. Five-membered heterocycles with two heteroatoms: O and S derivatives. In *Modern Heterocyclic Chemistry*, chapter 11, pages 925–988. Wiley, **2011**.

[112] L. A. Nafie. *Chirality*, 32(5):667–692, **2020**.

[113] E. C. Hsu and G. Holzwarth. *J. Chem. Phys.*, 59(9):4678–4685, **1973**.

[114] G. Holzwarth, E. C. Hsu, H. S. Mosher, T. R. Faulkner, and A. Moscowitz. *J. Am. Chem. Soc.*, 96(1):251–252, **1974**.

[115] L. A. Nafie, J. C. Cheng, and P. J. Stephens. *J. Am. Chem. Soc.*, 97(13):3842–3843, **1975**.

[116] L. A. Nafie, T. A. Keiderling, and P. J. Stephens. *J. Am. Chem. Soc.*, 98(10):2715–2723, **1976**.

[117] H. Kroto. *Molecular Rotation Spectra*. Dover books on physics and chemistry. Dover Publications, **1992**.

[118] A. G. Császár, C. Fábri, and J. Sarka. *WIREs Computational Molecular Science*, 10(1):e1432, **2019**.

[119] E. B. Wilson and J. B. Howard. *J. Chem. Phys.*, 4(4):260–268, **1936**.

[120] B. T. Darling and D. M. Dennison. *Phys. Rev.*, 57:128–139, **1940**.

[121] J. K. Watson. *Mol. Phys.*, 15(5):479–490, **1968**.

[122] L. Schaad and J. Hu. *J. Mol. Struct.: THEOCHEM*, 185:203 – 215, **1989**.

[123] B. Podolsky. *Phys. Rev.*, 32:812–816, **1928**.

[124] S. Carter and N. Handy. *Comput. Phys. Rep.*, 5(3):117 – 171, **1986**.

[125] D. Lauvergnat and A. Nauts. *J. Chem. Phys.*, 116(19):8560–8570, **2002**.

[126] A. Nauts and X. Chapuisat. *Mol. Phys.*, 55(6):1287–1318, **1985**.

[127] A. G. Császár and N. C. Handy. *J. Chem. Phys.*, 102(10):3962–3967, **1995**.

[128] S. B. Rempe and R. O. Watts. *J. Chem. Phys.*, 108(24):10084–10095, **1998**.

[129] J. H. Frederick and C. Woywod. *J. Chem. Phys.*, 111(16):7255–7271, **1999**.

[130] N. Handy. *Mol. Phys.*, 61(1):207–223, **1987**.

[131] M. Ndong, L. Joubert-Doriol, H.-D. Meyer, A. Nauts, F. Gatti, and D. Lauvergnat. *J. Chem. Phys.*, 136(3):034107, **2012**.

[132] M. Ndong, A. Nauts, L. Joubert-Doriol, H.-D. Meyer, F. Gatti, and D. Lauvergnat. *J. Chem. Phys.*, 139(20):204107, **2013**.

[133] H.-J. Werner, P. J. Knowles, G. Knizia, F. R. Manby, M. Schütz, P. Celani, W. Györffy, D. Kats, T. Korona, R. Lindh, A. Mitrushenkov, G. Rauhut, K. R. Shamasundar, T. B. Adler, R. D. Amos, S. J. Bennie, A. Bernhardsson, A. Berning, D. L. Cooper, M. J. O. Deegan, A. J. Dobbyn, F. Eckert, E. Goll, C. Hampel, A. Hesselmann, G. Hetzer, T. Hrenar, G. Jansen, C. Köppl, S. J. R. Lee, Y. Liu, A. W. Lloyd, Q. Ma, R. A. Mata, A. J. May, S. J. McNicholas, W. Meyer, T. F. Miller III, M. E. Mura, A. Nicklass, D. P. O'Neill, P. Palmieri, D. Peng, K. Pflüger, R. Pitzer, M. Reiher, T. Shiozaki, H. Stoll, A. J. Stone, R. Tarroni, T. Thorsteinsson, M. Wang, and M. Welborn. Molpro, version 2019.2, a package of ab initio programs, **2019**. see https://www.molpro.net.

[134] P. Jensen. *Mol. Phys.*, 98(17):1253–1285, **2000**.

[135] P. Jensen. *WIREs Computational Molecular Science*, 2(3):494–512, **2012**.

[136] R. Meyer. *J. Mol. Spectrosc.*, 76(1):266–300, **1979**.

[137] A. M. Rosnik and W. F. Polik. *Mol. Phys.*, 112(2):261–300, **2014**.

[138] E. Fermi. *Zeitschrift für Physik*, **1931**.

[139] J. M. L. Martin, T. J. Lee, P. R. Taylor, and J.-P. François. *J. Chem. Phys.*, 103(7):2589–2602, **1995**.

[140] J. M. Martin and P. R. Taylor. *Spectrochimica Acta Part A: Molecular and Biomolecular Spectroscopy*, 53(8):1039 – 1050, **1997**. Ab Initio and Ab Initio Derived Force Fields: State of the Science.

[141] L. Halonen. Local mode vibrations in polyatomic molecules. In *Advances in Chem. Phys.*, pages 41–179. John Wiley & Sons, Ltd, **1998**.

[142] L. Halonen. *Chem. Phys. Lett.*, 87(3):221 – 225, **1982**.

[143] S. Abbate, E. Castiglioni, F. Gangemi, R. Gangemi, and G. Longhi. *Chirality*, 21(1E):E242–E252, **2009**.

[144] F. Gangemi, R. Gangemi, G. Longhi, and S. Abbate. *Phys. Chem. Chem. Phys.*, 11:2683–2689, **2009**.

[145] F. Gangemi, R. Gangemi, G. Longhi, and S. Abbate. *Vib. Spectrosc.*, 50(2):257 – 267, **2009**.

[146] K. K. Lehmann. *J. Chem. Phys.*, 79(2):1098–1098, **1983**.

[147] I. Mills and A. Robiette. *Mol. Phys.*, 56(4):743–765, **1985**.

[148] W. Zou, R. Kalescky, E. Kraka, and D. Cremer. *J. Chem. Phys.*, 137(8):084114, **2012**.

[149] J. Bloino and V. Barone. *J. Chem. Phys.*, 136(12):124108, **2012**.

[150] L. Nafie. *Vibrational Optical Activity: Principles and Applications*. Wiley, **2011**.

[151] A. Willetts, N. C. Handy, W. H. Green, and D. Jayatilaka. *J. Phys. Chem.*, 94(14):5608–5616, **1990**.

[152] C. Secroun, A. Barbe, and P. Jouve. *J. Mol. Spectrosc.*, 45(1):1 – 9, **1973**.

[153] S. Yao and J. Overend. *Spectrochimica Acta Part A: Molecular Spectroscopy*, 32(5):1059 – 1065, **1976**.

[154] P. Geerlings, D. Berckmans, and H. Figeys. *J. Mol. Struct.*, 57:283 – 297, **1979**.

[155] J. Vázquez and J. F. Stanton. *Mol. Phys.*, 104(3):377–388, **2006**.

[156] V. Barone, J. Bloino, C. A. Guido, and F. Lipparini. *Chem. Phys. Lett.*, 496(1):157 – 161, **2010**.

[157] K. L. Bak, O. Bludský, and P. Jørgensen. *J. Chem. Phys.*, 103(24):10548–10555, **1995**.

[158] J. Bloino. *J. Phys. Chem. A*, 119(21):5269–5287, **2015**.

[159] J. F. Biarge, J. Herranz, and J. Morcillo. *An. R. Soc. Esp. Fis. Quim. A*, 57:81, **1961**.

[160] W. B. Person and J. H. Newton. *J. Chem. Phys.*, 61(3):1040–1049, **1974**.

[161] P. J. Stephens. *J. Phys. Chem.*, 91(7):1712–1715, **1987**.

[162] M. Fusè, G. Mazzeo, G. Longhi, S. Abbate, M. Masi, A. Evidente, C. Puzzarini, and V. Barone. *J. Phys. Chem. B*, 123(43):9230–9237, **2019**.

[163] L. P. Kuhn. *J. Am. Chem. Soc.*, 80(22):5950–5954, **1958**.

[164] K. Yamamoto, Y. Nakao, Y. Kyogoku, and H. Sugeta. *J. Mol. Struct.*, 242:75 – 86, **1991**.

[165] F. Wang and P. L. Polavarapu. *J. Phys. Chem. A*, 105(29):6991–6997, **2001**.

[166] A. J. Lopes Jesus, M. T. S. Rosado, I. Reva, R. Fausto, M. E. Eusébio, and J. S. Redinha. *J. Phys. Chem. A*, 110(12):4169–4179, **2006**.

[167] J. Paul, I. Hearn, and B. J. Howard. *Mol. Phys.*, 105(5-7):825–839, **2007**.

[168] X. Ma and J. Wang. *J. Phys. Chem. A*, 113(21):6070–6076, **2009**.

[169] S. Daly, M. Tia, G. A. Garcia, L. Nahon, and I. Powis. *Angew. Chem. Int. Ed.*, 55(37):11054–11058, **2016**.

[170] S. Daly, I. Powis, G. A. Garcia, M. Tia, and L. Nahon. *J. Chem. Phys.*, 147(1):013937, **2017**.

[171] X. Chen, D. A. Walthall, and J. I. Brauman. *J. Am. Chem. Soc.*, 126(39):12614–12620, **2004**.

[172] A. L. Jesus and J. Redinha. *J. Mol. Struct.*, 1067:104 – 111, **2014**.

[173] R. Sillanpää, M. Leskelä, and L. Hiltunen. *Acta Chemica Scandinavica*, 38 B:249–254, **1984**.

[174] P. Thorey, P. Bombicz, I. M. Szilágyi, P. Molnár, G. Bánsághi, E. Székely, B. Simándi, L. Párkányi, G. Pokol, and J. Madarász. *Thermochim. Acta*, 497(1):129 – 136, **2010**.

[175] E. Castiglioni, F. Lebon, G. Longhi, and S. Abbate. *Enantiomer*, 7(4-5):161–173, **2002**.

[176] C. Lee, W. Yang, and R. G. Parr. *Phys. Rev. B*, 37:785–789, **1988**.

[177] A. D. Becke. *Phys. Rev. A*, 38:3098–3100, **1988**.

[178] A. D. Becke. *J. Chem. Phys.*, 98(7):5648–5652, **1993**.

[179] E. Papajak and D. G. Truhlar. *J. Chem. Theory Comput.*, 7(1):10–18, **2011**.

[180] E. Papajak, J. Zheng, X. Xu, H. R. Leverentz, and D. G. Truhlar. *J. Chem. Theory Comput.*, 7(10):3027–3034, **2011**.

[181] L. Goerigk and S. Grimme. *J. Chem. Theory Comput.*, 6(1):107–126, **2010**.

[182] C. Cappelli, F. Lipparini, J. Bloino, and V. Barone. *J. Chem. Phys.*, 135(10):104505, **2011**.

[183] C. Cappelli, J. Bloino, F. Lipparini, and V. Barone. *J. Phys. Chem. Letters*, 3(13):1766–1773, **2012**.

[184] A. Schäfer, H. Horn, and R. Ahlrichs. *J. Chem. Phys.*, 97(4):2571–2577, **1992**.

[185] A. Schäfer, C. Huber, and R. Ahlrichs. *J. Chem. Phys.*, 100(8):5829–5835, **1994**.

[186] T. Kuppens, W. Langenaeker, J. P. Tollenaere, and P. Bultinck. *J. Phys. Chem. A*, 107(4):542–553, **2003**.

[187] J. Shen, C. Zhu, S. Reiling, and R. Vaz. *Spectrochimica Acta Part A: Molecular and Biomolecular Spectroscopy*, 76(3):418 – 422, **2010**.

[188] C. L. Covington and P. L. Polavarapu. *Chirality*, 29(5):178–192, **2017**.

[189] L. Dai and X. Hou, editors. *Chiral Ferrocenes in Asymmetric Catalysis: Synthesis and Applications*. Wiley, **2010**.

[190] Y. He, X. Cao, L. A. Nafie, and T. B. Freedman. *J. Am. Chem. Soc.*, 123(45):11320–11321, **2001**.

[191] P. Stephens, F. Devlin, C. Villani, F. Gasparrini, and S. L. Mortera. *Inorganica Chimica Acta*, 361(4):987 – 999, **2008**. Protagonists in Chemistry: Professor Edward I Solomon.

[192] C. Merten, K. Hiller, and Y. Xu. *Phys. Chem. Chem. Phys.*, 14:12884–12891, **2012**.

[193] G. Mazzeo, M. Fusè, G. Longhi, I. Rimoldi, E. Cesarotti, A. Crispini, and S. Abbate. *Dalton Trans.*, 45:992–999, **2016**.

[194] C. Latouche, F. Palazzetti, D. Skouteris, and V. Barone. *J. Chem. Theory Comput.*, 10(10):4565–4573, **2014**.

[195] F. Weigend and R. Ahlrichs. *Phys. Chem. Chem. Phys.*, 7:3297–3305, **2005**.

[196] J. Linderberg and Y. Öhrn. *Propagators in Quantum Chemistry*. Theoretical chemistry. Wiley, **2004**.

[197] J. V. Ortiz. *WIREs Computational Molecular Science*, 3(2):123–142, **2013**.

[198] R. Mattuck. *A Guide to Feynman Diagrams in the Many-body Problem*. Dover Books on Physics Series. Dover Publications, **1992**.

[199] Y. Öhrn and J. Ortiz. *Mol. Phys.*, 108(21-23):2871–2875, **2010**.

[200] T. Koopmans. *Physica*, 1(1):104 – 113, **1934**.

[201] B. Pickup and O. Goscinski. *Mol. Phys.*, 26(4):1013–1035, **1973**.

[202] O. Goscinski and B. Lukman. *Chem. Phys. Lett.*, 7(6):573 – 576, **1970**.

[203] J. Baker. *Chem. Phys.*, 79(1):117 – 128, **1983**.

[204] D. Bernstein. *Matrix Mathematics: Theory, Facts, and Formulas (Second Edition)*. Princeton University Press, **2009**.

[205] J. Baker and B. Pickup. *Chem. Phys. Lett.*, 76(3):537 – 541, **1980**.

[206] Y. Shigeta, A. M. Ferreira, V. G. Zakrzewski, and J. V. Ortiz. *Int. J. Quantum Chem.*, 85(4-5):411–420, **2001**.

[207] G. D. Purvis and Y. Öhrn. *J. Chem. Phys.*, 65(3):917–922, **1976**.

[208] J. V. Ortiz. *Int. J. Quantum Chem.*, 40(S25):35–42, **1991**.

[209] L. T. Redmon, G. Purvis, and Y. Öhrn. *J. Chem. Phys.*, 63(11):5011–5017, **1975**.

[210] S. Hirata, A. E. Doran, P. J. Knowles, and J. V. Ortiz. *J. Chem. Phys.*, 147(4):044108, **2017**.

[211] J. Simons and W. D. Smith. *J. Chem. Phys.*, 58(11):4899–4907, **1973**.

[212] G. D. Purvis and Y. Öhrn. *Chem. Phys. Lett.*, 33(2):396 – 398, **1975**.

[213] G. Born, H. A. Kurtz, and Y. Öhrn. *J. Chem. Phys.*, 68(1):74–85, **1978**.

[214] A. M. Ferreira, G. Seabra, O. Dolgounitcheva, V. G. Zakrzewski, and J. V. Ortiz. Application and testing of diagonal, partial third-order electron propagator approximations. In *Quantum-Mechanical Prediction of Thermochemical Data*, chapter 5.

[215] L. S. Cederbaum. *J. Phys. B*, 8(2):290–303, **1975**.

[216] W. von Niessen, J. Schirmer, and L. Cederbaum. *Comput. Phys. Rep.*, 1(2):57 – 125, **1984**.

[217] V. G. Zakrzewski, J. V. Ortiz, J. A. Nichols, D. Heryadi, D. L. Yeager, and J. T. Golab. *Int. J. Quantum Chem.*, 60(1):29–36, **1996**.

[218] M. S. Deleuze. *J. Chem. Phys.*, 116(16):7012–7026, **2002**.

[219] X.-B. Wang, C.-F. Ding, L.-S. Wang, A. I. Boldyrev, and J. Simons. *J. Chem. Phys.*, 110(10):4763–4771, **1999**.

[220] A. P. Wickrama Arachchilage, F. Wang, V. Feyer, O. Plekan, and K. C. Prince. *J. Chem. Phys.*, 136(12):124301, **2012**.

[221] P. M. Mishra, L. Avaldi, P. Bolognesi, K. C. Prince, R. Richter, and U. R. Kadhane. *J. Phys. Chem. A*, 118(17):3128–3135, **2014**.

[222] J. Schirmer, L. Cederbaum, W. Domcke, and W. von Niessen. *Chem. Phys.*, 26(1):149 – 153, **1977**.

[223] L. S. Cederbaum, J. Schirmer, W. Domcke, and W. von Niessen. *J. Phys. B*, 10(15):L549–L553, **1977**.

[224] J. V. Ortiz. *J. Chem. Phys.*, 108(3):1008–1014, **1998**.

[225] J. V. Ortiz. *J. Chem. Phys.*, 104(19):7599–7605, **1996**.

[226] V. G. Zakrzewski, O. Dolgounitcheva, and J. V. Ortiz. *Int. J. Quantum Chem.*, 75(4-5):607–614, **1999**.

[227] H. H. Corzo, A. Galano, O. Dolgounitcheva, V. G. Zakrzewski, and J. V. Ortiz. *J. Phys. Chem. A*, 119(33):8813–8821, **2015**.

[228] J. V. Ortiz. *Int. J. Quantum Chem.*, 70(4-5):651–658, **1998**.

[229] F. Duschinsky. *Acta Physicochimica U.R.S.S.*, 7:551–556, **1937**.

[230] A. Warshel and M. Karplus. *Chem. Phys. Lett.*, 17(1):7 – 14, **1972**.

[231] İlker Özkan. *J. Mol. Spectrosc.*, 139(1):147 – 162, **1990**.

[232] J. Franck. *Trans. Faraday Soc.*, 21:536–542, **1926**.

[233] E. U. Condon. *Phys. Rev.*, 32:858–872, **1928**.

[234] G. Herzberg and E. Teller. *Zeitschrift für Physikalische Chemie*, 21B(1):410–446, **1933**.

[235] T. E. Sharp and H. M. Rosenstock. *J. Chem. Phys.*, 41(11):3453–3463, **1964**.

[236] R. Islampour, M. Dehestani, and S. Lin. *J. Mol. Spectrosc.*, 194(2):179 – 184, **1999**.

[237] E. Doktorov, I. Malkin, and V. Man'ko. *J. Mol. Spectrosc.*, 64(2):302 – 326, **1977**.

[238] P. T. Ruhoff. *Chem. Phys.*, 186(2):355 – 374, **1994**.

[239] A. Hazra and M. Nooijen. *Int. J. Quantum Chem.*, 95(4-5):643–657, **2003**.

[240] R. Berger and M. Klessinger. *J. Comput. Chem.*, 18(10):1312–1319, **1997**.

[241] M. Dierksen and S. Grimme. *J. Chem. Phys.*, 122(24):244101, **2005**.

[242] H.-C. Jankowiak, J. L. Stuber, and R. Berger. *J. Chem. Phys.*, 127(23):234101, **2007**.

[243] F. Santoro, R. Improta, A. Lami, J. Bloino, and V. Barone. *J. Chem. Phys.*, 126(8):084509, **2007**.

[244] F. Santoro, A. Lami, R. Improta, and V. Barone. *J. Chem. Phys.*, 126(18):184102, **2007**.

[245] V. Barone, J. Bloino, M. Biczysko, and F. Santoro. *J. Chem. Theory Comput.*, 5(3):540–554, **2009**.

[246] J. Bloino, M. Biczysko, F. Santoro, and V. Barone. *J. Chem. Theory Comput.*, 6(4):1256–1274, **2010**.

[247] M. Nakazaki, K. Naemura, and Y. Kondo. *J. Org. Chem.*, 41(7):1229–1233, **1976**.

[248] M. Nakazaki, K. Naemura, H. Harada, and H. Narutaki. *J. Org. Chem.*, 47(18):3470–3474, **1982**.

[249] B. Kissler and R. Gleiter. *Tetrahedron Lett.*, 26(2):185 – 188, **1985**.

[250] R. Gleiter, B. Gaa, C. Sigwart, H. Lange, O. Borzyk, F. Rominger, H. Irngartinger, and T. Oeser. *Eur. J. Org. Chem.*, 1998(1):171–176, **1998**.

[251] R. Gleiter, H. Lange, and O. Borzyk. *J. Am. Chem. Soc.*, 118(20):4889–4895, **1996**.

[252] J. Cioslowski and J. V. Ortiz. *J. Chem. Phys.*, 96(11):8379–8389, **1992**.

[253] J. V. Ortiz. *J. Chem. Phys.*, 112(1):56–68, **2000**.

[254] J. V. Ortiz. *J. Chem. Phys.*, 97(10):7531–7536, **1992**.

[255] J. V. Ortiz. *J. Chem. Phys.*, 99(9):6727–6731, **1993**.

[256] J. Ortiz. *Chem. Phys. Lett.*, 214(5):467 – 472, **1993**.

[257] L. S. Cederbaum and W. Domcke. *J. Chem. Phys.*, 60(7):2878–2889, **1974**.

[258] L. S. Cederbaum and W. Domcke. *J. Chem. Phys.*, 64(2):603–611, **1976**.

[259] W. Domcke, L. Cederbaum, H. Köppel, and W. von Niessen. *Mol. Phys.*, 34(6):1759–1770, **1977**.

[260] D. Holland, A. Potts, L. Karlsson, I. Zaytseva, A. Trofimov, and J. Schirmer. *Chem. Phys.*, 353(1):47 – 58, **2008**.

[261] M. Wehrle, S. Oberli, and J. Vaníček. *J. Phys. Chem. A*, 119(22):5685–5690, **2015**.

[262] S. Melandri, L. Evangelisti, S. Canola, H. Sa'adeh, C. Calabrese, M. Coreno, C. Grazioli, K. C. Prince, F. Negri, and A. Maris. *Phys. Chem. Chem. Phys.*, 22:13440–13455, **2020**.

[263] M. Biczysko, J. Bloino, F. Santoro, and V. Barone. Time-independent approaches to simulate electronic spectra lineshapes: From small molecules to macrosystems. In *Computational Strategies for Spectroscopy*, chapter 8, pages 361–443. John Wiley & Sons, Ltd, **2011**.

[264] S. Knippenberg, J.-P. François, and M. S. Deleuze. *J. Comput. Chem.*, 27(14):1703–1722, **2006**.

[265] A. Baiardi. *Development of computational methods for the simulation of vibrational and electronic spectra of medium-to-large sized molecular systems*. PhD thesis, Scuola Normale Superiore, **2018**.

[266] E. B. Wilson. *J. Chem. Phys.*, 7(11):1047–1052, **1939**.

[267] K. Brandhorst and J. Grunenberg. *J. Chem. Phys.*, 132(18):184101, **2010**.

[268] M. Gussoni, G. Dellepiane, and S. Abbate. *J. Mol. Spectrosc.*, 57(3):323 – 330, **1975**.

[269] R. Meyer and H. H. Günthard. *J. Chem. Phys.*, 49(4):1510–1520, **1968**.

[270] H. M. Pickett. *J. Chem. Phys.*, 56(4):1715–1723, **1972**.

[271] A. Hoy, I. Mills, and G. Strey. *Mol. Phys.*, 24(6):1265–1290, **1972**.

[272] L. A. Nafie and T. B. Freedman. *J. Chem. Phys.*, 78(12):7108–7116, **1983**.

[273] L. A. Nafie. *J. Chem. Phys.*, 79(10):4950–4957, **1983**.

[274] G. Orlandi and W. Siebrand. *J. Chem. Phys.*, 58(10):4513–4523, **1973**.

[275] L. A. Nafie. *J. Phys. Chem. A*, 108(35):7222–7231, **2004**.

[276] P. J. Stephens. *J. Phys. Chem.*, 89(5):748–752, **1985**.

[277] D. L. Howard, P. Jørgensen, and H. G. Kjaergaard. *J. Am. Chem. Soc.*, 127(48):17096–17103, **2005**.

[278] K. M. Kuhler, D. G. Truhlar, and A. D. Isaacson. *J. Chem. Phys.*, 104(12):4664–4671, **1996**.

[279] V. Barone. *J. Chem. Phys.*, 122(1):014108, **2005**.

[280] J. Bloino, M. Biczysko, and V. Barone. *J. Chem. Theory Comput.*, 8(3):1015–1036, **2012**.

[281] R. D. Amos, N. C. Handy, W. H. Green, D. Jayatilaka, A. Willetts, and P. Palmieri. *J. Chem. Phys.*, 95(11):8323–8336, **1991**.

[282] P.-O. Löwdin. *Phys. Rev.*, 139:A357–A372, **1965**.

[283] N. W. Bazley. *J. Math. Mech.*, 10(2):289–307, **1961**.

[284] C. Nehrkorn, G. D. Purvis, and Y. Öhrn. *J. Chem. Phys.*, 64(4):1752–1756, **1976**.

[285] R. Flores-Moreno, V. G. Zakrzewski, and J. V. Ortiz. *J. Chem. Phys.*, 127(13):134106, **2007**.